UC San Diego

UC San Diego Electronic Theses and Dissertations

Title

Seismogeodesy and Rapid Earthquake and Tsunami Source Assessment /

Permalink

https://escholarship.org/uc/item/6s38g4h2

Author

Melgar Moctezuma, Diego

Publication Date

2014

Peer reviewed|Thesis/dissertation

eScholarship.org Powered by the California Digital Library
University of California

UNIVERSITY OF CALIFORNIA, SAN DIEGO

Seismogeodesy and Rapid Earthquake and Tsunami Source Assessment

A dissertation submitted in partial satisfaction of the
requirements for the degree
Doctor of Philosophy

in

Earth Sciences

by

Diego Melgar Moctezuma

Committee in charge:

Yehuda Bock, Chair
Thomas Guy Masters
Jose Ignacio Restrepo
David Thomas Sandwell
Peter Marston Shearer

2014

Copyright
Diego Melgar Moctezuma, 2014
All rights reserved.

The dissertation of Diego Melgar Moctezuma is approved, and it is acceptable in quality and form for publication on microfilm and electronically:

_____

_____

_____

_____

_____
Chair

University of California, San Diego

2014

DEDICATION

To my family.

EPIGRAPH

Every solution of a problem raises new unsolved problems; the more so the deeper the original problem and the bolder its solution. The more we learn about the world, and the deeper our learning, the more conscious, specific, and articulate will be our knowledge of what we do not know, our knowledge of our ignorance. For this, indeed, is the main source of our ignorance – the fact that our knowledge can be only finite, while our ignorance must necessarily be infinite.

— *Karl R. Popper*, Conjectures and Refutations

TABLE OF CONTENTS

Signature Page iii

Dedication iv

Epigraph v

Table of Contents vi

List of Figures ix

List of Tables xiii

Acknowledgements xiv

Vita xvii

Abstract of the Dissertation xix

Chapter 1 Introduction 1

Chapter 2 Seismogeodesy 7
2.1 Background on Strong Motion Sensing 7
2.2 The Role of GPS 14
2.2.1 Displacements in a Local Reference Frame 18
2.3 Optimal Combination of Seismic and Geodetic Data . . . 19
2.3.1 The Kalman Filter Formulation 20
2.3.2 Optimal Smoothing 25
2.3.3 Accelerometer Biases 26
2.4 Proof of Concept 28
2.4.1 Outdoor Shake Table Testing 28
2.4.2 The 2010 M_w7.2 El Mayor-Cucapah Earthquake . 35
2.4.3 Spectral Characteristics 41
2.4.4 Selecting the Kalman Filter Variances 43
2.4.5 Lessons and Insights 47
2.5 Application to the M_w9 Tohoku-oki Earthquake 51
2.5.1 Time Domain Analysis 53
2.5.2 Frequency Domain Analysis 57
2.5.3 Performance of the Filter and Prospects for Automated Baseline Corrections 61
2.6 Acknowledgments 66

Chapter 3 Rapid Static Modeling . . . 68
3.1 Centroid Moment Tensor Inversion . . . 70
3.1.1 Point Source Models . . . 72
3.1.2 Applications of the Point Source Approach . . . 76
3.1.3 Final Point Source Solutions . . . 85
3.1.4 Implementation Issues and Necessary Improvements 92
3.1.5 Violation of the Point Source Assumption, the M_w9 Tohoku-oki Earthquake . . . 96
3.1.6 The Finite Extent CMT Approach . . . 97
3.2 Static Slip Inversions . . . 103
3.2.1 Timeline of Event Analysis . . . 105
3.3 Acknowledgments . . . 107

Chapter 4 Kinematic Source Inversions . . . 109
4.1 Background . . . 109
4.2 The Inverse Problem . . . 114
4.2.1 Spatial Regularization . . . 116
4.2.2 Bayesian Modeling . . . 118
4.3 An Example with Seismogeodetic Data, the 2011 M_w9 Tohoku-oki Earthquake . . . 121
4.3.1 Kinematic Inversion Results . . . 124
4.3.2 The Effect of Spatial Regularization . . . 129
4.3.3 The Displacement-only Solution . . . 133
4.3.4 Implications of the Model . . . 135
4.3.5 Suitability for Rapid Implementation . . . 140
4.4 Acknowledgements . . . 143

Chapter 5 Offshore Data and Tsunami Modeling . . . 144
5.1 Background . . . 145
5.2 Static Modeling: Data and Method . . . 150
5.2.1 Description . . . 150
5.2.2 Linearity in Tsunami Propagation . . . 155
5.3 Inversion and Forecast Results . . . 159
5.4 Limitations and Implications for Warning . . . 164
5.5 Joint Kinematic Inversion of Land- and Ocean-Based Sensors . . . 174
5.5.1 Tsunami Generation with 3D Coseismic Motion . 175
5.5.2 Inversion Results . . . 177
5.5.3 Tsunami Modeling Results . . . 183
5.6 Acknowledgments . . . 192

Chapter 6 Conclusions and Future Outlook . . . 194
6.1 Acknowledgments . . . 202

Chapter 7 Bibliography 203

LIST OF FIGURES

Figure 1.1: Strong motion P_d scaling for 5 earthquakes 3

Figure 2.1: Effect of numerical integration on a strong motion accelerogram 9
Figure 2.2: Baseline corrections using the BI algorithm for the east component of motion at station IWT009 11
Figure 2.3: Typical 1 Hz GPS raw time series at station LAND (35°.8997 N, 120°.4731 W) in the Parkfield area 18
Figure 2.4: Experimental configuration for the 2006 shake table test 29
Figure 2.5: Accuracy of broadband displacement waveforms 34
Figure 2.6: California Real Time GPS Network (CRTN) stations in southern California and collocated California Integrated Seismic Network (CISN) strong-motion accelerometer stations 37
Figure 2.7: 1 Hz (East component) displacements estimated for 105 CRTN stations 38
Figure 2.8: Estimation of velocity and displacement waveforms 40
Figure 2.9: Comparison of 1Hz GPS and 100Hz smoothed Kalman filter displacement waveforms 41
Figure 2.10: Vertical displacement waveforms 42
Figure 2.11: Power spectral densities 42
Figure 2.12: Power spectral density comparisons between forward Kalman filter and smoothed Kalman filter displacements waveforms . . 44
Figure 2.13: Example of saw-tooth like irregularities introduced by the disparity in sensor sampling frequencies 44
Figure 2.14: 1Hz synthetic saw tooth and its power spectral density. 45
Figure 2.15: Variances for 50 seconds of displacements for some California Real Time GPS Network (CRTN) stations 46
Figure 2.16: Effect of choice of system dynamics variance in Kalman filter estimation 47
Figure 2.17: Displacement waveforms in East component 50
Figure 2.18: Station map depicting GPS only and GPS/accelerometer stations 52
Figure 2.19: Results of applying the automatic baseline correction of *Wang et al.* (2011) with no static field constraints 54
Figure 2.20: Comparison between the ABC waveforms with and without the static field constraint 55
Figure 2.21: TDifference between the KD and ABC waveforms for both constrained and unconstrained solutions 56
Figure 2.22: RMS of the difference between the ABC and GPS waveforms and the KD and GPS waveforms for all stations 57
Figure 2.23: Power spectral densities for the north displacements at K-net station AOM027 58

Figure 2.24: 5% damped displacement response spectra for the east component of K-net station MYG001 59
Figure 2.25: Logarithm of the ratio between the KD and ABC power spectra for all stations 60
Figure 2.26: Difference between the KD and ABC 5% damped response spectra for all stations 62
Figure 2.27: Comparison between static offsets determined from the automated baseline corrected procedure and the real-time GPS . . . 63
Figure 2.28: North displacement waveforms for station K-net station IWT009 64

Figure 3.1: First 300 s of displacement records at 355 GEONET stations with a 120 s moving average filter applied for the Tokachi-oki earthquake. 77
Figure 3.2: Summary of the inversion results for the Tokachi-oki earthquake 79
Figure 3.3: Snapshots of the inversion results comparing the Global CMT result with the replayed GPS real time inversion for the 2003 Mw 8.3 Tokachi-oki earthquake 80
Figure 3.4: Geometrical parameters of the best double couple solution extracted from the moment tensor inversion and compared to the global CMT post-processed result 81
Figure 3.5: 300s of displacement records at 50 of the 105 CRTN stations that exceeded the 15mm threshold with a 120s moving average filter applied for the 2010 Mw 7.2 El Mayor-Cucapah earthquake 82
Figure 3.6: Summary of the inversion results for the 2010 El Mayor-Cucapah earthquake 84
Figure 3.7: Snapshots of the inversion results for the El Mayor Cucapah earthquake comparing the USGS W phase result with the GPS real-time inversion 85
Figure 3.8: Geometrical parameters of the best double couple solution extracted from the moment tensor inversion and compared to the USGS W phase post-processed result for the 2010 El Mayor-Cucapah earthquake 86
Figure 3.9: (a) Maximum horizontal displacement and variance function used for determination of final offsets 88
Figure 3.10: Detailed comparison between the a) fastCMT and b) GCMT results for the 2003 Tokachi-oki event. 89
Figure 3.11: Detailed comparison between the a) fastCMT and b) USGS W-Phase results for the 2010 El Mayor-Cucapah event. 90
Figure 3.12: TResult of the point source *fast*CMT method applied to the Mw 9.0 Tohoku-oki event 98
Figure 3.13: (a) 3800 L-curves for line source *fast*CMT inversions performed at different locations and with different orientations 100
Figure 3.14: *fast*CMT and slip inversion results 101

Figure 3.15: *fast*CMT and slip inversion results 102
Figure 3.16: L-curve for the slip inversion plotting the model seminorm $\|\mathbf{Lm}\|_2$ versus model misfit $\|\mathbf{WGm} - \mathbf{Wd}\|_2$ with solutions at selected values of the smoothing parameter λ 104
Figure 3.17: Difference between slip inversions computed using the improved precision GPS/accelerometer displacements vs. the inversion carried out using the GPS-only derived displacements 106

Figure 4.1: Results of bandpass filtering the accelerometer recording at station MYG011 and integrating it to velocity and displacement . 114
Figure 4.2: Stencil for finite difference Laplacian 117
Figure 4.3: Computational molecules for the finite difference laplacian . . . 118
Figure 4.4: Map of 20 stations used in the seismogeodetic slip inversion . . 123
Figure 4.5: Values of ABIC for the kinematic inversion 125
Figure 4.6: (a) Total slip from the kinematic inversion, peak slip is 52m . . 126
Figure 4.7: Comparison between observed (black) and synthetic (red) 3-component displacement time series 127
Figure 4.8: Comparison between observed (black) and synthetic (red) 3-component velocity time series 128
Figure 4.9: Snapshots of slip propagation in 10s increments 130
Figure 4.10: Subfault source-time functions 131
Figure 4.11: Total slip from the kinematic inversion with a locked boundary condition at the trench 132
Figure 4.12: Total slip from the kinematic inversion with only seismogeodetic displacements 134
Figure 4.13: Comparison between the source time functions of the joint inversion of displacement and velocity data and the displacement-only solution 135
Figure 4.14: Subfault source-time functions (STFs) for the displacement-only solution 136
Figure 4.15: Coherence between 100s and 0.5Hz between observed and synthetic data for the joint inversion results 138
Figure 4.16: (a) Normalized power spectral densities for the slip rate functions of all sub faults 141

Figure 5.1: Distribution of stations used in this study. Blue triangles are land-based GPS/strong motion stations 152
Figure 5.2: A schematic of the measures of tsunami intensity used in this study 155
Figure 5.3: Result of testing the assumption of linearity in tsunami propagation 157
Figure 5.4: Result of testing the assumption of linearity in tsunami propagation 158

Figure 5.5: Inversion results . . . 161
Figure 5.6: Inversion results . . . 162
Figure 5.7: Tsunami forecast results . . . 164
Figure 5.8: Inundation forecast results . . . 165
Figure 5.9: (a) Terrain ruggedness index (TRI) of the topography/bathymetry grid used in this study . . . 169
Figure 5.10: Inundation of the survey points for the model obtained at 50min after origin time . . . 170
Figure 5.11: Inundation results at 157s after OT from the inversion employing the dense 816-station GPS network . . . 172
Figure 5.12: Schematic of tsunami generation from horizontal coseismic motion 176
Figure 5.13: Trench normal derivative of bathymetry computed in the direction indicated by the grey arrow . . . 178
Figure 5.14: Joint land- and ocean-based data inversion results . . . 179
Figure 5.15: Joint land- and ocean-based data inversion results . . . 180
Figure 5.16: Subfault source-time functions (STFs) . . . 181
Figure 5.17: Vertical deformation predicted by the joint slip inversion at t=180s after origin time . . . 184
Figure 5.18: Maximum tsunami amplitudes with several source models . . . 186
Figure 5.19: Trench perpendicular profile of tsunami propagation along profile A-A' . . . 187
Figure 5.20: (a) Inundation results for the land-only static inversion . . . 189
Figure 5.21: Four snapshots in time of inundation modeling of the coast surrounding Sendai Bay . . . 191

Figure 6.1: Ocean bottom strong motion recording for the M_w6.5 2014 Vancouver Island event . . . 200
Figure 6.2: DART buoy recordings following the M_w 6.8 Ferndale strike slip event off-shore Northern California . . . 201
Figure 6.3: Differential pressure gauge recordings at 26 ocean bottom stations during the 2006 Kuril Islands tsunami . . . 202

LIST OF TABLES

Table 2.1: A summary of Kalman filtering and smoothing equations 24
Table 2.2: RMS differences between computed displacement waveforms and the input registered by the shake table's MTS recorder 31
Table 2.3: RMS differences with smoother between computed displacement waveforms and the input registered by the shake table's MTS recorder 32
Table 2.4: Collocated GPS (California Real Time GPS Network) and strong-motion accelerometer (California Integrated Seismic Network) stations with a station separation of 1.5 km or less. 39

Table 3.1: Velocity model for the Tokachi-oki inversion 78
Table 3.2: Velocity model for the El Mayor-Cucapah inversion 83
Table 3.3: Summary timeline of results for the Tokachi-oki and El Mayor-Cucapah events 91

Table 4.1: Velocity model for the Tohoku-oki kinematic inversion 124

Table 5.1: Wave gauges used in the inversion 153
Table 5.2: Statistics of the inversions and inundation models 160
Table 5.3: Forecast statistics for kinematic models 188

ACKNOWLEDGEMENTS

I am indebted to all those who have been my teachers, it is the noblest endeavor to devote ones time to sharing knowledge. I am grateful for your patience and dedication. Especially to Xyoli Pérez Campos who first introduced me to seismology, our time working in the field and in the lab were the gateway drug for everything that followed. My Ph.D. advisor Yehuda Bock, you have mentored me in every aspect of the craft of science and prepared me for the times ahead, I will remember our time together fondly. My dissertation committee, Guy Masters, Jose Restrepo, Peter Shearer and Dave Sandwell, you have alway had open doors and have been ready to help me out.

The dedicated staff of the Scripps Orbital and Permanent Array Center have been instrumental in my research, they keep the shop running, Maria Turingan, Mindy Squibb, Anne Sullivan, Peng Fang and Glen Offield are often times the secret to our success.

I am grateful for the opportunity to have conducted my research at the Scripps Institution of Oceanography and in particular at the Institute of Geophysics and Planetary Physics. It may not have been apparent at the time to those who had the most insignificant of conversations, over a cup of coffee or a beer at TG with me, but our interactions have many times allowed me to push through a problem.

The Ph.D. has been the best time of my life and this is in no small part thanks to my wonderful friends and companions in the trenches. Robert Petersen, Michael Deflorio, Alain DeVerneil, Riley Gannon, Samer Naif, Elizabeth Vu, Alan Foreman, Fernando Paolo, Soli Garcia, Scott DeWolf, Brendan Crowell and everyone at SIO whom I can rely on every Friday to help me unwind and enjoy life hoping for a green flash.

Valerie you have been my confidant, partner in crime and my best friend, always ready for anything and yearning for bigger and better things. I've never met a person as full of life as you. Here's to hoping for many more reckless adventures in the times ahead.

I'd be nothing without the love of my family who have been there with me

and for me through the good times and the hard times. Daniela, big sister, I am grateful for your unconditional love and support. To my parents I owe the largest debt of all, you taught me to love knowledge and encouraged me to be curious about the world, to ask questions and never dogmatically accept anything that could not be critically evaluated. Your unrelenting love and support have allowed me to pursue a career in science. I am here because of you.

Some formalities: portions of this dissertation have been published in peer reviewed journals. Except for the discussion of accelerometer biases in Kalman filtering, Chapter 2 is published in its entirety in:

- **Melgar, D.**, Bock, Y., Sanchez, D., and Crowell, B.W., "On Robust and Reliable Automated Baseline Corrections for Strong Motion Seismology", *J. Geophys. Res.*, 118(3), 2013.

- Bock, Y., **Melgar, D.**, and Crowell, B.W., "Real-Time Strong-Motion Broadband Displacements from Collocated GPS and Accelerometers", *Bull. Seism. Soc. Am.*, 101(6), 2011.

Chapter 3 has been published in:

- **Melgar, D.**, Crowell, B.W., Bock, Y., and Haase, J.S, "Rapid modeling of the 2011 Mw 9.0 Tohoku-oki earthquake with seismogeodesy", *Geophys. Res. Lett*, 40(12), 2013.

- **Melgar, D.**, Bock, Y., and Crowell, B.W., "Real-Time Centroid Moment Tensor Determination for Large Earthquakes from Local and Regional Displacement Records", *Geophys. J. Int.*, 188(2), 2012.

Chapter 4 consists of previously unpublished material. Sections 5.1 through 5.4 of Chapter 5 have been published in

- **Melgar, D.** and Bock, Y. "Near-Field Tsunami Models with Rapid Earthquake Source Inversions from Land- and Ocean-Based Observations: The Potential for Forecast and Warning", *J. Geophys. Res.*, 118(11), 2013.

and relies heavily on code modified from its original form as it appeared for the publication

- Crowell, B.W., Bock, Y., and **Melgar, D.**, "Real-time inversion of GPS data for finite fault modeling and rapid hazard assessment", *Geophys. Res. Lett*, 39(9), 2012.

the remainder is unpublished material. I have had the privilege to co-author these and other papers with a talented ensemble of scientists. I am indebted to them for lively and uplifting debates.

VITA

2009	B.Eng. in Geophysics, Universidad Nacional Autónoma de México
2010	M.Sc. in Earth Sciences University of California, San Diego
2014	Ph.D. in Earth Sciences, University of California, San Diego

PUBLICATIONS

Crowell, B.W., **Melgar, D.**, Bock, Y., Haase, J.S, and Geng, J., "Earthquake Magnitude Scaling using Seismogeodetic Data", *Geophys. Res. Lett*, 40(23), 2013.

Melgar, D. and Bock, Y. "Near-Field Tsunami Models with Rapid Earthquake Source Inversions from Land- and Ocean-Based Observations: The Potential for Forecast and Warning", *J. Geophys. Res.*, 118(11), 2013.

Geng, J., **Melgar, D.**, Bock, Y., Pantoli, E., and Restrepo, J.I., "Recovering coseismic point ground tilts from collocated high-rate GPS and accelerometers", *Geophys. Res. Lett*, 40(19), 2013.

Melgar, D., Pantoli, E., Bock, Y., and Restrepo, J.I., "Displacement Acquisition for the NEESR:BNCS Building Shaketable Test via GPS Sensors", *Network for Earthquake Engineering Simulation (distributor)*, DOI:10.4231/D3V97ZR5H, 2013.

Melgar, D., Crowell, B.W., Bock, Y., and Haase, J.S, "Rapid modeling of the 2011 Mw 9.0 Tohoku-oki earthquake with seismogeodesy", *Geophys. Res. Lett*, 40(12), 2013.

Geng, J., Bock, Y., **Melgar, D.**, Crowell, B.W., and Haase, J.S, "A new seismogeodetic approach applied to GPS and accelerometer observations of the 2012 Brawley seismic swarm: Implications for earthquake early warning", *Geochem. Geophys. Geosyst*, 14(7), 2013.

Melgar, D., Bock, Y., Sanchez, D., and Crowell, B.W., "On Robust and Reliable Automated Baseline Corrections for Strong Motion Seismology", *J. Geophys. Res.*, 118(3), 2013.

Perez-Campos, X., **Melgar, D.**, Singh, S.K., Cruz-Atienza, V., Iglesias, A., and Hjorleifsdottir, V., "Determination of tsunamigenic potential of a scenario earthquake in the Guerrero seismic gap along the Mexican subduction zone", *Seism. Res. Lett*, 84(3), 2013.

Crowell, B.W., Bock, Y., and **Melgar, D.**, "Real-time inversion of GPS data for finite fault modeling and rapid hazard assessment", *Geophys. Res. Lett*, 39(9), 2012.

Singh, S.K., Perez-Campos, X., Iglesias, A., **Melgar, D.**, "A Method for Rapid Estimation of Moment Magnitude for Early Tsunami Warning Based on Coastal GPS Networks", *Seism. Res. Lett*, 83(3), 2012.

Melgar, D., Bock, Y., and Crowell, B.W., "Real-Time Centroid Moment Tensor Determination for Large Earthquakes from Local and Regional Displacement Records", *Geophys. J. Int.*, 188(2), 2012.

Bock, Y., **Melgar, D.**, and Crowell, B.W., "Real-Time Strong-Motion Broadband Displacements from Collocated GPS and Accelerometers", *Bull. Seism. Soc. Am.*, 101(6), 2011.

Melgar, D. and Perez-Campos, X., "Imaging the Moho and Subducted Oceanic Crust at the Isthmus of Tehuantepec, Mexico, from Receiver Functions", *Pure Appl. Geophysics*, 168, 2010.

ABSTRACT OF THE DISSERTATION

Seismogeodesy and Rapid Earthquake and Tsunami Source Assessment

by

Diego Melgar Moctezuma

Doctor of Philosophy in Earth Sciences

University of California, San Diego, 2014

Yehuda Bock, Chair

This dissertation presents an optimal combination algorithm for strong motion seismograms and regional high rate GPS recordings. This *seismogeodetic* solution produces estimates of ground motion that recover the whole seismic spectrum, from the permanent deformation to the Nyquist frequency of the accelerometer. This algorithm will be demonstrated and evaluated through outdoor shake table tests and recordings of large earthquakes, notably the 2010 M_w 7.2 El Mayor-Cucapah earthquake and the 2011 M_w9.0 Tohoku-oki events.

This dissertations will also show that strong motion velocity and displacement data obtained from the seismogeodetic solution can be instrumental to quickly determine basic parameters of the earthquake source. We will show how GPS and seismogeodetic data can produce rapid estimates of centroid moment tensors, static

slip inversions, and most importantly, kinematic slip inversions. Throughout the dissertation special emphasis will be placed on how to compute these source models with minimal interaction from a network operator.

Finally we will show that the incorporation of off-shore data such as ocean-bottom pressure and RTK-GPS buoys can better-constrain the shallow slip of large subduction events. We will demonstrate through numerical simulations of tsunami propagation that the earthquake sources derived from the seismogeodetic and ocean-based sensors is detailed enough to provide a timely and accurate assessment of expected tsunami intensity immediately following a large earthquake.

Chapter 1

Introduction

Mitigation of the effects of natural hazards on public safety and civilian infrastructure is a multidisciplinary problem. It includes both the societal aspects of how we respond to hazards and the physics behind these phenomena. As we seek to gain knowledge about Earth processes we must also consider the practical implications of our research. The number of people and infrastructure located in areas of earthquake and tsunami hazard is growing constantly. The problem of mitigating risk can be confronted from two perspectives. One is to minimize the hazard by moving people and infrastructure away from earthquake and tsunami-prone areas. This is unfeasible for densely populated areas (such as Japan) or already existing cities. The second approach is to minimize vulnerability by making infrastructure more resistant to the effects of natural hazards. In earthquake engineering, for example, this has lead to the creation of building codes that take into account some estimate of the expected local hazard. This is a tricky proposition, in general the stronger a structure becomes the more expensive it is to build. Thus building codes aim to provide a balanced assessment of what can realistically be expected in terms of hazard offset by economic considerations.

Additionally, as technology and science have advanced knowledge of Earth processes it is become increasingly commonplace to provide early warnings and rapid assessments immediately following large scale disasters. In seismology several countries operate some form of earthquake early warning (*Allen et al.*, 2009a) system, some, such as Japan and Mexico, have been operational for well over 20

years. Philosophies on how to approach this problem vary and are mostly contingent on the type of hazard the system is planned for (subduction zone vs. transform boundary events). Some systems rely on networks of stations that analyze the peak displacement and frequency of the P wave (*Kamigaichi et al.*, 2009) providing a faster assessment of the source but with increased uncertainty. Others use the S wave (*Espinosa-Aranda et al.*, 2009) which provides less uncertainty albeit with a longer waiting period. Other systems are capable of issuing warnings with a single station (*Nakamura and Saita*, 2007) and are typically used for stopping trains, power plants and other critical infrastructure.

Whichever strategy is employed, earthquake early warning systems rely on traditional seismic sensors, seismometers and accelerometers. However, it is been observed that these systems suffer from a condition known as saturation (*Brown et al.*, 2011) where at large magnitude it becomes increasingly difficult to separate one earthquake from another. Consider the Figure 1.1 from *Crowell et al.* (2013) where a typical scaling law often used in earthquake early warning, P_d, the peak ground displacement of the P wave (*Wu et al.*, 2007) is calculated for a range of earthquake magnitudes. The figure shows that at about M_w7 the peak displacement of the P wave is very similar for earthquakes between M_w7 and M_w9. There is debate in the literature as to whether this is due to the physics of the source, i.e. is rupture deterministic or not (*Olson and Allen*, 2005).

Theoretically, it is well known that as magnitude increases the spectrum of seismic radiation will become enriched in long period energy (*Haskell*, 1964; *Brune*, 1970) so it is tantalizing to consider that perhaps the saturation problem is instrumental rather than physical. At local distances from large earthquakes, where saturation occurs in early warning scaling laws, seismologists must rely on strong motion sensors whose low gains permit the instrument to stay on scale during shaking. These sensors, however, are affected by un-modeled rotational motions (*Trifunac and Todorovska*, 2001) that render the long period part of the spectrum, at periods roughly longer than 10s, difficult if not impossible to reliably use (*Boore and Bommer*, 2005). In Chapter 2 we present a solution to this problem. By incorporating direct measurements of ground displacement from GPS through a

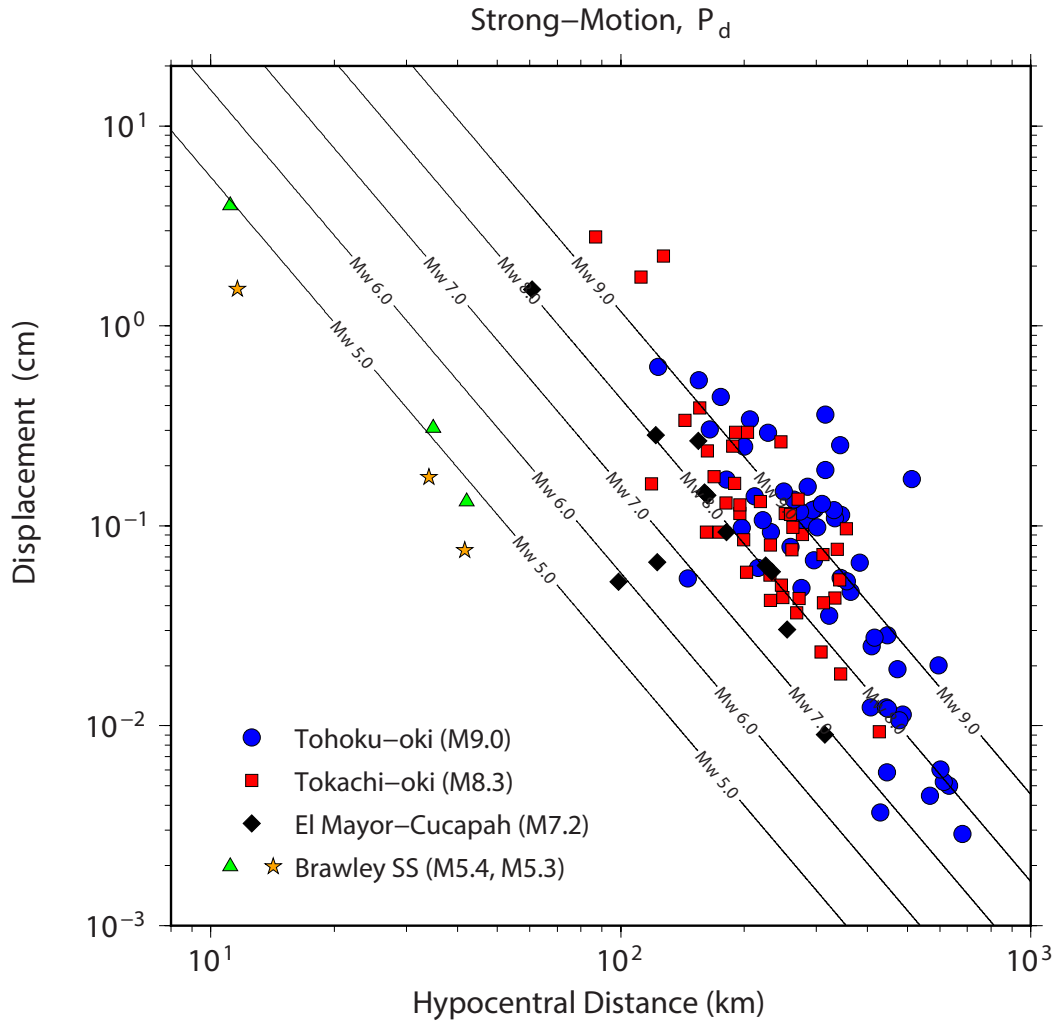


Figure 1.1: Strong motion P_d scaling for 5 earthquakes. The solid black lines show the regression relations for magnitude as a function of hypocentral distance. Modified from *Crowell et al.* (2013).

real-time Kalman filter framework we show through extensive shake table tests, the M_w7.2 El Mayor-Cucapah and M_w9 Tohoku-oki earthquakes that the combination dataset, which we dub *seismogeodetic* provides complete spectral recovery from 0 frequency to the accelerometer Nyquist frequency regardless of the intensity of shaking. In fact (*Crowell et al.*, 2013) used the seismogeodetic method described in Chapter 2 to demonstrate substantial improvement in the saturation problem of the P_d scaling law.

For early warning a simple characterization of the earthquake suffices, only a rough location and estimate of magnitude or of expected shaking intensity is necessary to trigger an alert. However, immediately following rupture more elaborate models of the source are necessary to guide rapid response. For example the USGS's Shakemap (*Allen et al.*, 2009b) and PAGER (*Jaiswal and Wald*, 2010) data products provide a rapid assessment of expected shaking thoughout the epicentral area as well as of economic impacts and loss of life. The first iterations of these data products rely on simple point source models. They are often revised hours after the event when more complex source models become available. In fact, considering a point source vs. a finite extent source model can have a significant impact in the Shakemap computation (*Colombelli et al.*, 2013). In Chapter 3 we will show how both GPS and the seismogeodetic framework can be used to rapidly compute source models of increasing complexity. In particular using the permanent deformation (the static field) from an earthquake we can construct a suite of models that range from point source moment tensors to line source moment tensors and fully heterogenous slip inversions. The static field is the longest period information that is measurable from an earthquake, effectively nullifying any saturation concerns. We will demonstrate this for the M_w7.2 El Mayor-Cucapah, M_w8.3 Tokachi-oki and M_w9 Tohoku-oki events. Throughout that chapter we will place particular emphasis in techniques and strategies for automation of the algorithms; removing the network operator from the computation is paramount to the success of any rapid source assessment strategy.

A more complete description of the source must include the time dependent behavior of rupture. Due to the unreliability of strong motion sensors at low frequencies, automated kinematic slip inversions are only computed with teleseismic data (*Ji et al.*, 2002a) and are only available hours after the event. In Chapter 4 we will demonstrate how seismogeodetic data can be used to compute kinematic models of the source. With the combination of local and regional GPS and strong motion recordings these models could be available within minutes of rupture initiation. We will argue that such modeling approaches are not only suitable for rapid computation but also provide a detailed picture of the seismic source that is consis-

tent with a posteriori studies. Notably, we show that including the seismogeodetic strong motion velocity estimates as well as the displacement data provides a more detailed picture of the source process. The model thus derived is broadband in the sense that it captures higher frequency detail of rupture at depth which consists of short, sharp slip pulses as well as the long and smooth shallow source time functions. The seismogeodetic solution is largely in agreement with tele-seismic slip inversions and back projection studies. We also show the depth-dependent behavior of rupture through analysis of the frequency domain properties of the sub fault source time functions and find that it is in agreement with conceptual models of subduction zones (*Lay et al.*, 2012).

The choice of static and kinematic models can have a significant impact in tsunami early warning as well. The tsunami warning centers (TWCs) operated by the National Oceanographic and Atmospheric Administration (NOAA) utilize tele-seismic measurement and ocean bottom pressure measurements from DART buoys in the deep ocean. TWCs routinely provided basin scale warnings in the hours following a large event (*González et al.*, 2005; *Titov et al.*, 2005; *Mungov et al.*, 2013). This reliance on sensors in the far field of the tsunami source means there is no warning issued to the near-source area surrounding the earthquake. Japan operates the only system designed to provide near-source warnings (*Tatehata*, 1997; *Ozaki*, 2011). It utilizes rapidly determined hypocenters and magnitudes from the Japanese Meteorologcal Agency (JMA) to perform a database query of precomputed scenarios. These scenarios, computed offline and well in advance of the event include intensity estimates at predetermined locations along the near-shore coast. Thus when the earthquake strikes these parameters seed the database query and the resulting model guides the warning issued to the public. During the 2011 M_w9 Tohoku-oki event however, a strict reliance on seismic data for estimation of the earthquake source parameters lead to a severe underestimation of magnitude (*Hoshiba et al.*, 2011), once again, due to saturation. This lead to underestimates of the extent and intensity of the tsunami, which were not revised until may hours after the event. (*Ozaki*, 2011). In Chapter 5 we discuss the tsunami warning problem in great detail. We will propose an *indirect* form of warning where the rapid

models determined in Chapters 3 and 4 are used to compute the deformation of the ocean bottom; this is in turn is used as the initial condition in a fully non-linear tsunami simulation. Using the open-source code *GeoClaw* (*LeVeque et al.*, 2011) we will produce detailed forecasts of tsunami intensity. By comparison to tsunami survey data collected immediately after the Tohoku-oki event (*Mori et al.*, 2011, 2012) we will assess the suitability of these models for forecasting. Furthermore, we will demonstrate that offshore data in the form of ocean bottom pressure and GPS buoys that directly measure the tsunami can be incorporated into a joint inverse problem. We conclude that this joint model, which includes both land-based and ocean-based observations produces the most accurate forecast of the tsunami, as compared to post-earthquake field surveys. With existing geophysical infrastructure it is reasonable to expect detailed tsunamis warnings in the shore immediately adjacent to large events.

Chapter 2

Seismogeodesy

Sesmic and geodetic networks for observation of earthquakes at regional distances (a few hundred kilometers) have developed mostly independently over the last few decades. it is unsurprising then that the different sensors types are infrequently collocated. Throughout this chapter we discuss and demonstrate that although both kinds of sensors make important contributions to the characterization of strong ground motions, each has limitations when used independently. We propose and demonstrate a Kalman filter algorithm that optimally combines seismic and geodetic data in real time. As a consequence of our analysis we conclude that if a seismic (or geodetic) network requires the computation of broadband strong motion displacement and velocity waveforms as part of its observational goals then priority should be given to the collocation of instruments and the optimal combination of data sets.

2.1 Background on Strong Motion Sensing

The range of motions produced by the seismic source is broad both in frequency and dynamic range. It is well known that no one sensor can capture all signals of interest to seismology and earthquake engineering (*Havskov and Alguacil*, 2006). Seismologists typically rely on inertial sensors, seismometers, whose response is related to velocity of the ground, for measurement of small amplitude signals (weak motion). For large amplitude signals these sensitive instruments me-

chanically clip. In such a case, strong motion sensors, whose response is related to the acceleration of the ground and have lower gains, are preferred. Modern observatory grade accelerometers rely on the force feedback principle and can measure motions as small as 1nm at 1Hz and 100nm at 0.1Hz and accelerations of up to 4g. Furthermore their frequency response is flat from 0Hz (often called the DC-level) to 50-200Hz (*Havskov and Alguacil*, 2006).

In principle there should be no difficulty in integrating a strong motion record to velocity and displacement. This is not the case; in practice the simple integration of an accelerogram produces unphysical velocity and displacement waveforms that grow unbounded as time progresses. Computation of broadband displacements from strong motion recordings is a thoroughly studied procedure that is fraught with many known problems and has no known single solution. By "broadband displacement" we mean a strong motion displacement waveform that captures both transient or dynamic phenomena (waves) and permanent or static deformation, i.e. a recording reliable from DC to the Nyquist frequency.

The problems associated with the double integration of accelerometer recordings have been comprehensively studied and many sources of error have been suggested: numerical error in the integration procedure, mechanical hysteresis, cross-axis sensitivity and unresolved rotational motions (*Graizer*, 1979; *Iwan et al.*, 1985; *Boore*, 1999, 2001; *Boore et al.*, 2002; *Smyth and Wu*, 2007). A consequence of the afore mentioned problems is that small offsets are introduced in the acceleration time series; upon integration these *baseline offsets* produce the linear and quadratic trends observed in the velocity and displacement time series, respectively. Of the possible sources of these offsets unresolved rotational motion is often invoked as the main error (*Graizer*, 2006; *Pillet and Virieux*, 2007). Motion is described by six degrees of freedom, three translations and three rotations. Accelerometers, as inertial sensors, are incapable of discerning between rotational and translational motions, thus, rotational motions are recorded as spurious translations. Effectively, this results in a change of the baseline of the accelerometer, even if by a small amount, leading to unphysical drifts in the singly-integrated velocity waveforms and doubly-integrated displacement waveforms (Figure 2.1).

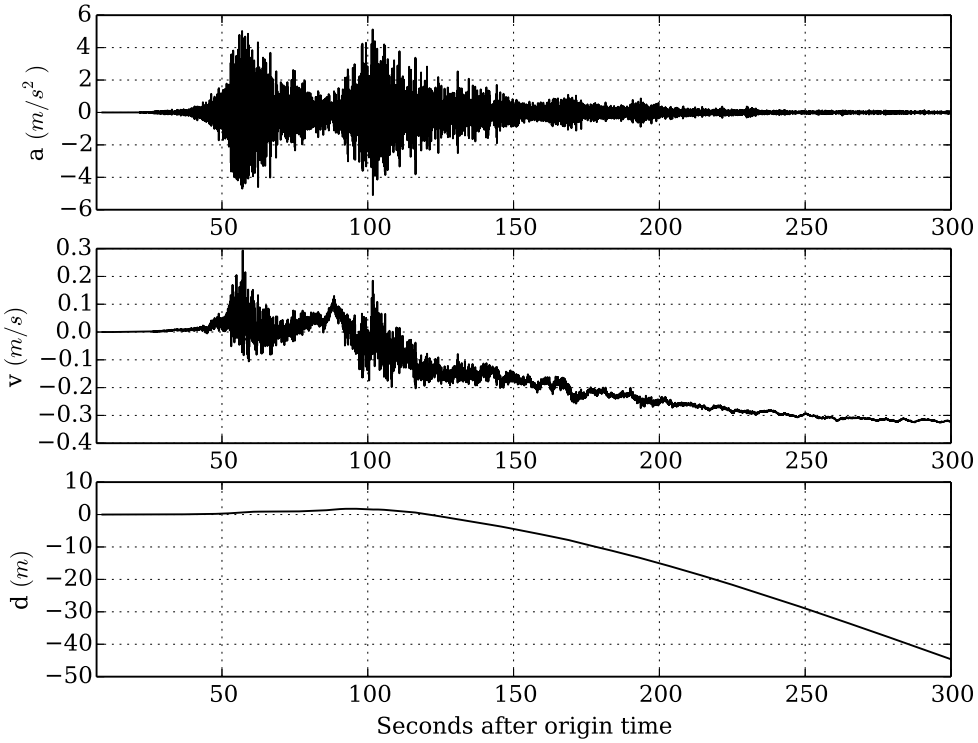


Figure 2.1: Effect of numerical integration on a strong motion accelerogram. This example is for the east component of motion at station IWT009 192 km from the centroid of the 2011 M_w9 Tohoku-oki earthquake. Note the unphysical drifts in both the velocity and displacement time series.

Many correction schemes, collectively known as baseline corrections, have been proposed over time to deal with this problem. Rotational motions become more prevalent close to the source and at long periods. In particular, *Trifunac and Todorovska* (2001) have shown that rotational motions have significant contributions to radiated spectra and can sometimes be the predominant source of seismic energy, particularly at very long periods and for very large earthquakes. For this reason, the simplest baseline correction scheme is a high-pass filter (*Boore and Bommer*, 2005), eliminating the baseline-shifted long period portion of the time series. This leads to accurate recovery of the mid to high frequency parts of the displacement record but suppresses completely low frequency information, especially the static offset (Figure 2.2). To ameliorate this, a number of more elab-

orate correction schemes exist (*Boore and Bommer*, 2005) that rely on function fitting to the singly integrated velocity time series. The most reliable scheme that routinely produces plausible displacement waveforms (which include a measure of the static offset) is described in *Boore* (1999, 2001) and is a modification of the scheme proposed by *Iwan et al.* (1985) and henceforth referred to as the Boore-Iwan or BI correction scheme. In this method a piecewise linear function is fit to the uncorrected velocity time series, the slope of each straight line segment represents an acceleration step which is then subtracted from the original acceleration data. This baseline corrected acceleration record is subsequently integrated to velocity and displacement. If the intervals for fitting the linear functions to the velocity data are selected appropriately this algorithm will produce waveforms that look plausible. They will contain both permanent and transient motions. The difficulty then lies in determining what these appropriate time intervals are from the data themselves. As discussed by *Boore* (1999, 2001) this is an ambiguous process. To diminish this uncertainty, subsequent research has focused on determining plausible times for the fits and then grid searching for waveforms that most resembles a ramp or step function (*Wu and Wu*, 2007; *Chao et al.*, 2010; *Wang et al.*, 2011).

This is better understood through an example. Consider the time series of Figure 2.1. The traditional BI correction procedure starts by removing the pre-event mean or baseline, this is called the zeroth-order corrected waveform. Then for some analyst-determined initial correction time t_i and final correction time t_f, two baselines, or acceleration steps, can be computed from the drift in the velocity data and subsequently removed. Underlying this process is the assumption that from time t_i to some intermediate time t_1 (determined by the analyst) a baseline offset due to strong shaking is introduced into the time series and subsequently from this intermediate time t_1 to the final correction time t_f a permanent baseline offset is introduced into the data. Thus, the first acceleration step is determined by a least squares straight line fit to the velocity data between times t_1 and t_f such that

$$v_f(t) = v_0 + a_f(t) \; ; \; t \in (t_1, t_f) \; , \tag{2.1}$$

where the regression parameters are v_0 and the acceleration step a_f. Subsequently,

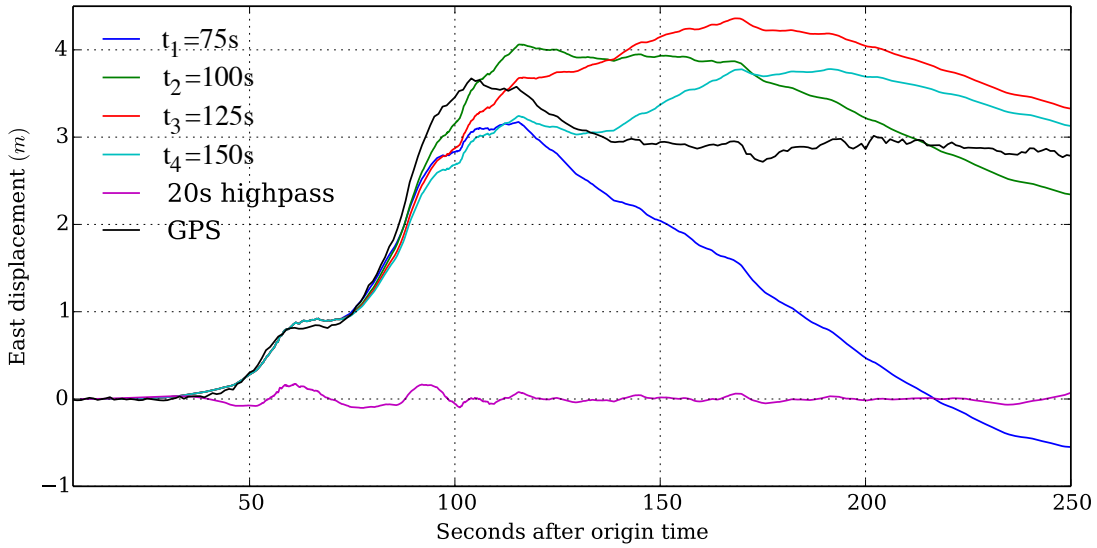


Figure 2.2: Baseline corrections using the BI algorithm for the east component of motion at station IWT009 192 km from the centroid of the 2011 M_w9 Tohoku-oki earthquake using different values of the correction parameter t_1. Also shown is the result of a 20s high pass filter corrected waveform and the GPS displacements recorded at the same site

another straight line is fit from t_i to t_1 with the constraint that velocity be zero at the start of the record and that the final velocity averages to zero. These constraints are satisfied if (*Boore*, 1999)

$$a_m = \frac{v_f(t_1)}{t_1 - t_i} \ . \tag{2.2}$$

Then, the acceleration baseline, a_m, is subtracted from the uncorrected record from times t_i to t_1 and the baseline offset, a_f, is subtracted from the zeroth order corrected record for times t_1 to t_f. The record is then integrated to velocity and displacement. This scheme produces waveforms that look plausible; they contain both transient and permanent motions. However an ambiguity lies in the selection of times t_i and t_1. As has been amply discussed by *Boore* (1999, 2001), this ambiguity is not easily resolved without external information and each investigator relies on subjective judgment to ascertain what looks best. Figure 2.2 illustrates such an example where the same waveform has been baseline corrected for several values of t_1 while holding t_i fixed at the P wave arrival time with varying results. If the waveform is complex, as in this example, with two distinct pulses of very

strong shaking, then more baselines might need to be subtracted. However, if there is already ample ambiguity in the simple determination of the two baselines a_m and a_f, the problem is exacerbated with the introduction of more baselines.

The correction times t_i and t_1 can and do vary for each station-event pair and even for different channels at the same station during the same event. Practically this means that analysis of broadband displacements from baseline-corrected accelerometer records is inherently ambiguous and complicated for real-time seismological applications or across large networks both for real-time and post-processing purposes.

Research into automated baseline correction from accelerometer data alone (we shall refer to this as ABC) has focused on variations of the BI scheme. *Wu and Wu* (2007) proposed a variant in which the times for each linear segment of the baseline correction are determined by a grid search such that the resulting time series best matches a ramp function. *Chao et al.* (2010) elaborated on the formulation of *Wu and Wu* (2007) by adding an extra restriction that the times be selected after certain threshold values of acceleration energy have been accrued. Both studies compared their results to static offsets determined from GPS and found that their estimates are somewhat similar. There is still scatter in the comparison between the static field derived from the corrected data and that determined from nearby GPS. Additionally, no analysis on the adequacy of the remaining part of the waveform is performed. It is implicitly assumed that if the static field is well fit then the rest of the waveform will be reliable as well.

An important advance in automatic baseline correction is presented in *Wang et al.* (2011) who present another variation of the BI bilinear scheme that performs better than those discussed thus far. They developed some simple heuristics for determination of the interval of possible correction times based on analysis of the uncorrected acceleration and displacement waveforms. From an analysis of the time at which the peak ground acceleration (PGA) occurs and the time of last zero crossing in the uncorrected displacement they determine bounds for the grid search of baseline correction times. They then perform the grid search among these possible correction times and fit, via a non-linear regression, a step function

to all possible waveforms. An optimum correction (the one that best fits this step function) is then selected. Unlike previous studies they compare their results not only to measured static offsets but to observed 1Hz GPS data; they do this for a single station. They find for that one station an error of ∼20% in the static field estimation but a very good agreement between the corrected displacement and the GPS for the first 200s of the waveform.

In a follow up study *Wang et al.* (2013) apply their methodology to accelerometer records for the 2011 M_w9.0 Tohoku-oki earthquake. They obtain reasonable estimates of the static field for many stations in the KiK-net network in Japan (*Okada et al.*, 2004) but also find numerous outliers. They then develop a simplified scheme to screen the outliers by excluding coseismic offsets that deviate more than 15° from the predictions of a static slip inversion. Furthermore, they compare their automatic corrections for selected borehole sensors in the KiK-net network with nearby high-rate GPS stations with mixed results. They find that while parts of the waveforms might be a good match, the static estimates can be in error by a significant amount. To ameliorate this they then propose to use the static field from nearby GPS stations as a constraint in the correction procedure. From the pool of all candidate baseline corrections they select the one that fits a step function of amplitude given by the static field. In a follow up study *Tu et al.* (2014) showed that substantial improvement was possible if corrections were correlated between neighboring stations of a dense network. It is noteworthy that *Wang et al.* (2013) and *Tu et al.* (2014) do not provide baseline corrected solutions for the sister strong motion network K-net. They readily acknowledge that K-net stations, which generally have less favorable site responses (*Tsuda et al.*, 2006), are not well modeled by this automatic approach. This will be important later on in this chapter when it is shown that K-net data can be corrected as well as KiK-net data by introducing Global Positioning System (GPS) data. In general while these algorithms have demonstrated incremental improvements to the original BI correction scheme they are far from being routinely applicable, objective or automatable.

The availability of suitable correction algorithms for strong motion wave-

forms that can produce broadband displacements is of broad interest especially for source analysis and hazards assessment. There has been ample interest in recent years to access to such real-time broadband displacements. Recall that it is the long periods of the seismic spectrum down to the static offset that provide the most obvious demarcation between large events. Static offsets and long period radiation can be used to rapidly compute moment tensors, source dimensions, static and kinematic source models and tsunami models. Indeed in Chapters 3,4 and 5 we will show how broadband strong motion waveforms facilitate such computations.

2.2 The Role of GPS

An alternative to baseline corrections of strong motion data is to measure displacements directly using the (GPS). There are two basic approaches to precise GPS data analysis: network positioning and precise point positioning (PPP). In both approaches stations positions are estimated with respect to a global Cartesian terrestrial reference system. This system is realized by the published coordinates and velocities of hundreds of global geodetic stations in the International Terrestrial Reference Frame (ITRF) (*Altamimi et al.*, 2007). Precise GPS satellite orbital products distributed by the International GNSS Service (IGS) (*Kouba and Héroux*, 2001) are tied to this underlying reference frame, and without loss of generality, are assumed to be fixed in the GPS data analysis.

In network positioning, data from a network of stations are analyzed simultaneously to estimate station positions and integer-cycle phase ambiguities (*Dong and Bock*, 1989; *Blewitt*, 1989), and other parameters such as zenith troposphere delays. Analyzing the data as a network, results in the effective cancellation of GPS receiver clock and satellite clock errors, which are common to multiple satellite and stations, respectively. Precise point positioning (*Zumberge et al.*, 1997) relies on fixed satellite orbits, as well as satellite clock parameters also available through the IGS and/or its different analysis centers . These parameters are held fixed in the process of estimating ITRF positions of individual GPS stations, phase ambiguities, zenith troposphere delays and station clock parameters.

Network positioning and precise point positioning approaches can be considered equivalent, in terms of the underlying physics. However, to achieve geodetic quality positions (mm- to cm-level), it is essential to resolve integer-cycle phase ambiguities to their correct integer values (*Blewitt*, 1989; *Dong and Bock*, 1989). This is straightforward for batch post-processing, which includes the simultaneous analysis of multiple GPS data records, usually sampled at rates of 15-30 s, to derive a single station position over the entire sampled interval. This is the source of the typical 24-hour GPS position time series used to study permanent deformation, including long-term tectonic motion, as well as coseismic, postseismic and other transient deformation. Batch post-processing plays a role in seismological applications by providing highly-accurate, true-of-date ITRF station positions with respect to which displacement waveforms can be estimated during an event. There are several analysis groups that are producing 24-hour position time series on an operational basis.

Of primary importance in seismological applications is the estimation of cm-level or better displacements at the GPS receiver sampling rate, typically 1Hz. Since the first pioneering efforts over a decade ago (*Nikolaidis et al.*, 2001; *Larson et al.*, 2003; *Bock et al.*, 2004; *Miyazaki et al.*, 2004) post-processed single-epoch network positioning with resolution of integer-cycle phase ambiguities is now routinely applied to seismology. However, a general real-time solution is still elusive, and analysis of multiple data epochs is usually required to resolve integer-cycle phase ambiguities and estimate single-epoch positions.

In the network positioning approach typically, and for computational efficiency, the larger network is divided into multiple subnetworks with a 2-station overlap between adjacent subnetworks, and positions are estimated relative to the true-of-date ITRF coordinates of an arbitrary station within each subnetwork. Then, a network adjustment is performed to estimate coordinates for all stations with respect to the true-of-date ITRF coordinates of one or more stations outside the zone of deformation (*Crowell et al.*, 2009) easily providing centimeter level resolution.

Precise point positioning has been limited in GPS seismology, in particular

for real-time applications, because of unresolved integer-cycle phase ambiguities and slow convergence rates and re-convergence rates when loss of lock on the satellite signals occurs. JPL's Global Differential GPS (GDGPS) System employs a large global ground network of real-time reference receivers and real-time data processing software, which allows a single GPS receiver to be point positioned with 10-20 cm accuracy anywhere in the world. This level of accuracy is considered useful for global tsunami warning generated by great earthquakes. A relatively new area of geodetic research is rapid integer cycle ambiguity resolution in precise point positioning (PPP-AR), without the need for specific reference stations. Besides fixed satellite orbits and clocks, and estimation of positions, receiver clocks and tropospheric delays of the GPS signals, it also requires prediction of ionospheric delays. Recent results have been encouraging in that reliable ambiguity resolution and cm-level positioning accuracies have been achieved with only a few epochs of 1Hz GPS data for re-convergence (*Geng*, 2010). It has since been shown with a study of modestly sized earthquakes (M5) during the 2013 Brawley swarm (*Geng et al.*, 2013a) and shake table tests (*Geng et al.*, 2013b) that the PPP-AR method is evolving to a state were it can be considered viable technology for real-time and rapid position calculations with cm-level precision.

It is important for the reader to understand the benefits and shortcomings of these two competing technologies. The network adjusted positions have routinely provided cm-level waveforms (*Crowell et al.*, 2009). However, they require that the base station for the adjustment be located outside the zone of deformation and that it not move during the event. Evidently this requires a large network with good connectivity and some strategy for detecting motions of the reference station and a fall back plan to another station that has not moved during the event. Furthermore this approach requires converting the baselines between stations in subnetworks (e.g., triangles) into absolute motions. This is essentially a solution to an inverse problem at each epoch. While this is not numerically troublesome for modest networks as the number of stations increases and as sampling rates grow the numerical load will mount. In contrast the PPP-AR approach does not require such a reference station (although it does rely on a sparse continental

network for computation of certain positioning parameters, (*Geng et al.*, 2013a) and is thus, in principle, more desirable. However ambiguity resolution might fail and re-convergence periods, at least initially, can still be long. Throughout this dissertation data from both network adjusted and PPP-AR positions will be employed. It is not the aim of this work to assess the suitability of one technique over the other although some general recommendations will be given in the conclusions. Hence for the purpose of the research discussed both approaches will be considered equal.

In general GPS seems desirable over traditional seismometry for displacement computations. it is not an inertial sensor and thus not affected by baseline offsets. This has the practical effect of making GPS a very good long and ultra-long period sensor. It can easily measure signals with very long periods, such as plate tectonic motions and post-seismic relaxation. Consider Figure 2.3. Note how the time series shows the (relative) long term plate rate as a linear trend, the coseismic offset from the September 28, 2004 M_w=6.0 Parkfield earthquake and the postseismic relaxation as well as some shaking during the earthquake. GPS seamlessly captures most key components of the seismic cycle.

However, noise levels in high rate real-time GPS (rtGPS) displacements (*Genrich and Bock*, 2006) far exceed those of observatory grade accelerometers. Furthermore GPS data is far more verbose than seismic data. While a traditional telemetry packet for a seismic sensor at a given epoch might include three single or double precision floating point numbers corresponding to the three components of motion and a UTC time string, the GPS message includes observables to every visible satellite. This has limited the sampling rates of rtGPS to around 1-5Hz even though 10-50Hz is achievable (*Genrich and Bock*, 2006). These slow sampling rates can introduce significant aliasing in GPS positions (*Smalley*, 2009). In spite of these limitations, it will be shown that without GPS positions it is exceedingly difficult to recover the long period component of ground motions and that GPS plays an important role in modern strong motion seismology.

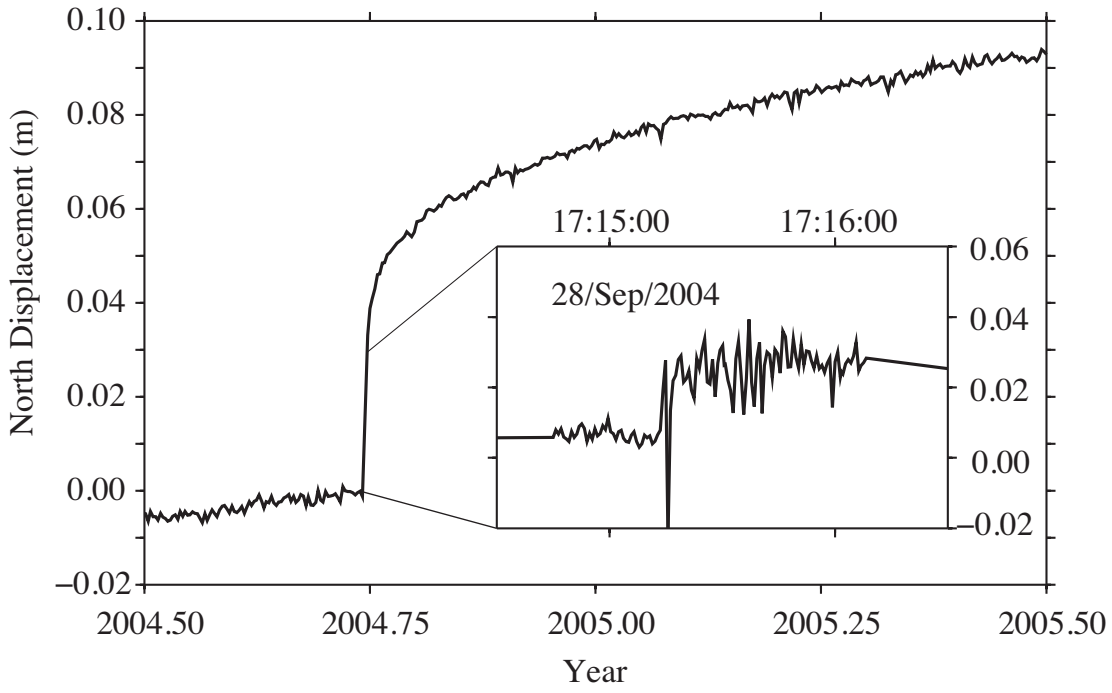


Figure 2.3: Typical 1 Hz GPS raw time series at station LAND (35°.8997 N, 120°.4731 W) in the Parkfield area over a one-year period. Shown is the north component, in this case relative to station CRBT (N 35°.7916, 120°.7507 W) whose coordinates were fixed in the GPS analysis. Note how the time series shows the (relative) long term plate rate as a linear trend, the coseismic offset from the September 28, 2004 M_w=6.0 Parkfield earthquake and the postseismic relaxation. In the inset, 2 minutes of data are shown where as opposed to the daily solutions time series we can also observe the (relative) dynamic shaking during the earthquake.

2.2.1 Displacements in a Local Reference Frame

GPS positions are typically computed in a global reference frame (the International Terrestrial Reference Frame, ITRF) in what is known as Earth-centered Earth-fixed coordinates. This is a right handed system where the three Cartesian axes have an origin at the geocenter of the planet, one axis points towards the geodetic pole and two towards the equator. Without loss of generality or consideration for the particular GPS analysis technique used, or whether or not performed in real time or post processing, we assume that displacement waveforms are available for a geophysical event (e.g., earthquake) for one of more continuous GPS (CGPS)

stations with centimeter-level or better single-epoch precision at, for example, the typical 1Hz sampling rate of current real-time geodetic networks. Consider that we know the precise coordinates (x_0, y_0, z_0) of a CGPS station in a global Cartesian reference frame just prior to an earthquake, at time t_0. The prior coordinates represent "true-of-date" values. The station is then subjected to a combination of dynamic and static displacements. The subsequent coordinates of the station are denoted by (x_i, y_i, z_i), where i denotes the i-th epoch after the event. The displacement at the i-th epoch can be simply computed as $(x_i - x_0, y_i - y_0, z_i - z_0)$. In order to compare the geodetic displacements to displacements derived from a single integration of a seismometer or double integration of an accelerometer, we need to transform the displacements from a (right-handed) global Cartesian frame (x, y, z) into a (left-handed) local North, East, Up frame (N, E, U) by the following transformation

$$\begin{pmatrix} \Delta N_i \\ \Delta E_i \\ \Delta U_i \end{pmatrix} = \begin{pmatrix} 1 & 0 & 0 \\ 0 & 1 & 0 \\ 0 & 0 & 1 \end{pmatrix} \mathbf{R}_2 \left(\frac{3\pi}{2} - \phi \right) \mathbf{R}_3(\lambda) \begin{pmatrix} x_i - x_0 \\ y_i - y_0 \\ z_i - z_0 \end{pmatrix} ; \qquad (2.3)$$

where $\mathbf{R}_2$ and $\mathbf{R}_3$ are rotation matrices around the y and z axes, respectively, and (ϕ, λ) is the geodetic latitude and longitude of the station. The geodetic displacements in the (N, E, U) frame can then be compared directly to local displacements derived through single integration of seismometer data or double integration of accelerometer data. Thus, Equation 2.3 simplifies to:

$$\begin{pmatrix} \Delta N_i \\ \Delta E_i \\ \Delta U_i \end{pmatrix} = \begin{pmatrix} -\sin\phi\cos\lambda & \sin\phi\sin\lambda & \cos\phi \\ -\sin\lambda & \cos\lambda & 0 \\ \cos\phi\cos\lambda & \cos\phi\cos\lambda & \sin\phi \end{pmatrix} \begin{pmatrix} x_i - x_0 \\ y_i - y_0 \\ z_i - z_0 \end{pmatrix} . \qquad (2.4)$$

2.3 Optimal Combination of Seismic and Geodetic Data

As discussed in the previous section both traditional seismometry and GPS have advantages and disadvantages when it comes to sensing strong ground motions. GPS and strong motion networks are complementary in the sense that ones

weakness can be complemented by anothers strengths. In particular GPS has slow sampling rates while accelerometers have fast sampling rates; in turn, accelerometers suffer from problems at long periods while GPS excels in this frequency band. Throughout this section we will show that the combination of these two sensor types provides an accurate representation of ground motion at all frequencies of interest to seismology.

We define the term *seismogeodesy* as the optimal combination of geodetic and seismic data. *Nikolaidis et al.* (2001) showed that accelerometer data could be manipulated to fit 30s sampled data recorded during the 1999 M_w7.1 Hector Mine earthquake. *Emore et al.* (2007) used 1Hz GPS data and 100Hz strong motion data recorded during the M_w8.3 Tokachi-oki event in 2003 to compute *seismogeodetic* displacements. They did so by solving an inverse problem for the baseline offsets in the accelerometer record. In that approach the model parameters were the baseline offsets that when subtracted from the accelerometer record would best fit, after double integration, the GPS record. This approach yielded good results, however the setup of the inverse problem is cumbersome and not practical in real time. In the following section we will show an alternate approach. Using a Kalman filter, we optimally combine raw very-high-rate (e.g., 100-200Hz) accelerations with high-rate (e.g., 1-10Hz) displacements derived from collocated GPS receivers to estimate very-high-rate displacements. This approach is suitable for dense networks and real-time processing required by early warning systems and rapid earthquake response.

2.3.1 The Kalman Filter Formulation

In the theory of control and estimation the problem of extracting, separating or detecting a random signal in the presence of noise is known as the Wiener problem. Kalman filters are a solution to this problem using the state-space representation of dynamical systems (*Kalman*, 1960). A dynamical system can be characterized by its state. The state can be understood as all the information about the past behavior of the system necessary to predict its future behavior. The dynamics of the system are then described by state transitions. If the goal

is to track the one-dimensional motion of a particle subject to Newton's laws plus some stochastic noise then a simple continuous difference equation can be setup (*Lewis et al.*, 2008). The system states will be the position d and velocity v of the particle, such that

$$\frac{d}{dt}\begin{pmatrix} d(t) \\ v(t) \end{pmatrix} = \frac{d}{dt}\mathbf{x}(t) = \mathbf{A}(t)\mathbf{x}(t) + \mathbf{B}(t)u(t) + \epsilon(t) \ , \tag{2.5}$$

where

$$\mathbf{x}(t) = \begin{pmatrix} d(t) \\ v(t) \end{pmatrix} \ ; \ \mathbf{A} = \begin{pmatrix} 0 & 1 \\ 0 & 0 \end{pmatrix} \ ; \ \mathbf{B} = \begin{pmatrix} 0 \\ 1 \end{pmatrix} \ ; \ u = a \ ; \ \epsilon = \begin{pmatrix} 0 \\ \epsilon_a \end{pmatrix} \ . \tag{2.6}$$

ϵ_a is the noise in the acceleration of the particle at any given time step. For the traditional Kalman filter Gaussian noise is assumed and the noise vector will be distributed like $\epsilon \sim (0, \mathbf{Q})$ where the covariance $\mathbf{Q}$ depends just on the acceleration noise σ_a

$$\mathbf{Q} = \begin{pmatrix} 0 & 0 \\ 0 & \sigma_a \end{pmatrix} \ . \tag{2.7}$$

We can combine Equations 2.5 and 2.6 to verify the system

$$\frac{d}{dt}\begin{pmatrix} d(t) \\ v(t) \end{pmatrix} = \begin{pmatrix} \dot{d} \\ \dot{v} \end{pmatrix} = \begin{pmatrix} v \\ a \end{pmatrix} \ . \tag{2.8}$$

This definition for such a simple system seems tautological, however verifying the setup of the continuous difference equation will be important later on when we build extra complexities into the filter. Next we must discretize this continuous representation of the system such that

$$\mathbf{x}_{k+1} = \mathbf{A}^s\mathbf{x}_k + \mathbf{B}^s a_k + \epsilon_k \ , \tag{2.9}$$

where the superscript s denotes the discretized or sampled version of the state transition matrices and the subscript k denotes a discrete time step. The discretized noise vector is assumed to be distributed as $\epsilon_k \sim (0, \mathbf{Q}^s)$. If we sample the continuous system at the sampling rate τ_a of the acceleration steps affecting the system then the state transition matrices are altered. From the canonical solution

to Equation 2.5 *Lewis et al.* (2008) show that the state transition matrices are obtained by the first two terms of a MacLaurin expansion of the integral forms such that

$$\mathbf{A}^s = \mathbf{I} + \mathbf{A}\tau_a + \frac{\mathbf{A}^2\tau^2}{2} = \begin{pmatrix} 1 & \tau_a \\ 0 & 1 \end{pmatrix} , \tag{2.10}$$

$$\mathbf{B}^s = \mathbf{B}\tau_a + \frac{\mathbf{AB}\tau_a^2}{2} = \begin{pmatrix} \tau_a^2/2 \\ \tau_a \end{pmatrix} , \tag{2.11}$$

$$\mathbf{Q}^s = \mathbf{Q}\tau_a + \frac{1}{2}(\mathbf{AQ} + \mathbf{QA}^T)\tau_a^2 + \frac{1}{3}\mathbf{AQA}^T\tau_a^3 = \begin{pmatrix} \sigma_a\tau_a^3/3 & \sigma_a\tau_a^2/2 \\ \sigma_a\tau_a^2/2 & \sigma_a\tau_a \end{pmatrix} . \tag{2.12}$$

This completes the description of the linear system. The Kalman filter is the sequence of mathematical manipulations necessary to estimate the state $\mathbf{x}_k$ of the system at each time step k given the noisy accelerations affecting the system. The formulation of the filter begins by introducing a measurement of the system states, that, unlike the transition matrices, is not altered by the discretization process (*Lewis et al.*, 2008). Assuming we are measuring only displacement this can be written like

$$z_k = d_k^{obs} = \mathbf{H}^s\mathbf{x}_k + \eta_d , \tag{2.13}$$

where d_k^{obs} is the GPS measurement of displacement at epoch k with white Gaussian noise such that $\eta_d \sim (0, R^s)$. Sampling at the rate of the GPS, τ_d the discretized matrices are simply:

$$\mathbf{H}^s = \mathbf{H} = \begin{pmatrix} 1 & 0 \end{pmatrix} , \tag{2.14}$$

$$R^s = \sigma_d/\tau_d . \tag{2.15}$$

To begin the filtering procedure first we estimate the system state covariance $\mathbf{P}$. After initializing the system states and covariance to $\mathbf{x}_0$ and $\mathbf{P}_0$ (usually zero or the identity) *Kalman* (1960) showed, and subsequent workers proved (*Lewis et al.*, 2008) that an unbiased minimum error estimate of the system states could be obtained by computing the *a priori* covariance as

$$\mathbf{P}_{k+1}^- = \mathbf{A}_k\mathbf{P}_k\mathbf{A}_k^T + \mathbf{Q}_k , \tag{2.16}$$

and the a priori state estimate as

$$\hat{\mathbf{x}}_{k+1}^{-} = \mathbf{A}_k \hat{\mathbf{x}}_k + \mathbf{B}_k u_k \ , \tag{2.17}$$

where recall from Equation 2.6 that $u_k = a_k$, the acceleration of the system. The hat notation $\hat{\mathbf{x}}$ indicates the obtained quantity is an estimate and the super index $^-$ indicates a quantity obtained before the measurement process. This is termed the *a priori* or *time update* stage of the filter, where the system states are estimated without consideration of the measurements. The second step is to incorporate the measurements into the *measurement update* or *a posterior* state estimation by updating the covariance to

$$\mathbf{P}_{k+1} = [(\mathbf{P}_{k+1}^{-})^{-1} + \mathbf{H}_{k+1}^{T} \mathbf{R}_{k+1}^{-1} \mathbf{H}_{k+1}]^{-1} \ , \tag{2.18}$$

and then the state estimates to

$$\hat{\mathbf{x}}_{k+1} = \hat{\mathbf{x}}_{k}^{-} + \mathbf{P}_{k+1} \mathbf{H}_{k+1}^{T} \mathbf{R}_{k+1}^{-1} (z_{k+1} - \mathbf{H}_{k+1} \mathbf{x}_{k+1}^{-}) = \hat{\mathbf{x}}_{k}^{-} + \mathbf{K}_{k+1} (z_{k+1} - \mathbf{H}_{k+1} \mathbf{x}_{k+1}^{-}) \ , \tag{2.19}$$

where the matrix $\mathbf{K}$ is known as the Kalman gain. In this final form it is easiest to understand the behavior of the filter. The Kalman gain weights the adjustment to the a priori estimate $\hat{\mathbf{x}}_k^-$ once a measurement of the system states z_k is available by modulating the correction to be applied due to the measurement residual, $z_{k+1} - \mathbf{H}_{k+1}\mathbf{x}_{k+1}^-$, which is the difference between the a priori state estimate and the actual measurement. In turn, the Kalman gain $\mathbf{K}$ depends on both the covariance matrix $\mathbf{Q}$ of the accelerations affecting the system and the covariance $\mathbf{R}$ of the measurements. Thus, the noise characteristics of both information sources is considered in the estimation process. Equations 2.16-2.19 define what is traditionally called a the Kalman filter solution.

In the above formulation, also referred to as the *forward* filter, the accelerometer time series at sampling interval τ_a provides what is often referred to as the *system input*, u_k, while the GPS displacements at sampling interval τ_d feed the measurement process, z_k. GPS sampling frequencies are traditionally lower (1 - 10Hz) than strong-motion accelerometer sampling frequencies (80 - 250Hz), thus the formulation needs to be adapted to this multi-rate environment (*Smyth and*

Table 2.1: A summary of Kalman filtering and smoothing equations

Forward Filter	
Initialize states	$\hat{\mathbf{x}}_0 = \mathbf{0}$
Initialize covariance	$\mathbf{P}_0 = \mathbf{I}$
Time update covariance	$\mathbf{P}^-_{k+1} = \mathbf{A}_k \mathbf{P}_k \mathbf{A}_k^T + \mathbf{Q}_k$
Time update system states	$\hat{\mathbf{x}}^-_{k+1} = \mathbf{A}_k \hat{\mathbf{x}}_k + \mathbf{B}_k a_k$
Introduce measurement	$z_k = d_k$
Compute Kalman gain	$\mathbf{K}_{k+1} = \mathbf{P}_{k+1} \mathbf{H}_{k+1}^T \mathbf{R}_{k+1}^{-1}$
Measurement update of covariance	$\mathbf{P}_{k+1} = [(\mathbf{P}^-_{k+1})^{-1} + \mathbf{H}_{k+1}^T \mathbf{R}_{k+1}^{-1} \mathbf{H}_{k+1}]^{-1}$
Measuremment update system states	$\hat{\mathbf{x}}_{k+1} = \hat{\mathbf{x}}^-_k + \mathbf{K}_{k+1}(z_{k+1} - \mathbf{H}_{k+1} \mathbf{x}^-_{k+1})$
RTS N-sample Smoother	
Initialize states	$\mathbf{x}_N = \mathbf{x}_k$
Initialize covariance	$\mathbf{P}_N = \mathbf{P}^f_k$
Compute smoother gain	$\mathbf{F}_k = \mathbf{P}^f_k \mathbf{A}_k (\mathbf{P}^{f-}_{k+1})^{-1}$
Update covariance	$\mathbf{P}_k = \mathbf{P}^f_k - \mathbf{F_k}(\mathbf{P}^{f-}_{k+1} - \mathbf{P}_{k+1}) \mathbf{F}_k^T$
Update system states	$\hat{\mathbf{x}}_k = \hat{\mathbf{x}}^f_k + \mathbf{F}_k(\hat{\mathbf{x}}_{k+1} - \hat{\mathbf{x}}^{f-}_{k+1})$

Wu, 2007) by performing the time update stage (Equations 2.16-2.17) at every time step and applying the measurement update stage (Equations 2.18-2.19) only when a GPS sample becomes available. This is equivalent to having a Kalman gain of zero in the absence of measurements. For algorithmic simplicity it is useful if the sampling frequency of the strong-motion accelerometer is a multiple of GPS sampling frequency. In this way the measurement update can be done at regular intervals but this is not a requirement. Also if the sampling frequencies remain constant throughout and the noise characteristics do not change then $\mathbf{A}^s$, $\mathbf{B}^s$, $\mathbf{Q}^s$, and $\mathbf{R}^s$ remain unchanged. However, the sampling frequencies for both instruments can vary throughout the filtering process as long as the corresponding matrices are modified accordingly. An attractive feature of this formulation is that the matrices involved have small dimensions making the numerical computation in the two stages of the process simple. Additionally, the Kalman filter only requires knowledge of the current sample and thus can be implemented in real time and across large networks. It must be noted that the Kalman filter will also produce estimates of velocity in conjunction with the displacement computations. A summary of the filter equations can be found in Table 2.1

2.3.2 Optimal Smoothing

Applying the Kalman filter in the forward direction solves what is known as the prediction problem. If data are available over some interval and all that data past and future are used in the estimation then the estimate at any given point can be improved. This is known as the smoothing problem and is a non-real-time or batch operation. It can be performed, nonetheless, as a near real-time operation by limiting the smoothing to short intervals of time. If smoothing happens only over a fixed window behind the real-time stream the smoother is called a fixed interval smoother. Any smoother consists of three conceptual steps: the forward Kalman filter described in the previous section, then a backward filter known as the information filter which is applied in reverse time order to the smoothing interval. The third step utilizes the information from the first two steps (forward Kalman filter and information filter) and combines them to generate state estimates. *Rauch et al.* (1965) showed that the forward Kalman and information filters could be applied in a single step. This has come to be known to as the Rauch,Tung and Striebel smoother (RTS). The smoother gain, which is analogous to the Kalman gain, defines the amount of smoothing and can be defined by

$$\mathbf{F}_k = \mathbf{P}_k^f \mathbf{A}_k (\mathbf{P}_{k+1}^{f-})^{-1} \ , \tag{2.20}$$

where $\mathbf{P}_k^f$ and $\mathbf{P}_{k+1}^{f-}$ are the a priori and a posteriori covariance matrices, respectively, from the forward filter. The smoothed covariances are given by

$$\mathbf{P}_k = \mathbf{P}_k^f - \mathbf{F_k}(\mathbf{P}_{k+1}^{f-} - \mathbf{P}_{k+1})\mathbf{F}_k^T \ , \tag{2.21}$$

and the smoothed state estimates by

$$\hat{\mathbf{x}}_k = \hat{\mathbf{x}}_k^f + \mathbf{F}_k(\hat{\mathbf{x}}_{k+1} - \hat{\mathbf{x}}_{k+1}^{f-}) \ . \tag{2.22}$$

Note that the smoothing stage works backwards in time using the $k+1$-th time step to estimate the k-th step and it does not depend on the measurements or system inputs. The RTS smoother consists of applying the forward filter first, and then smoothing using Equations 2.20-2.22. The RTS algorithm requires the totality of the Kalman filtered time series over the smoothing interval to be available as well

as all the a priori estimates, covariances, and a posteriori covariances making it a data intensive operation. For a particular waveform the best possible results are obtained by applying the smoother over the entire duration of the data. For near-real-time computation one can apply the RTS algorithm to segments of data by lagging N samples behind the end of the real time stream. In this fashion it is assumed that the N samples behind the real-time stream constitute a complete time series and the RTS smoother is applied to them. Initialization is performed by setting the N-th sample to $\mathbf{x}_N = \mathbf{x}_k$ and $\mathbf{P}_N = \mathbf{P}_k^f$. Further on we shall show that the important parameter in near-real-time smoothing with this scheme is the number of GPS samples over which one can smooth rather than the actual time lag. A summary of the smoother equations can be found in Table 2.1.

2.3.3 Accelerometer Biases

A subtle point to be considered in this application-specific formulation of the Kalman filter is that the DC-level of most accelerometers is seldom zero. Often due to small tilts or rotations introduced during installation, variations in site and installation conditions, or simply because of drift in the instrument as it ages the DC level of the instrument will be non-zero. In a post-processing scenario one can subtract the pre-event baseline from the accelerometer recording. For real-time calculation however, this cannot be done, and can have a large effect in the Kalman filter output because it introduces a constant acceleration. It can be easily dealt with by incorporating the accelerometer bias as an additional system state. If the measured or observed acceleration a^{obs} is related to the true acceleration, a^{true} by

$$a_k^{true} = a_k^{obs} - \Omega_k + \epsilon_a \ , \tag{2.23}$$

where Ω_k is the DC offset at epoch k and ϵ_a is as before the accelerometer noise. If we augment the system states to include the DC offset we can once again write

the continuous difference equation for this system:

$$\frac{d}{dt}\begin{pmatrix} d(t) \\ v(t) \\ \Omega(t) \end{pmatrix} = \frac{d}{dt}\mathbf{x}(t) = \mathbf{A}(t)\mathbf{x}(t) + \mathbf{B}(t)u(t) + \epsilon(t) \ , \tag{2.24}$$

where

$$\mathbf{A} = \begin{pmatrix} 0 & 1 & 0 \\ 0 & 0 & -1 \\ 0 & 0 & 0 \end{pmatrix} \ ; \ \mathbf{B} = \begin{pmatrix} 0 \\ 1 \\ 0 \end{pmatrix} \ ; \ u = a^{obs} \ ; \ \epsilon = \begin{pmatrix} 0 \\ \epsilon_a \\ \epsilon_\Omega \end{pmatrix} \ , \tag{2.25}$$

and ϵ_Ω is the DC offset noise. A small value of ϵ_Ω will allow the DC offset to vary slowly through time, for example, to deal with diurnal or other seasonal variations in the zero baseline. Assuming that the noise vector is described by $\epsilon \sim (0, \mathbf{Q})$ where the covariance $\mathbf{Q}$ depends on the accelerometer and DC offset noise variances σ_a and σ_Ω like

$$Q = \begin{pmatrix} 0 & 0 & 0 \\ 0 & \sigma_a & 0 \\ 0 & 0 & \sigma_\Omega \end{pmatrix} \tag{2.26}$$

The last two equations can be expanded to verify the system:

$$\frac{d}{dt}\begin{pmatrix} d(t) \\ v(t) \\ \Omega(t) \end{pmatrix} = \begin{pmatrix} \dot{d} \\ \dot{v} \\ \dot{\Omega} \end{pmatrix} = \begin{pmatrix} v \\ -\Omega + a^{obs} + \epsilon_a \\ \epsilon_\Omega \end{pmatrix} \ . \tag{2.27}$$

We can discretize the continuous system at the sampling rate τ_a of the accelerometer following the strategy outlined in Section 2.3.1

$$\mathbf{A}^s = \mathbf{I} + \mathbf{A}\tau_a + \frac{\mathbf{A}^2\tau^2}{2} = \begin{pmatrix} 1 & \tau_a & -\tau_a^2/2 \\ 0 & 1 & -\tau_a \\ 0 & 0 & 1 \end{pmatrix} \ ; \tag{2.28}$$

$$\mathbf{B}^s = \mathbf{B}\tau_a + \frac{\mathbf{A}\mathbf{B}\tau_a^2}{2} = \begin{pmatrix} \tau_a^2/2 \\ \tau_a \\ 0 \end{pmatrix} \ ; \tag{2.29}$$

$$\mathbf{Q}^s = \mathbf{Q}\tau_a + \frac{1}{2}(\mathbf{AQ}+\mathbf{QA}^T)\tau_a^2 + \frac{1}{3}\mathbf{AQA}^T\tau_a^3 = \begin{pmatrix} \sigma_a\tau_a^3/3 & \sigma_a\tau_a^2/2 & 0 \\ \sigma_a\tau_a^2/2 & \sigma_a\tau_a + \sigma_\Omega\tau_a^3/3 & -\sigma_\Omega\tau_a^2/2 \\ 0 & -\sigma_\Omega\tau_a^2/2 & \sigma_\Omega\tau_a \end{pmatrix}. \tag{2.30}$$

Equations 2.28-2.30 can then be used with the standard Kalman filter definition (Table 2.1), except that the output of the filter will now be estimated displacement, velocity and accelerometer bias at each epoch.

2.4 Proof of Concept

Following are examples from shake table tests of collocated GPS and accelerometers as well as recordings at collocated stations during recent earthquakes to demonstrate the behavior of the Kalman filter.

2.4.1 Outdoor Shake Table Testing

A series of earthquake simulations were conducted in 2006-2007 on a full-scale seven-story reinforced concrete wall building at the George E. Brown, Jr. Network for Earthquake Engineering Simulation (NEES) Large High-Performance Outdoor Shake Table (LHPOST) at University of California San Diego (*Panagiotou*, 2008; *Moaveni et al.*, 2010). The four simulations allowed us to test the Kalman filter algorithms in a controlled environment. The LHPOST includes a steel table platform (platen), a reinforced concrete reaction mass, two servo-controlled dynamic actuators with large servo-valves, a platen sliding system with hydrostatic pressure balance bearings, and a real time multi-variable MTS 469DU digital controller with an output of 1024Hz in displacement. The system is uniaxial and oriented East-West. It can achieve maximum peak-to-peak displacement of $\pm$0.75m, velocity of $\pm$1.8m/s, and acceleration of $\pm$3g, with a frequency bandwidth of 0-20 Hz.

The building with a total height of 19.2m and total weight of 250 tons was constructed on the shake table platen and subjected to four low to high intensity ground motions, as recorded by accelerometers during the 1971 M_w6.6 San Fer-

nando and 1994 M_w6.7 Northridge earthquakes (Figure 2.4). The lowest intensity input motion (EQ1) consisted of the longitudinal component from the VNUY station recorded during the San Fernando earthquake. The two medium intensity input motions were the transverse component recorded at the VNUY station obtained during the San Fernando earthquake (EQ2) and the longitudinal component from the WHOX station recorded during the Northridge earthquake (EQ3). The large intensity input motion corresponded to the near-fault Sylmar Olive View Med 360 record during the Northridge earthquake (EQ4), which induced significant nonlinear response. This last class of earthquake is expected to have a 10% probability of exceedance every 50 years. For calibration purposes, the earthquake records were preceded by a sinusoidal signal with peak-to-peak amplitude of about 0.1m.

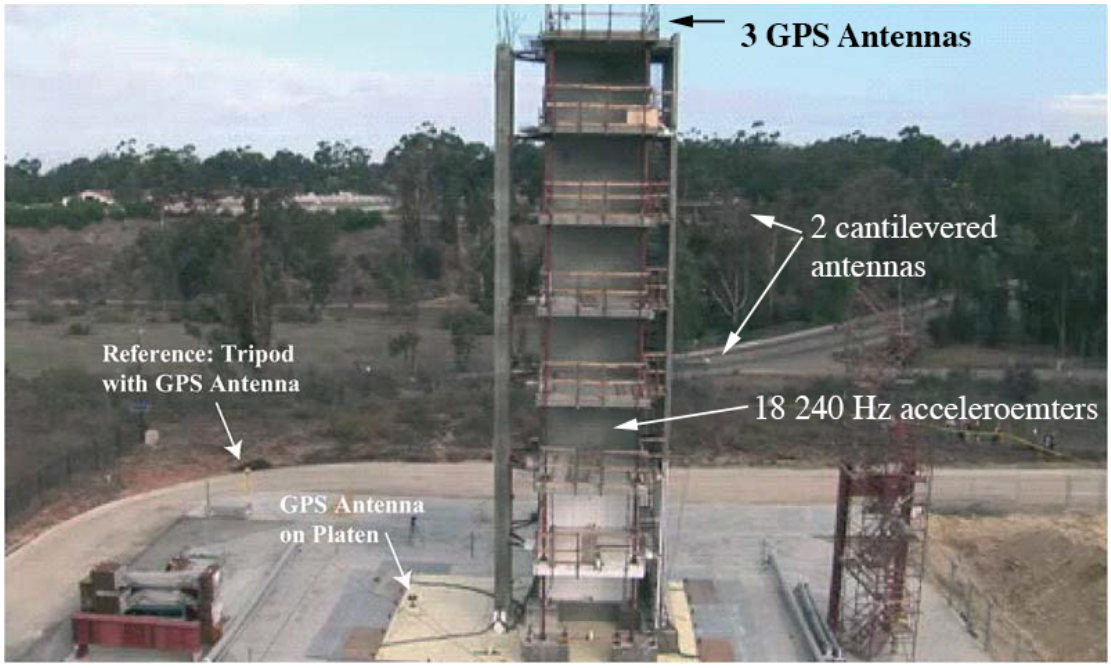


Figure 2.4: Experimental configuration for the 2006 shake table test

The building was instrumented with seven geodetic-quality Navcom NCT-200D GPS receivers sampling at 50Hz and MEMS-Piezoresistive MSI model 3140 accelerometers sampling at 240Hz. Three GPS receivers were mounted on the roof (7th floor near the north, south and east corners), and two receivers were can-

tilevered on the 3rd and 5th floors of the flange wall (east side). A 6th receiver was located just off the shake table's platen as a stable reference point for measuring displacements. A 7th GPS receiver was situated on the platen. The 15 accelerometers were mounted as follows: 2 on the platen, 4 on the building foundation, 3 on the first floor, 3 on the fifth floor and 3 on the seventh floor (roof). Unfortunately, the north receiver on the roof of the building was not operational during EQ4 due to a loose antenna cable.

GPS phase and pseudorange data were streamed to a PC workstation and 50 Hz displacement waveforms were estimated on-the-fly using the method of instantaneous positioning (*Bock et al.*, 2000) . The "GPS-only" displacements are relative to the fixed coordinates of the GPS receiver just off the platen, which were pre-determined with respect to the true-of-date ITRF2005 coordinates (*Altamimi et al.*, 2007) of Plate Boundary Observatory (PBO) station P472 at Camp Elliot (32°.8892N, 117°.1047W), approximately 656 m away. The accelerometer data were doubly-integrated by high-pass filtering to determine "accelerometer-only" displacements. We re-sampled the 240Hz raw accelerometer data to 250Hz to be able to align the times of every 5th point with the 50Hz Navcom GPS data. Displacement waveforms were then computed using both the forward and the smoothed Kalman (RTS) filter using the GPS platen data as input and, in turn, the raw data from the two platen and four foundation accelerometers. To assess accuracy, we compared the GPS-only, accelerometer-only, and Kalman filter displacements to the input ground truth displacements provided at 1024Hz by the MTS digital controller. To assess precision, we compared the root-mean-square (RMS) of the distances between pairs of accelerometers and pairs of GPS receivers on the roof of the building (7th floor). The results of these comparisons are given in Table 2.3.

Table 2.2: RMS differences between computed displacement waveforms and the input registered by the shake table's MTS recorder for four earthquake simulations (EQ1-EQ4). We show the results of high pass filtered accelerometer derived displacements for platen accelerometers (PA1 and PA2) and building foundation accelerometers (FA1-4) as well as Kalman filtered waveforms obtained from the platen GPS and platen and foundation accelerometers. We also show the results from decimated data (5 Hz for GPS and 100 Hz for accelerometers, and 1 Hz for GPS and 100Hz for accelerometers). The peak displacements are 0.16-0.17 m for EQ1-EQ3 and 0.40 m for EQ4

Sensors	**EQ1**	**EQ2**	**EQ3**	**EQ4**
GPS Displacements RMS (m)				
Platen GPS	0.0026	0.0040	0.0029	0.0037
Accelerometer Derived Displacements RMS (m)				
PA1	0.0193	0.0181	0.0151	0.0120
PA2	0.0177	0.0184	0.0131	0.0175
FA1	0.0308	0.0278	0.0037	0.0027
FA2	0.0304	0.0274	0.0036	0.0028
FA3	0.0307	0.0276	0.0037	0.0027
FA4	0.0307	0.0276	0.0036	0.0027
Forward Filter RMS (m)				
PA1+GPS	0.0021	0.0041	0.0034	0.0033
PA2+GPS	0.0021	0.0041	0.0034	0.0033
FA1+GPS	0.0016	0.0021	0.0020	0.0020
FA2+GPS	0.0016	0.0020	0.0020	0.0020
FA3+GPS	0.0016	0.0021	0.0020	0.0020
FA4+GPS	0.0016	0.0021	0.0020	0.0020
Forward Filter + 5 Hz Decimation RMS (m)				
PA1+GPS	0.0041	0.0074	0.0074	0.0046
PA2+GPS	0.0040	0.0074	0.0074	0.0046
FA1+GPS	0.0042	0.0067	0.0063	0.0037
FA2+GPS	0.0042	0.0066	0.0063	0.0037
FA3+GPS	0.0042	0.0066	0.0063	0.0037
FA4+GPS	0.0042	0.0066	0.0063	0.0037
Forward Filter + 1 Hz Decimation RMS (m)				
PA1+GPS	0.0353	0.0211	0.0625	0.0341
PA2+GPS	0.0353	0.0211	0.0625	0.0341
FA1+GPS	0.0333	0.0313	0.0612	0.0273
FA2+GPS	0.0333	0.0305	0.0607	0.0265
FA3+GPS	0.0333	0.0308	0.0609	0.0275
FA4+GPS	0.0333	0.0309	0.0601	0.0277

Table 2.3: RMS differences with smoother between computed displacement waveforms and the input registered by the shake table's MTS recorder for four earthquake simulations (EQ1-EQ4). We show the results of high pass filtered accelerometer derived displacements for platen accelerometers (PA1 and PA2) and building foundation accelerometers (FA1-4) as well as Kalman filtered waveforms obtained from the platen GPS and platen and foundation accelerometers. We also show the results from decimated data (5 Hz for GPS and 100 Hz for accelerometers, and 1 Hz for GPS and 100Hz for accelerometers). The peak displacements are 0.16-0.17 m for EQ1-EQ3 and 0.40 m for EQ4

Sensors	**EQ1**	**EQ2**	**EQ3**	**EQ4**
Forward Filter + RTS Smoothing RMS (m)				
PA1+GPS	0.0016	0.0036	0.0024	0.0028
PA2+GPS	0.0016	0.0036	0.0024	0.0028
FA1+GPS	0.0017	0.0021	0.0021	0.0025
FA2+GPS	0.0017	0.0021	0.0021	0.0025
FA3+GPS	0.0017	0.0021	0.0021	0.0025
FA4+GPS	0.0017	0.0021	0.0021	0.0025
Forward Filter + RTS Smoothing + 5 Hz Decimation RMS (m)				
PA1+GPS	0.0015	0.0038	0.0027	0.0028
PA2+GPS	0.0015	0.0038	0.0027	0.0028
FA1+GPS	0.0017	0.0022	0.0024	0.0025
FA2+GPS	0.0017	0.0022	0.0024	0.0025
FA3+GPS	0.0017	0.0022	0.0024	0.0025
FA4+GPS	0.0017	0.0022	0.0024	0.0025
Forward Filter + RTS Smoothing + 1 Hz Decimation RMS (m)				
PA1+GPS	0.0077	0.0102	0.0152	0.0130
PA2+GPS	0.0077	0.0102	0.0152	0.0130
FA1+GPS	0.0097	0.0117	0.0168	0.0115
FA2+GPS	0.0097	0.0118	0.0166	0.0115
FA3+GPS	0.0098	0.0117	0.0167	0.0114
FA4+GPS	0.0096	0.0117	0.0167	0.0115
Roof Baselines RMS (m)				
GPS (N-S)	0.0033	0.0026	0.0035	n/a
GPS (N-E)	0.003	0.0019	0.0034	n/a
GPS (S-E)	0.0036	0.0033	0.0023	0.0031
Accelerometer (N-S)	0.0008	0.0007	0.001	0.0012

Accuracy of the Displacement Waveforms

Accuracy was determined by comparing the various displacement waveforms with the"true" displacements provided by the MTS recorder, for each of the

four experiments, using the RMS difference as the statistical measure. The results are given in Figure 2.5 and Table 2.3. The peak-to-peak displacements are on the order of 0.17 m for EQ1-EQ3, and 0.4 m for the high intensity Northridge event (EQ4). The RMS statistic is computed over the entire record including dynamic and static periods. The displacements for the single GPS on the platen have an RMS difference of 2.6-4.0mm, while the displacements for the two accelerometers on the platen have an RMS difference of 12.0-19.3mm. The larger differences for the accelerometer-derived displacements result from mismatches in amplitude and phase compared to the MTS displacements. The forward Kalman filter solutions reduce the RMS differences by about 10% (except for EQ2 where there is a 10% increase) compared to the GPS-only solutions (2.2-4.1mm), and there is an additional 10% improvement for all four experiments with the smoothed Kalman filter solutions (1.6-2.3mm). For the foundation accelerometers, the RMS differences are higher for EQ1 and EQ2 (about 30mm), but unexpectedly an order of magnitude less for EQ3 and EQ4. In any case, we can conclude that the combined GPS and accelerometer displacement waveforms provide overall mm-level accuracy over the entire range of sampled frequencies, and improved accuracy when compared to GPS-only or accelerometer-only solutions. The improvement is generally more pronounced when compared to the accelerometer-only solutions. This is not surprising because of the inherent limitations and biases encountered in the double integration of accelerometer data. It is interesting to note that the RMS statistics for either the static or dynamic periods did not differ significantly from the RMS values computed for the entire period (static and dynamic) for any of the experiments. We saw only insignificant degradation (10%) in accuracy during periods of strong shaking.

We repeated the previous analysis with two decimation schemes: the first one decimating the accelerometer to 100Hz and the GPS to 5Hz and the second one decimating the accelerometer to 100Hz and the GPS to 1Hz (Table 2.3). The latter corresponds to the sampling rates of real-time GPS and strong motion sensors in southern California during the 2010 M_w7.2 El Mayor-Cucapah earthquake. We find that the fit of the Kalman filtered waveforms is only mildly degraded in the

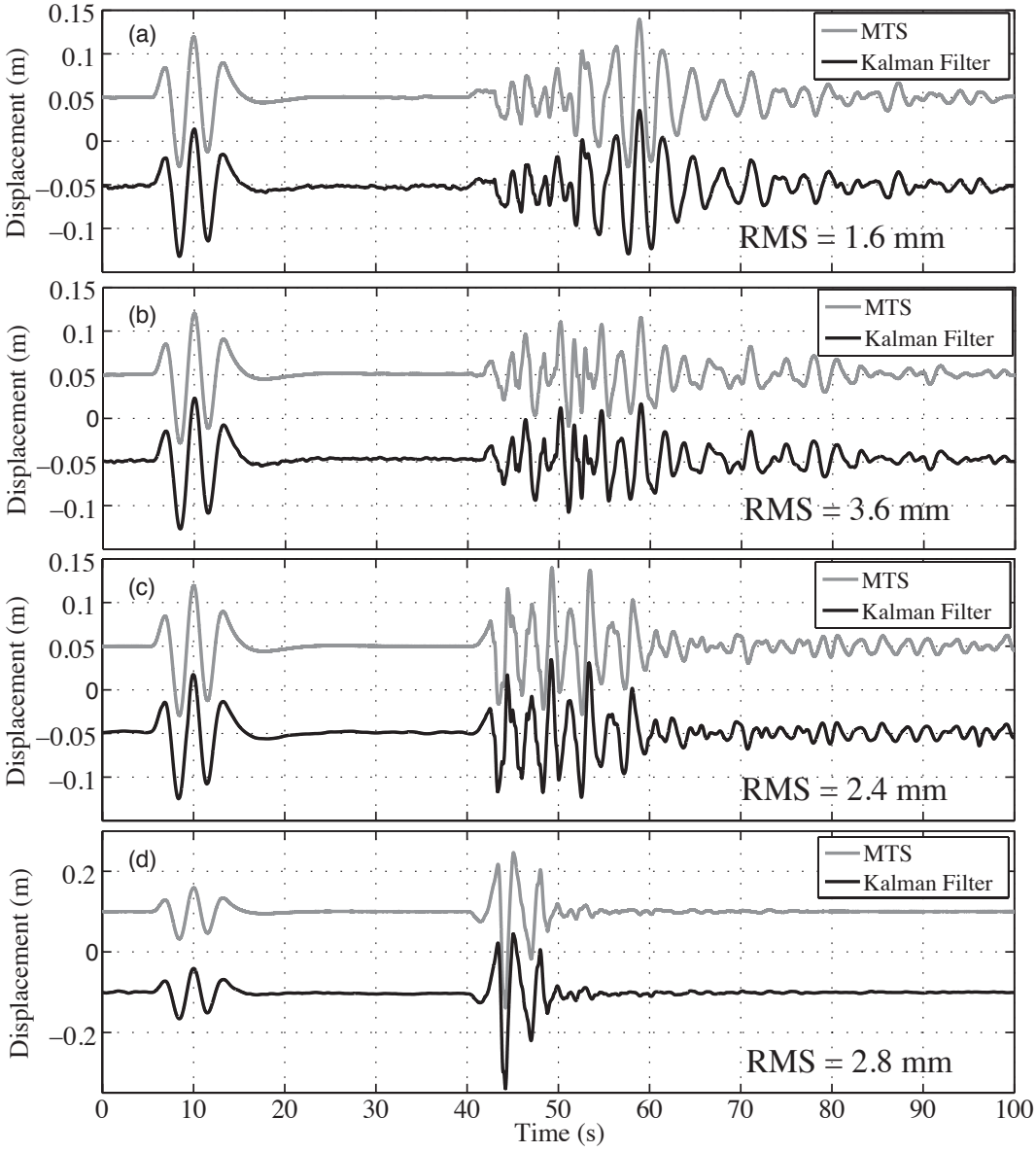


Figure 2.5: Accuracy of broadband displacement waveforms. Root-mean-square (RMS) of the differences between the smoothed Kalman filter displacement waveforms estimated for the four earthquake simulations and the deterministic input as registered at 1024 Hz by the shake table's MTS digital recorder (see also Table 2.3). The waveforms are estimated from the platen GPS and one of the accelerometers on the platen. Note that the vertical scale is the same for (a) through (c) but changes for (d). The two waveforms in each graph have been offset for clarity.

first decimation scheme, and significantly degraded with the second decimation scheme. However smoothing provides a significant improvement, especially at the lower GPS sampling rates (1Hz). This is an important practical consideration since GPS data are considerably more verbose than strong motion data.

Precision of the Displacement Waveforms

In order to evaluate precision we examined the RMS of the difference in displacements estimated for pairs of GPS and pairs of accelerometers on the roof of the building (7th floor) for each of the four experiments (Figure 2.3), including periods of both quiet and dynamic motion. The assumption is that the roof is rigid, and that there is no permanent deformation occurring between the sensors. The displacements obtained from high pass filtering of the accelerometer data show smaller RMS differences on the order of only 1mm while the GPS-only displacements show RMS differences on the order of 3mm. This makes sense since accelerometer data are more sensitive to ground motion than GPS data, that is, they are more precise. However, as we have seen accuracy is degraded for the accelerometer displacements due to biases in the double integration process, which in this case appear to be common to both accelerometers on the roof. GPS precision of about 3mm is what we would expect from earlier studies of high-rate GPS horizontal displacements on short baselines (*Genrich and Bock*, 2006).

2.4.2 The 2010 M_w7.2 El Mayor-Cucapah Earthquake

The shake table experiments differed from a real-world event in several important ways. First, only the dynamic motions could be simulated. In a real event there would be no nearby stable GPS reference station and displacements would need to be referred to one or more stations outside the region of deformation. Also, GPS noise would increase with longer station separations, by a factor of about 3 in the horizontal components and up to an order of magnitude in the vertical component (*Langbein and Bock*, 2004; *Genrich and Bock*, 2006). Finally, the ability to resolve integer-cycle phase ambiguities in real-time scenarios is diminished as station separations increase (*Bock et al.*, 2000). The 2010 M_w7.2 El Mayor-Cucapah

earthquake in northern Baja California and observations from southern California high-rate GPS and very-high-rate accelerometers provide us with a real-world event to highlight the advantages of combining GPS displacements and acceleration data.

The El Mayor-Cucapah earthquake broke a subset of northwest-trending strike-slip faults that are separated by pull-apart basins that accommodate northwest-southeast oriented extension, and are parallel to the main strands of the San Andreas fault system (Imperial, Elsinore, San Jacinto, Laguna Salada, and Cerro Prieto faults). It caused significant ground motions at distances up to several hundred kilometers from the epicenter (*Hauksson et al.*, 2011; *Wei et al.*, 2011). A robust set of 1Hz GPS phase and pseudorange data were collected for this earthquake at 105 California Real-Time Network (CRTN) and PBO stations (Figure 2.6) and on-the-fly displacement waveforms were estimated.

In order to evaluate the Kalman filter performance, we reprocessed the entire set of 1 Hz GPS-derived displacement waveforms (Figure 2.7) in simulated real-time mode using the network approach. We divided the network into 9 subnetworks with at least 2-station overlap and estimated relative displacement waveforms in the ITRF2005 frame for each subnetwork relative to an arbitrary station within each. The maximum relative motion encountered between adjacent stations closest to the epicenter was 0.58 m between stations P494 and P497 located 16.7km apart (Figure 2.6). Then, we performed a network adjustment to estimate coordinates for all stations with respect to the true-of-date coordinates of station GNPS, and transformed the coordinates for each station into displacements in the local (N,E,U) frame using Equation 2.3. GNPS was chosen not only because it is the farthest from the epicenter (it is 245 km to the northeast, Figure 2.6), but also because of directivity considerations.

We then combined the GPS-derived 1Hz displacements with raw 100Hz accelerometer data using the Kalman forward and smoothed filters to estimate the velocity and displacement waveforms. This was performed on a station-by-station basis for those 12 GPS stations that were within 1.5km of an accelerometer. The instruments closest to the earthquake's epicenter were the accelerometer at WES

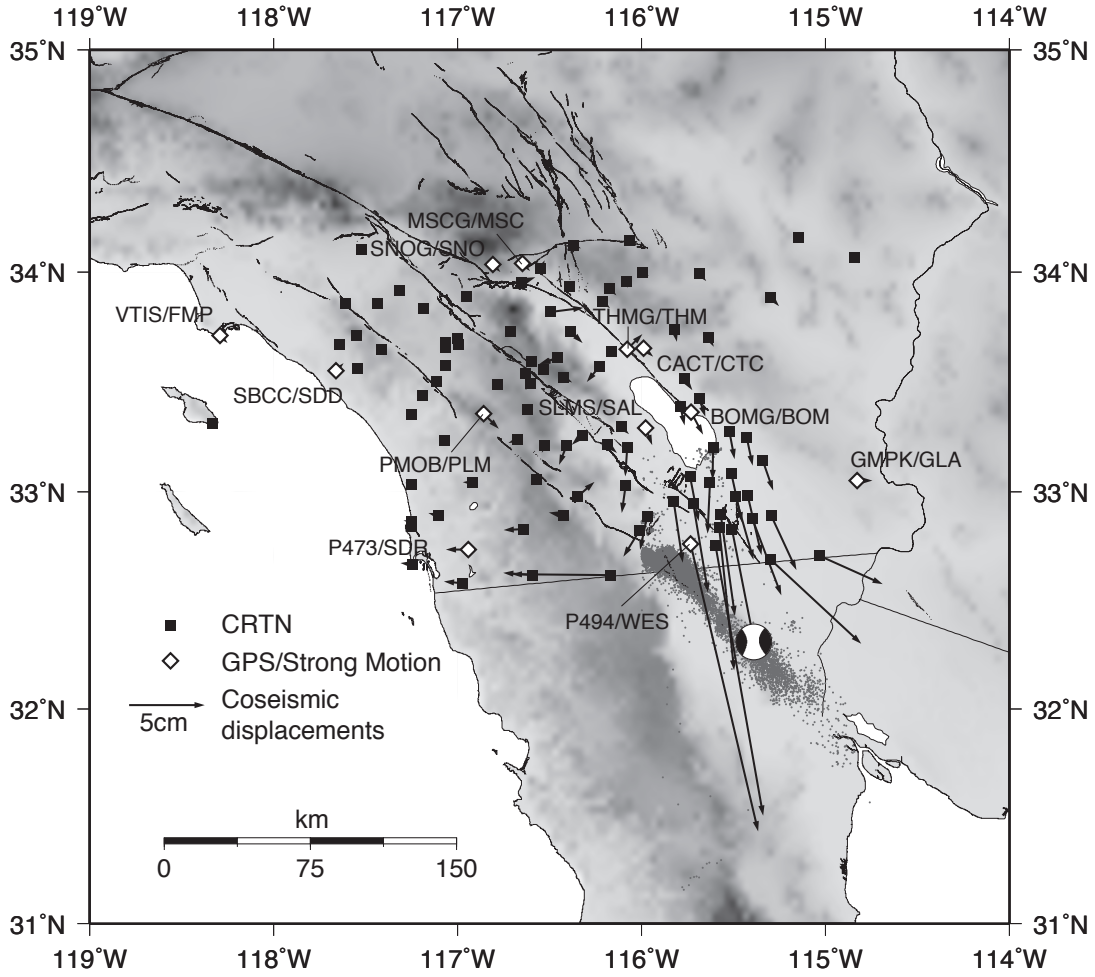


Figure 2.6: California Real Time GPS Network (CRTN) stations in southern California and collocated California Integrated Seismic Network (CISN) strong-motion accelerometer stations. The arrows indicate horizontal coseismic offsets from the 2010 M_w7.2 El Mayor-Cucapah earthquake. The 12 collocated stations (where the GPS and strong-motion accelerometers are within 1.5 km) are denoted by white diamonds. The GPS station name is given by its 4-character code, and the seismic station by its 3-character code. P494/WES has a broadband seismometer, an accelerometer, and a GPS receiver and is featured in several subsequent figures.

and GPS at P494 (Table 2.4). The two sensors are about 72km from the epicenter just north of the U.S.-Mexico border and 80m from each other (Figure 2.6).

In Figure 2.8a, we show the entire period of seismic shaking at P494/WES in the vertical component. The observed broadband velocities clip before the arrival of the S wave at the station, while the estimated velocity waveforms record the entire

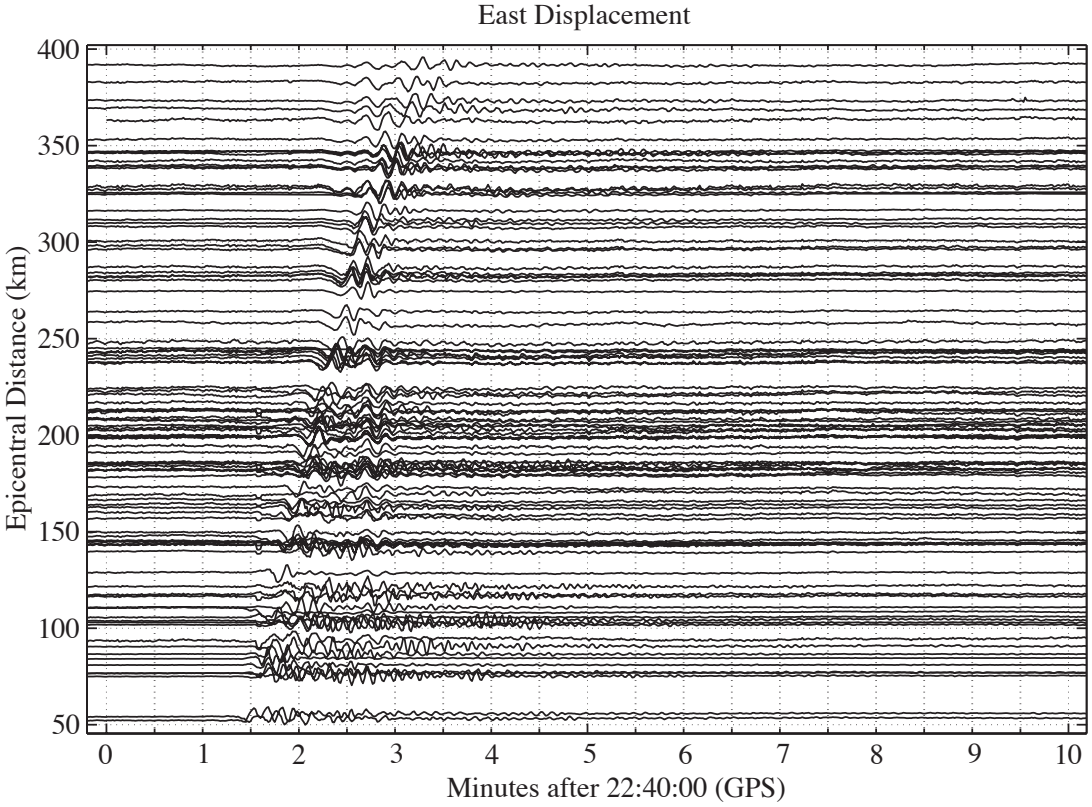


Figure 2.7: 1 Hz (East component) displacements estimated for 105 CRTN stations are plotted according to epicentral distance for the April 4, 2010 M_w7.2 El Mayor-Cucapah earthquake. The earthquake initiated at 22:40:40 UTC, or equivalently 22:40:55 GPS time. All waveforms have been normalized for clarity

event at the 100Hz rate of the accelerometer. In Figure 2.8b, we show the first 12s of the vertical broadband seismometer record at WES after the Southern California Earthquake Center's P wave pick and overlay the Kalman-filter-estimated velocities. That the broadband seismic data and the waveform estimated by Kalman smoothing are indistinguishable is striking, given also that the GPS resolution is poorest in the vertical direction. In Figure 2.8c, we compare displacements derived by (single) integration of the (12s) seismometer record at WES, and the 100Hz smoothed Kalman filter broadband displacements. it is clear that we can detect the small-amplitude P wave recordings with a precision (and accuracy) of about 1mm. This is a significant improvement over the 1Hz GPS-only solutions where the vertical precision is on the order of several tens of millimeters, often

Table 2.4: Collocated GPS (California Real Time GPS Network) and strong-motion accelerometer (California Integrated Seismic Network) stations with a station separation of 1.5 km or less.

CRTN Station	Latitude °N	Longitude °W	SCSN Station	Latitude °N	Longitude °W	Separation km
P473	32.7338	116.9495	SDR	32.7356	116.9424	0.7
P494	32.7597	115.7321	WES	32.7590	115.7316	0.08
GMPK	33.0511	114.8273	GLA	33.0512	114.8271	0.05
SLMS	33.2922	115.9778	SAL	33.2801	115.9859	1.50
PMOB	33.3572	116.8595	PLM	33.3536	116.8626	0.5
BOMG	33.3646	115.7297	BOM	33.3647	115.7296	0.01
SBCC	33.5530	117.6615	SDD	33.5526	117.6617	0.05
THMG	33.6506	116.0773	THM	33.6507	116.0773	0.01
CACT	33.6551	115.9900	CTC	33.6551	115.9901	0.01
VTIS	33.7126	118.2938	FMP	33.7126	118.2938	0.00
SNOG	34.0352	116.8078	SNO	34.0352	116.8078	0.01
MSCG	34.0385	116.6480	MSC	34.0385	116.648	0.00

precluding P wave detection.

Figure 2.8c also shows the poor results obtained by on-the-fly double integration of the accelerometer data. Of course, better results could be obtained after the fact with post-processed baseline corrections. To investigate this we computed displacements for WES from uncorrected double integration of accelerometer data (0-th order correction), correcting with the BI baseline removal scheme (Section 2.1), and with high pass filtering. Although the dynamic motions could be extracted through baseline corrections or function fitting, the static displacements were lost. With the addition of high-rate GPS displacements, high pass filtering or function fitting is not required, and the double integration can be performed on-the-fly using just the raw accelerometer records. In Section 2.5 we will quantify the performance of baseline correction schemes when compared to the Kalman filter when we consider the Tohoku-oki data.

In Figure 2.9, we show the broadband displacement waveforms for P494/WES in all 3 components, where the 0.2m horizontal static offset in the North component is clearly seen. The corresponding smoothed Kalman filter vertical displacement waveforms for P494/WES, as well as those for two other collocated GPS/accelerometer stations (BOMG/BOM and THMG/TGM, 129 and 192 km

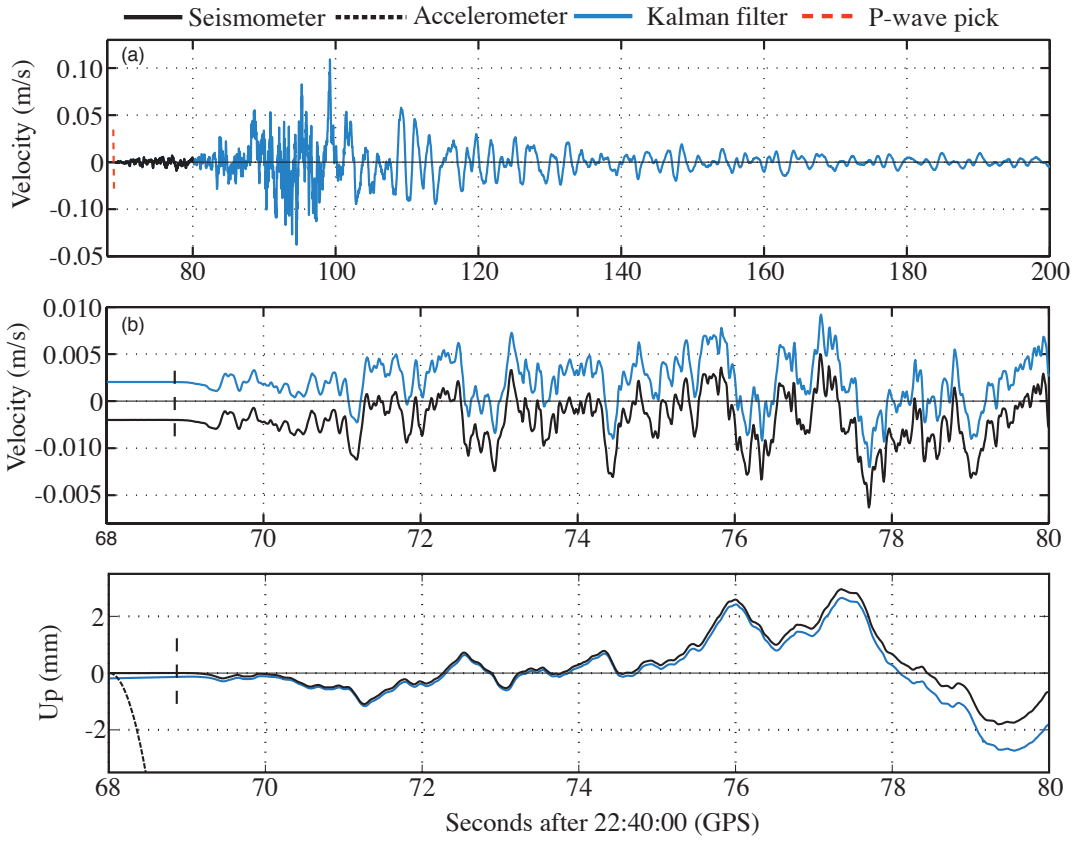


Figure 2.8: Estimation of velocity and displacement waveforms. (a) Comparison between vertical velocity records registered by a broadband seismometer at station WES (Figure 2.6) which clipped 11 seconds after the onset of shaking and the smoothed Kalman filter estimated velocities for P494/WES. (b) Blowup of the same time series showing agreement between the observed velocity and the estimated Kalman velocity waveforms. The two waveforms have been offset for clarity. The SCEC P wave pick denoted by vertical dashes is at 22:41:09 GPS time, or 29 seconds after earthquake initiation. (c) Comparison of single integration of the vertical seismometer record at WES, 100 Hz smoothed Kalman filter displacements (GPS/accelerometer), and double integration of only the accelerometer data. Note the magnitude of displacement, indicating that the broadband displacements have a precision and accuracy of about 1 mm.

from the epicenter, respectively; Figure 2.6 and Table 2.4) are shown in Figure 2.10. In spite of the larger epicentral distance and the diminished precision of the GPS vertical component, the Kalman filter with the aid of the accelerometer data is still capable of producing a precise waveform.

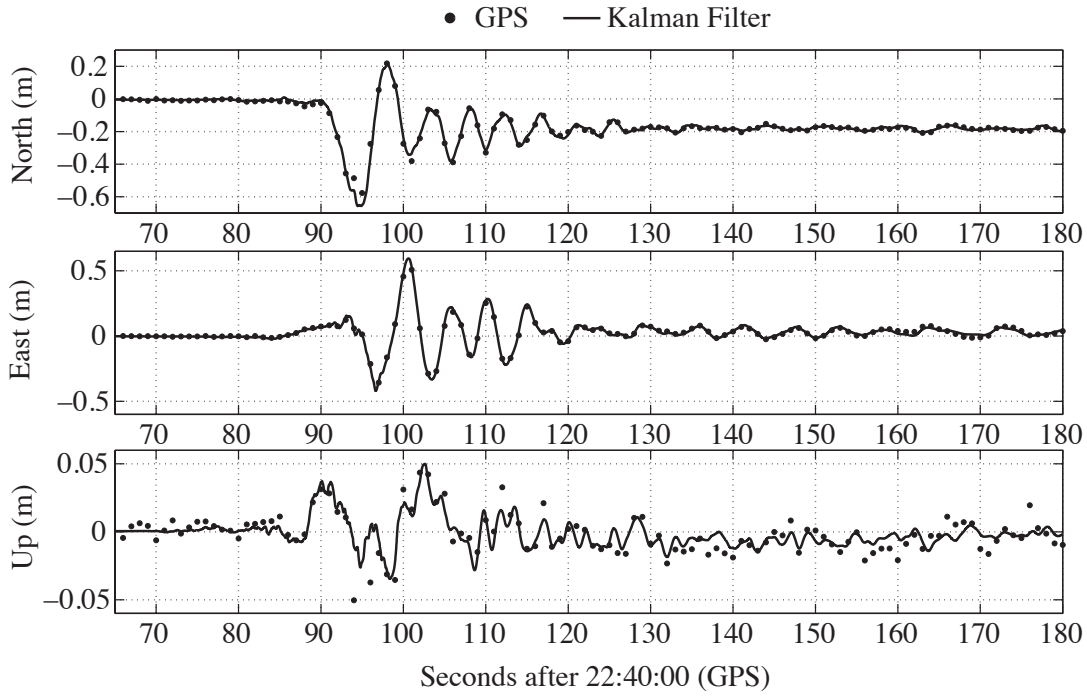


Figure 2.9: Comparison of 1Hz GPS and 100Hz smoothed Kalman filter displacement waveforms. Shown are 1Hz GPS displacements for P494 and 100Hz smoothed Kalman filter displacements for P494/WES. The SCEC P wave pick for station WES is at 22:41:09 GPS time. Note the 0.2m static (coseismic) offset in the North component

2.4.3 Spectral Characteristics

Spectral analysis of the smoothed Kalman filter displacement time series for the shake table experiments (Figure 2.11a) and the El Mayor-Cucapah earthquake (Figure 2.11b) highlights two attractive features: the power spectral densities follow the GPS-only spectrum at the low frequencies and the accelerometer-only spectrum at the high frequencies. This is desirable because it is in these two frequency bands that each instrument performs best (GPS at the lower frequencies and accelerometers at the higher frequencies). We can infer from the power spectral densities and the shake table experiments that the combined (100 Hz) waveform is more precise and accurate than the (1Hz) GPS-only or (100Hz) accelerometer-only displacement waveforms, and that we have achieved an accurate broadband record of this event.

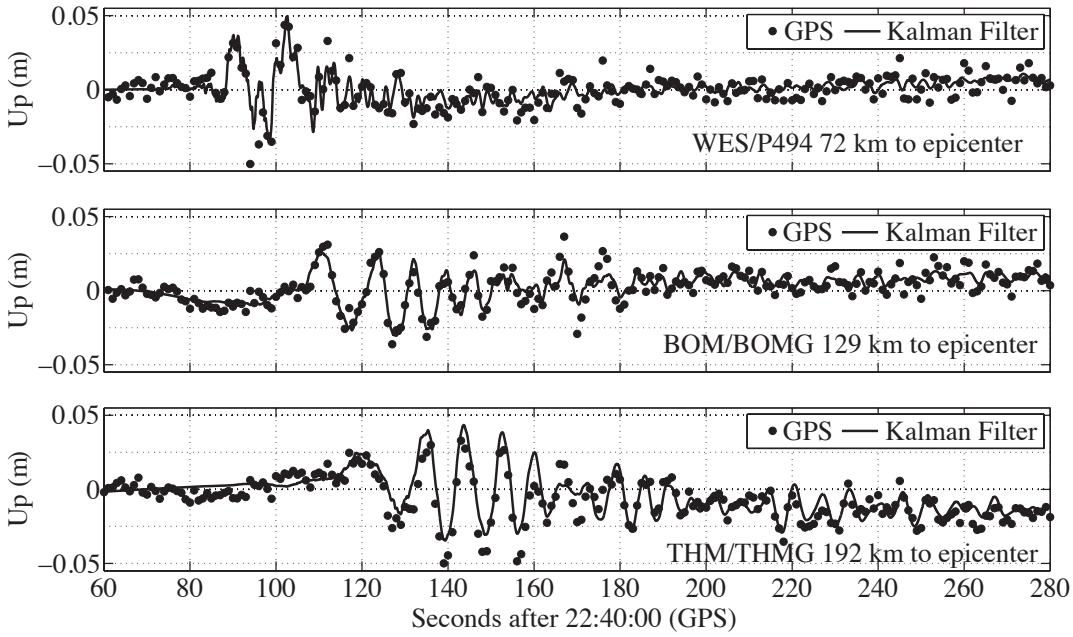


Figure 2.10: Vertical displacement waveforms. Comparison of 1Hz GPS and 100Hz smoothed Kalman filter estimates for P494 and P494/WES, BOMG and BOMG/BOM, and THMG and THMG/THM.

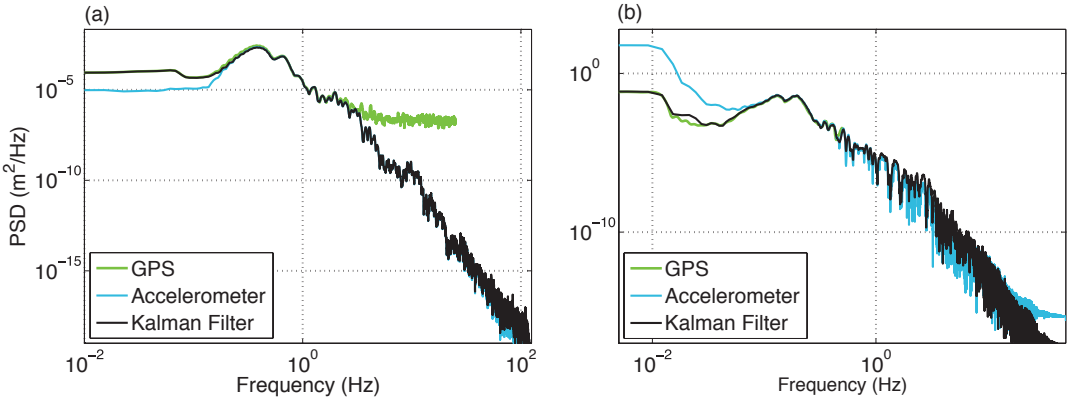


Figure 2.11: Power spectral densities. (a) High intensity Northridge earthquake simulation (EQ4) on shake table platen for 50Hz GPS-only displacements, 240Hz accelerometer-derived high-pass filtered displacements, and 250Hz smoothed Kalman filter displacements; (b) 2010 El Mayor-Cucapah earthquake for 1Hz GPS displacements at P494, 100Hz accelerometer-derived high-pass filtered displacements at WES, and 100Hz smoothed Kalman filter displacements for P494/WES.

The smoothed Kalman filter cannot be performed in real time since it requires both a forward and backward step. However, an examination of the spectral characteristics of the forward filter displacements indicates spurious spectral peaks that coincide with multiples of the GPS sampling frequency for both the shake table experiments (Figure 2.12a) and the El Mayor-Cucapah earthquake (Figure 2.12). it is easy to see why this happens by examination of a blowup of 1s of the unsmoothed forward time series for the shake table experiment (Figure 2.13). In between the 50Hz GPS samples, the series drifts during successive time updates when only new accelerometer data are available (every 250th of a second for the shake table and every 100th of a second for the earthquake). But as soon as the next GPS measurement becomes available there is an adjustment to the displacement time series, explaining the observed saw tooth pattern, a pattern also evident in the El Mayor-Cucapah earthquake data. In Figure 2.14, we show the results of a synthetic test of a saw tooth with a period of 1s and estimate its power spectral density using the multitaper method. It shows broad peaks centered at multiples of the saw tooth period, which corresponds to the GPS sampling frequency in our data sets. This is a minor problem because for real-time seismological applications the increase in noise introduced by the peaks is small compared to the signal. Furthermore, the increase in noise is only at frequencies higher than 1-2 Hz. In any case, the fixed interval smoother removes the spurious peaks altogether, while the near-real-time smoother will reduce the noise peaks as a function of the smoother lag time.

2.4.4 Selecting the Kalman Filter Variances

The Kalman filter has two parameters that dictate its performance, the measurement variance r and the system dynamics variance q (Section 2.3.1). To maintain objectivity and to simulate a real-time environment we compute the measurement variance from 50s windows of pre-event noise on the 3 components of the GPS displacements (Figure 2.15). These tend to be very stable across a network with the East component showing the least variance, then the North component and the vertical component being the noisiest, as expected, due to the

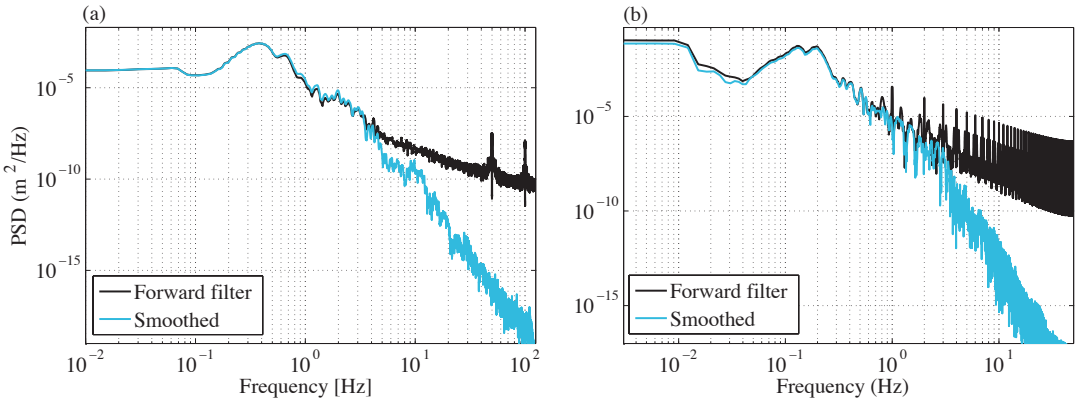


Figure 2.12: Power spectral density comparisons between forward Kalman filter and smoothed Kalman filter displacements waveforms for (a) High intensity Northridge earthquake simulation (EQ4) 250 Hz displacements on shake table platen; (b) 2010 El Mayor-Cucapah earthquake 100Hz displacements for P494/WES. Note the spikes in the forward filter corresponding to the GPS sampling frequency, 50Hz for (a) and 1Hz for (b).

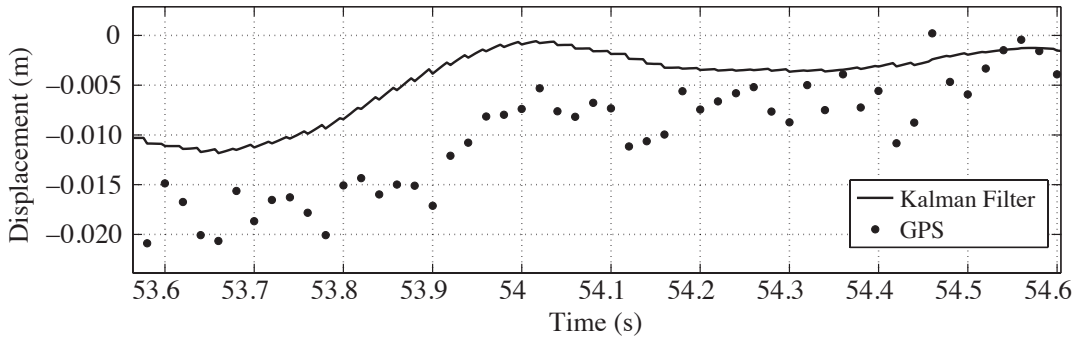


Figure 2.13: Example of saw-tooth like irregularities introduced by the disparity in sensor sampling frequencies. Shown is a blowup of the high intensity Northridge earthquake simulation (EQ4) with a 250Hz sampling frequency for the forward Kalman filter displacements and 50Hz sampling frequency for the GPS-only displacements.

satellite constellation configuration and unmodeled tropospheric refraction (*Bock et al.*, 2000). The observed GPS variances are also consistent with the results of *Genrich and Bock* (2006) who analyzed high-rate real-time data in Southern California.

Estimating the system dynamics variance is more complicated. At first glance it could be determined simply by taking the variance of windows of pre-

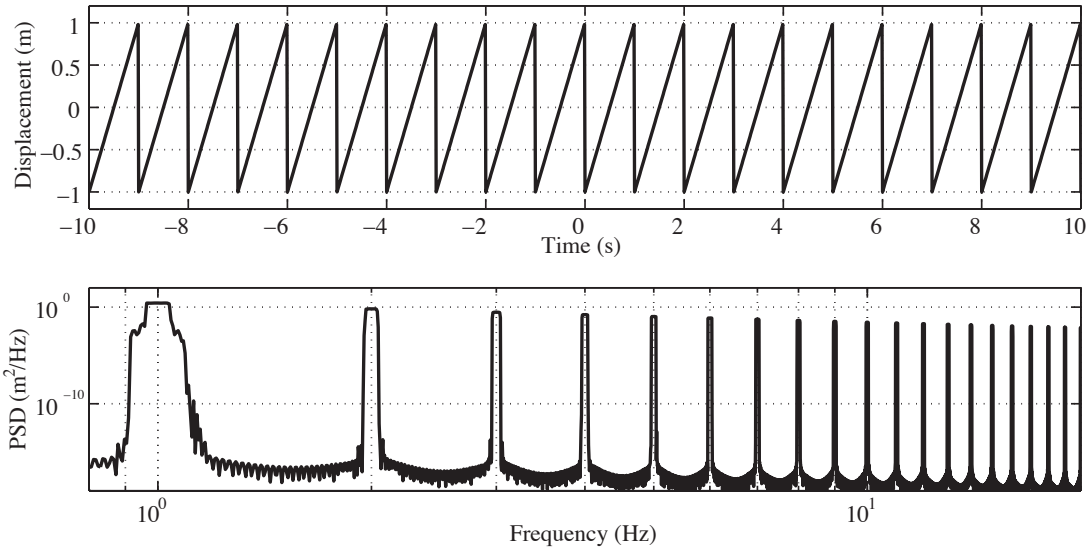


Figure 2.14: 1Hz synthetic saw tooth and its power spectral density.

event accelerometer noise. However, there are several sources of noise in the accelerometer that preclude this. Perhaps the most important is sensor rotation and tilt (*Trifunac and Todorovska*, 2001; *Pillet and Virieux*, 2007) whose net effect is to raise the noise floor. This does not manifest itself until shaking starts and is thus not present in pre-event noise estimation. *Trifunac and Todorovska* (2001) show that as one utilizes an increasing number of bits to digitize the transducer signal and as earthquake magnitude increases the problem becomes more insidious. *Lee and Trifunac* (2009) obtained empirical relations for computing the Fourier spectra of rotation and tilt from translational acceleration spectra. The empirical relations depend on multiple factors including magnitude, focal depth, soil conditions, thickness of the sedimentary layer and epicentral distance. When compared to the amplitudes of processing and recording noise however, they find that the most extreme behavior of the rotational and tilting spectra is about 3 orders of magnitude greater than translational noise levels. We show the effect of using q measured from pre-event noise windows by taking the more extreme value of $1000q$ as the system dynamics variance for input into the Kalman filter. In Figure 2.16a we show the East component (because it displays the largest sensitivity to changes in q) and observe that when applying the forward Kalman filter without smoothing

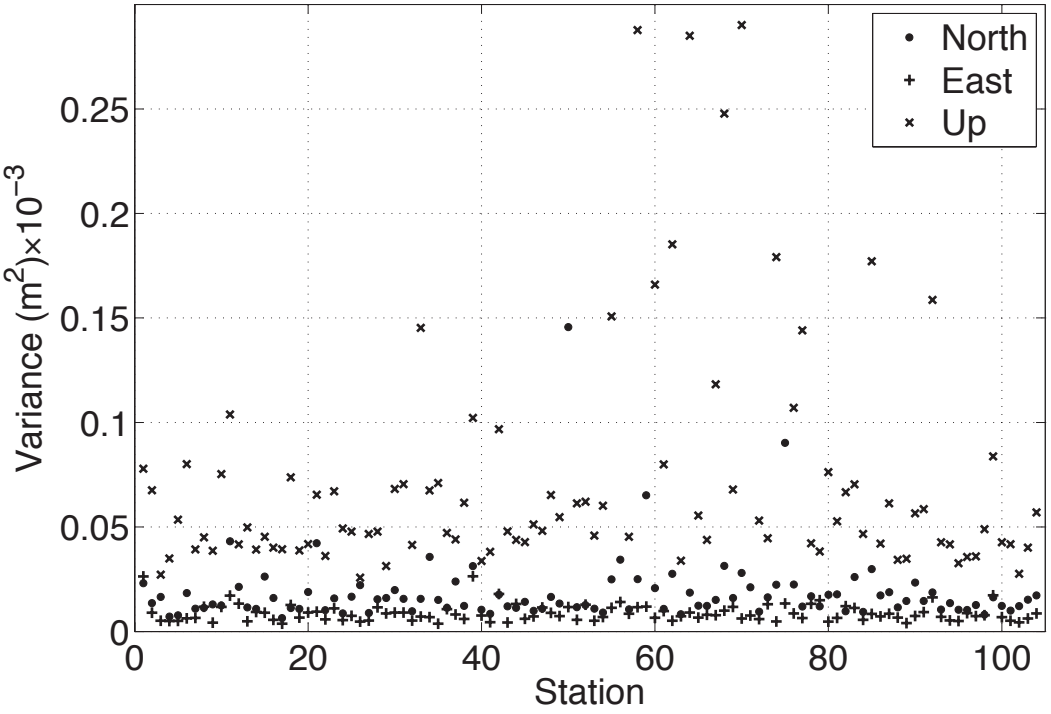


Figure 2.15: Variances for 50 seconds of displacements for some California Real Time GPS Network (CRTN) stations estimated prior to the 2010 El Mayor-Cucapah earthquake in North, East, and Up components.

and comparing it to GPS measurements the filter miscomputes the resulting static displacements by as much as 0.08m. If we adjust the variance to $1000q$ then the static offset is adequately recovered but the amplitudes of dynamic shaking can vary by as much as 0.25m.

In spite of these large variations, the problem becomes, in effect, moot using Kalman smoothing, where using a scaled value of q has a limited effect on the recovered waveform (Figure 2.16b). Applying a near-real-time smoother (Section 2.3.1) with a 10s lag, even with an extreme value of the variance, fully recovers the waveform (Figure 2.16c). We find that the 10 s lag, in this case, is the minimum necessary to recover an adequate waveform, that is, one without bias in dynamic shaking amplitude or in static offset. This lag, however, might be too long for real-time applications in which case the sampling rate of the GPS must be increased to reduce the lag of the near-real-time smoother (recall that misfits

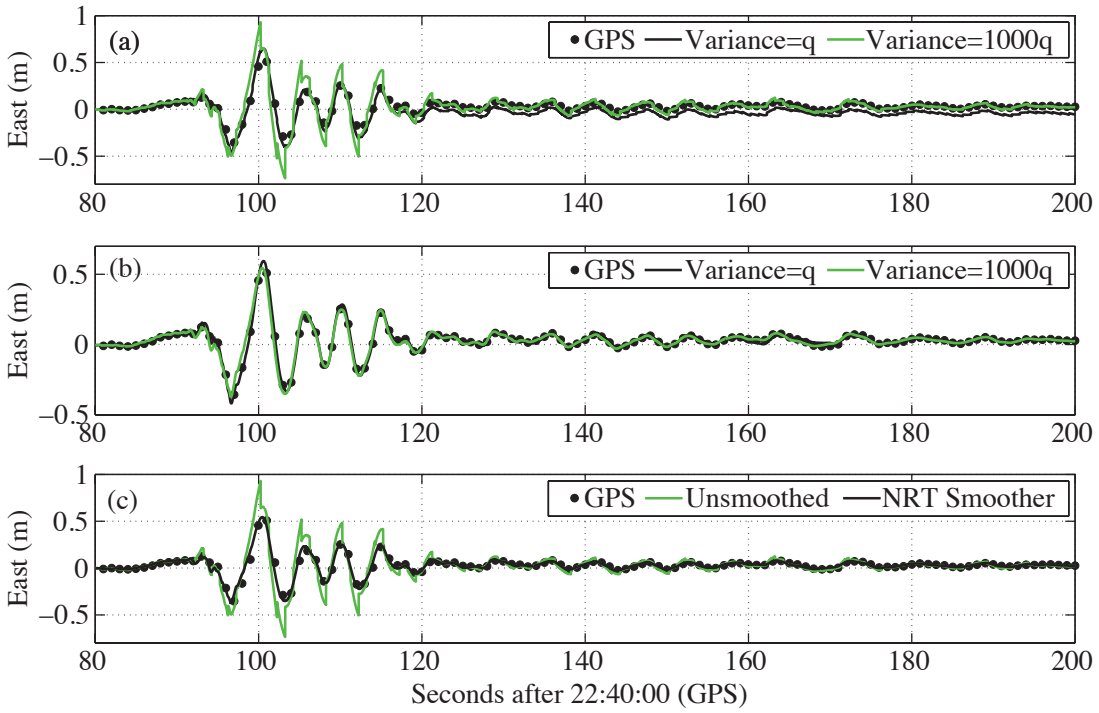


Figure 2.16: Effect of choice of system dynamics variance in Kalman filter estimation, in the East component. (a) Comparison between forward Kalman filter waveforms using q and $1000q$ as the system dynamics variance, where q is the pre-event variance estimate for the accelerometer data. (b) Comparison between RTS smoothed waveforms using q and $1000q$ as system dynamics variance. (c) Comparison between forward Kalman filter and smoothed Kalman filter with a lag of 10s using $1000q$.

arise from the saw tooth pattern effect of GPS sampling frequency). Alternatively, if the station conditions are known, the empirical relations of *Lee and Trifunac* (2009) or some yet to be determined empirical scheme can be used to assess the proper scaling of q.

2.4.5 Lessons and Insights

As a proof of concept, the shake table tests and the recordings of the El Mayor-Cucuapah earthquake allowed us to better understand the operational characteristics of the Kalman filtering operation.

The very-high frequency response of GPS-derived displacements is flat above

0.05-0.5Hz (<2-20 s) so that GPS data are capable of providing essentially uncorrelated single-epoch estimates of displacement over a large range of frequencies at the (10-50Hz) sampling rate of modern GPS receivers (*Genrich and Bock*, 2006). The California Real-Time Network project (http://sopac.ucsd.edu/projects/realtime) has demonstrated that 10Hz data can be reliably streamed over dedicated microwave and radio modem communication links but this requires a ten-fold increase in the transmitted data compared to the current 1Hz rate. The Plate Boundary Observatory project (http://pbo.unavco.org) streams 1Hz data from their GPS stations but stores 10Hz measurements in receiver memory which can be downloaded in the case of a significant seismic event. It is not practical to stream at higher data rates with current costs and limitations in telemetry. A more cost-effective approach is to, wherever possible, add accelerometer instruments at existing GPS stations, stream the very-high-rate but lower volume accelerometer data over the same communications links as the GPS data, and use the Kalman filter to optimally combine both data sets. One might even consider performing the filtering operation which is computationally simple at the station itself. This approach provides displacements at the sampling rate of the accelerometers (e.g., 100Hz) with the precision of the accelerometer data and the accuracy of the GPS data. Our shake table results indicate that there is little benefit in increasing the GPS sampling rate to greater than 5-10Hz.

We find that the basic state vector representation is sufficient for the Kalman filter, where the acceleration driving the system is assumed to be constant in between time steps. A complete description of motion is achieved with the displacement, velocity and accelerometer DC-bias as state variables. There is no apparent need for additional state vector parameters, for example, possible tilts or other biases in the accelerometer data. Furthermore, while the variance factor q is tricky to characterize the filtering operation is relatively insensitive over to a few orders of magnitude of change in its value. The corresponding GPS variance factor r is well known and the high-rate GPS displacements are uncorrelated from epoch to epoch. This has been demonstrated in previous work (*Genrich and Bock*, 2006) and further verified here. In fact, one can provide an overly pessimistic value for

the accelerometer variance factor (say $1000q$, or 1000 times the pre-event noise) because the periodic GPS displacement measurements are sufficiently accurate to provide tight constraints on the single and double integration of accelerometer data to velocity and displacement, which is implicit in the Kalman filter formulation. One way to explain this is that the GPS displacements allow one to use definite integrals in the integration process by providing for explicit constants of integration. Without the GPS displacements, the integration process is highly affected by accelerometer biases and noise and the limited dynamic range in seismometers. In addition, the effect of overestimating the system dynamics variances is nullified if a smoother is employed. Similarly, introduction of the accelerometer data stream into the Kalman filter helps to better estimate vertical static and dynamic displacements which are very noisy in a GPS-only scenario. This improved estimation of vertical motion will have a significant effect later on when we discuss modeling of megathrust earthquakes.

To better illustrate the immediate advantages of the filter we compare the North components of the estimated displacement waveforms from GPS alone (Fiagure 2.17) with those estimated using the smoothed Kalman filter (Figure 2.17b) for 12 collocated stations (Table 2.4). The signal quality improves significantly in the latter. The pre-event noise levels are lower and the artifacts in the GPS waveforms (at 1.6 and 5 minutes in Figure 2.7 and at 95 seconds in Figure 2.17a) are eliminated. The artifacts are due primarily to variations in position of the GPS reference station. These variations will propagate to all other stations in the network and are due to random and systematic errors in the GPS data and/or analysis and could be mistaken for actual seismic phases. The optimal combination of GPS displacements with accelerometer data provides distinct advantages, for the El Mayor-Cucuapah earthquake case the P wave arrivals could be detected in the combined solution, taking advantage of the greater precision of the accelerometers. They were not detectable in the GPS-only approach because of the reduced sensitivity of GPS to vertical motions. The detection of the P wave arrival is critical for many real-time seismology applications such as earthquake early warning.

We note that there are certain limitations in the real-time estimation of

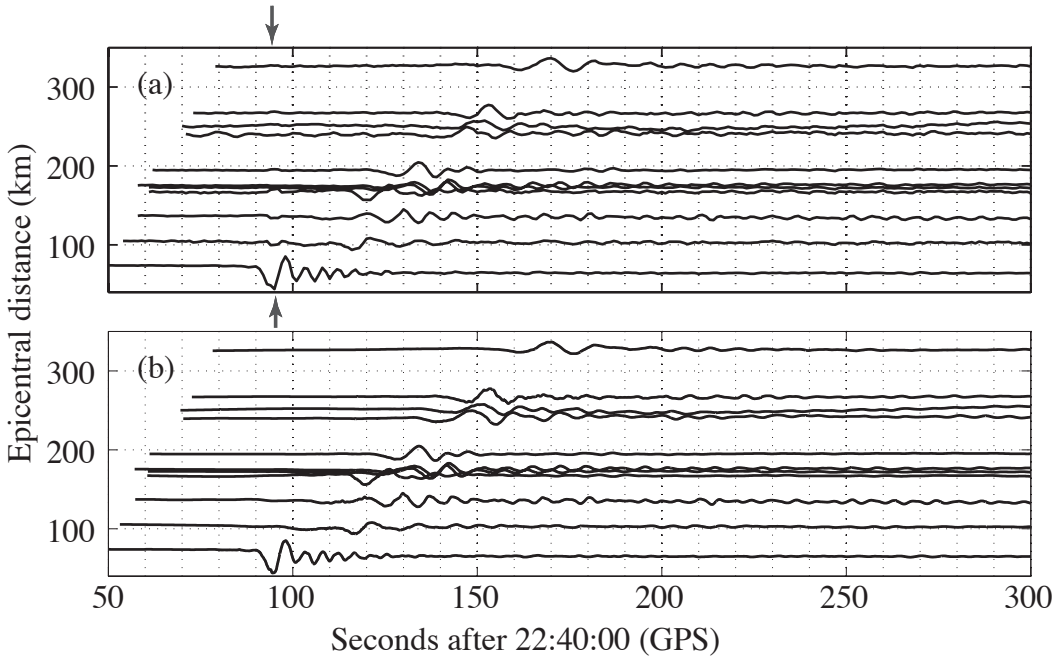


Figure 2.17: Displacement waveforms in East component for (a) 1 Hz GPS only and (b) smoothed Kalman filter solutions for 12 collocated GPS/seismic stations in Southern California (Figure 2.6). Note the artifact (denoted by grey arrows) introduced by the GPS network adjustment at 95 seconds in (a) which is absent in (b), and the flatter (more precise) pre-event displacements in (b) compared to (a). All waveforms have been normalized for clarity.

displacements from GPS phase and pseudorange data. The introduction of very-high-rate precise accelerometer data at the GPS stations could help reduce the above problems in real-time applications by introducing independent confirmation of significant station displacement. For this purpose, a tightly coupled Kalman filter approach might be suitable (*Geng et al.*, 2013a). Instead of analyzing the already estimated GPS displacements with the raw accelerometer data, *Geng et al.* (2013a) designed a Kalman filter that instead uses the raw GPS phase and pseudorange observations and the raw accelerometer data, in order to improve the on-the-fly resolution of phase ambiguities.

Finally station siting, monumentation, and mounting of GPS and seismic instruments at collocated stations is an important consideration. Seismic and geodetic networks developed independently and are seldom collocated. An inter-

esting question for future consideration is whether costs can be reduced by using less sensitive and cheaper accelerometers (such as MEMS), or whether the current practice of installing high-end accelerometers in boreholes or shallow vaults is necessary. During a recent test (January 2014) at the LHPOST we evaluated low cost MEMS sensors which were collocated with observatory grade accelerometers. Analysis of this data should help answer this question in the future. *Evans et al.* (2014) recently tested the performance of several low-cost sensors in the laboratory and found that while many of the very low cost ones are far from being useful for seismology many mid range ones seem to perform well enough for reliable strong motion sensing.

2.5 Application to the M_w9 Tohoku-oki Earthquake

One of the most relevant data sets for strong motions seismology in recent times is from the 2011 M_w9.0 Tohoku-oki earthquake. Complex waveforms with long durations of shaking recorded across dense geodetic and seismic networks make this an ideal test of the Kalman filter methodology.

For this event we process data from 816 GPS stations throughout Honshu and Hokkaido Islands (Figure 2.18). As with the El Mayor-Cucapah event we process the GPS data in a simulated real-time mode using the method of instantaneous positioning (*Bock et al.*, 2000). We triangulate the GPS network using a Delaunay triangulation scheme, and individual triangles are processed independently for relative station positions. The triangles are combined through a real-time network adjustment (*Crowell et al.*, 2009), and station positions are referenced to station 0848 on Hokkaido Island, 900km northwest of the hypocenter (Figure 2.18).

We identified 139 collocated GPS/accelerometer station throughout Japan. As before, we define a collocation as a pair of instruments separated by 1500m or less. Accelerometers in Japan function in triggered mode and many of those stations did not trigger in time. Furthermore, given the large duration of the source (*Simons et al.*, 2011) many of those instruments terminated recording while

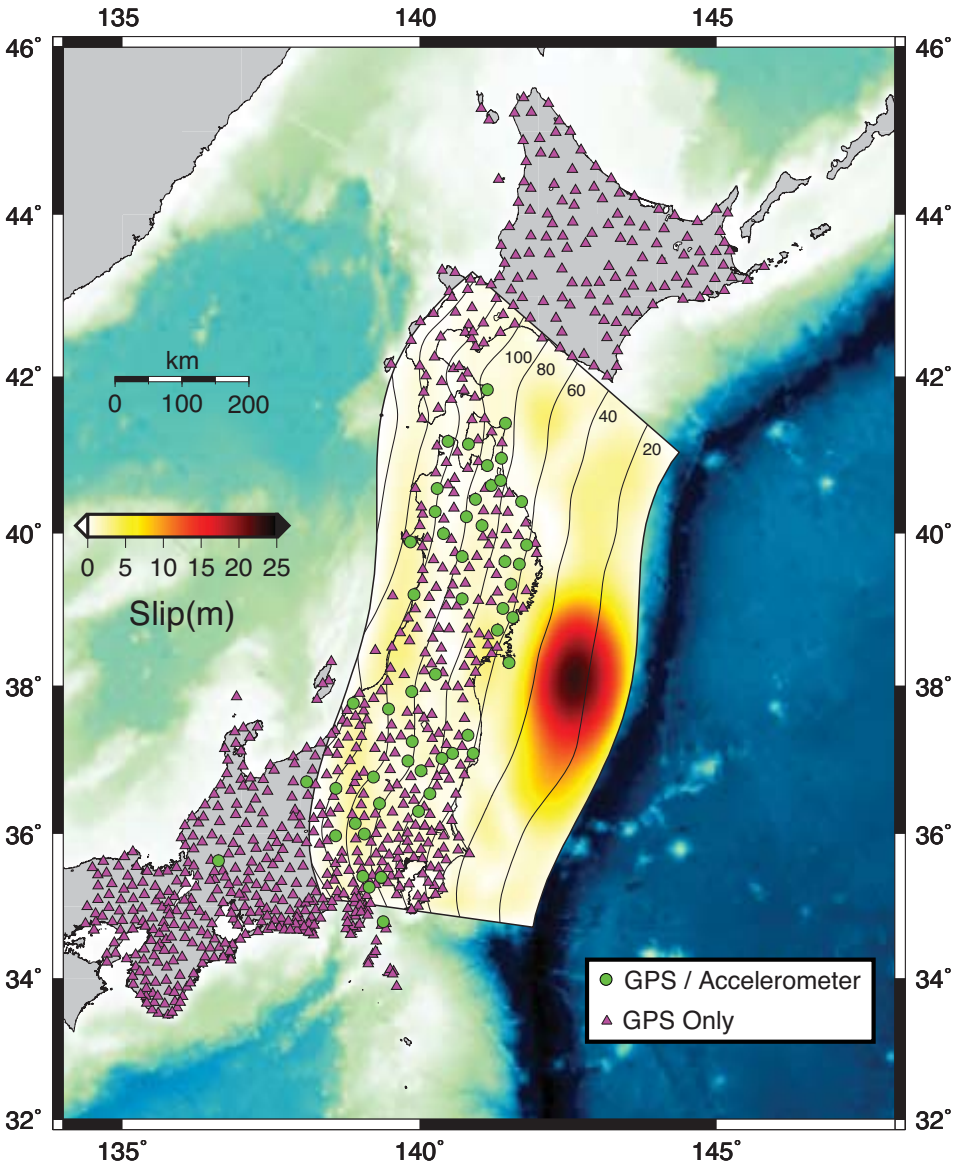


Figure 2.18: Station map depicting GPS only and GPS/accelerometer stations. Also included is the static slip inversion computed from real-time GPS (Chapter 3) and the iso-depth contours of the slab geometry determined in *Hayes et al.* (2012)

significant shaking was ongoing. Thus, we culled the data set to 48 stations (Figure 2.18) that contain at least 2 seconds of pre-event noise and enough record to discern static offsets in the corrected data. Of these 48 stations 40 are K-net accelerometer sites and 8 are KiK-net accelerometer sites.

To establish a comparison with seismic-only data we compare the Kalman

filtered displacements (KD) to displacements obtained from two automatic baseline correction (ABC) algorithms described in section 2.1. The first algorithm (*Wang et al.*, 2011) performs, for the 3 channel accelerometer data, a grid search for the best correction parameters defining the optimal correction as that which best resembles a step function. This algorithm is presumed to be suitable for real-time computation because it requires no operator interaction. The second algorithm (*Wang et al.*, 2013) computes automatic baseline corrections on the raw accelerometer data with the added constraint that the final waveforms best fit the static offset from the neighboring GPS station.

We computed power spectral density for the three displacement data sets: ABC corrected according to *Wang et al.* (2011), ABC plus static field constraint corrected according to (*Wang et al.*, 2013) and the Kalman filter algorithm described in section 2.3. We also computed 5% damped displacement response spectra for all 3 data sets. This was done numerically by finite difference solution to the single degree of freedom oscillator differential equation (*Bozorgnia and Bertero*, 2004).

2.5.1 Time Domain Analysis

Figure 2.19 illustrates the results of ABC waveforms for 2 stations where no static field constraint has been applied according to *Wang et al.* (2011). K-net station AOM011 is 296km from the event centroid and is an example of a station that is well corrected by the automated procedure. When compared to the KD waveform we see that the static offsets roughly match as does the shaking for all 3 components. In contrast K-net station GNM004, 430km from the centroid is an example of a failed correction. The displacement converges to the wrong value for the static field and as a result the shaking is also miscomputed. These two stations are the extremes of the behavior that we observe at the remaining stations.

Figure 2.20 compares the result of applying a static field constraint according to *Wang et al.* (2013) for K-net station AOM010, 323km from the centroid. This station is representative of the breadth of behavior we observe at all stations. The vertical channel fit to the ABC waveform is greatly improved by adding the

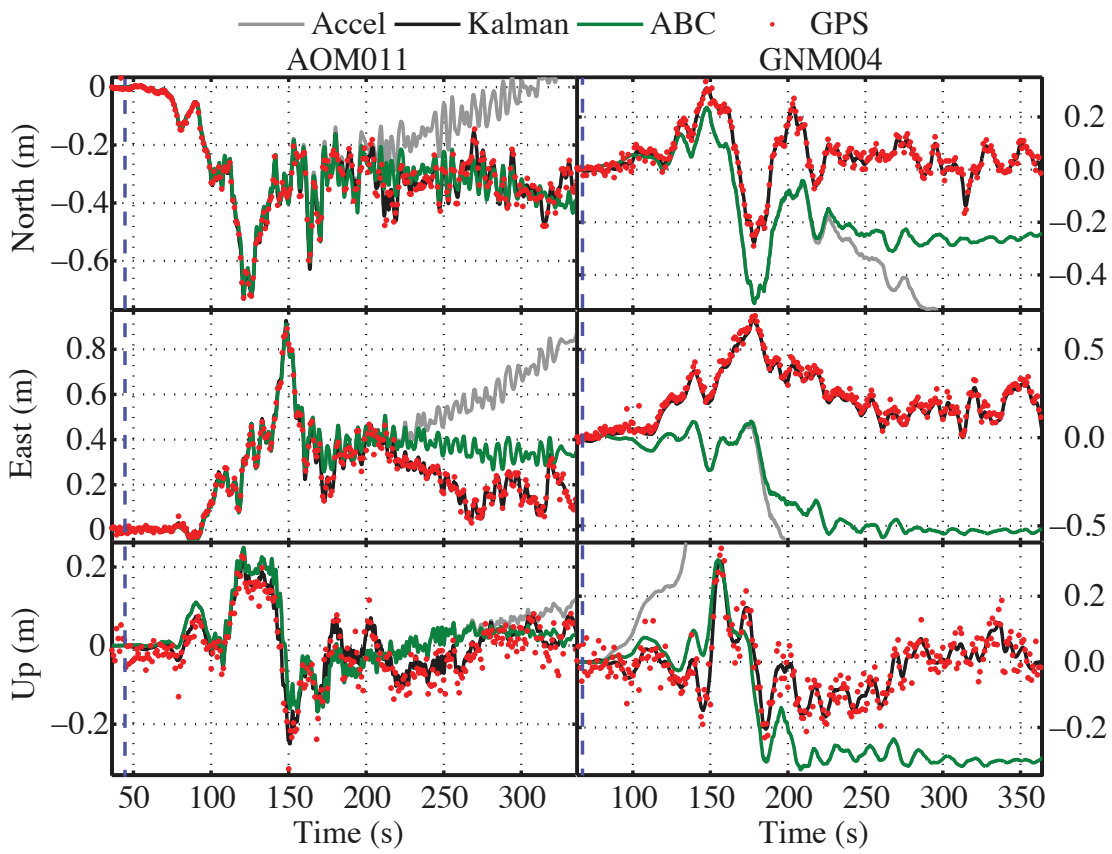


Figure 2.19: Results of applying the automatic baseline correction of *Wang et al.* (2011) with no static field constraints. The comparison is made to the Kalman filter, uncorrected accelerometer integration and 1 Hz GPS. K-net station AOM011 is 296 km from the centroid and K-net station GNM004 is 430 km from the centroid. The dotted line is the P wave pick.

constraint. The east component is mildly improved but does not reach the level defined by the KD waveform. The improvement in the north component is only marginal and a large difference (20cm) remains in the static field between ABC and KD waveforms. Recall that we determine the optimum correction to be the one that best fits a step function of amplitude given by the static field. What these results indicate is that there might not be a combination of baseline correction times that provides a sufficient improvement to the displacement computation.

For both the constrained and unconstrained solutions there are records that compare favorably with the KD waveforms (Figures 2.19 and 2.20). However, given the large amplitude motions present at most of these stations it is difficult

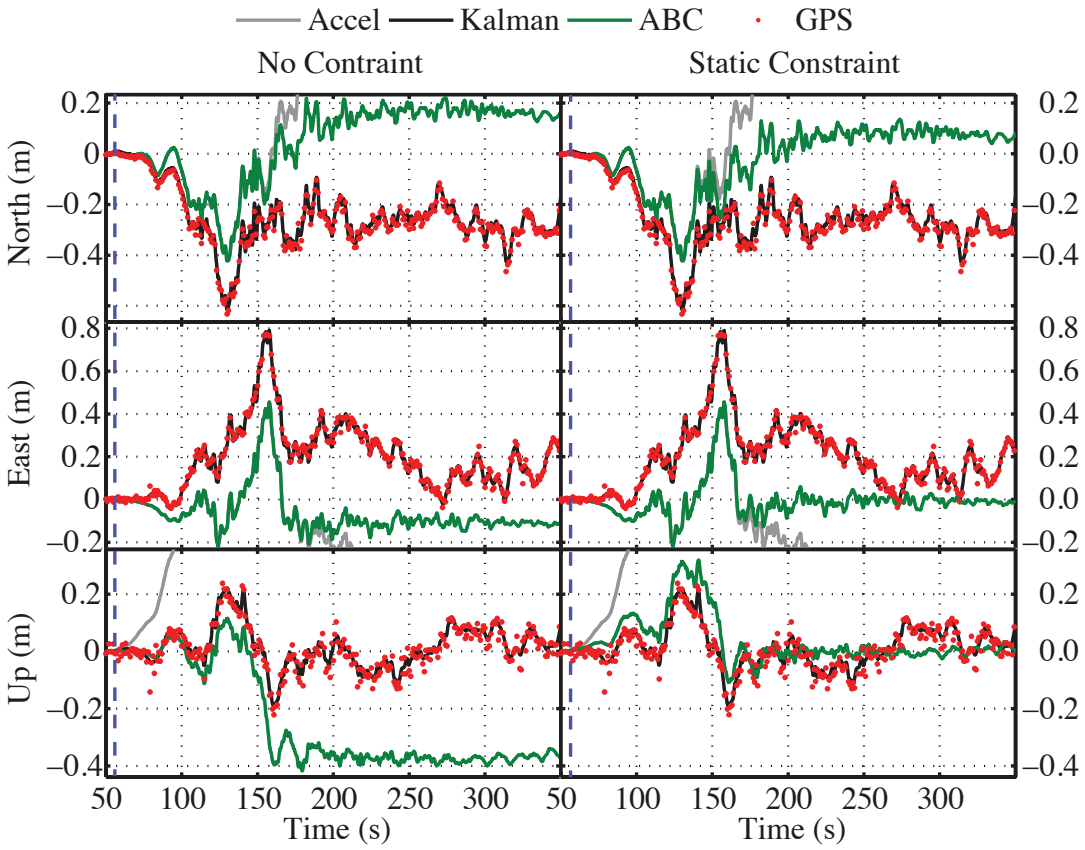


Figure 2.20: Comparison between the ABC waveforms with and without the static field constraint. The results are for K-net station AOM010 323 km from the centroid and compared to the Kalman filter, uncorrected accelerometer integration and 1 Hz GPS. The dotted line is the P wave pick.

to judge by simple visual inspection the adequacy of this comparison. Figure 2.21 presents a record section with the difference between the KD waveforms and the ABC waveforms for all 48 stations ordered by distance to the centroid. We find that the difference is smallest in the earlier parts of the waveform. Additionally we see that the static field constraint improves the fit to the KD waveforms but large differences of several tens of centimeters remain. Also notice that the stations closest to the centroid are the ones with the poorest fits that even with the addition of the static field constraint improve little.

Inspection of the KD waveforms (Figures 2.19 and 2.20) shows that the Kalman filter method better corrects the 3 components of motion at all 48 sta-

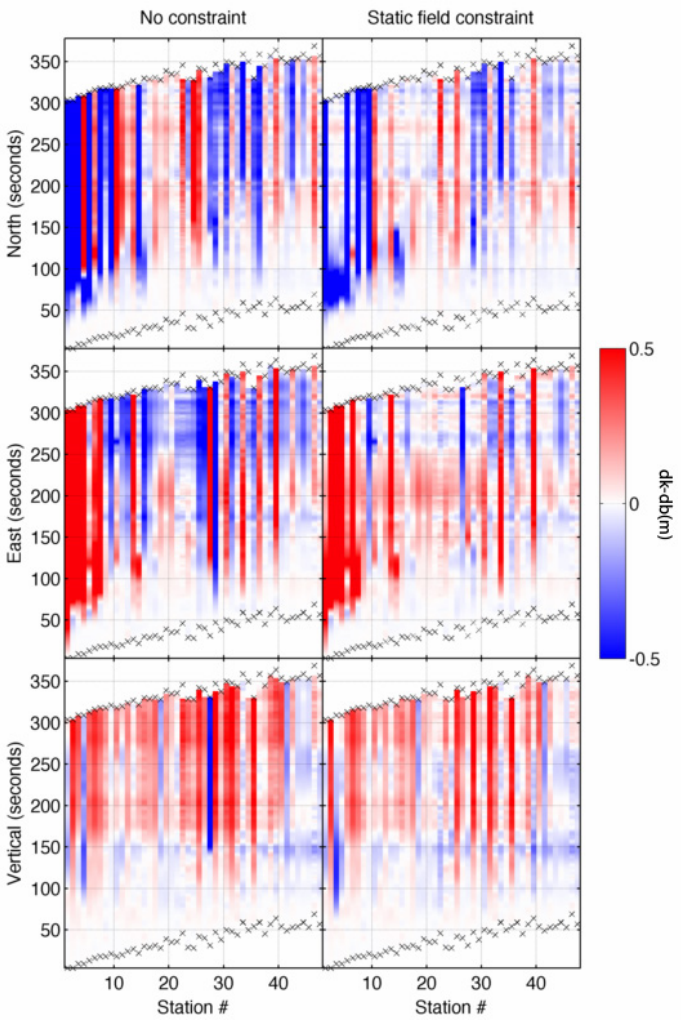


Figure 2.21: Difference between the KD and ABC waveforms for both constrained and unconstrained solutions. The stations are ordered by increasing distance to the centroid and the crosses denote the start and end of each waveform.

tions. We decimate the KD and ABC static field constrained waveforms to the GPS sample times and compute the RMS of the difference between both sets of waveforms and the GPS (Figure 2.22). In the north direction the RMS for the ABC waveforms ranges from 4.3 cm to 150 cm, for the KD waveforms the range is from 0.6cm to 5cm. In the east direction, the ABC waveforms have RMS values from 6 cm to 320 cm and the KD waveforms from 1cm to 10cm. In the vertical direction the ABC waveforms have RMS values that range from 4cm to 43cm and the KD waveforms from 2cm to 10cm. For all stations on all channels we find that

the KD waveforms have a smaller RMS than the ABC waveforms.

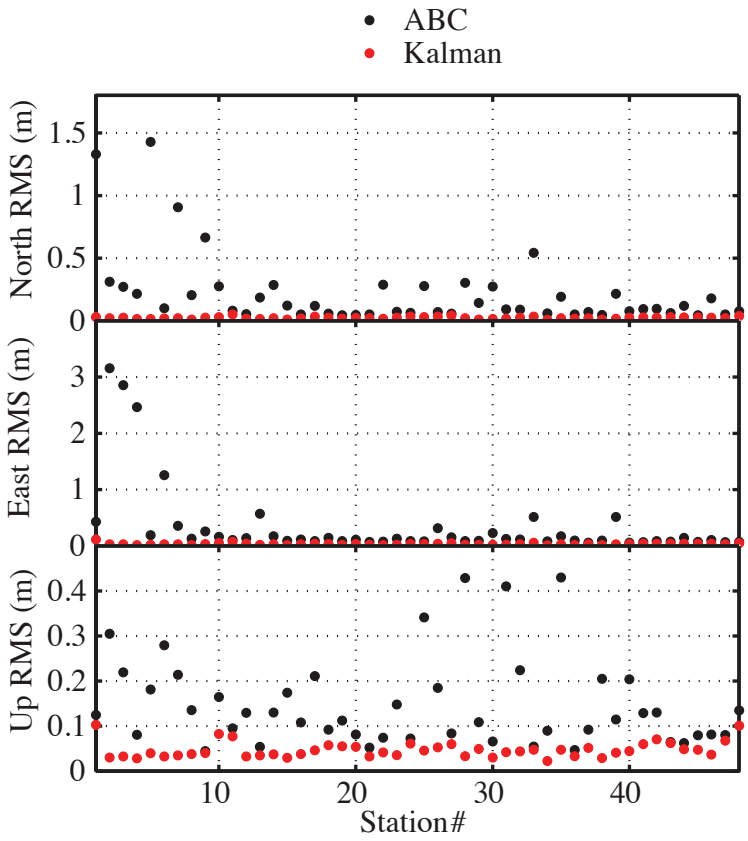


Figure 2.22: RMS of the difference between the ABC and GPS waveforms and the KD and GPS waveforms for all stations. The stations are ordered by increasing distance from the centroid.

2.5.2 Frequency Domain Analysis

It remains unclear at which frequencies baseline corrections introduce errors into measurements. This is of consequence for earthquake source modeling and strong motion analysis. Also, it is generally assumed that baseline corrections have no effect at frequencies of engineering interest (*Boore*, 2001; *Boore and Bommer*, 2005). The following presents a frequency domain analysis where we compare ABC and KD waveforms.

Figure 2.23 is an example of the power spectral density (PSD) for ABC, KD, uncorrected accelerometer integration and GPS data for the north compo-

nent of K-net station AOM027, 363km from the centroid. These results are for the unconstrained baseline correction. The results are consistent with Section 2.4, namely that the accelerometer over estimates long period content and that GPS overestimates the spectral content at the higher end of its frequency band. Furthermore one can observe the desirable characteristics of the KD waveforms; they follow the GPS spectra at low frequencies and transition to the accelerometer at high frequencies. It is also interesting to note that the ABC waveform has different frequency content than the KD waveforms at frequencies at least as high as 0.5Hz and that the ABC waveform does not agree with the GPS at any part of the long period spectrum.

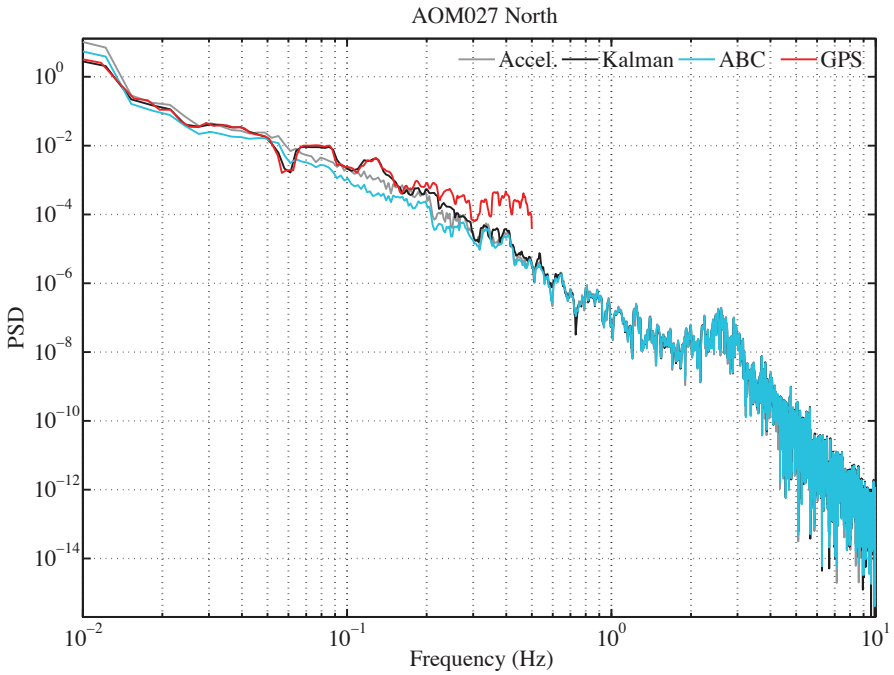


Figure 2.23: Power spectral densities for the north displacements at K-net station AOM027, 363 km from the centroid. These results are for the unconstrained baseline correction.

Figure 2.24 is a similar analysis for the displacement response spectra. The results are for the east component of station K-net station MYG001 138km from the centroid. The ABC solution is unconstrainted. In line with the PSD analysis, we find that the KD waveform tracks the GPS result at long periods and the

uncorrected accelerometer at high frequencies. Similarly we find that the uncorrected accelerometer spectrum differs from the KD result at periods longer than 11s while the ABC spectrum begins to diverge from the KD spectrum at around 13s. It is also important to note that for periods shorter than 10s the GPS only spectrum is unreliable.

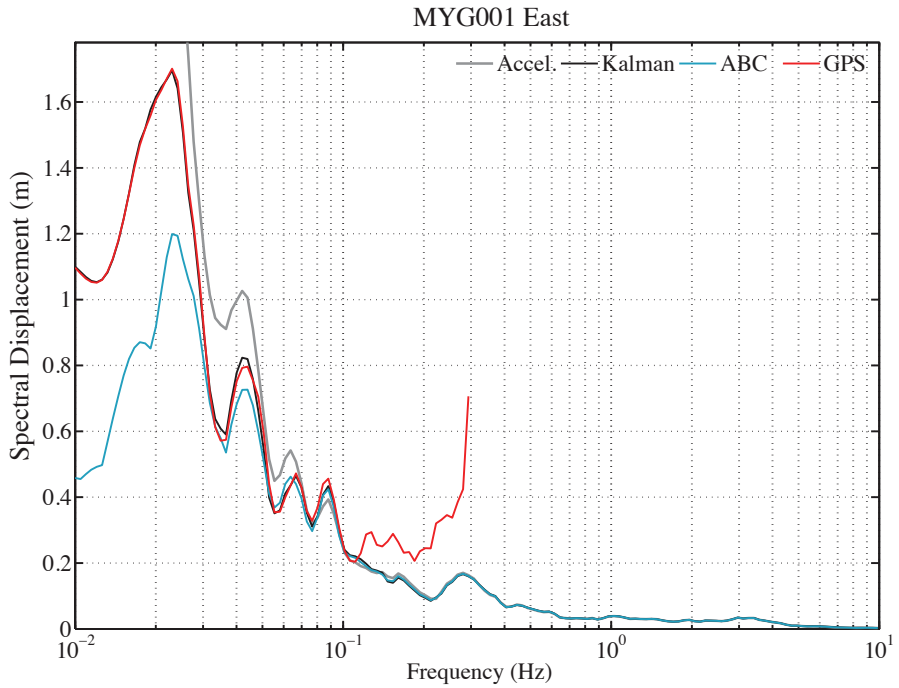


Figure 2.24: 5% damped displacement response spectra for the east component of K-net station MYG001 138km from the centroid. These results are for the unconstrained baseline correction.

To better understand the relationship between the ABC and KD PSDs we computed the ratio between the KD PSDs and ABC PSDs for all stations. This is shown in logarithmic scale in Figure 2.25 for both the constrained and unconstrained corrections and ordered by distance to the centroid. Several features are of interest, first that the discrepancy between the KD and ABC spectra are larger for stations close to the source. At long periods there is mixed behavior between over and under estimation of the spectra by the ABC results in the horizontal components. However, for the vertical component we find that the ABC spectra consistently overestimate the frequency content. It is also important to note that

the differences in spectral content are of consequence for frequencies as high as 0.5 Hz. We also find that addition of the static field constraint provides only a marginal improvement in the estimation at long periods. Addition of this constraint leads to little to no improvement in the recovery of the mid-range frequencies.

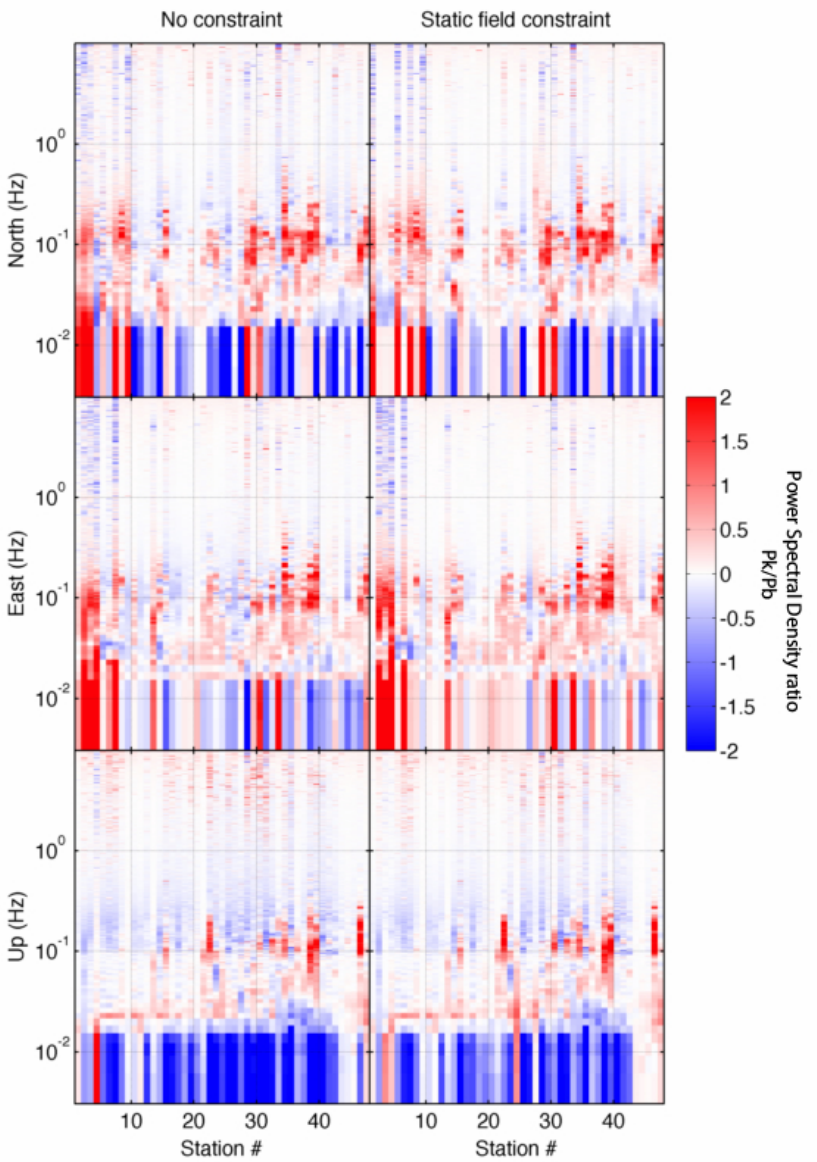


Figure 2.25: Logarithm of the ratio between the KD and ABC power spectra for all stations ordered by increasing distance to the centroid. Results are for both constrained and unconstrained waveforms.

Figure 2.26 is a similar plot for the response spectra, here we present the

difference between the KD and ABC derived spectral displacements for both constrained and unconstrained results. Similar to what we described for the PSD comparison, we find a better fit by the ABC spectra in the vertical direction than in the horizontal directions. Additionally we find little improvement in the spectral displacement estimates from addition of the static field constraint. We also find that for the response spectra the largest differences occur at periods longer than 8-9s.

2.5.3 Performance of the Filter and Prospects for Automated Baseline Corrections

Even though GPS has higher noise levels and aliasing effects are present, whatever method is chosen to compute the displacements (KD or ABC) it must agree broadly with the GPS time series. Figures 2.19-2.21 demonstrate this and show that with the Kalman filter we achieve accurate recovery of both permanent and transient motions while serious difficulties arise when employing the ABC method. We assert that this verifies that the Kalman filter methodology described in Section 2.3.1 has no substantive problems in resolving broadband displacements for the M_w9.0 Tohoku-oki earthquake. That we have done so using the K-net acceleration data is important. As acknowledged by *Wang et al.* (2013) recovery of displacements from those records is difficult because of the large baseline offsets, ostensibly introduced because of unfavorable site conditions. The incorporation of real-time GPS with the Kalman filter resolves these offsets with little difficulty.

However, we recognize that collocation of GPS and strong motion sensors are still the exception rather than the norm, and baseline corrected displacements are important. We have evaluated the suitability of automated baseline correction procedures in both the time and frequency domain. We independently verified that automatic baseline correction schemes such as that of *Wang et al.* (2011) can indeed produce in some cases waveforms that accurately capture both static and dynamic motions. However for the subset of 48 stations we found that there can be very large differences in the estimated static offsets when compared to actual offsets measured by the real-time GPS (Figure 2.27). This is important because as

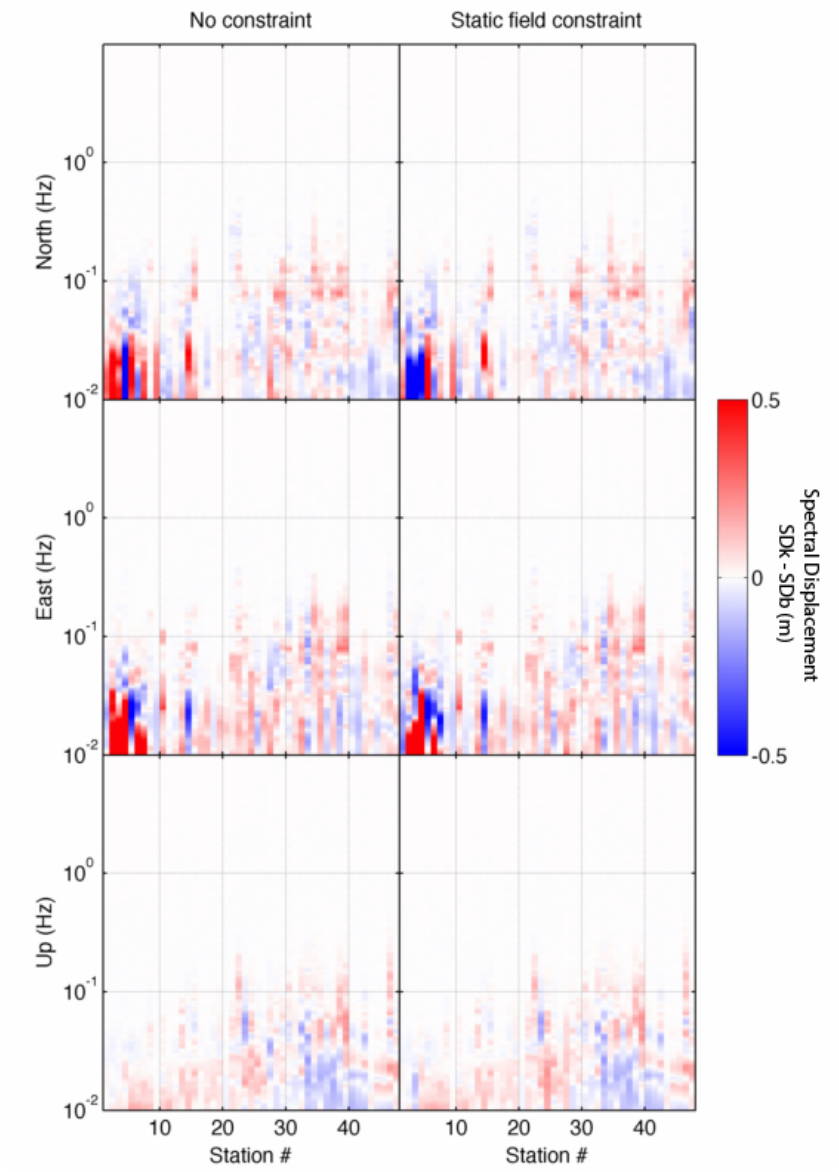


Figure 2.26: Difference between the KD and ABC 5% damped response spectra for all stations ordered by increasing distance to the centroid. Results are for both constrained and unconstrained waveforms.

previously discussed current areas of research for rapid earthquake response include modeling of the source with static offsets. If the offsets determined from the ABC scheme are unreliable their utility for rapid response will be very limited. *Wang et al.* (2013) proposed detecting outliers in the static field estimation by comparison with synthetics determined from a static slip inversion. This necessitates some

important assumptions, for example for 2011 Tokachi-oki that the earthquake has ruptured the mega-thrust and that the mechanism is reverse faulting. These assumptions are critical and will not always hold up. Outer rise normal faulting events can be sizeable and are not uncommon. Large strike slip events close to the trench such as the M_w8.6 strike-slip event Wharton Basin off Sumatra, Indonesia on 11 April 2012 (*Satriano et al.*, 2012) will be significantly mis-modeled. Furthermore quiescent borehole stations such as those of the KiK-net deployment used in *Wang et al.* (2013) are not the norm. Rather, stations of heterogeneous site response like those of the K-net deployment are more common in networks worldwide.

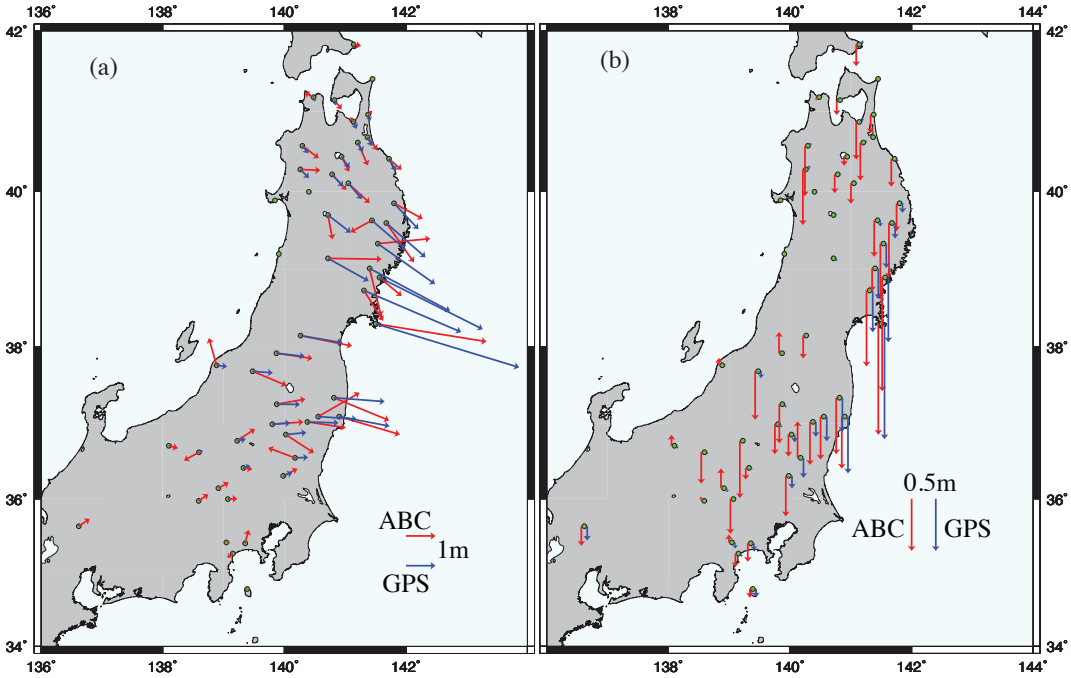


Figure 2.27: Comparison between static offsets determined from the automated baseline corrected procedure and the real-time GPS. (a) Are horizontal and (b) are vertical offsets

We have identified important discrepancies between ABC and KD waveforms. The automatic corrections can converge to solutions that look plausible but as shown in Figure 2.19 can be very far from the correct solution. Even with addition of the static field constraint the baseline offsets might be so large that the

simple bilinear scheme is not enough to correct the data. But the most troubling case is shown in Figure 2.28. This presents the north component of K-net station IWT009 157km from the centroid and corrected with the static offset constraint. The plot shows that the ABC waveform converges to the correct static value but the shaking is miscomputed by as much as 0.5m. This type of behavior is not uncommon in the corrections. Thus, the assumption that convergence to the static field value ensures reliability of the waveform is not routinely satisfied. It is possible for a correct static field to be computed but to be in error by large amounts in the dynamic component of the waveform.

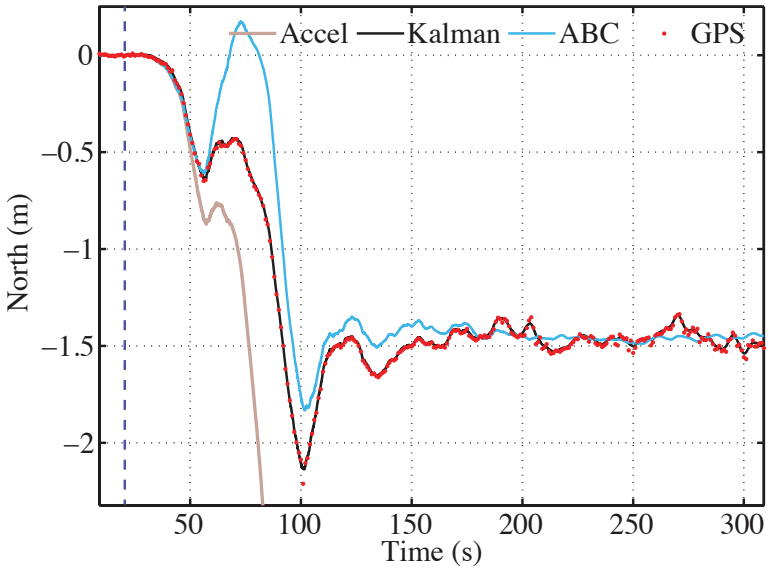


Figure 2.28: North displacement waveforms for station K-net station IWT009 157 km from the centroid.

We find that addition of the static field constrained as proposed by *Wang et al.* (2013) improves the time domain solution. Nonetheless we have also shown that ABC waveforms even when they converge to the correct static offset value can still be in error in regards to the transient component of the waveform (Figure 2.28).

The frequency domain analysis also shows some interesting behavior. We have once again demonstrated the performance of the Kalman filter displacements, following the GPS spectra at long periods and the accelerometer spectra at higher

frequencies. We have also shown that the ABC PSD can be miscomputed at frequencies as high as ∼0.5Hz. Furthermore we have demonstrated that addition of the static field constraint does little to improve the spectral recovery.

With the response spectra we have found a similar pattern except that the ABC spectra incurred in an error at lower frequencies, usually at periods longer than 8-9s. These discrepancies in both PSD and response spectra are well within the frequencies that are of interest to engineering seismology, especially for the PSD estimation. Furthermore the frequency domain error incurred by the ABC waveforms is not simple. Sometimes it is an overestimate and sometimes an underestimate. This has relevance for seismological applications that seek to use baseline corrected waveforms for strong ground motion analysis, source studies and response. This is true as well for engineering purposes. *Boore et al.* (2002) had already shown that this might be the case but found that for most stations the bias was introduced at much longer periods. However, that conclusion was reached from accelerometer data alone and no comparison was made to the frequency content of high rate GPS or combined data, which was unavailable at the time. Tangentially we have demonstrated that the useful frequency content of GPS-only waveforms is also limited to periods longer than 10 s. Higher-frequency studies from high rate data will be impeded by over estimates of the spectral content.

If indeed rotational motions account for most of the baseline offsets, and this seems to be the case (*Trifunac and Todorovska*, 2001; *Graizer*, 2006), then aspiring to design an algorithm that can accurately and objectively correct acceleration from acceleration data alone is a frustrating proposition. There is no way to simply distinguish between rotations and translations with enough sensitivity from the inertial sensor itself. Furthermore, although the incorporation of outside constraintts, such as the static field, improves matters it does not solve the problem. For a simple waveform with short duration and small accelerations, incorporating the static constraint might suffice. However for the Tohoku-oki waveforms, which have complex shapes, this simple constraint is insufficient. Rotational motions happen continuously throughout the record and introduce baseline offsets of different amplitudes in a continuous fashion, not in the simple piecewise manner in

which we have traditionally tried to model them. Thus constrainting the end of the record is not enough and there is no way to objectively determine offsets that happen earlier in the record

The aggregate of results and analysis we show here is by no means proof by exhaustion of the unsuitability of automatic baseline corrections. Other schemes might yet be developed that provide better results. However we have shown that the corrections in this particular case are suspect for static field determination; that they might miscompute the dynamic component of the seismogram and that the errors are incurred at frequencies well within what is of interest to seismology and engineering. Furthermore, we have shown that broadband displacements computed from collocated GPS and accelerometers via a Kalman filter have none of those problems.

While collocations are still not the norm, this work as well as that of *Wang et al.* (2013) argue that low-cost micro electro-mechanical sensors (MEMS) are increasingly desirable for regional monitoring. MEMS accelerometers are a fraction of the cost of observatory grade accelerometers. Thus, given the current limitations of baseline correction procedures, the superior performance of collocated processing techniques and the availability of cheaper sensors we advocate that if broadband displacements are a priority target of a particular network, then retrofitting of existing geodetic infrastructure with accelerometers should be given a high priority. We find it unlikely that displacements from accelerometer data alone will reach the robustness or reliability required for real-time and rapid observations.

2.6 Acknowledgments

For Sections 2.1-2.4 the data were provided by the Southern California Integrated GPS Network and its sponsors, the W. M. Keck Foundation; NASA; NSF; USGS; and SCEC; the Plate Boundary Observatory operated by UNAVCO for EarthScope and supported by NSF grant EAR-0323309; the USGS Pasadena office; and by Jose Restrepo and Marios Panagiotou for the University of California, San Diego LHPOST seven-story building experiments. Use of the Geodetics, Inc. RTD

software was provided by the University of California, San Diego. We thank Rob Clayton, Sharon Kedar, Richard Allen, and Mike Jackson for comments on earthquake early warning systems. Thanks to Peng Fang, Melinda Squibb, and Anne Sullivan for handling of CRTN data at SOPAC and to Fan Yang for early shake table results. This work was funded by NASA/AIST Grant No. NNX09AI67G and Conacyt project No. C82595. The work is published in **Bock, Y., Melgar, D., and Crowell, B.W., "Real-Time Strong-Motion Broadband Displacements from Collocated GPS and Accelerometers", *Bull. Seism. Soc. Am.*, 101(6), 2011**. Diego Melgar Moctezuma was involved in planning of the study, he wrote all the code for analysis and performed the data processing. He also analyzed the data and co-wrote the manuscript with the advisor Yehuda Bock.

For Section 2.5 we would like to thank the National Research Institute for Earth Science and Disaster Prevention for access to K-NET and KiK-net data and the Geospatial Information Authority of Japan for GEONET GPS data. The work was funded by NASA AIST-11 grant NNX09AI67G, NASA ROSES grant no. NNX12AK24G, and the Earth and Space Science Fellowship (NASA grant no. NNX12AN55H). We would like to acknowledge Thomas O'Toole, Rongjiang Wang, and Masumi Yamada for helpful comments. The work is published in **Melgar, D., Bock, Y., Sanchez, D., and Crowell, B.W., "On Robust and Reliable Automated Baseline Corrections for Strong Motion Seismology", *J. Geophys. Res.*, 118(3), 2013**. Diego Melgar Moctezuma conceived this study, wrote the code and analyzed a large portion of the data. He was also the lead author and coordinated the manuscript preparation.

Chapter 3

Rapid Static Modeling

In the introductory chapter we discussed how recent response to large earthquakes has been limited by a strict reliance on seismic data for early characterization of the earthquake source. In Chapter 2 we discussed briefly the problems facing traditional seismological instrumentation at local and regional distances of large events. Seismometers clip during strong shaking and strong motion sensors are affected by baseline offsets. The latter problem, baseline offsets, is particularly important because it affects the long period band of seismic time series; it is precisely this frequency band that is most useful for discerning the broad features of large earthquakes. If a geophysical instrument is band limited then it will become increasingly difficult to differentiate between say a magnitude 7 and a magnitude 8 event. This is a condition known as saturation and it is common in early warning algorithms that rely on seismometers and accelerometers alone *Brown et al.* (2011).

Large events induce a permanent deformation of the Earth's crust, the static field. If the earthquake is large enough, and the geophysical sensor close enough or sensitive enough it is possible to measure the static field. For hazards applications this is of great interest because the static field is a zero frequency wave and as such the longest period information we can obtain for an event. Thus characterization of the static field and of its contribution to a seismogram solves the problem of saturation. Furthermore the static field can be to first order assumed to have no time dependence, this makes it simple to extend earthquake source models from point sources to more realistic and complex geometries without consideration for

the time-dependent effects of linear superposition.

Although noisier than accelerometers, GPS can easily record the permanent deformation at regional distances of large earthquakes, this was first documented for the 1992 M7.2 Landers earthquak (*Bock et al.*, 1993; *Blewitt et al.*, 1993). It has since become routine to observe coseismic offsets in post-processed GPS time series after medium to large events and discussion in the literature of the potential of static field modeling for rapid response has become vigorous. *Blewitt et al.* (2006) showed that given an epicentral location and assuming thrust faulting for the 2004 Mw 9.2 Sumatra-Andaman earthquake, one could have estimated an accurate magnitude within 15 minutes of the origin time using global GPS stations at regional to teleseismic distances. *Sobolev et al.* (2007) proposed and demonstrated the viability of a system that uses coseismic offsets from GPS to directly invert for a heterogeneous slip model. *Crowell et al.* (2012) produced heterogeneous coseismic slip inversions from real-time data for two large events and *Wright et al.* (2012) produced source models with 4 fault patches from precise point positioning data for the M9 Tohoku-oki earthquake. *Ohta et al.* (2012) were able to produce in simulated real-time mode a simple uniform slip source model for the 2011 Tohoku-oki event and discussed the viability of using such a model to simulate tsunami propagation. *Pérez-Campos et al.* (2013) computed similar models for one scenario and one recorded subduction event in Mexico with a sparse network. This patchwork of studies demonstrate to varying degrees the viability, interest and importance of rapid modeling algorithms that employ the static field.

Throughout this chapter we will discuss a coherent framework that demonstrates how such recordings can be used. We will demonstrate the logical progression from point source centroid moment tensor models to finite extent moment tensors and finally slip inversions.

The Kalman filter method discussed in the previous chapter aides these algorithms insofar as it allows for better quantification of static offsets by reducing the noise in the displacement time series. Most notably there can be an order or more magnitude improvement in the resolution of vertical offsets. Nonetheless, its net effect, while non-negligible, is not of paramount importance for point

source and finite extent moment tensor computation. These methods can be quite successful with GPS data alone. The along-dip resolution in slip inversions does improve with seismogeodetic estimates of the static field, although again, it can still be adequately computed with GPS data alone. Later on in Chapter 4 we will see the true benefit of the filtered data for source estimation when we compute kinematic models.

3.1 Centroid Moment Tensor Inversion

Computation of the seismic moment tensor (MT) for a given earthquake is one of the fundamental kinds of modeling performed to study the source. The moment tensor can be calculated from a number of methods such as polarity of first arrivals (*Havskov and Ottemoller*, 2010) or waveform matching (*Dreger*, 2003) and is a compact representation of the source that contains basic information on the size of the event, the fault plane geometry and the style of faulting. Moment tensor solutions are of use over a range of earthquake magnitudes. Small to medium events are utilized for tectonic studies and to determine the stress regime within a region. For large events, rapid determination of the centroid location as well as the moment tensor (CMT) provides valuable information for earthquake response, tsunami early warning and as a starting point for finite fault source modeling.

Currently there are a number of efforts that routinely compute moment tensor solutions for earthquakes worldwide. The most comprehensive catalogue of such solutions is contained in the Global Centroid Moment Tensor (GCMT) Project. At its inception the GCMT project included inversion of body and surface waves (*Dziewonski et al.*, 1981; *Dziewonski and Woodhouse*, 1983) and has seen numerous refinements since such as inclusion of aspherical Earth structure, attenuation, etc. This method however employs only teleseismic data and its emphasis is in data collection and catalogue compilation not in rapid modeling. Real-time moment tensors can be obtained for small to medium events using time domain waveform matching inversion schemes (*Dreger and Helmberger*, 1990, 1993). However, real-time CMT determination of medium to large events is still an active area

of research.

One of the most important advances in computing CMTs as quickly as possible for large events is contained in the work of *Kanamori and Rivera* (2008) who elaborated on *Kanamori* (1993)'s observation of the W phase, a long period phase arriving in between the direct P and S waves. They showed that inversion for the moment tensor using data as close as 15° from the source is viable. W phase inversion algorithms currently run in real time at the USGS, Pacific Tsunami Warning Center (PTWC) and Institut du Physique du Globe de Strasbourg (IPGP-EOST) (*Hayes et al.*, 2009). Since the W phase arrives well before large amplitude surface waves and remains on-scale far longer such inversion algorithms have shown to be a marked improvement in rapid computation of moment tensor solutions for large events over traditional waveform matching techniques.

Following the Mw 9.0 Tohoku-oki earthquake, *Duputel et al.* (2011) showed that it was feasible to use data at distances as small as 11° from the source. However, W phase based inversion schemes, while very robust, require long period displacement records (e.g. 200-1000s for the 2011 Tohoku-oki event) (*Duputel et al.*, 2011). Such recordings, as discussed before, are almost always unusable close to the source in real time; velocity instruments clip and it is difficult to extract long period motions from strong-motion accelerometer data in real time.

Thus, there seems to be a limitation in how fast moment tensor solutions can be obtained operationally for large events using seismic instruments and existing seismological methods. For example, for the 2011 Tohoku-oki event it took 20 minutes after origin time to arrive at the first CMT solutions by agencies running W phase algorithms (*Duputel et al.*, 2011), even though the rupture had a duration of three minutes (*Simons et al.*, 2011). This delay was due to the reliance on teleseismic data. After several iterations using progressively more data, the final CMT solution (*Hayes et al.*, 2011) was obtained 90 minutes after origin time using data up to 90° from the rupture. The first estimate of moment magnitude was obtained in about 3 minutes by the Japan Meteorological Agency (JMA), but was underestimated at Mw 7.2. *Duputel et al.* (2011) documented that in the numerous iterations between agencies the nodal planes were somewhat consistent with only

minor variations in strike dip and rake, the magnitudes oscillated between Mw 8.8-9.0 after the 20-minute mark, but the centroid locations varied by as much as 2° and 60km in depth.

3.1.1 Point Source Models

We present a robust method for determining CMT solutions that is considerably faster than current seismic methods, based on real-time high-rate displacement data from near-source GPS stations. Although we are not explicitly solving for the style and geometry of faulting, that information is implicit in the moment tensor solution. In general, we do not require prior knowledge of the sense or extent of faulting, although that information could be used if available. We demonstrate the new algorithm by replaying the estimation of 1Hz displacements for the 2003 Mw 8.3 Tokachi-oki earthquake using GPS data from the Japanese GPS network (GEONET) (*Miyazaki et al.*, 1998) and for the 2010 Mw 7.2 El Mayor-Cucapah earthquake using data from the California Real Time Network (CRTN) (*Bock et al.*, 2004). We will also discuss the limitations of the point source strategy as illustrated by the 2011 Mw 9.0 Tohoku-oki earthquake.

Extracting Coseismic Offsets

Our inversion schemes use coseismic offsets; we apply a 120s moving average filter to the 1Hz displacement waveforms to remove the dynamic component and retain the information on the permanent deformation. GPS data have much higher noise levels than traditional seismological data sets in particular in the vertical direction, thus, we set a threshold of 15mm on the total horizontal component at a given station. This is roughly 3 times the usual noise level in the horizontal component of real-time GPS measurements (*Genrich and Bock*, 2006). At any given epoch only stations over this threshold are considered for the inversion.

Inversion Scheme

The inversion scheme employed here relates the coseismic offset measured at the surface to source parameters at depth. *Amoruso et al.* (2004) and *Hearn*

and Bürgmann (2005) showed that crustal layering can have a significant effect when inverting for source parameters using static offsets, thus we must account for, at least, a simple one-dimensional structure. To do so we compute Green's functions (GFs) using Fortran codes EDGRN/EDCMP (*Wang et al.*, 2003) for a 1D layered Earth. This numerical approach starts from the closed form solutions of the partial differential equations of motion obtained from the Hankel transform and then applies a Thomson-Haskell propagator matrix to relate the deformation at depth with that at the surface. We extract the GFs from the code output and set up the kernel matrix **G** for the inversion :

$$\begin{pmatrix} u_1^1 \\ u_2^1 \\ u_3^1 \\ \vdots \\ u_1^n \\ u_2^n \\ u_3^n \end{pmatrix} = \begin{pmatrix} G_{11}^1 & G_{12}^1 & G_{13}^1 & G_{14}^1 & G_{15}^1 \\ G_{21}^1 & G_{22}^1 & G_{23}^1 & G_{24}^1 & G_{25}^1 \\ G_{31}^1 & G_{32}^1 & G_{33}^1 & G_{34}^1 & G_{35}^1 \\ \vdots & & \cdots & & \vdots \\ G_{11}^2 & G_{12}^2 & G_{13}^2 & G_{14}^2 & G_{15}^2 \\ G_{21}^2 & G_{22}^2 & G_{23}^2 & G_{24}^2 & G_{25}^2 \\ G_{31}^2 & G_{32}^2 & G_{33}^2 & G_{34}^2 & G_{35}^2 \end{pmatrix} \begin{pmatrix} m_1 \\ m_2 \\ m_3 \\ m_4 \\ m_5 \end{pmatrix} , \tag{3.1}$$

or more succinctly

$$u_i^k = G_{ij}^k m_j \; ; \; \{i = x, y, z \; , \; j = 1, 2, \ldots, 5 \; , \; k = 1, 2, \ldots, n\} \; , \tag{3.2}$$

where u_i^k is the i-th component of displacement measured at the k-th station, m_j is the j-th component of the moment tensor and G_{ij}^k are the i-th component GFs that relate the j-th component of the moment tensor to the k-th station. Thus the GF matrix is very compact, having only 5 elements per direction of motion per station.

The moment tensor in this case is composed of 5 components since we restrict the inversion to the deviatoric portion such that for the general six component symmetric Cartesian MT

$$\mathbf{M} = \begin{pmatrix} m_{xx} & m_{xy} & m_{xz} \\ m_{xy} & m_{yy} & m_{yz} \\ m_{xz} & m_{yz} & m_{zz} \end{pmatrix} , \tag{3.3}$$

the deviatoric restriction means that the following equivalences between Equations 3.2 and 3.3 hold

$$\begin{aligned} m_1 &= m_{xy} \\ m_2 &= m_{xz} \\ m_3 &= m_{zz} \\ m_4 &= (1/2)(m_{xx} - m_{yy}) \\ m_5 &= m_{yz} \, . \end{aligned} \tag{3.4}$$

We have retained the *Aki and Richards* (2002) convention where x is north, y is east and z is down. This is just one of many possible moment tensor coordinate representations; however we have chosen this one to be consistent with the notation used by the EDGRN/EDCMP software.

Since we are making a point source approximation and neglecting fault finiteness, we assume that despite the coseismic motions the source to receiver distances remain unchanged and so the Greens function matrix remains unaltered throughout the inversion process. Next we assemble the data vector from that epochs measured coseismic offset and weigh the data by the pre-event standard deviations as

$$\mathbf{Wu} = \mathbf{WGm} \, , \tag{3.5}$$

where

$$\mathbf{W} = \mathrm{diag}\left(\frac{1}{\sigma_1^1}, \frac{1}{\sigma_2^1}, \frac{1}{\sigma_3^1}, \frac{1}{\sigma_1^2}, \frac{1}{\sigma_2^2}, \frac{1}{\sigma_3^2}, \ldots, \frac{1}{\sigma_1^n}, \frac{1}{\sigma_2^n}, \frac{1}{\sigma_3^n} \right) \, , \tag{3.6}$$

and the σ_i^ks are the standard deviations obtained from 60 s of pre-event noise at the k-th station on the i-th channel. This is a reasonable assumption since, in the absence of motion, the pre-event time series are many realizations of a zero measurement. The weight matrix remains constant across all epochs, since we assume that the noise characteristics of the GPS time series are the same for the duration of the inversion. The noise characteristics of real-time GPS displacements should be stable on the scale of minutes (*Genrich and Bock*, 2006). Furthermore in Chapter 2 we found no appreciable increase in the noise level between quiescent periods and periods of shaking during the shaketable tests. Thus, to first order, the noise can be assumed to be constant for the duration of strong shaking.

An additional weighting is applied based on the distance r from the source to the receiver. Because the static field decays according to $1/r^2$ (*Aki and Richards*, 2002) we divide each time series by a weight w_r to avoid having the largest offsets overwhelm the norm minimized by the inversion. This is a technique analogous to the one used in time domain waveform moment tensor inversion (*Dreger*, 2003). For a centroid to station distance r_i the weight is defined as

$$w_r^i = \frac{[\min(r_i)]^2}{r_i^2} \,, \tag{3.7}$$

thus, we have two weighting factors, one that determines how trustworthy an offset is when compared to background noise levels and a second one that ensures that the largest offsets do not dominate the inversion.

The inversion is performed at each time step (once per second in this case) utilizing the coseismic offset measured at that epoch to produce a new moment tensor. We experimented with L2-norm inversion using a QR decomposition and L1-norm inversion (*Boyd and Vandenberghe*, 2004). We found that L1-norm minimization converges to a stable solution before the L2-norm inversion.

For analysis of the inversion we obtain the seismic scalar moment M_0 as the scaled Frobenius norm of the moment tensor (*Silver and Jordan*, 1982)

$$\|\mathbf{M}\| = \frac{1}{\sqrt{2}} \left(\sum_{i=1}^{3} \sum_{j=1}^{3} M_{ij}^2 \right)^{1/2} \,, \tag{3.8}$$

to then compute the moment magnitude using the relationship of *Hanks and Kanamori* (1979). Additionally we compute the deviation of the model from a pure double couple source as gauged by the parameter ϵ (*Dziewonski et al.*, 1981) which is computed from the moment tensor eigenvalues as

$$\epsilon = \frac{\gamma_{min}}{\gamma_{max}} \,, \tag{3.9}$$

where γ_{min} is the smallest eigenvalue in the absolute sense and γ_{max} is the largest. $\epsilon = 0$ denotes a pure double couple source and $\epsilon = 0.5$ a pure compensated linear vector dipole (CLVD) source.

The hypocenter and centroid locations can vary substantially since the hypocenter is the point of initiation of rupture while the centroid is the point

of mean moment release. The hypocenter can be determined rapidly from traditional seismic data but the centroid location is harder to compute. To locate the centroid we employ a grid searching approach by defining a discrete grid around the stations that first detect the coseismic offsets. We invert simultaneously at each epoch on all grid points (inversion nodes) assuming that each node is the centroid. We then compute the misfit of the inversion at each node and define the final centroid location for that epoch as the one with the largest variance reduction (VR):

$$\mathrm{VR} = \left(1 - \frac{\sum_{i=1}^{n}[d_i - (\mathbf{Gm})_i]^2}{\sum_{i=1}^{n} d_i^2}\right) \times 100 \; . \tag{3.10}$$

In order to build the grid of nodes on which the inversion will take place, it is possible to use a precomputed slab model (in the case of subduction zone events) or have a library of fault surfaces (for strike slip environments) as a template for a grid. Alternatively it is possible discretize the known geological surfaces to define the inversion nodes thus forcing the centroid to lie on known faults. We prefer to minimize assumptions and simply build a sufficiently large three dimensional prism of grid points around a preliminary hypocentral location. The choice of strategy will depend on the observational goals of a network. In any case, we combine a formal inversion with a grid search to solve for the CMT using an algorithm that we call *fast*CMT.

3.1.2 Applications of the Point Source Approach

To demonstrate our approach, we apply here the *fast*CMT algorithm for a subduction zone earthquake and for an earthquake in a strike-slip environment, using near-field 1Hz GPS network data replayed in a simulated real-time mode to estimate displacements.

2003 Mw 8.3 Tokachi-oki Earthquake

The first example of *fast*CMT is for the 2003 Mw 8.3 Tokachi-oki earthquake. This megathrust event ruptured a segment of the Kuril-Japan trench, sharing most of the source area and rupture characteristics of the 1953 Mw 8.1

Tokachi-oki earthquake (*Hamada and Suzuki*, 2004). We estimated displacements in simulated real-time mode for 300 seconds of GEONET 1Hz data from 355 stations in Honshu and Hokkaido islands. Some very near source stations lost telemetry and have incomplete records so we excluded those from processing. We applied a 120s moving average to each displacement record in each coordinate component to extract the permanent deformation from the displacement waveforms; the resulting time series can be seen in Figure 3.1. The static offset at the stations closest to the source is discernible at around 160s. As is usual with GPS time series, the vertical component is noisier than the horizontals (*Genrich and Bock*, 2006).

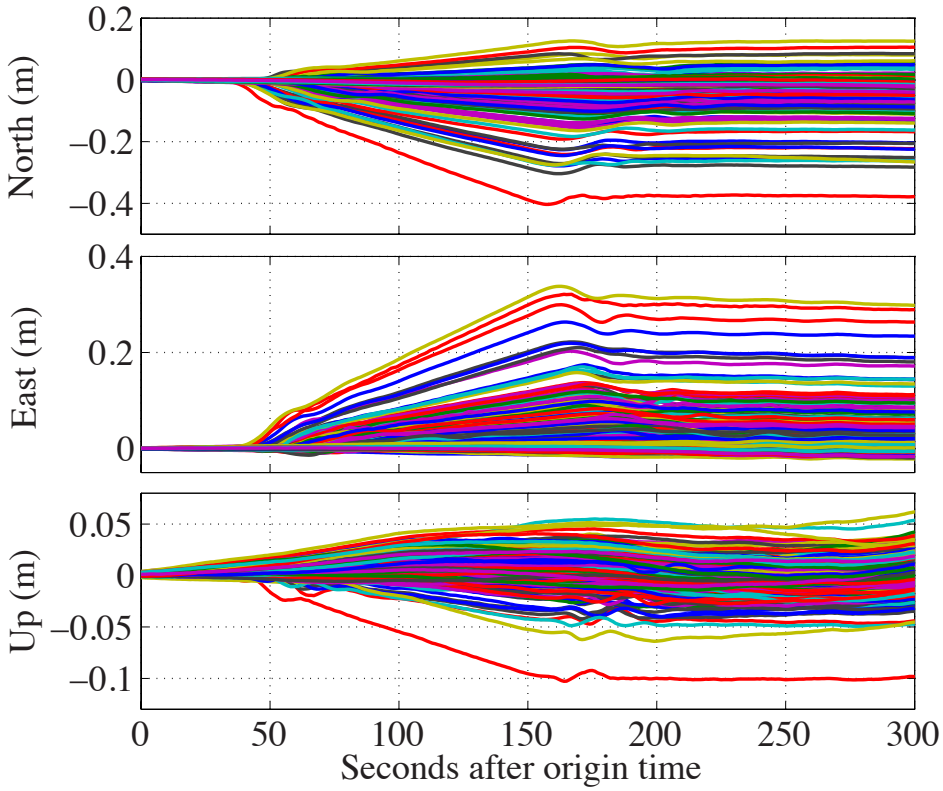


Figure 3.1: First 300 s of displacement records at 355 GEONET stations with a 120 s moving average filter applied for the Tokachi-oki earthquake.

Green's functions were computed from EDGRN on a 1 km horizontal and vertical grid using the four-layer velocity model employed by *Yagi* (2004) for near source slip inversion (Table 3.1). This is a much denser coverage than the actual station distribution, thus, at any given station the resulting GF is the spline in-

Table 3.1: Velocity model for the Tokachi-oki inversion

Layer	v_p (km/s)	v_s (km/s)	Density (kg/m^3)	Thickness (km)
1	3.80	2.19	2.30	4.0
2	5.50	3.18	2.60	4.0
3	5.80	3.34	2.70	10.0
4	6.50	3.74	2.90	10.0
Half-space	7.80	4.50	3.20	∞

terpolation of the closest grid points. For this scenario we used a 3-D $3^\circ \times 3^\circ$ prism of gridpoints spaced at 0.2° and every 3km in depth between 3 and 60km centered around the mean latitude and longitude of the first stations to meet a detection criterion.

We defined the criterion that displacements from 5 stations over the 15mm threshold are required to start the inversion; for the 2003 Tokachi-oki event this occurred at 43s after origin time. The results of the inversion are shown in Figures 3.2 and 3.3. Figure 3.2 shows the centroid determination as a function of time, Figure 3.3 shows snapshots of the resulting CMT as well as the observed and synthetic horizontal displacements. Figure 3.2 shows that by 50 s a rough centroid location is available with oscillations between adjacent nodes. The magnitude reaches Mw 8.0 at 75s, with a 75% variance reduction. However, as evidenced by the time series (Figure 3.1) the full coseismic offset has not yet occurred. The magnitude continues to grow and settles at 8.3 by 170s. The plot of the variance reduction also shows that at 200s (when the final offset is in place) the fit to the data is maximum (85%) degrading towards the end of the inversion. Figure 3.2 shows the oscillation between adjacent nodes for the centroid solution and also indicate how by 65s a thrusting mechanism is already resolved although the magnitude is still underestimated. However, by 180s and onwards the inverted mechanism is close to that of the GCMT solution (http://www.globalcmt.org/).

To further evaluate the quality of the solution we extracted the strike, dip and rake of the nodal planes from the moment tensor solution every second by decomposing it into its best double couple. The results are shown in Figure 3.4 and compared to the GCMT results. They illustrate that the geometrical parameters

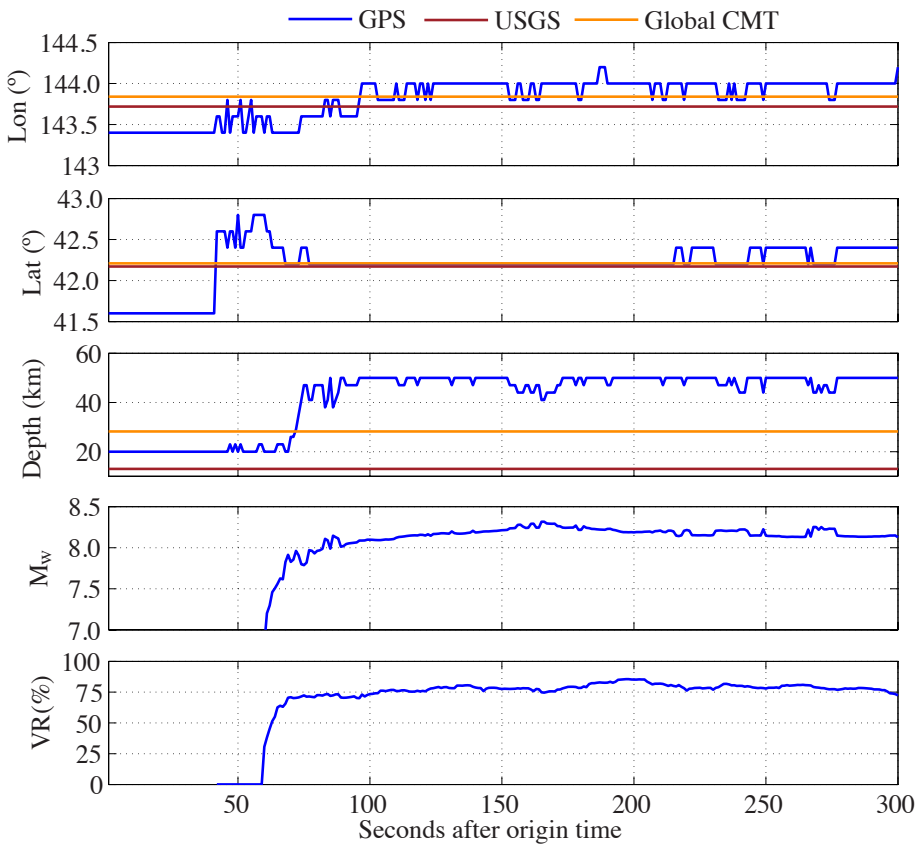


Figure 3.2: Summary of the inversion results for the Tokachi-oki earthquake. The top three panels are the centroid determination as a function of time compared to the location reported by the USGS and the Global Centroid Moment Tensor Project. The fourth panel is the computed magnitude and the fifth panel is the misfit (variance reduction).

of the best double couple are well determined at 65s, before the full coseismic deformation occurs, and remain fairly similar to the post-processed GCMT solution throughout. Furthermore the size of the compensated linear vector dipole (CLVD) (*Aki and Richards*, 2002) component of the solution is fairly small throughout the inversion, never exceeding $\epsilon = 0.05$.

The 2010 Mw 7.2 El Mayor Cucapah Earthquake

The 2010 Mw 7.2 El Mayor-Cucapah earthquake ruptured roughly 120km of the Pacific-North America plate boundary in northern Baja California, Mexico.

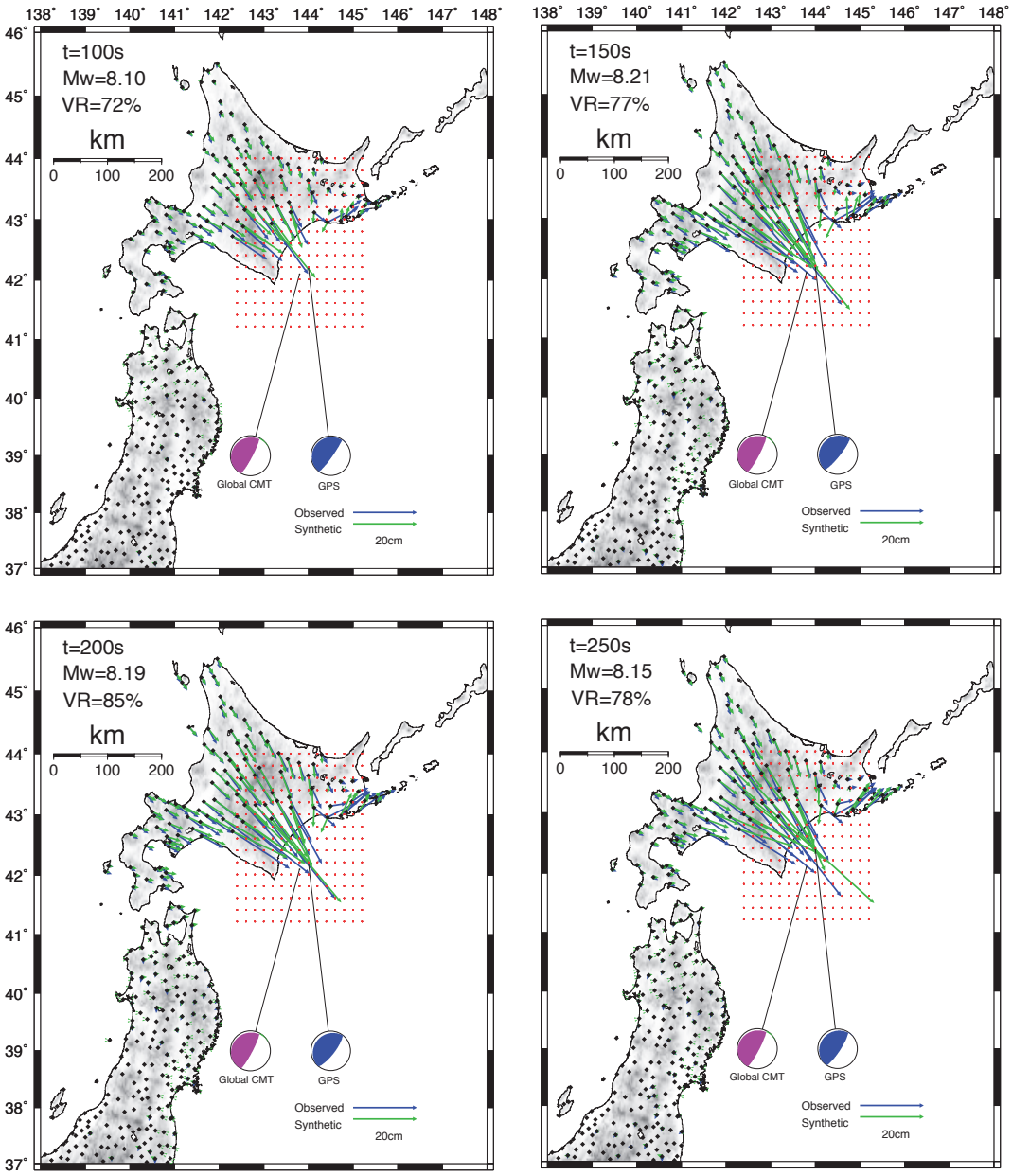


Figure 3.3: Snapshots of the inversion results comparing the Global CMT result with the replayed GPS real time inversion for the 2003 Mw 8.3 Tokachi-oki earthquake. Mw is the moment magnitude and VR the variance reduction. The red dots indicate the inversion nodes of the 3° by 3° grid used for the grid search. Also shown is the comparison between the observed (blue) and modeled (green) horizontal offsets.

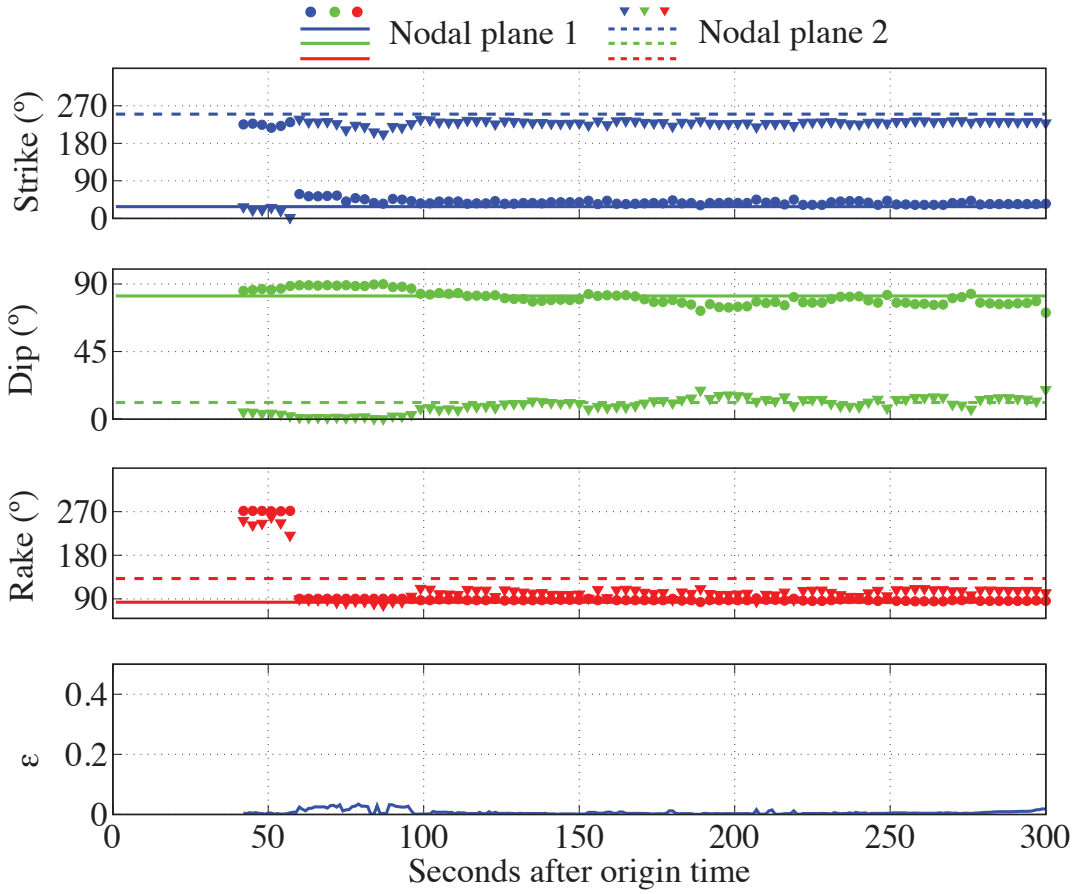


Figure 3.4: Geometrical parameters of the best double couple solution extracted from the moment tensor inversion and compared to the global CMT post-processed result. Data for both nodal planes (NP1 and NP2) are plotted at 3s intervals for clarity. ϵ is defined in Equation 3.9. Data starts at 43s when enough stations detect an offset.

The rupture was complex possibly starting with a normal faulting event followed by simultaneous normal and right lateral faulting (*Hauksson et al.*, 2011). The rupture plane showed evidence of a warped fault, was bilateral and the rake changed along strike away from the epicenter from pure strike slip to a mixture of strike slip and dip slip motion (*Wei et al.*, 2011).

Displacements at a 1Hz sampling rate were estimated in a simulated real-time mode for 105 stations of the California Real Time Network in southern California as described in Chapter 2. As in the first event, we applied the 120 s moving

average filter, at each epoch we exclude stations with horizontal offsets smaller than 15 mm (Figure 3.5), and started the inversion process when 5 stations detected motion over the threshold; at 41s after origin time for the 2010 El Mayor-Cucapah event. The horizontal coseismic offsets are apparent at the stations closer to the source by 150s in both components although some shaking is still visible in the form of small oscillations. By 200s the shaking ceases and only the offset remains. Offsets are not easily discernible in the vertical components, which remain noisy throughout. This is reasonable since this earthquake produced only small vertical offsets of ∼5mm from the stations closer to the source as estimated, for example, from the more accurate, standard 24 hour displacement time series.

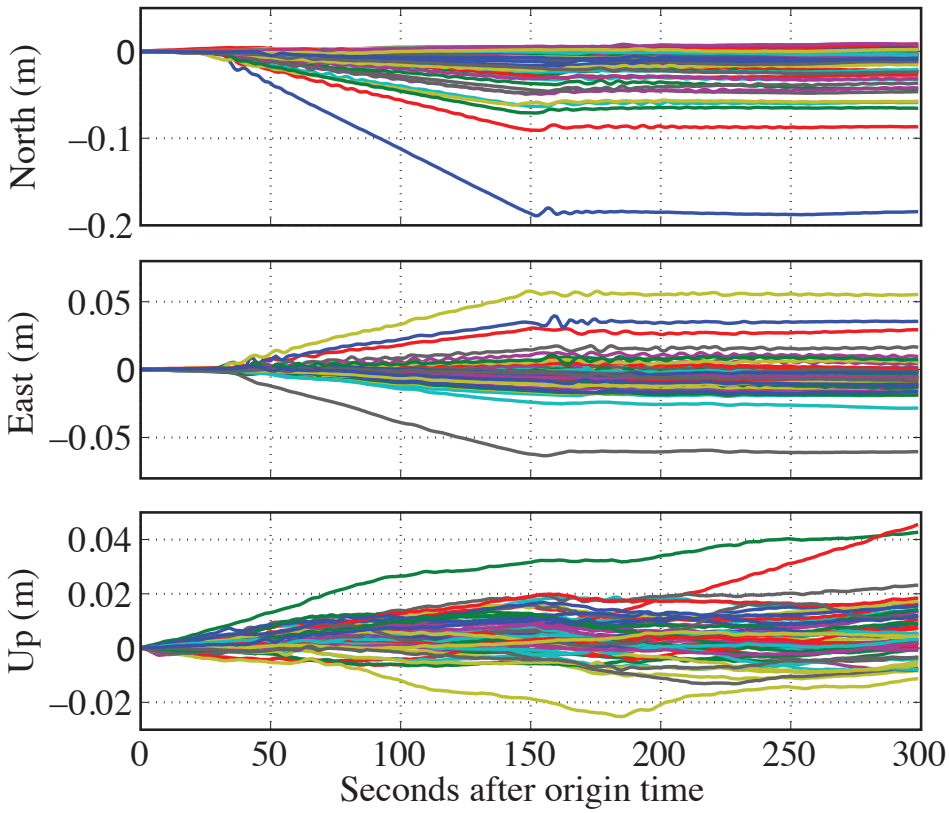


Figure 3.5: 300s of displacement records at 50 of the 105 CRTN stations that exceeded the 15mm threshold with a 120s moving average filter applied for the 2010 Mw 7.2 El Mayor-Cucapah earthquake

The seismic velocity model used in the inversion is obtained from a simplification of the California Community Velocity Model version 4 (CVM4) (*Kohler*

Table 3.2: Velocity model for the El Mayor-Cucapah inversion

Layer	v_p (km/s)	v_s (km/s)	Density (kg/m^3)	Thickness (km)
1	4.14	2.18	2.33	4.16
2	5.73	3.34	2.67	4.16
3	6.37	3.66	2.80	8.32
4	6.64	3.74	2.87	8.32
Half-space	7.69	4.38	3.218	∞

et al., 2003). The structure in this zone is highly heterogeneous so our model is an average of the grid with corners (117°W, 32°N) and (115°W, 34°N). We assume a constant Moho depth, which is taken as the mean value inside the grid. We define 4 layers between the Moho and the free surface, and assume a half space below the Moho (Table 3.2). The GFs for this model are computed at 1 km horizontal and vertical intervals with EDGRN and as before, at a particular station the GF is the result of the spline interpolation of the closest grid points.

In order to avoid the use of a library of fault surfaces we place a rectangular 3° by 3° grid of inversion nodes around the mean latitude and longitude of the first 5 stations to detect 15mm of horizontal motion and spaced at 0.1° in latitude and longitude and 2km in depth from 2-20km. As before, we prefer an L1-norm inversion. Figure 3.6 shows a summary of the centroid determination and magnitude results of the inversion. The centroid is well located by 50s. After 50s the centroid location oscillates between adjacent nodes; the depth oscillates between 2 and 8km before settling at 2km by 280s. The variance reduction is maximum (∼85%) by 150s and worsens slightly towards the end of the inversion, the style of faulting is not well resolved until 150s (Figures 3.7 and 3.8). The moment magnitude estimate reaches 7.2 by 60s but continues to grow and oscillates between 7.0 and 7.5, before becoming fairly stable at 7.2 by 160s.

The focal mechanisms display some interesting characteristics during the inversion; Figure 3.7 shows snapshots of the inversion and centroid location at 50s intervals and Figure 3.8 shows the strike, dip and rake of the best double couple solutions. By 120s the best double couple solution is almost pure strike-slip with strike and dip very similar to the W phase solution and a centroid ∼30km from

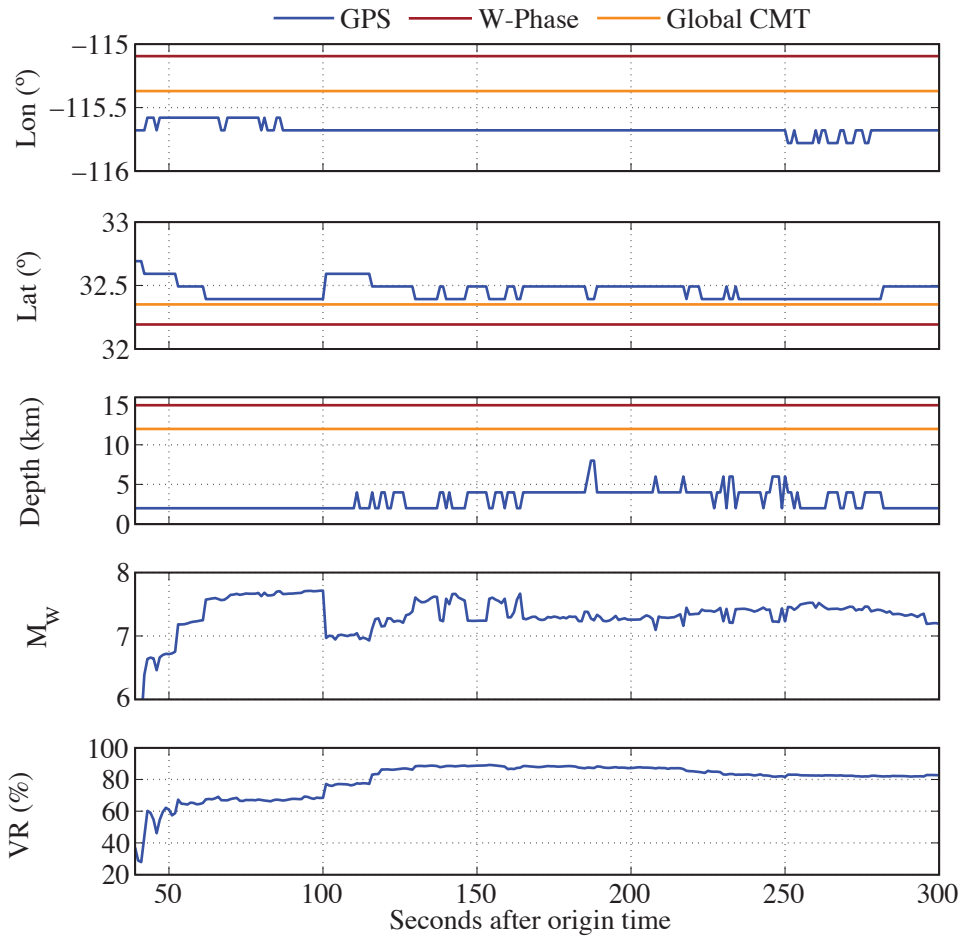


Figure 3.6: Summary of the inversion results for the 2010 El Mayor-Cucapah earthquake. The top three panels are the centroid determination as a function of time compared to the location reported by the USGS W-Phase inversion and the Global Centroid Moment Tensor Project. The fourth panel is the computed magnitude and the fifth panel is the misfit (variance reduction).

the W phase centroid. The strike of both nodal planes remains fairly consistent throughout as does the rake and the dip of the first nodal plane. However the dip of the second nodal plane oscillates throughout the inversion. Furthermore, the size of the CLVD component is quite large with a mean value of 0.25 during the inversion period. This is consistent with the observations of *Hauksson et al.* (2011) who obtain similar results from post-event W phase inversions and analysis of satellite geodesy data *Wei et al.* (2011) which indicate that a large CLVD reflects source complexity and is a real signal.

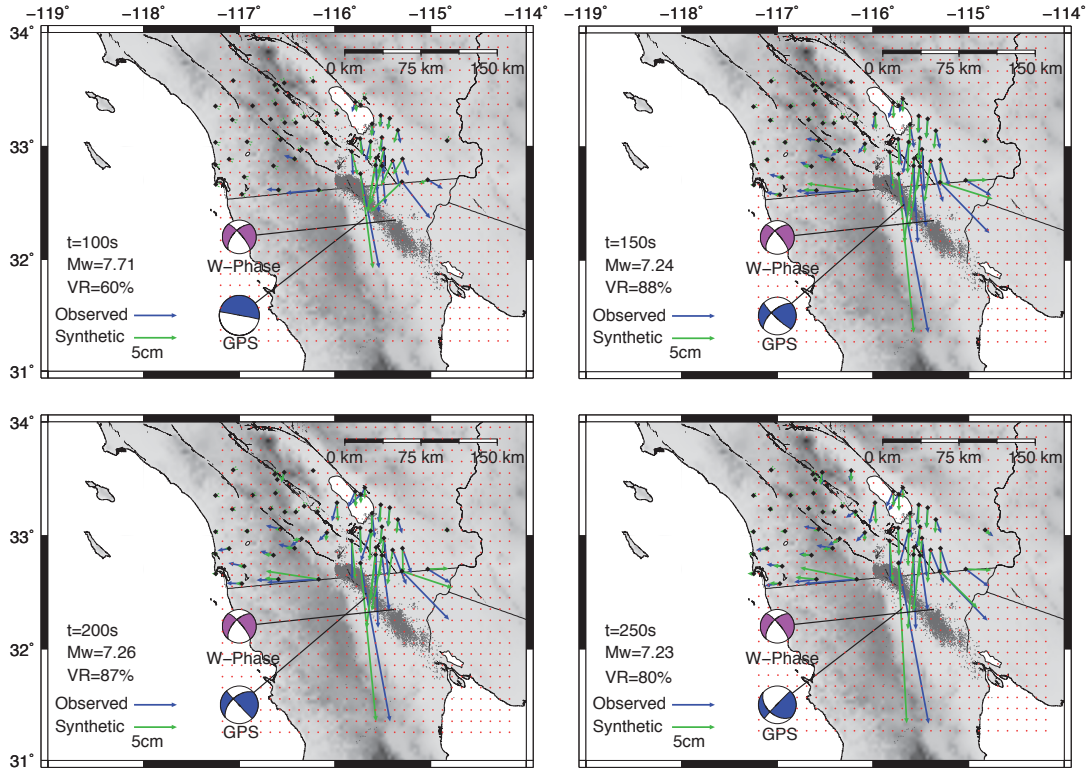


Figure 3.7: Snapshots of the inversion results for the El Mayor Cucapah earthquake comparing the USGS W phase result with the GPS real-time inversion. Also shown is the comparison between the observed and modeled horizontal offsets. The red dots indicate the nodes used for the grid search, dark grey dots are one year of aftershocks reported by the Southern California Seismic Network (www.data.scec.org) and black lines indicate Quaternary faults in southern California.

3.1.3 Final Point Source Solutions

We have shown that the final CMT solution is quickly obtained after the end of the rupture process as soon as the full permanent deformation has been discerned. The convergence to the final CMT solution is illustrated in Figure 3.9 for both earthquakes. The procedure in initiated as described earlier when 5 stations have a total horizontal displacement that exceeds the 15mm threshold. We refer to this instant as the time of first detection t_d; it is the time at which we launch the procedure to determine the final coseismic offsets. The mean latitude and longitude of the 5 GPS stations is computed, and a 3° by 3° grid around that value is

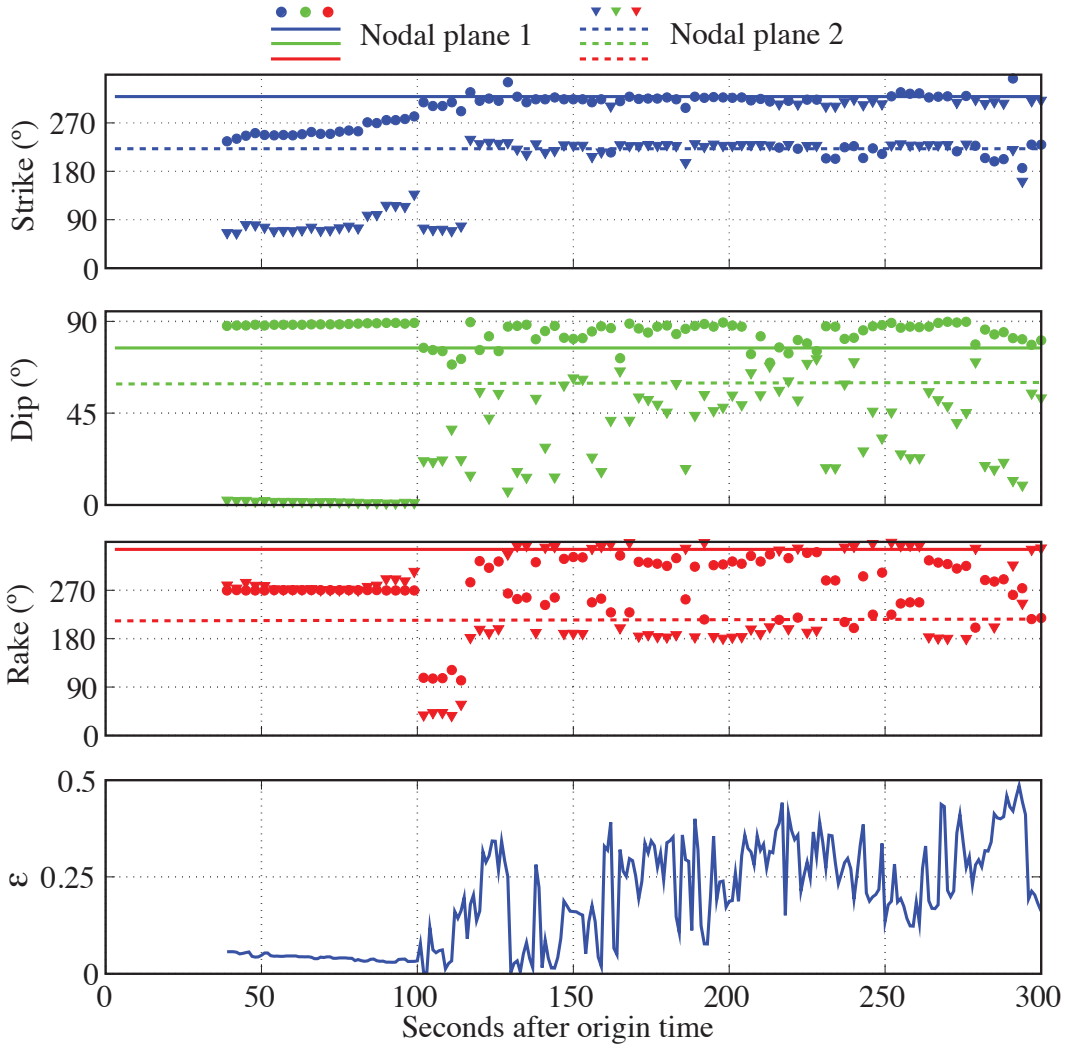


Figure 3.8: Geometrical parameters of the best double couple solution extracted from the moment tensor inversion and compared to the USGS W phase post-processed result for the 2010 El Mayor-Cucapah earthquake. Data for both nodal planes (NP1 and NP2) are plotted at 3s intervals for clarity. ϵ is defined in Equation 3.9. Data starts at 41s when enough stations detect an offset.

defined. The pre-computed GFs are spline interpolated to compute values at each grid point. A grid search is initiated to determine the event centroid. In addition to the 120s moving average computed for the total horizontal displacements. We also compute the variance of 20 samples previous to the current epoch (Figure 3.9a and 3.9e); as the offset grows, the variance will be high and when the displacement

stabilizes to its final level the variance will diminish and stabilize. Only the station with the maximum horizontal displacement is considered at this point of the analysis. At each epoch, the station that obeys this constraint is tracked; it can change from epoch to epoch depending on the location of the network with respect to the earthquake source. Thus, the displacement traces shown in Figure 3.9 (a, e) could be a composite of several stations. The variance at each epoch is computed over the previous 20 samples (or the previous 20s for 1Hz data). At every instant we track whether the observed variance is the maximum observed one (s^2_{max}) up to that given point (the time of maximum variance is t_{max}). Simultaneously, we track whether the variance has dropped below an empirically set threshold $p \cdot s^2_{max}$ where $p = 0.25$. The epoch where that threshold is exceeded is time t_1 and we assume this to be the instant when the final offset at the station with the maximum horizontal displacement has been reached. Evidently some error is incurred here from stations not yet developing the full offset, but after experimenting with values of p ranging from 0.01 to 0.5, and comparing with post-processed inversions we conclude that 0.25 is optimum. A high value for p detects the final offset earlier but does not allow for enough stations to have reached a final offset, conversely a low value of 0.1 waits an unnecessarily long time for the final offset solution.

As evidenced by Figure 3.4 and 3.8 there is still a considerable amount of scatter in the MT solutions so taking data from a single epoch is not desirable and more averaging is necessary. Thus the *fast*CMT algorithm waits (a somewhat arbitrary) 20 seconds after t_1. At $t_2 = t_1 + 20$, the displacements of the three directions of motion are averaged, in between t_1 and t_2, for all stations over the 15 mm threshold, and at that point the inversion procedure begins. Assuming negligible computation times, t_2 is also the time at which a final solution is available. Figures 3.9a and 3.9e show the maximum displacement and its corresponding variance function for the Tokachi-oki and El Mayor-Cucapah events; Figures 3.9b through 3.9d and 3.9f through 3.9h show the computed final offsets compared to the original time series for all 3 directions of motion for both events. Figures 3.10 and 3.11 show the final CMT solutions for the Tokachi-oki and El Mayor-Cucapah events, respectively, and compare them to the GCMT solution in the Tokachi-oki

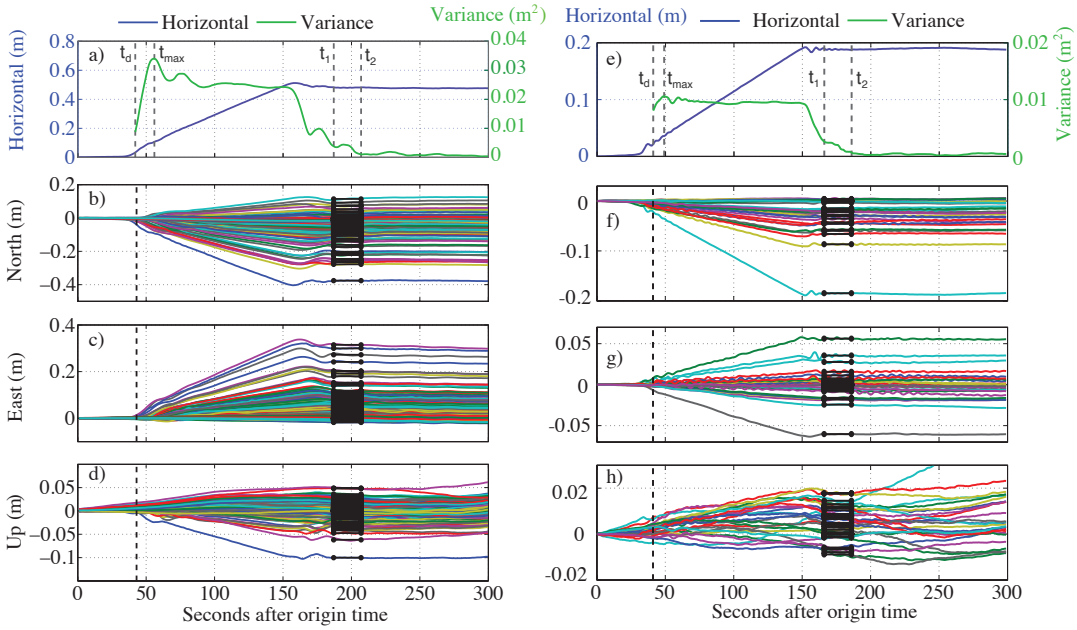
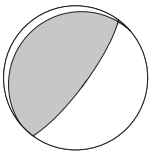


Figure 3.9: (a) Maximum horizontal displacement and variance function used for determination of final offsets for the 2003 Tokachi-oki earthquake (see text for detailed description). t_d is the time at which anomalous motion is detected, t_{max} is the time of maximum variance, t_1 is the time when the variance function drops to 25% of the maximum value and defines the start of the averaging interval and t_2 is 20s after t_1 and is the end of the averaging interval and the time at which a final solution is available. b)-d) Final offsets determined for the 3 directions of motion for the Tokachi-oki event. d) Maximum horizontal displacement and variance function used for determination of final offsets for the 2010 El Mayor-Cucapah earthquake (see text for detailed description); t_d, t_{max}, t_1 and t_2 have the same definition as in 9a. f)-h) Final offsets determined for the 3 directions of motion for the El Mayor-Cucapah event.

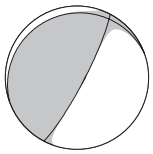
case and the W phase solution in the El Mayor-Cucapah case. In addition, Table 3.3 summarizes the times at which different milestones are reached for each event.

The origin time for the Tokachi-oki event according to the global CMT solution is 19:50:06 UTC; our fastCMT solution is available 211 seconds after that. The *fast*CMT centroid is located 4.6 km north of the Global CMT centroid, however the GCMT solution is at a depth of 28km compared to the 48km computed by *fast*CMT. From the Slab 1.0 model of *Hayes et al.* (2012), the *fast*CMT solution, lies 10km below the slab, while the GCMT solution lies some 10 km above the position of the slab. The moments are very similar, 2.9×10^{21}Nm for the *fast*CMT

a)



b)



fastCMT Event Report			
Event ID: 2003 Tokachi–oki			
Lat = 42.20	Lon = 144.00	Depth = 48 km	
Final Solution Time: 19:53:15		Mw = 8.2	
Moment Tensor (Scale 1x10^21 Nm)			
Mrr = 1.001	Mtt = -0.463	Mpp = –0.539	
Mrt = 1.353	Mrp = 1.871	Mtp = –0.518	
Prinicpal Axes			
Axis	Value	Plunge	Azimuth
T P B	2.518 –2.523 –0.005	57 33 3	303 129 37
Best Double Couple (Mo = 2.932e+21 Nm)			
Plane	Strike	Dip	Rake
NP1 NP2	229 36	12 78	103 87
Inversion Summary			
#Stations = 151		Var. Red. = 79.76%	
%DC = 99.60	%CLVD = 0.40	%ISO = (null)	

Global CMT Solution			
Event ID: 2003 Tokachi–oki			
Lat = 42.21	Lon = 143.84	Depth = 28.2 km	
Final Solution Time: N/A		Mw = 8.3	
Moment Tensor (Scale 1x10^21 Nm)			
Mrr = 0.777	Mtt = –0.411	Mpp = –0.366	
Mrt = 1.320	Mrp = 2.590	Mtp = –0.662	
Prinicpal Axes			
Axis	Value	Plunge	Azimuth
T P B	2.980 –3.130 0.150	53 36 7	289 124 29
Best Double Couple (Mo = 3.050e+21 Nm)			
Plane	Strike	Dip	Rake
NP1 NP2	250 28	11 82	132 83
Inversion Summary			
#Stations = N/A		Var. Red. = N/A	
%DC = 90.42	%CLVD = 9.58	%ISO = (null)	

c)

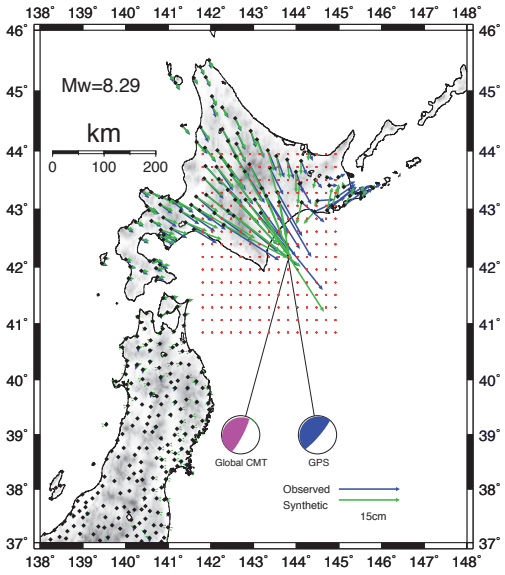
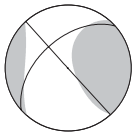


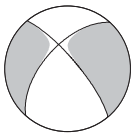
Figure 3.10: Detailed comparison between the a) fastCMT and b) GCMT results for the 2003 Tokachi-oki event. c) Comparison between the best double-couple solutions as computed in (a) and (b) and the synthetic and observed displacements of (a).

a)



fastCMT Final Report			
Event ID: 2010 El_Mayor–Cucapah			
Lat = 32.39	Lon = –115.68	Depth = 4 km	
Final Solution Time: 22:43:51	Mw = 7.2		
Moment Tensor (Scale 1x10^19 Nm)			
Mrr = –1.016	Mtt = –4.254	Mpp = 5.270	
Mrt = 1.153	Mrp = –3.949	Mtp = –0.207	
Prinicpal Axes			
Axis	Value	Plunge	Azimuth
T P B	7.216 –4.778 –2.438	26 26 52	86 190 137
Best Double Couple (Mo = 5.997e+19 Nm)			
Plane	Strike	Dip	Rake
NP1 NP2	228 318	52 90	0 217
Inversion Summary			
#Stations = 31		Var. Red. = 87.78%	
%DC = 34	%CLVD = 64	%ISO = (null)	

b)



W-Phase Solution			
Event ID: 2010 El_Mayor–Cucapah			
Lat = 32.19	Lon = –115.10	Depth = 15 km	
Final Solution Time: N/A	Mw = 7.2		
Moment Tensor (Scale 1x10^19 Nm)			
Mrr = –1.720	Mtt = –4.900	Mpp = 6.610	
Mrt = 2.90	Mrp = –1.710	Mtp = 0.140	
Prinicpal Axes			
Axis	Value	Plunge	Azimuth
T P B	6.960 –6.690 –0.280	11 31 55	87 185 150
Best Double Couple (Mo = 6.800e+19 Nm)			
Plane	Strike	Dip	Rake
NP1 NP2	222 319	59 77	346 213
Inversion Summary			
#Stations = N/A		Var. Red. = N/A	
%DC = 90	%CLVD = 10	%ISO = (null)	

c)

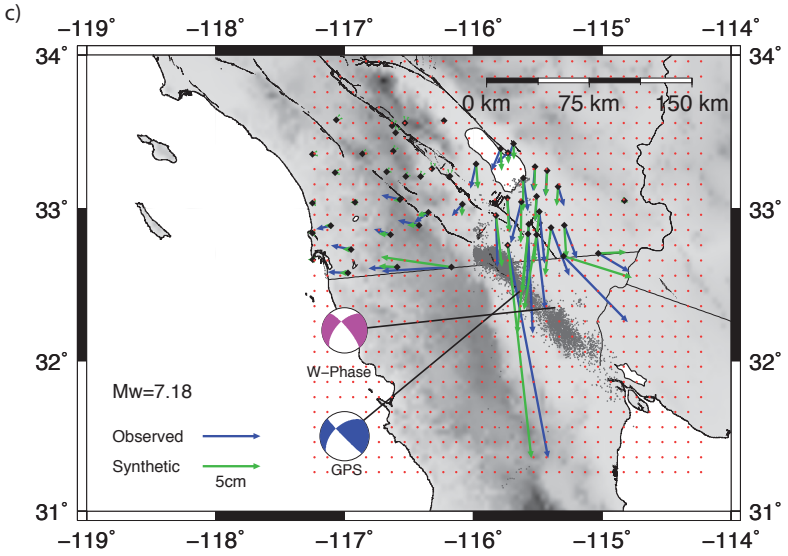


Figure 3.11: Detailed comparison between the a) fastCMT and b) USGS W-Phase results for the 2010 El Mayor-Cucapah event. c) Comparison between the best double-couple solutions as computed in (a) and (b) and the synthetic and observed displacements of (a).

solution and 3.1×10^{21}Nm for the GCMT solution, yielding Mw 8.2 and Mw 8.3 respectively. The largest difference is in the geometrical characteristics of the

Table 3.3: Summary timeline of results for the Tokachi-oki and El Mayor-Cucapah events

Milestone	Tokachi-oki	El Mayor-Cucapah
Origin time (OT)	19:50:06 UTC	22:40:45 UTC
5 stations detect motion (t_d)	OT+43s	OT+41s
Maximum variance reached (t_{max})	OT+51s	OT+49s
Final offset defined (t_1)	OT+192s	OT+166s
Final solution available (t_2)	OT+212s	OT+186s

first nodal plane. The GCMT solution has a strike of 250° while our rapid solution computes a strike of 229°. The strike in the Slab 1.0 model at 38km depth increases smoothly from South to North from 200° at 41°N to 245° at 42.4°N, decreasing to 230° by 43°N thus the *fast*CMT solution seems to be closer to the strike in the slab model. Both solutions show a shallow dipping fault, 12° for *fast*CMT and 11° for GCMT, the rake angle is 103° for *fast*CMT while the GCMT solution has a significant strike-slip component with a rake of 132°. A strike-slip component seems to be supported by joint strong motion and GPS inversions (*Koketsu et al.*, 2004) although not as large as suggested by the GCMT result. This difference is also evident in the azimuths of the principal axes although the plunge angles between the two solutions are fairly similar. Finally, it is interesting to note that the GCMT solution has a large CLVD component (10%) while our rapid solution favors almost a pure double couple solution with a CLVD of 0.4%.

For the El Mayor-Cucapah earthquake we compare the *fast*CMT solution with the W phase result available from the USGS. The origin time for this event is 22:40:45 UTC; the *fast*CMT solution is available 186 seconds after that and locates the centroid 55km northwest of the W phase centroid but still well within the aftershock cloud. This could reflect a bias in the GPS station distribution, all north of the rupture and across the U.S.-Mexico border. Nonetheless, comparison with the static slip inversion of *Wei et al.* (2011) shows that the W phase solution is 25km southeast of the main slip patch while our rapid solution lies within it. Similarly, the *fast*CMT solution favors a shallow centroid at a 4km depth while the W phase centroid is at 15km depth. A shallow centroid at 2-8km depth is consistent with the results of *Wei et al.* (2011). The moments of both the W phase

and *fast*CMT solutions are similar at 6.8 and 6.0×10^{21}Nm, respectively (Mw 7.2). The strike and dip of the first nodal plane are similar for both solutions, although W phase favors a small dip-slip component while the *fast*CMT solution has none. The second nodal plane, which from the aftershock distribution is the actual fault plane, has similar strike for both solutions (318° and 319° respectively) although the *fast*CMT solution favors a vertical fault plane while the W phase nodal plane has a dip of 77°. Both solutions have similar rakes (217° and 213°) indicating predominant strike-slip motion with a significant dip-slip component consistent with regional transtensional tectonics (*Hauksson et al.*, 2011). The largest difference between both solutions is in the size of the CLVD component, the W phase solution has a 10% CLVD while the *fast*CMT solution has a 64% CLVD. This seems unrealistically large for a normal tectonic earthquake; nonetheless other MT solutions exhibit large CLVD components as well. The GCMT solution has CLVD of 52% for this event while the Southern California Seismic Network's solution has a CLVD of 76%. Furthermore, *Hauksson et al.* (2011) performed post-event W phase inversions and show that a large CLVD is required; in those inversions it ranges from 56% to 72%. Thus the real-time W phase estimate seems to under estimate the CLVD considerably while the *fast*CMT accurately assesses it for this particular event.

3.1.4 Implementation Issues and Necessary Improvements

Thus far we have shown with the two test cases that obtaining rapid moment tensor solutions and centroid locations from displacement waveforms is viable with our new technique. There are, however, a number of important issues that have to be addressed if *fast*CMT is to be implemented in real time.

A preliminary hypocentral determination needs to be made. In this discussion, because of the computational economy of the method where we can try thousands of different centroid locations and thus only a rough location estimate need be made, we opted for a self contained rapid method that does not incorporate outside data and centers the inversion grid around the first stations to detect anomalous motion. As *Crowell et al.* (2009) showed, one can determine

hypocenters with GPS. However given the greater sensitivity of traditional seismic instrumentation it would be more desirable to have weak motion and strong motion instrument based methods emit a trigger and compute a hypocenter. Provided of course this can be done before time t_1 when the final offset estimation is made, $\sim$3 minutes for the two events discussed above.

Another issue is whether to set the inversion nodes on a pre-defined set of fault surfaces, populate a rectangular prism of nodes around the hypocenter, or have a more complex geometry of inversion nodes. For strike-slip environments having a library of fault surfaces and setting the inversion nodes on known geological surfaces close to the epicenter might seem appealing. However experience has shown that moderate to large events can occur on unknown faults and with dip-slip or oblique mechanisms. A good example of this is the 1994 Mw 6.7 Northridge earthquake in southern California, which occurred on a previously unknown blind thrust fault. Thus, it may be more desirable to simply populate a prism of inversion nodes around the hypocenter.

For subduction zones it might be adequate to set the nodes on the plate interface. This would ensure correct centroid placement for traditional megathrust events, however outer rise, intraplate events on the overriding crust or in the downgoing slab, which can be sizable, may not be located properly. Evidently there are many ways to make these grids and the selected approach must be tailored to the observational goals of a particular network. To minimize assumptions we have adopted the simpler approach of defining a 3° by 3° grid based on the location of the first 5 GPS stations that detect the event.

The speed of the inversion, the number of inversion nodes and the coarseness of the grid is also an important consideration. Our inversion scheme is computationally efficient but the computing power required will depend on the number of inversion nodes. For reference each inversion using three component static offsets for 355 stations for the 2003 Tokachi-oki earthquake on one node every epoch takes about 75 ms, on an single 800 MHz CPU with 2 GB of RAM. This will improve significantly when translated into a real-time amenable language and distributed over a cluster.

Another important point is that a GF library and the selected velocity models must be constructed beforehand. Even though the functions are very succinct, because we can only accommodate one dimensional velocity structure, the region over which the algorithm will be implemented must be adequately parsed. That is to say, based on the location of the desired inversion node and the station a suitable velocity model must be determined. In this case because we already knew the region of interest we selected a known velocity model for that region and applied it to all station-event paths. Nevertheless when building a large GF database the most sensible way to do this would be to select the average velocity model for each station-event path from a community model such as the CVM4. Additionally, in the Tokachi-oki case we simply neglected stations that experienced telemetry outages and did not register data long enough to extract a reliable offset. In a real-time implementation this problem is easily solved by ignoring that station, should an outage occur, and removing it from the GF matrix.

Finally, in terms of epistemic error there seem to be two important issues to consider. Firstly whether neglecting fault finiteness has any impact on inversion results. *Adamová and Šílenỳ* (2010) found that neglecting fault finiteness in waveform inversions can lead to spuriously large non double-couple model parameters, however our Tokachi-oki inversion is almost pure double couple. Similarly the El Mayor-Cucapah result seems to require a large CLVD and that is most likely a real signal, thus it is not clear how large an error the point source assumption introduces in the inversions using static displacement data. Further on we will show the Tohoku-oki data set clearly violates this assumption although a point source model can still yield reasonable results.

The second important source of epsitemic error is the assumption of a 1D Earth structure. *Amoruso et al.* (2004) and *Hearn and Bürgmann* (2005) demonstrated the need for at least this simple approximation in inversions with coseismic offsets. *Hingee et al.* (2011) discuss both synthetic and observed results that indicate that waveform matching inversion techniques for MTs of medium sized events can be significantly affected by neglecting 3D variations in Earth structure. Nonetheless it is not clear in their results if the same is true for a method such as

the one presented here that employs only coseismic offsets. In any case, for the moment, it seems that for large events 1D structure will suffice for rapid results.

The most important implication of the work discussed thus far is the speed with which one can obtain basic earthquake source parameters. The algorithm presented here is amenable to real-time implementation and could potentially be performed on-the-fly as the data reach the processing facility and are processed for displacement (usually less than one second for real-time GPS networks) (*Bock et al.*, 2004; *Langbein and Bock*, 2004). In our two examples we were able to converge to a usable solution within 2-3 minutes of processed data becoming available. The access to near source real-time displacement records is invaluable as they can be used to quickly distinguish the salient features of large events. Furthermore, the method is computationally efficient; this has the benefit of allowing one to invert simultaneously for the centroid at multiple geographical test locations (inversion nodes) to determine which one is a better fit to the data and assign a centroid location.

For the larger 2003 Mw 8.3 Tokachi-oki earthquake, the method is very stable and provides a robust centroid location and focal mechanism estimate. This bears directly on the issue of tsunami early warning. Being able to have a reliable estimate of a thrust earthquake's magnitude and proximity to the trench within 2-3 minutes is invaluable. For example during the 2011 Mw 9.0 Tohoku-oki event small tsunami first arrivals at near source tide gauges were observed 10 minutes after origin time (*Hayashi et al.*, 2011) while peak tsunami height at the closest tide gauge to the source at Ofunato was registered 29 minutes after the origin time. The contribution of moment tensor inversions to tsunami modeling and warning will be poignantly demonstrated in Chapter 5.

From the basic moment tensor information one could go a step further in real-time modeling of the source. A full slip inversion using the coseismic offsets should be straight forward to determine (*Crowell et al.*, 2012). Indeed one can use the nodal planes from the moment tensor thus determined to define the slip plane. Further on in this chapter we will discuss strategies for doing this.

3.1.5 Violation of the Point Source Assumption, the M_w9 Tohoku-oki Earthquake

For the 2003 Mw 8.3 Tokachi-oki and 2010 Mw 7.2 El Mayor-Cucapah events the point source model works very well. However, when we apply the *fast*CMT method to the Mw 9.0 Tohoku-oki event serious problems arise.

The 2011 M_w 9.0 Tohoku-oki earthquake (*Simons et al.*, 2011; *Lay et al.*, 2011) generated a tsunami with inundation amplitudes as high as 40m resulting in over 15,000 casualties (*Mori et al.*, 2012). Sea floor geodetic and repeat multibeam bathymetry measurements suggest rupture extended from the hypocenter at 30km depth to the shallowest portions of the megathrust (*Hayashi et al.*, 2011; *Sato et al.*, 2011) all the way to the trench. Deep water drilling and borehole temperature anomaly measurements (*Fulton et al.*, 2013) support this and indicate that the earthquake ruptured a portion of the subduction zone usually considered to slip seismically (*Lay et al.*, 2012) perhaps as a result of dynamic weakening (*Noda and Lapusta*, 2013). The large extent of the rupture area, spanning about 350km along strike and 150km along dip and high slip (upwards of 50-60m) (*Lay et al.*, 2011) as well as the high density and variety of geophysical networks observing the event make it a benchmark test case for hazards algorithms.

We use data from 785 GEONET GPS stations throughout Honshu and Hokkaido Islands. We process the raw GPS data in a simulated real-time mode to estimate displacement waveforms using the method of instantaneous relative positioning as described in Chapter 2 and in *Crowell et al.* (2009). Here the network is subdivided using a Delaunay triangulation and the three baselines from each triangle are processed independently. For the network adjustment, station positions are referenced to GEONET station 0848 on the northern tip of Hokkaido Island, 900km northwest of the hypocenter.

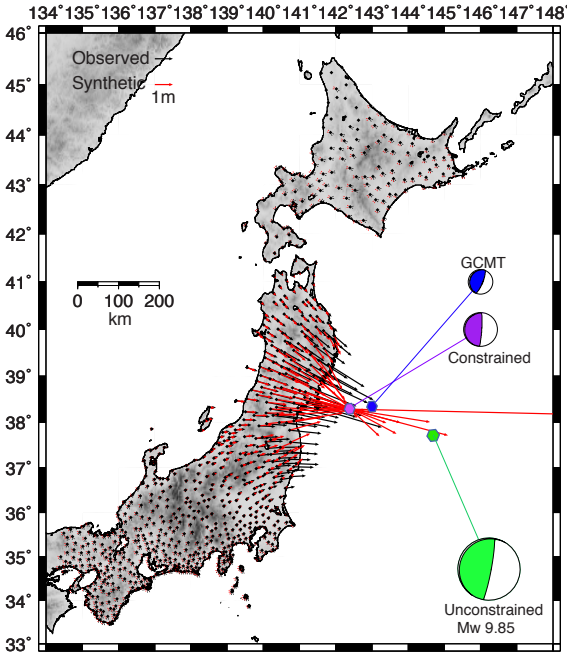
We then apply the CMT determination algorithm exactly as described in the previous section. Coseismic offsets are extracted from the time series at 157s after origin time using the trailing variance technique with the same detection parameters as for the Tokachi-oki and El Mayor-Cucuapah test cases. However, the grid search portion of the algorithm fails to locate the centroid correctly (Figure

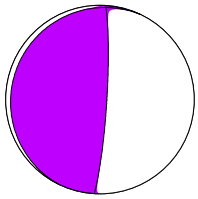
3.12) placing it more than 200km away from that computed by the GCMT project and outboard of the trench. Furthermore, the grid search moment tensor result has a moment magnitude of 9.85. Conceptually this can be understood by comparing this to the inversion result constrained to the USGS epicentral location (Figure 3.12). A point source solution tends to *focus* the coseismic vectors towards the centroid while a finite extent source will have a more *diffuse* coseismic pattern. Thus, the grid search tends to push the solution away from the earthquake in an attempt to find such a point source. The result is an overestimate of the moment (albeit with a good fit, 72%VR). It is interesting to note that forcing the solution to the epicenter produces a moment tensor that is a good representation of the source. The moment magnitude is 9.1, the strike and dip are very close to those from the Slab 1.0 model (*Hayes et al.*, 2012) and the rake angle indicates mostly thrust. However the variance reduction is only 0.6%. There is little use for a model that explains the data so poorly, even if in truth it is a good description of the actual source.

3.1.6 The Finite Extent CMT Approach

To account for source finiteness we extend the *fast*CMT algorithm to a linear geometry by superposition of point sources. This is straightforward because static deformation modeling has no temporal dependence. We invert for several moment tensors at predefined points along the line source, and perform a grid search for the proper line azimuth and spatial location. For the Tohoku-oki case we assume that the Green's functions are pre-determined at inversion nodes on a 0.1° by 0.1° by 2km in depth grid to cover all of Japan with the same strategy as originally described in Section 3.1.2. The line source length is set to 7° with 30 point sources. These numbers are for the time being arbitrary and upon implementation must be tailored according to the observational goals of a particular network. We then solve the minimization problem

$$\min \{\|\mathbf{WGm} - \mathbf{Wd}\| + \lambda\|\mathbf{Lm}\|\} \ , \tag{3.11}$$





fastCMT Event Report			
Event ID: 2011 Tohoku–oki			
Lat = 38.30	Lon = 142.37	Depth = 30 km	
Final Solution Time: 157s	Mw = 9.1		
Moment Tensor (Scale 1x10^22 Nm)			
Mrr = 1.089	Mtt = –0.003	Mpp = –1.086	
Mrt = 0.303	Mrp = 5.303	Mtp = –0.289	
Prinicpal Axes			
Axis	Value	Plunge	Azimuth
T	5.415	51	271
P	–5.444	39	96
B	0.029	2	4
Best Double Couple (Mo = 5.430e+22 Nm)			
Plane	Strike	Dip	Rake
NP1	205	6	112
NP2	3	84	88
Inversion Summary			
#Stations = 785	Var. Red. = 0.60%		

Figure 3.12: Result of the point source *fast*CMT method applied to the Mw 9.0 Tohoku-oki event. The green moment tensor labeled "unconstrained" is the result of the grid search. The purple is the result of containing the inversion to the USGS epicenter and blue is the GCMT result. The summary table is for the inversion constrained to the USGS epicenter. Note the low variance reduction of 0.6% in spite of the apparently good inversion parameters.

where as in Section 3.1 $\mathbf{m}$ is the source model, $\mathbf{G}$ the GFs, $\mathbf{W}$ the data weights determined from the variance of the pre-event noise, and $\mathbf{d}$ the coseismic offsets determined using the trailing variance technique. A major difference with the point source algorithm is that the multiple source inversion is ill-posed and requires regularization. We define $\mathbf{L}$ the smoothness matrix and λ the smoothing parameter. The inversion scheme is, again, L1-norm minimizing with first order Tikhonov smoothing for the five deviatoric MT components. This regularization is applied to each of the 5 components of the MT with regards to the same component of the neighboring MTs along the line direction. Thus sharp variations in a particular component of the MT between neighboring point sources are penalized.

To determine the line location and azimuth we invert for multiple combi-

nations of line geometries by varying the center of the line source, its azimuth and depth. The line source geometry that minimizes misfit in the L1 sense is the best solution. Because this inversion is computationally simple we can perform thousands of such inversions without a large computational overhead and without any assumptions required about the geometry of the source. The smoothing parameter λ determines the roughness of the model (*Hansen*, 2010) and thus controls the complexity of the inversion results. It is critical to have an objective way of determining the smoothing parameter so that no user interaction is required during an event. For this purpose we compute the tradeoff curves of data misfit $\|\mathbf{WGM} - \mathbf{Wd}\|$ versus model semi-norm $\|\mathbf{Lm}\|$ (L-curves) for a range of values of λ (Figure 3.13a) and their optimal corners from their point of maximum curvature (*Hansen et al.*, 2007; *Hansen*, 2010) for all possible source geometries. We then compute the probability density function (pdf) of all values (Figure 3.13b) of λ using the non-parametric kernel smoothing density estimate (*Bowman and Azzalini*, 1997). We select the mode of the resulting pdf as the preferred smoothing parameter λ^*. Then, we compare the misfit of all inversions at the λ^* optimum smoothing level and, as in the point source *fast*CMT method, select the one with the smallest misfit.

The final inversion yields a variance reduction of 84% with the GPS data alone and a slight improvement to 86% with the seismogeodetic displacement data. We contend that the marginal improvement with the seismogeodetic data is in part due to the one dimensional nature of the line source which does not account for along dip variations in moment release. As mentioned earlier the Kalman filter's most notable contribution to static modeling is that it better constraints the vertical offset. Later, when we discuss slip inversions we will show better control of the vertical yields improved resolution in the along dip direction. Since we have no such direction in the line source there is little improvment with the seismogeodetic derived coseismic offsets. Next, we compute the weighted average of all individual moment tensors over that line source based on their moment and place the average moment tensor at the location of mean moment release to obtain a single CMT estimate, shown in Figure 3.14. This implementation of the expanded *fast*CMT

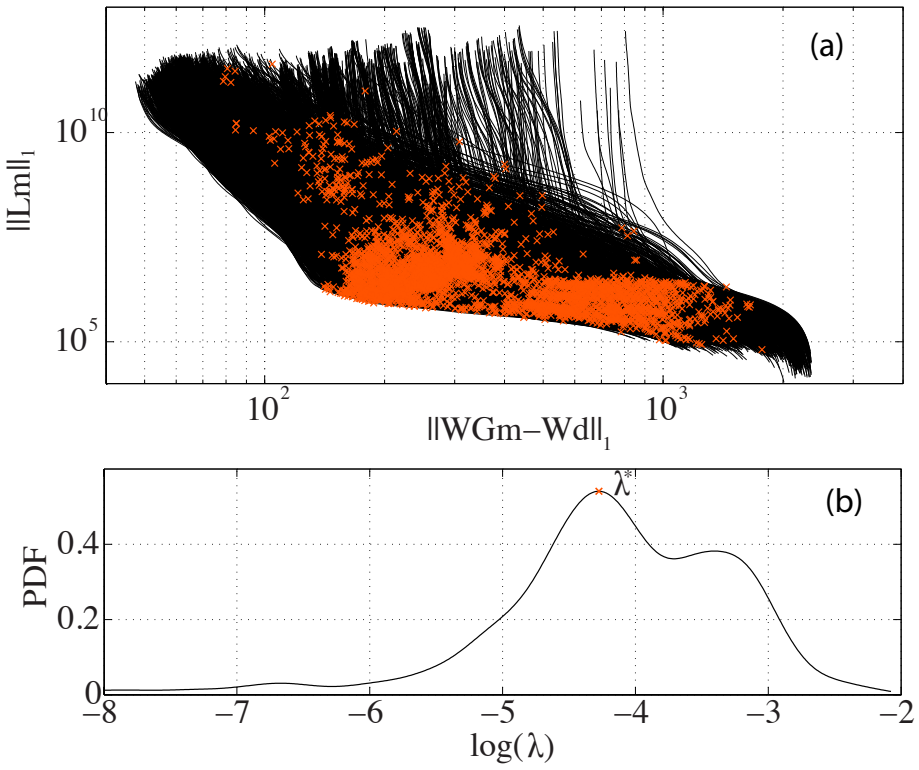


Figure 3.13: (a) 3800 L-curves for line source *fast*CMT inversions performed at different locations and with different orientations. Orange crosses depict the corners of each curve computed from the maximum curvature. (b) Probability density function of the smoothing parameter that corresponds to the L-curve corners. The optimum smoothing parameter λ^* is selected from the mode of the pdf.

is unique in that no a priori information is required on the fault geometry or that the source be confined to the slab. The process is computationally simple and automatable. For this earthquake we obtain a magnitude of 9.0, average strike, dip, and rake of 204°, 30°, and 95° respectively, with a source extent of 340 km along strike. A single line inversion takes 0.4s on a single 2.5GHz processor so the number of line sources computed in this process must be determined based on computational resources available. Also in Figure 3.14 is a static slip inversion obtained from inverting the seismogeodetic data, the details of this will be discussed further on, but note that the moment release of the line source bounds the main asperity in the slip inversion.

The finite extent moment tensor solution can be applied to smaller earth-

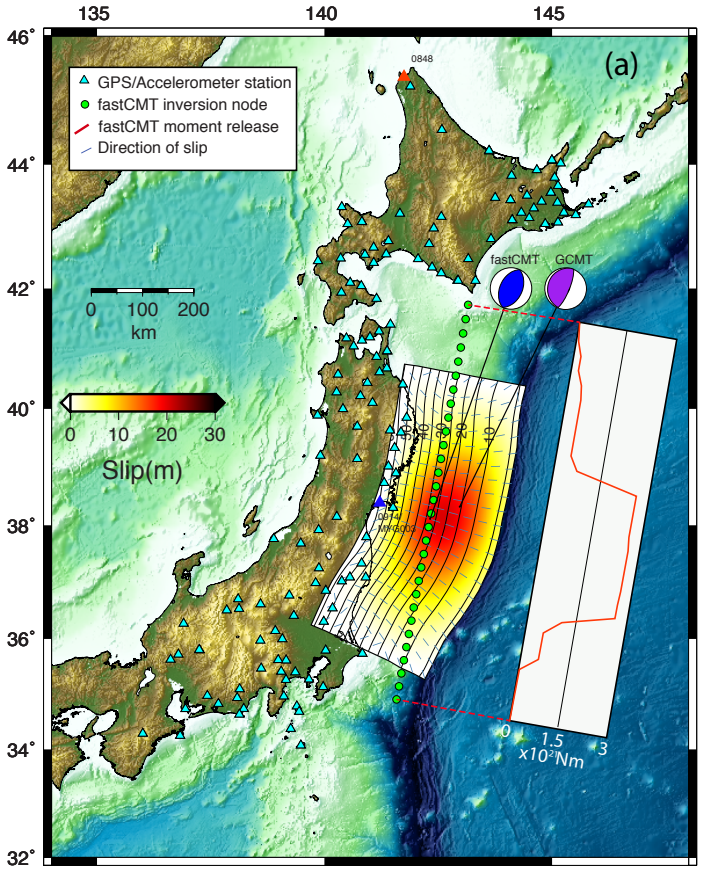


Figure 3.14: *fast*CMT and slip inversion results. Green circles are the point sources superimposed to compute the line source of CMT solutions, the final averaged solution shown labeled as fastCMT, and the Global CMT solution (GCMT) shown for comparison. The inset shows the moment release from the line source as a function of distance along fault. Shown along the fault interface with 10 km depth contours from the Slab 1.0 model (*Hayes et al.*, 2012) is the result of the slip inversion; the blue lines represent the direction of slip. The triangles indicate the locations of all the GPS/accelerometer stations used for computing the slip inversion. The large triangles represent the fixed GPS station (0848, red).

quakes, not just to the very large such as the Tohoku-oki event. Consider the case of the M7.2 El Mayor-Cucapah event, we employ the same data as was used in the point source inversion and compute the line source solution, Figure 3.15, shows the result. The line source extent parameters are kept the same as for the Tohoku-oki case, a 0.1° by 0.1° grid of GFs is computed surrounding the event with a 2km depth interval from 0 to 30km. The line source length is set once again to 7° with

30 point sources. The grid search result for the best fitting line is at 4km depth and its azimuth is close to the fault plane used by *Crowell et al.* (2012) for a static slip inversion, which is obtained from the aftershock distribution. Note the moment release of the line source solution brackets the slip inversion from *Crowell et al.* (2012). This illustrates that the *fast*CMT algorithm is useful, whether in its point source or line source mode for at least events between magnitudes 7 and 9.

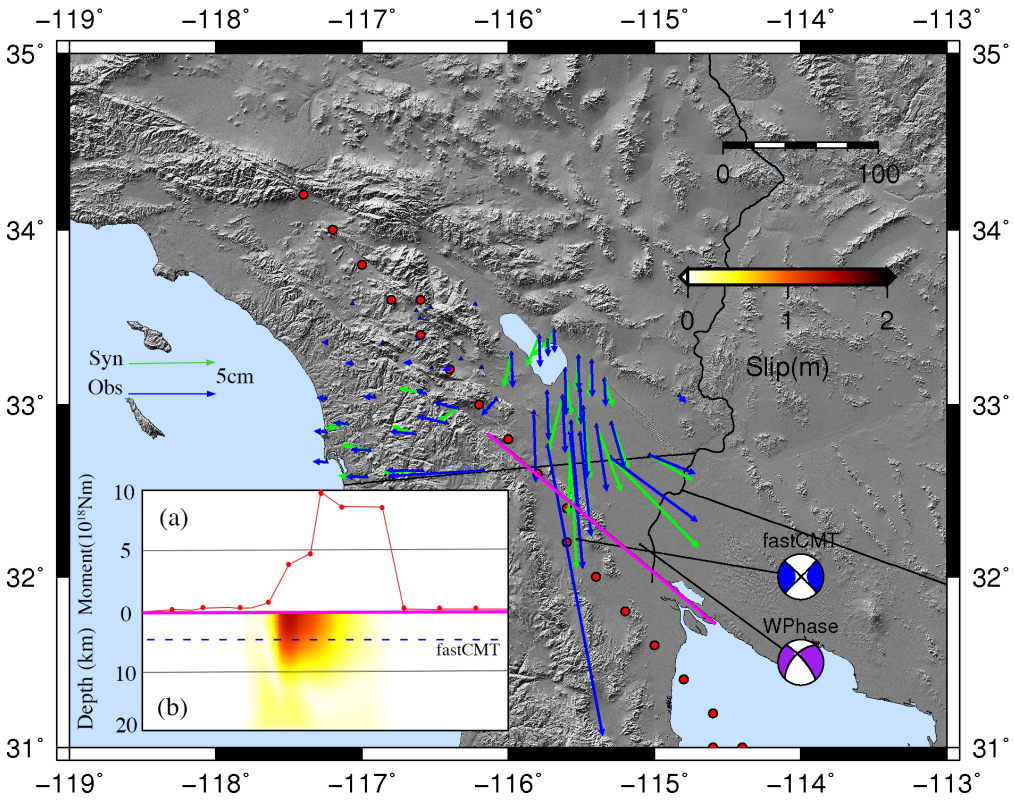


Figure 3.15: *fast*CMT and slip inversion results. Red circles are the point sources superimposed to compute the line source of CMT solutions, the final averaged solution shown labeled as fastCMT, and the USGS W-Phase solution shown for comparison. The inset (a) shows the moment release from the line source as a function of distance along fault. (b) is the slip inversion from *Crowell et al.* (2012) which uses the same GPS data as the moment tensor inversion. The blue dashed line shows tend depth of the *fast*CMT solution

3.2 Static Slip Inversions

After determining the style off faulting and the approximate geographical extent of rupture the next logical step is to perform a slip inversion with the static field data. We will not discuss this in great depth because it was thoroughly discussed in a previous dissertation (*Crowell*, 2013). However, we have expanded on the automatic determination of the regularization parameter and analyzed the benefits of inverting with the seismogeodetic as opposed to just the GPS data.

Modifications to the work of *Crowell* (2013) are best illustrated by analyzing the 2011 Tohoku-oki case. For a real-time implementable system one cannot simply assume that all large ruptures occur on the megathrust. Several recent event events illustrate this. The Mw 8.6 event in the Wharton Basin off Sumatra, Indonesia, on 11 April 2012 (*Satriano et al.*, 2012) was a predominantly a strike-slip event on the oceanic plate whose rupture arrested very close to the trench. The Mw 8.1 Samoa event on 29 September 2009 was a normal faulting, outer-rise type event that produced a sizeable tsunami with 189 fatalities (*Okal et al.*, 2010). Furthermore, the 2012-2013 Haida Gwaii and Craig events where a thrust and strike-slip earthquake a few months apart (*Lay et al.*, 2013) on the same oblique plate boundary. Subduction zones can and do produce many types of earthquakes. Thus it is critical to analyze the CMT information before computation of a slip inversion.

For the 2011 Tohoku-oki event, after receiving information on the style of faulting and the centroid from the *fast*CMT analysis and determining that it is a thrust event close to the slab, we invert for static slip using the same coseismic offsets and data weights. For the static slip inversion, we first locate the closest fault segment from the Slab1.0 model (*Hayes et al.*, 2012) to the line source. The fault is then subdivided into 25×25km segments. GFs are then computed for every subfault-station pair. We use Laplacian smoothness as $\mathbf{L}$ with the traditional $(1, 1, -4, 1, 1)$ finite difference stencil in Equation 3.11. As in the *fast*CMT solution, an optimal smoothing parameter λ^* is determined from the maximum curvature of the L-curve (Figure 3.16). We constrain the edges and bottom of the fault to zero to avoid non-physical slip distributions in the model (i.e., step-function

motion at the edges). The fault segments at the trench are left freely slipping to accommodate shallow slip. The inverse problem is solved by minimizing the L2-norm in Equation 3.11. This solution takes several seconds to complete after the extended CMT solution becomes available.

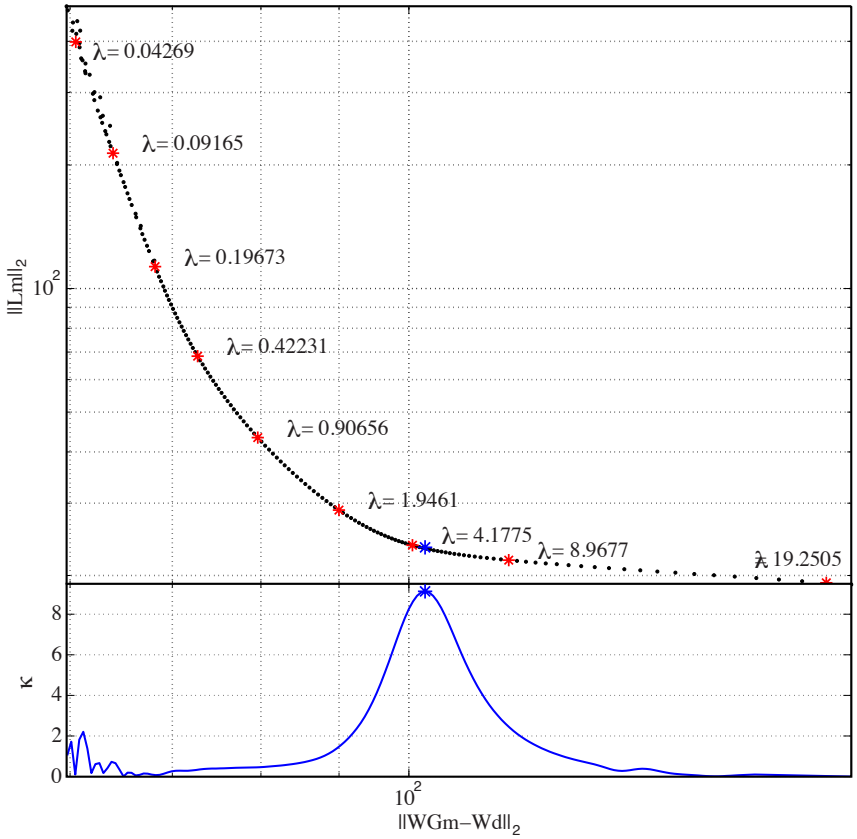


Figure 3.16: L-curve for the slip inversion plotting the model seminorm $\|\mathbf{Lm}\|_2$ versus model misfit $\|\mathbf{WGm} - \mathbf{Wd}\|_2$ with solutions at selected values of the smoothing parameter λ plotted as red stars. Also plotted is the curvature κ of the L-curve, the optimum smoothing parameter λ^* is selected as the value that corresponds to the maximum curvature (blue star).

Our model indicates a moment magnitude of 8.9, a slip patch that is roughly 340km along-strike and 155km along-dip, and maximum slip of 27m located near the center of the *fast*CMT location at 14km depth. We know now that in order to fit seafloor geodetic measurements of displacement outboard of the trench that were surveyed up to a month after the earthquake, static slip inversions with a maximum slip closer to 50m (*Sato et al.*, 2011) are necessary. However, seafloor geodetic

measurements are currently not available in real time and would include some amount of postseismic deformation, so our model is indicative of a realistic real-time scenario using just land-based seismogeodetic data. In Chapter 5 we will show that using cabled seafloor pressure gauge data and seismogeodetic offsets one can produce maximum slip of 62m. It is of course, possible to obtain models with higher amounts of slip by reducing the smoothing constraint, but these are not selected under the automated operator-independent L-curve criterion we present here. The moment release from the line source *fast*CMT overlain upon the slip distribution in Figure 3.14 shows the slip distribution is bounded by the line source moment release along strike, indicating that both methods independently agree on the spatial extent of slip. The dip of the *fast*CMT solution (30°) is larger than the average dip for the slab in the region ($\sim 15°$), possibly because of the unmolded along-dip dimension. This demonstrates the importance of having both the slip inversion and *fast*CMT to independently validate results and guide response. We also perform the slip inversion and *fast*CMT using just the GPS data for the same stations to investigate improvements with seismogeodetic data. We find that vertical bias (median difference of 18mm) in the GPS-only slip inversion solution leads to far more deep slip and significantly less shallow slip than the seismogeodetic solution (Figure 3.17) and a 4° difference in the average rake (84° for combined data and 88° for GPS-only data). This is due to the improved precision in the vertical offset estimates from seismogeodetic data and greater weights assigned to the improved vertical channel in the inversion, yielding better along-dip model resolution.

3.2.1 Timeline of Event Analysis

Based upon the aforementioned approach, we propose the following timeline of effective warnings for an augmented seismogeodetic earthquake early warning and rapid response system. Based on our experience with operational real-time networks in Western U.S. that employ a variety of communication links, raw data are continuously collected from the stations within a fraction of a second (*Bock et al.*, 2004), and seismogeodetic displacements and velocities are estimated continuously with a latency of about 1s. The origin time and hypocenter can be calculated

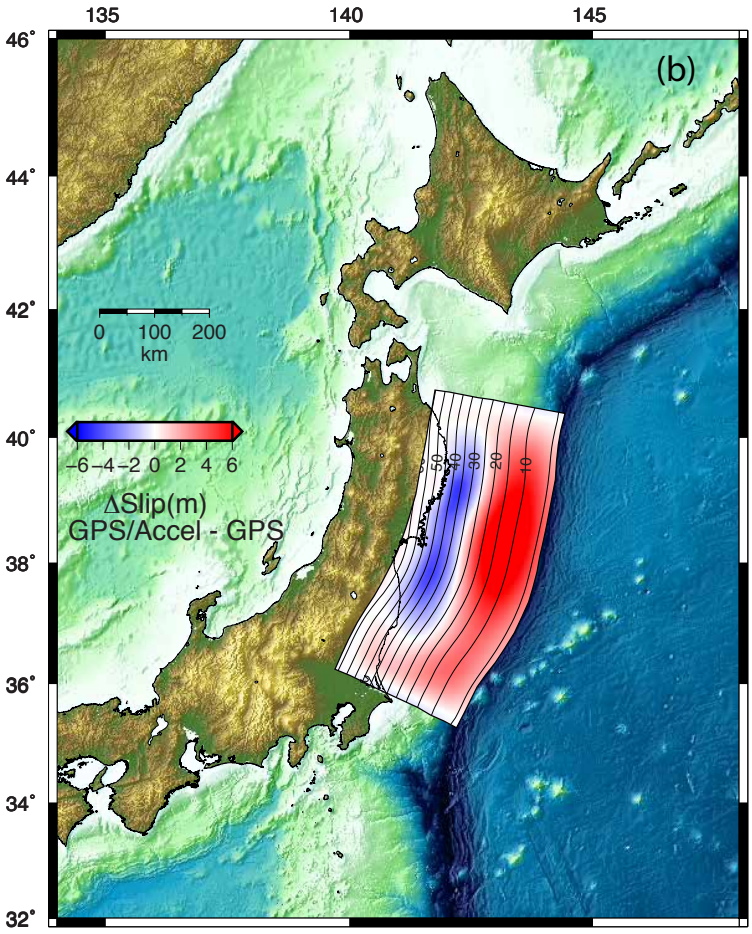


Figure 3.17: Difference between slip inversions computed using the improved precision GPS/accelerometer displacements vs. the inversion carried out using the GPS-only derived displacements. Red indicates more slip with the seismogeodetic solution and blue indicates more slip with the GPS-only solution.

from the first detections of P waves at a subset of seismic or seismogeodetic instruments using existing methodologies. For the Tohoku-oki data set, the time of arrival of P waves at the first stations is 24 seconds after earthquake initiation. Line-source CMT solutions are initiated based on the displacements exceeding a threshold (Section 3.1) and thus independently confirm, rather than rely on, the seismic network hypocenter. The line-source CMT solutions computed from the coseismic offsets by 157s after rupture initiation determine an initial magnitude, location and style of faulting, as well as provide rough constraints on the lateral extent of moment release; the duration of the Tohoku-oki earthquake rupture was

$\sim 180s$ (*Simons et al.*, 2011). From the line source CMT solutions, we are able to determine an appropriate section of fault to perform a heterogeneous static slip inversion. The slip inversion can run immediately after the CMT computation, so a full heterogeneous slip distribution is determined within seconds of the CMT solution. Model resolution in the along-dip direction is significantly improved with seismogeodetic offset estimates; this is critical for accurate tsunami modeling since it directly impacts vertical seafloor deformation estimates. After the slip inversion, obvious next steps would include ingestion into ShakeMap, PAGER maps, tsunami forward modeling to ascertain near-field inundation models (*Ohta et al.*, 2012), kinematic slip inversions, and further analysis to capture aftershocks and postseismic deformation.

This is all assuming satisfactory solution of an inverse problem. In any such problem the critical determination of the smoothing parameter typically requires operator decision-making. Here we have presented and implemented a simple algorithm that adds minimal computational overhead to guide the determination of this critical parameter that requires no human interaction and produces actionable models. In summary, the methods proposed here are computationally efficient and are able to be implemented in real time, with minimal prior assumptions.

3.3 Acknowledgments

For sections 3.1.1 to 3.1.4 The work was funded by NASA/AIST Grant No. NNX09AI67G and is published in **Melgar, D., Bock, Y., and Crowell, B.W., "Real-Time Centroid Moment Tensor Determination for Large Earthquakes from Local and Regional Displacement Records", *Geophys. J. Int.*, 188(2), 2012.**. Diego Melgar Moctezuma conceived this study, wrote the code and analyzed a large portion of the data. He was also the lead author and coordinated the manuscript preparation. For Sections 3.1.5-3.1.6 and 3.2 we would like to thank NIED for access to K-NET and KiK-net accelerometer data and GSI for GEONET GPS data. Suggestions provided by Rob Clayton, Sharon Kedar, and Tim Melbourne are appreciated. The work was funded by NASA Grants

NNX09AI67G, NNX12AK24G, and NNX12AN55H and SCEC award 12083. The work is published in **Melgar, D., Crowell, B.W., Bock, Y., and Haase, J.S, "Rapid modeling of the 2011 Mw 9.0 Tohoku-oki earthquake with seismogeodesy", *Geophys. Res. Lett*, 40(12), 2013**. Diego Melgar Moctezuma conceived this study, and analyzed a large portion of the data. He was also the lead author and coordinated the manuscript preparation.

Chapter 4

Kinematic Source Inversions

In Chapter 3 we discussed a framework for static slip inversions. Elaborating on the work of *Crowell et al.* (2012) we demonstrated it is possible to construct static models for large earthquakes objectively with minimal interaction from a human operator. Static dislocation models are limited in the sense that they provide only the total slip on the assumed rupture surface and provide no information on the time evolution of rupture. They are just a before and after snapshot of the event. They do not illuminate important kinematic parameters of the rupture process. How fast was the rupture? What is the shape of the source time function, both at individual sub-faults and for the earthquake as a whole? Answers to questions like these have important implications not only for hazards applications but to furthering our understanding of the physics that governs the rupture process.

4.1 Background

As instrumental seismology matured in the mid 20th century and observatory grade seismological stations and strong motion sensors proliferated it became possible to consider kinematic models of the earthquake source process. Perhaps the first successful macroscopic model, containing simple parameters, was the Haskell fault model (*Haskell*, 1964, 1969) which consisted of a rectangular fault with constant, unidirectional rupture velocity (a boxcar source time function). It successfully explained phenomena such as directivity and made predictions about

the shape of source spectra. This propagating dislocation model was successfully used to model data observed at only 80m from the fault trace of the 1966 Parkfield earthquake (*Aki*, 1968).

As systematic studies of source properties evolved it became apparent that large earthquakes had more complexity than a simple propagating line source with a prescribed rise time and rupture velocity and homogenous slip. Indeed it was clear that some events could only be modeled by relaxing these constraints. *Kanamori and Stewart* (1978) demonstrated that the far field body waves of the 1976 M_w7.6 Guatemala earthquake were best explained by superposition of ten sources, while *Trifunac* (1974) employed strong motion records of the 1971 M_w 6.6 San Fernando earthquake to solve the first heterogeneous slip inversion proper.

Following the 1979 M_w6.4 Imperial Valley earthquake, which was well recorded by numerous strong motion stations, there was renewed interest in an efficient way to parametrize the temporal and spatial variations of the source and invert for them. *Olson and Apsel* (1982) and *Hartzell and Heaton* (1983) introduced what is now known as the *multi-time window* method, whereby slip on a sub-fault is allowed to occur over contiguous time windows. In this way heterogeneities of the spatial and temporal behavior of the fault can be modeled.

Formally, an inversion problem for the time dependent slip of an earthquake can be set-up by discretizing an assumed fault surface into a grid of N sub-faults. Then, the response at a given station can be computed from

$$u(t) = \sum_{j=1}^{N} D_j[\cos(\lambda_j)G_j^{ss}(v_j,t) + \sin(\lambda_j)G_j^{ds}(v_j,t)]\dot{S}_j(t) \ , \tag{4.1}$$

where $u(t)$ is the displacement seismogram at a given station and D_j the dislocation amplitude at the j-th sub-fault. The dislocation is decomposed into its strike-slip (ss) and dip-slip (ds) contributions by taking the cosine and sine, respectively, of the rake angle λ. $G^{ss}(v,t)$ and $G^{ds}(v,t)$ are the dip-slip and strike-slip Green's functions which represent the response of a point, impulsive source. $\dot{S}(t)$ is the source time function which regulates the temporal dependence of moment release at a subfault. The Green's functions depend on the rupture velocity, v insofar as they need to be delayed by the time required for the rupture to propagate from

the hypocenter to each subfault. Evidently, if the timing of slip is considered an unknown quantity, then the general expression in Equation 4.1 is non-linear. Furthermore the source time function itself must be parametrized, the choice of such parametrization will also have an effect on the linearity of the problem.

The main difference in the approaches to the kinematic slip inversion problem is that of the assumption of linearity. To treat Equation 4.1 as linear one can assume a rupture speed and allow slip at each sub-fault to happen in one or many subsequent time windows following the main arrival of the rupture front (*Olson and Apsel*, 1982; *Hartzell and Heaton*, 1983). The source time function can be parametrized in a number of ways, usually overlapping triangles or boxcars, but is in general treated as being decomposed into basis functions (*Ide et al.*, 1996). In this way the inversion is linear and can be solved with any least squares algorithm. Typically a nonnegative least squares (NNLS) solver is employed (*Lawson and Hanson*, 1974) to prevent the direction of slip from reversing. In this inversion approach it is important to have sufficient time windows, or basis functions, to allow for some complexity in the time evolution of slip. If the parametrization is overly simple then unexpected errors can occur in the final result (*Hartzell and Langer*, 1993).

If the timing of slip is treated as an unknown quantity the non-linear inverse problem can be solved provided one assumes a parametrization of the source time function $\dot{S}$. In this approach the rupture is linear with regards to the amount of slip but non-linear with regards to its timing. Of benefit in this inversion scheme is that source time functions whose shape is based on rupture dynamics can be used. Examples of this can be found in *Beroza and Spudich* (1988) who use a source time function derived from dynamic crack propagation and *Ji et al.* (2003) who use a source time function that simulates a starting and stopping phase. Non-negativity can still be enforced in the non-linear case by employing an error function that grows asymptotically as slip approaches zero (*Yoshida and Koketsu*, 1990). These non-linear approaches however, use only one time window per subfault and cannot model complex source time histories. The importance of this remains unclear; there is uncertainty as to the robustness of complex source time functions obtained with

the linear method. *Ide* (2007) compared several linear and nonlinear inversions for the M_w7.6 Chi-Chi, Taiwan earthquake and found that while the gross features of slip are consistent there can be significant variations in the timing of slip. *Ide* (2007) also found that models that include geodetic data show improved consistency.

There is also a class of slip inversions that analyzes the data in the frequency domain. This has been a less popular but well studied approach. The first solutions in the frequency domain were reported by *Olson and Anderson* (1988) and *Cotton and Campillo* (1995). Later *Ji et al.* (2002a) proposed a more innovative approach by using wavelet analysis to quantify the contributions of finite frequency signals to the slip inversion. Both time domain and frequency domain methods rely on low pass filtered time series. That is, they depend on the long period component of the seismic record for the inversion. This is irrespective of the data type used and whether far field or near field seismograms are employed. The choice of data type can have an effect on the final model, furthermore, whether the time series are studied as velocity or displacement waveforms can also affect the inversion result (*Ide*, 2007). Velocity waveforms display higher levels of coherent short period waves, while displacement waveforms are dominated by long period energy. Due to this large suite of options available to the seismologist who wishes to study the time dependent behavior of earthquake rupture, there is still much heterogeneity in the results reported by independent research groups for any given earthquake. Nonetheless, kinematic inversion has become a routine analysis and important tool for the study of medium to large events.

For rapid response the USGS routinely produces automated slip inversions for large events using the wavelet method of *Ji et al.* (2002a) and relying on far field body and surface waves. These models are computed several hours after the event and are usually the first source of kinematic information about large events. Inversions with regional data are only performed in post processing. They typically rely on baseline corrected or high-pass filtered strong motion data. Recently, for example, *Suzuki et al.* (2011) inverted strong motion data from the M_w9 Tohoku-oki event using the multi-time window method. In that study the acceleration waveforms were integrated once to velocity and band-pass filtered between 100s

and 8s. The results show a smooth slip distribution with large slip near the trench. However, approaches such as this one for regional inversions are limited. Consider Figure 4.1 where we have applied a bandpass filter between 100s and 8s to the east component of station MYG011. This is the same procedure as that in *Suzuki et al.* (2011) (station MYG011 was used in that inversion). The figure shows the filtered accelerogram integrated to velocity and then displacement. Notice that the filtering operation has eliminated the static field and the integrated displacement waveform compares very poorly to the displacements directly estimated at the nearby GPS station. It is not mentioned in that study how the smoothing parameters were selected, but, it is difficult to consider a model which does not constrain the static field very well a robust one. It is still informative, but, for certain applications, such as tsunami modeling, of limited use.

An alternative approach is to directly invert high-rate GPS data. Given the problems with signal aliasing discussed in Chapter 2 and the elevated noise levels, especially in the vertical channel it is only advisable to invert the longer period portion of the GPS recording. For example *Yue and Lay* (2011) low-pass filtered GPS recordings of the Tohoku-oki event at 80mHz. This approach yields very smooth models which tend to be very similar to simple static models derived just from coseismic offsets. It is easy to understand why; at such long periods the largest signal in the time series is the coseismic ramp. Higher frequency waves are obscured and there is only limited information about the time dependent rupture process. Differentiating the GPS time series to velocity is not advisable because of the slow sampling rates and high noise.

The Kalman filter solution of GPS and strong motion data for reliable velocity and displacement waveforms presented in section Section 2.3.1 contains information across of a broad frequency range is well suited for kinematic inversion at regional distances, as we show here.

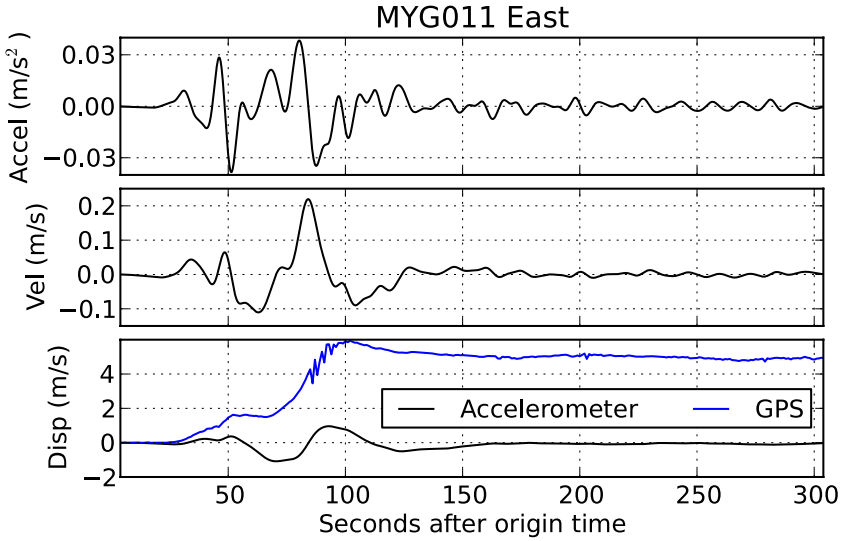


Figure 4.1: Results of bandpass filtering the accelerometer recording at station MYG011 and integrating it to velocity and displacement

4.2 The Inverse Problem

Throughout this chapter we will employ for our analysis the multi-time window method. Following *Ide et al.* (1996) we can consider the decomposition of the source time function at the j-th subfault into K basis functions

$$D_j \dot{S}_j(t) = \sum_{k=1}^{K} b_k \phi_k(t) \ , \tag{4.2}$$

where b_k is the expansion coefficient of the k-th basis function $\phi_k(t)$. In the multi-time window approach we consider overlapping basis functions with a simple geometry. Commonly used are b-splines with equally spaced knots which yield a simple isosceles triangle shape (*Ide et al.*, 1996; *Wu et al.*, 2001). One assumes a maximum rupture velocity v^{max} and delays the GFs depending on the distance to the hypocenter and this assumed rupture velocity. Then we allow slip to happen on any of a number of subsequent overlapping *windows* which are offset at regular time intervals, typically 50% of the of the rise time of the triangle basis function. In this way we have effectively linearized the problem by assuming known rupture times, while still allowing flexibility in the timing of slip by permitting dislocations at later times after the maximum rupture velocity time. The inverse problem will

now be a solution for the expansion coefficients b_k which represent the amplitude of each triangle source time function at each sub-fault for strike- and dip-slip motions yielding a total of $2KN$ model parameters.

Green's functions must be computed numerically. If one assumes Earth structure is a 1D layerered model then at regional distances (hundreds to a few thousand kilometers) GFs can be obtained by the frequency-wavenumber (fk) integration method (*Saikia*, 1994). Importantly, the fk method is capable of computing the ultra-long period band of the seismogram down to the zero frequency static offset (*Zhu and Rivera*, 2002). It can be employed to model strong motion displacement data from the seismogeodetic solution. Other approaches involve normal mode summation (*Yue and Lay*, 2011). Ideally it would be desirable to use three dimensional GFs for the inverse problem solution. This is a computationally intensive operation, sometimes prohibitively so. However, it is becoming prevalent to use fully 3D Earth models for forward computation of wave propagation (*Bielak et al.*, 2010; *Tromp et al.*, 2010). As our knowledge of Earth structure progresses it will become important to consider more complex velocity models. However, 3D velocity models only exist for a very small fraction of the Earth and while *Graves and Wald* (2001) and *Wald and Graves* (2001) demonstrated that 3D structure enhances model resolution, they also showed that this improvement is only possible with accurate 3D models. In fact they demonstrated that a well calibrated 1D model is preferable over an imprecise 3D Earth model.

Thus, with Green's functions in hand we can set up the traditional linear inverse problem, as in Chapter 3:

$$\mathbf{GM} = \mathbf{d} \, , \tag{4.3}$$

where the data column-vector $\mathbf{d}$ is the concatenation of observed seismograms at all stations, the GFs$\mathbf{G}$ are the motions at every station from every subfault for a triangle source time function of given rise-time and the model parameters $\mathbf{m}$ are the amplitude of the allowed source time functions at each sub-fault. As in the static case $\mathbf{G}$ is not full rank. Even though this is an over-determined problem the data are not always independent and parts of the model often cannot be resolved by the data. This rank deficiency produces a large condition number which

effectively yields extremely irregular models with sharp, unphysical variations between neighboring subfaults and overlapping time windows. Regularization must be employed; one popular form of regularization in slip inversions is to fix the total amount of seismic moment at a value suggested from other sources (*Ji et al.*, 2002b). However for our case we prefer that the moment be determined by the data themselves and we employ a spatial and a temporal regularization to resolve the rank deficiency. For the spatial regularization we use the Laplacian finite difference operator as in the static case of Chapter 3. We request that the sum of the slip of all windows at a given sub-fault be smooth in this sense. This penalty function is applied only to the total slip, not to the individual time windows. For a temporal regularization we apply a simple first derivative penalty function to each subfault's windows, such that sharp variations between the amplitudes of contiguous time-windows are possible but receives a larger penalty.

4.2.1 Spatial Regularization

For slip inversions we have relied on the finite difference Laplacian operator for spatial regularization. For static inversions in Chapter 3 we used the traditional 5 point stencil approximation to the Laplacian. At a given sub-fault (position i, j) the 4 neighboring sub-faults are used to compute the finite difference Laplacian of a given component of slip m_{ij} as

$$\nabla^2 m_{i,j} = \frac{-4m_{i,j} + m_{i+1,j} + m_{i-1,j} + m_{i,j+1} + m_{i,j-1}}{h} \,, \tag{4.4}$$

where h is the distance between the centers of the sub-faults. If this term is constant then it can be treated as unity. This formulation is easily derived by applying the second order accurate expressions for the second derivative in the along strike and along dip directions. The situation is illustrated schematically in Figure 4.2 and the computational molecule for a slip patch within the model is shown in Figure 4.3a A survey of the literature will reveal that seldom do authors indicate what course of action to take at the edges of the model. At the boundaries of the fault one can simply drop one term of Equation 4.4 (or two if you are at a corner). For example at the top edge of the fault model (Figure 4.2, position $i, 1$)

we would write

$$\nabla^2 m_{i,1} = 4m_{i,1} + m_{i+1,1} + m_{i-1,1} + m_{i,2} + 0 \ , \tag{4.5}$$

where we have set $m_{i,0} = 0$. This simplifies the computational molecule from 5 elements to 4 (Figure 4.3b). Indeed, this is equivalent to assuming that there exists a ghost cell $m_{i,0}$ beyond the edge of the fault model that has no slip. This is a reasonable assumption for a buried fault where slip must taper off towards the edges. This regularization, while not precluding slip at the fault boundary, will put a large penalty on it. Large slip at the edge will mean a large derivative and will be discouraged in the inversion

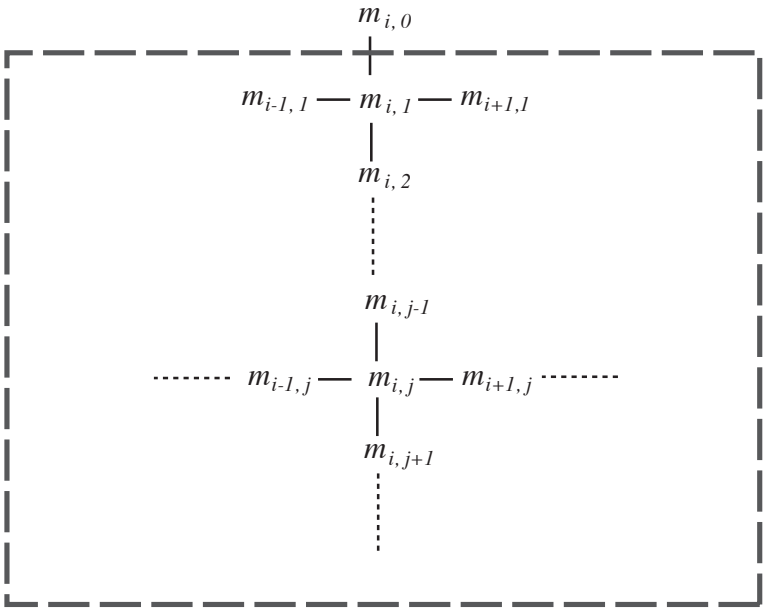


Figure 4.2: Stencil for finite difference Laplacian

This assumption is problematic for a subduction zone megathrust that extends all the way to the trench. The zero-slip boundary condition is unreasonable since large slip can and should be allowed to occur at the trench. In Chapter 3 we used this boundary condition for the static slip inversion. The result is a model that does not have large amounts of motion at the trench. In order to penalize slip at the top edge of the model less harshly the stencil must be modified. We

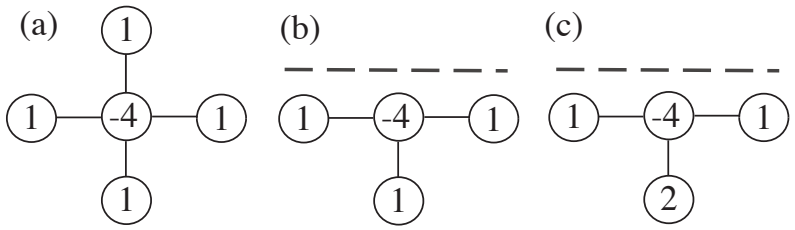


Figure 4.3: Computational molecules for the finite difference laplacian. (a) is somewhere within the fault model. (b) is for a zero-slip condition at the top edge and (c) is a free boundary condition at the top edge.

can instead require that the derivative of slip normal to the fault edge (in the dip direction, index j) be zero. If we approximate the first derivative by a second order accurate central difference then at the top edge we have the condition

$$\frac{dm_{i,1}}{dy} = m_{i,0} - m_{i,2} = 0 \ , \tag{4.6}$$

where once again we assume the spacing between subfault centers is unity. This free boundary condition means that $m_{i,0} = m_{i,2}$ and yields the expression for the Laplacian at the top edge

$$\nabla^2 m_{i,1} = 4m_{i,1} + m_{i+1,1} + m_{i-1,1} + 2m_{i,2} \ . \tag{4.7}$$

Once again we have a 4 point stencil but the computational molecule (Figure 4.3c) value for the along-dip element has changed from 1 to 2. It is a subtle modification but an important one if slip is to be allowed at the trench. Further on we will demonstrate the effect of this small change to the regularization matrix.

4.2.2 Bayesian Modeling

The spatial Laplacian regularization matrix $\mathbf{L}_s$ and the temporal first derivative regularization $\mathbf{L}_t$ are incorporated into the problem as

$$\begin{pmatrix} \mathbf{G} \\ \lambda_s \mathbf{L}_s \\ \lambda_t \mathbf{L}_t \end{pmatrix} \mathbf{m} = \begin{pmatrix} \mathbf{d} \\ \mathbf{0} \\ \mathbf{0} \end{pmatrix} \ . \tag{4.8}$$

This has the well known canonical solution (*Menke*, 2012)

$$\mathbf{m}^0 = (\mathbf{G}^\top\mathbf{G} + \lambda_s^2\mathbf{L}_s^\top\mathbf{L}_s + \lambda_t^2\mathbf{L}_t^\top\mathbf{L}_t)^{-1}\mathbf{G}^\top\mathbf{d}\ . \tag{4.9}$$

A known complication in this formulation is to objectively decide the values of the smoothing parameters λ_s and λ_t. In Chapter 3, where we have only a spatial regularization, we employed the L-curve curvature criterion (*Hansen et al.*, 2007). However such a heuristic criterion is somewhat tricky and quite cumbersome to apply in a two dimensional parameter space. Furthermore it is somewhat unsatisfactory in that it is not grounded in a strictly objective statement about source properties. Often when perusing the literature on slip inversions it is common to find statements that indicate that for a particular study the author used his or her judgment and intuition on the physics of an earthquake to decide on a regularization parameter. It is preferable to use a probabilistic formalism that can provide objective criteria for selection of the smoothing parameters of the slip inversion.

Following *Ide et al.* (1996) we can write the posterior likelihood function, a statement about the likelihood of the inversion result, as

$$p(\mathbf{d}|\mathbf{m};\sigma^2) = (2\pi\sigma^2)^{-Q/2}\exp\left[-\frac{1}{2\sigma^2}\|\mathbf{d}-\mathbf{G}\mathbf{m}\|^2\right]\ , \tag{4.10}$$

where Q is the number of data and σ^2 is the variance. Without any prior information maximization of this likelihood function will lead to the traditional normal equations (*Menke*, 2012). If however, we consider the regularization matrices as a form of prior information we can write the following probability density functions:

$$p(\mathbf{m}|\sigma_s^2) = (2\pi\sigma_s^2)^{-P_s/2}\|\Lambda_s\|^{1/2}\exp\left[-\frac{1}{2\sigma_s^2}\|\mathbf{L}_s\mathbf{m}\|^2\right]\ , \tag{4.11}$$

$$p(\mathbf{m}|\sigma_t^2) = (2\pi\sigma_t^2)^{-P_t/2}\|\Lambda_t\|^{1/2}\exp\left[-\frac{1}{2\sigma_t^2}\|\mathbf{L}_t\mathbf{m}\|^2\right]\ , \tag{4.12}$$

where σ_s^2 and σ_t^2 are hyper-parameters that represent the smoothing variance. P_s and P_t are the ranks of the two smoothing matrices and $\|\Lambda_s\|$ and $\|\Lambda_t\|$ are the absolute values of the product of the non-zero eigenvalues of the smoothing matrices. *Ide et al.* (1996) combined these two pdfs by simple multiplication. However *Fukahata et al.* (2003) subsequently showed that this produces a prior pdf whose integral is not unity and thus is improper. After introducing the correct

normalization, the prior pdf that combines both smoothing constraints can be expressed as

$$p(\mathbf{m}|\sigma_s^2,\sigma_t^2) = (2\pi)^{-M/2}\left\|\frac{1}{\sigma_s^2}\mathbf{L}_s + \frac{1}{\sigma_t^2}\mathbf{L}_t\right\|^{1/2} \exp\left[-\frac{1}{2\sigma_s^2}\|\mathbf{L}_s\mathbf{m}\|^2\right]\exp\left[-\frac{1}{2\sigma_t^2}\|\mathbf{L}_t\mathbf{m}\|^2\right] , \tag{4.13}$$

where M is the total number of model parameters. We can then use Bayes' theorem to define the posterior pdf of the model as

$$p(\mathbf{m};\sigma_s^2,\sigma_t^2,\sigma^2|\mathbf{d}) = Cp(\mathbf{d}|\mathbf{m};\sigma^2)p(\mathbf{m}|\sigma_s^2,\sigma_t^2) , \tag{4.14}$$

where C is a factor introduced to ensure the integral of the pdf is unity. It is, however, independent of the model parameters and hyper parameters and thus not necessary to compute. From this definition of the posterior pdf, *Jackson and Matsu'Ura* (1985) showed that the optimal model $\mathbf{m}^0$ obtained from maximizing the posterior pdf is exactly the damped least squares solution of Equation 4.9 where the ratio of the hyperparameters are actually the regularization parameters such that $\lambda_s = \sigma^2/\sigma_s^2$ and $\lambda_t = \sigma^2/\sigma_t^2$. The added benefit of taking the Bayesian approach to deriving the inverse solution is that we can use the posterior pdf to select the optimal regularization parameters.

Akaike (1980) proposed an information theory and entropy maximization based criterion, now known as the Akaike information criterion (ABIC) for selecting the adequate hyper-parameters. The parameter is obtained from the marginal likelihood as

$$\text{ABIC} = -2\ln\left[\int p(\mathbf{m};\sigma_s^2,\sigma_t^2,\sigma^2|\mathbf{d})d\mathbf{m}\right] , \tag{4.15}$$

thus the optimal model is the one which minimizes information loss and thus has the *smallest* value of ABIC. *Fukahata et al.* (2004) showed that the ABIC can then be expressed as

$$\text{ABIC}(\lambda_s^2,\lambda_t^2) = Q\ln s(\mathbf{m^0}) - \ln\|\lambda_s^2\mathbf{L}_s + \lambda_t^2\mathbf{L}_t\| + \ln\|\mathbf{G}^\top\mathbf{G} + \lambda_s^2\mathbf{L}_s + \lambda_t^2\mathbf{L}_t\| , \tag{4.16}$$

where $s(\mathbf{m})$ is the residual

$$s(\mathbf{m}) = \|\mathbf{d} - \mathbf{G}\mathbf{m}\|^2 + \lambda_s^2\|\mathbf{L}_s\mathbf{m}\| + \lambda_t^2\|\mathbf{L}_t\mathbf{m}\| \tag{4.17}$$

and the optimal model $\mathbf{m}^0$ is obtained from the damped solution in Equation 4.9. To use the ABIC to determine smoothing parameters we carry out inversions at several values of both smoothing parameters, for every result we compute the ABIC. The final model is obtained by selecting the smoothing parameter pair that produced the smallest value of ABIC. If the smoothing is too strong then the second and third terms in Equation 4.16 almost cancel each other, but the residual $s(\mathbf{m})$ is large and so is the ABIC. If the smoothing is weak then the residual is small but second term in Eqaution 4.16 is large and so is the ABIC. The minimum value of ABIC is somewhere between these two extremes and in a sense represents the tradeoff between he residual $s(\mathbf{m})$ and the condition number of the regularized matrix (*Ide*, 2007). This approach is a combination of traditional inversion with Bayesian modeling and has been employed by several researchers for kinematic inversions. It has been used, for example, to study the M_w 6.0 Kobe earthquake (*Sekiguchi et al.*, 2000) the M_w7.6 Chi-Chi earthquake (*Wu et al.*, 2001) and the M_w9.0 Tohoku-oki event (*Yoshida et al.*, 2011). A benefit of this Bayesian framework is that if the covariance matrix of the data, $\mathbf{C_d}$ is known (or assumed) we can compute the covariance of the model parameters as (*Yabuki and Matsu'Ura*, 1992; *Ide*, 2007)

$$\mathbf{C}_m = \sigma^2(\mathbf{G}^\top \mathbf{C}_d \mathbf{G} + \lambda_s^2 \mathbf{L}_s^\top \mathbf{L}_s + \mathbf{L}_t^\top \mathbf{L}_t)^{-1} \,, \tag{4.18}$$

where

$$\sigma^2 = \frac{s(\mathbf{m}^0)}{Q} \,. \tag{4.19}$$

This allows us to make statistical statements about the reliability of a given solution, something that is not straight forward for traditional high order Tikhonov regularized inverse solutions (*Aster et al.*, 2013).

4.3 An Example with Seismogeodetic Data, the 2011 M_w9 Tohoku-oki Earthquake

As discussed in Section 4.1, for inversion with regional data there are limitations to using just strong motion or high-rate GPS data. We will now demonstrate

the performance of the seismogeodetic data for a kinematic inversion of the Tohoku-oki event and argue that it produces a more robust solution than with either data set alone. We select 20 stations from the Kalman filtered dataset described in Chapter 2 and invert the three component displacements and velocities for a total of 120 waveforms. As mentioned in the previous section, displacement based inversions will be biased by the predominance of longer period data while velocity based inversions will provide higher frequency information. In order to obtain a model that is suitable across as broad a frequency range as possible we invert both displacement and velocity. The stations are selected to provide adequate coverage of the rupture area (Figure 4.4) while also taking into account the site conditions. For a static slip inversion the site response is not of great importance, so long as there is no ground failure, the coseismic offset will be largely independent of site response. However many of the GPS/accelerometer pairs belong to the Knet strong motion network which can often have significant site response (*Tsuda et al.*, 2006). Luckily, for every strong motion station in Japan there exists a soil profile (http://www.kyoshin.bosai.go.jp/). We ensured that all the selected sites for the inversion had a v_{s30} larger than 500m/s in order to avoid any site effects contaminating the inversion results. v_{s30}, the average shear wave speed in the top 30m below a station is a common parameter used to assess site conditions and distinguish between soft and hard rock sites. Of the 20 sites selected 6 belong to the KiKnet network and 14 to the Knet network.

The fault model (Figure 4.4) is the same as that of Chapter 3. It is a discretized version of the Slab 1.0 model of (*Hayes et al.*, 2012). It consists of 21 along strike and 9 down-dip 25×25km sub-faults (189 in total). We use a 1D layered model calibrated for Japan. The model, shown in Table 4.1, is used for automated computation of CMT's with long period data (*Fukuyama et al.*, 1998; *Tsuruoka et al.*, 2009). For the Green's functions calculation we use the fk code provided by (*Zhu and Rivera*, 2002) and compute GFs for every subfault/station pair from 0 to 0.5Hz. The data are lowpass filtered to 0.5Hz to match the GFs. We use triangular source-time functions with a 10s rise time. This choice is rather arbitrary and this is perhaps the most ad-hoc parameter in the process. However,

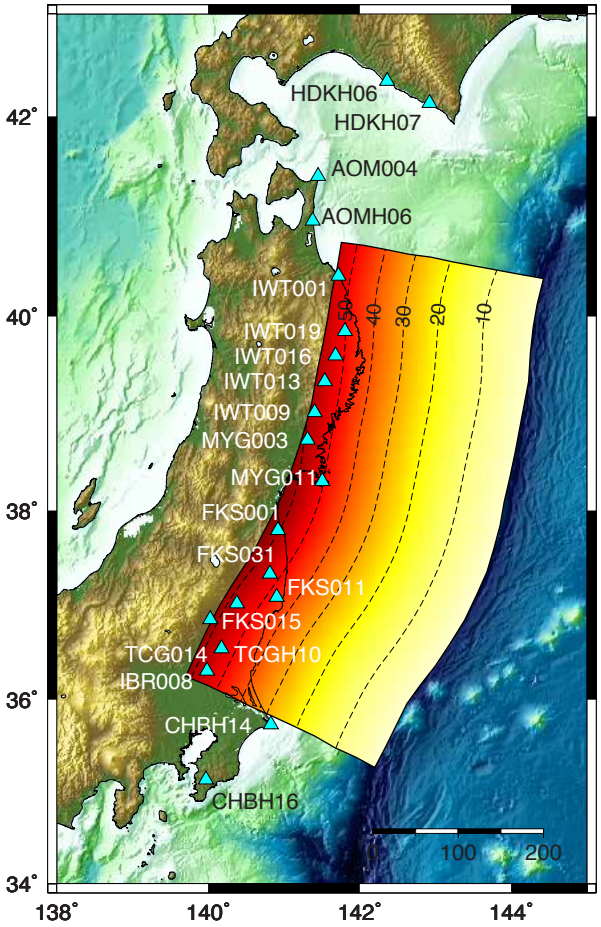


Figure 4.4: Map of 20 stations used in the seismogeodetic slip inversion. The slab geometry used for the inversion is the same as that of Chapter 3 from *Hayes et al.* (2012). The contours are depth to the slab in kilometers.

a rise time of 10s allows for the rupture front to traverse the subfault at a sensible velocity and is in broad agreement with the source-time function scaling laws of (*Tanioka and Ruff*, 1997). The maximum rupture velocity allowed is 3.5km/s which corresponds to 0.8 times the shear wave speed (0.8β) of the fastest layer spanned by the slab model (layer 4). We then allow slip on 20 subsequent 50% overlapping triangle source time functions with equal rise time (10s) yielding a total of 7560 model parameters. This parametrization allows each subfault to slip for a total of 105s. Recall that this does not mean that rupture speed is forced to 0.8β, rather that this is the fastest possible velocity in the model. In fact choosing instead

Table 4.1: Velocity model for the Tohoku-oki kinematic inversion

Layer	v_p (km/s)	v_s (km/s)	Density (kg/m^3)	Thickness (km)	Q_p	Q_s
1	5.50	3.14	2.30	3.0	600	300
2	6.00	3.55	2.40	15.0	600	300
3	6.70	3.83	2.80	15.0	600	300
4	7.80	4.46	3.20	67.0	600	300
Half-space	8.00	4.57	3.30	∞	600	300

a maximum rupture velocity of 0.9β or 4km/s has little effect on the inversion results. The model does not require earlier ruptures than the ones allowed by a 3.5km/s maximum velocity. Subsequently, the inversion is run using a NNLS solver to enforce positivity. To sample a large portion of the parameter space spanned by λ_s and λ_t we first invert on a coarse gird of smoothing parameters (between 10^{-5} and 10^2). A total of 64 different (λ_s, λ_t) pairs are used. We then refine the smoothing parameter grid twice more around the minimum ABIC inversion result to define the smoothing parameters that are used for final inversion. Furthermore, because the displacement time series are significantly larger in magnitude than the velocity time series (peak displacement is several meters, while peak velocity is tens of centimeters per second) it is necessary to weigh the data appropriately. We normalize both data sets and their corresponding GFs by dividing the waveforms by the norm of the concatenated vectors of waveforms. In this way we ensure that the inversion penalizes misfit to the displacements and velocities equally. If this weight is not applied the inversion will preferentially fit the displacement data.

4.3.1 Kinematic Inversion Results

Figure 4.5 shows the values of the ABIC for 100 inversions with different levels of regularization. As discussed we select the preferred values of λ_s and λ_t from the global minimum of that plot. The total slip from this preferred kinematic inversion is shown in Figure 4.6a and has a peak slip value of 52m on the shallowest subfault. Large slip, in excess of 20m happens on an asperity of about 300x150km up dip of the hypocenter at depths shallower than 20km. Slip at depth tapers of quickly but there is a large area of roughly 200x100km with more than 5-20m of

slip extending from a depth of about 50km up dip to the hypocenter. Figure4.6b is the source time function for the preferred model. Moment rate begins very slowly between 0 and 20s but increases sharply to its peak at 75s. Afterwards it decreases smoothly, the total duration of moment release is around 185s for this model. The total moment is 4.9×10^{22}N-m or M_w9.06.

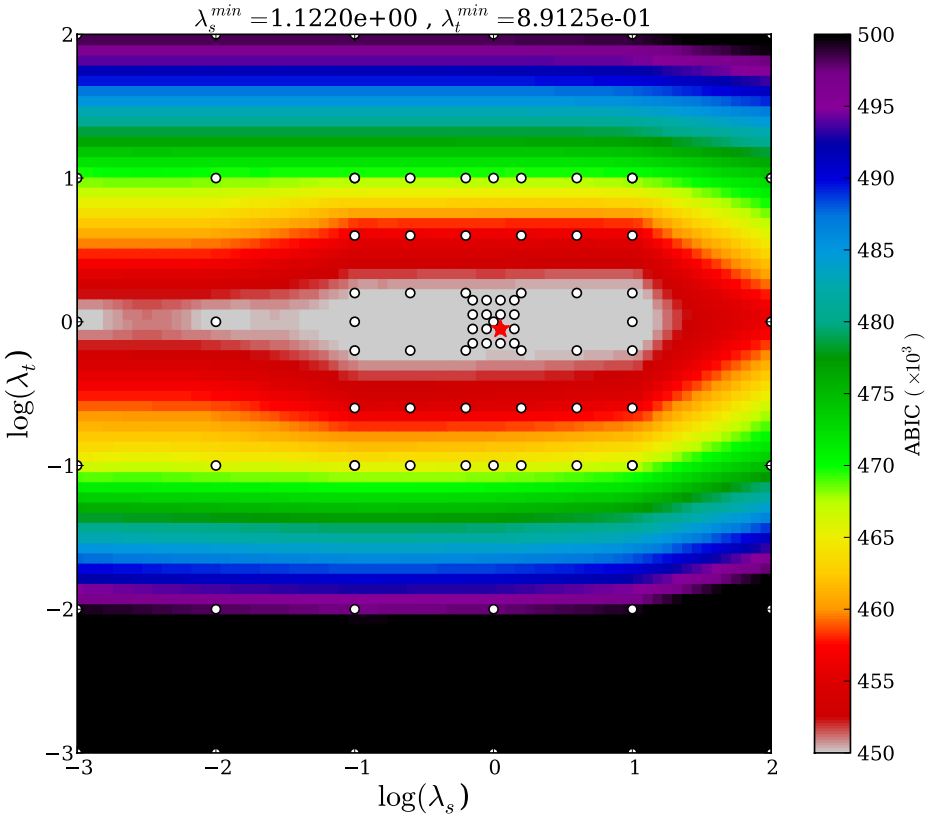


Figure 4.5: Values of ABIC for the kinematic inversion. The white dots are the values used for 100 inversions to determine the minimum ABIC. The red star is the minimum.

The fits to the data are shown in Figure 4.7 for the displacement time series and in Figure 4.8 for the velocity time series. Variance reduction is high for the displacements (90%) and somewhat lower (77%) for the velocity time series. The displacement times rise are mostly well modeled, the notable exception is in the two northern stations in Hokkaido island HDKH06 and HDKH07 were the amplitude of surface waves arriving between 200 and 300s are under-estimated. This is also true

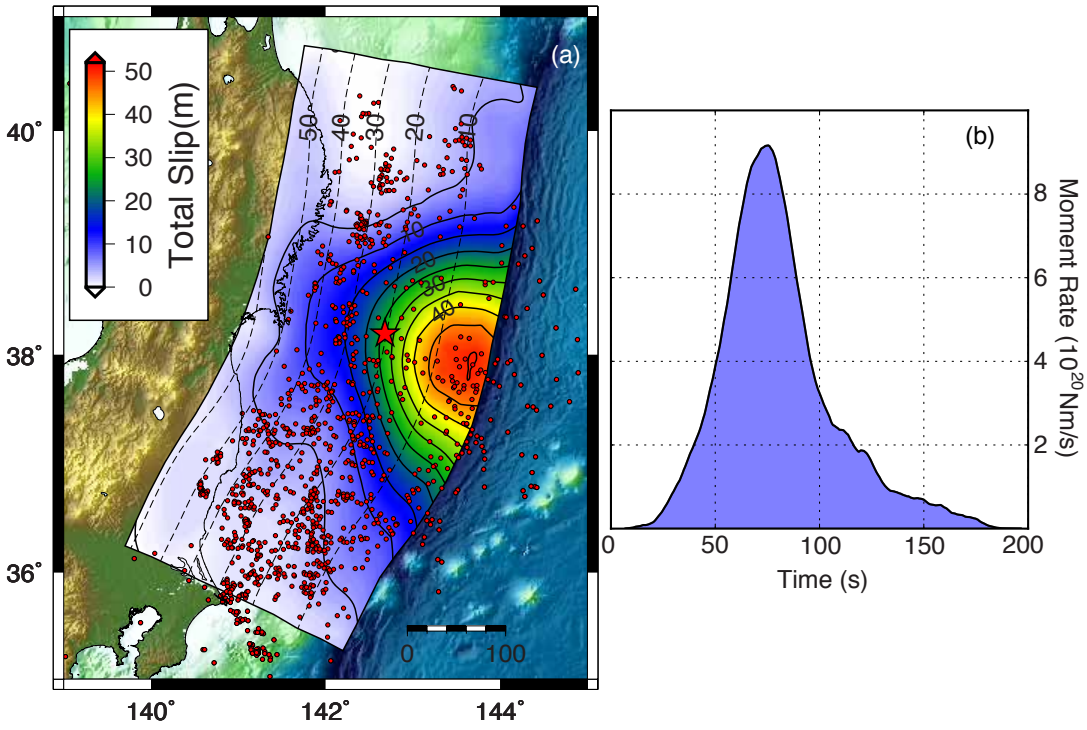


Figure 4.6: (a) Total slip from the kinematic inversion, peak slip is 52m. The red star is the epicenter and the red circles are two weeks of aftershocks from the NIED catalogue. Slip is contoured every 10m and the slab depths are contoured every 10km in dotted lines. (b) The source time function for the kinematic model.

for the velocity time series. However we also observe in the velocity time series an underestimation of the higher frequencies. This is obvious for example for stations TCGH10 and IBR008 both in the Kanto region and also for the northern stations in Aomori prefecture (AOM004 and AOMG06) and in Hokkaido island (HDKH06 and 07)

The time evolution of slip can be seen in Figure 4.9 where we present 10s snapshots of 160s of rupture. We have include 3 pseudo-rupture fronts in the plot that show the approximate distance a rupture from traveling at 1.5, 2.5 and 3.5km/s would have traveled. In agreement with the source time function of Figure 4.6b, the rupture starts slowly, propagating both up and down-dip. At around 30s the rupture accelerates up dip and expands along strike rapidly reaching peak slip at around 70s. Up dip there is slip of at least 10m on a segment of about 350km

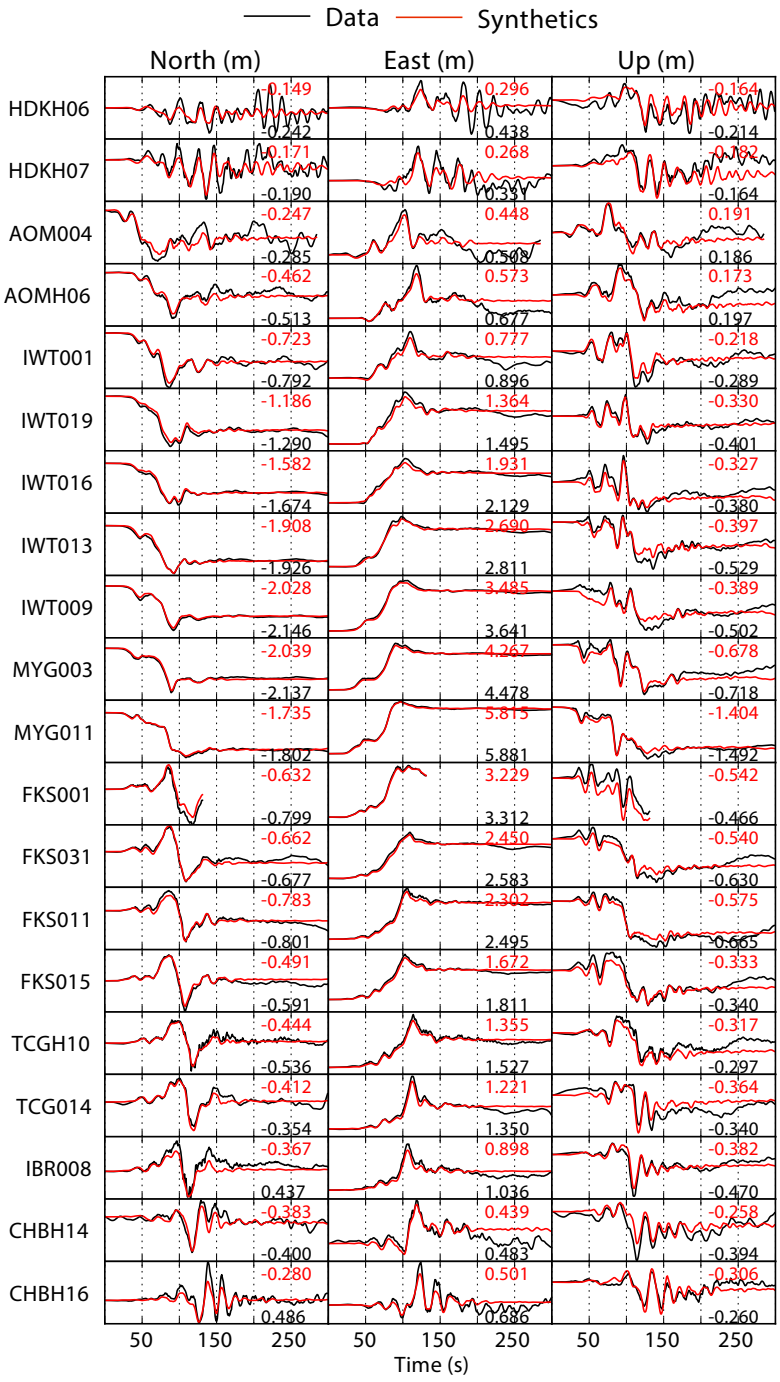


Figure 4.7: Comparison between observed (black) and synthetic (red) 3-component displacement time series. The stations are sorted by latitude from north to south (see Figure 4.4). The numbers next to the time series represent the value of peak displacement

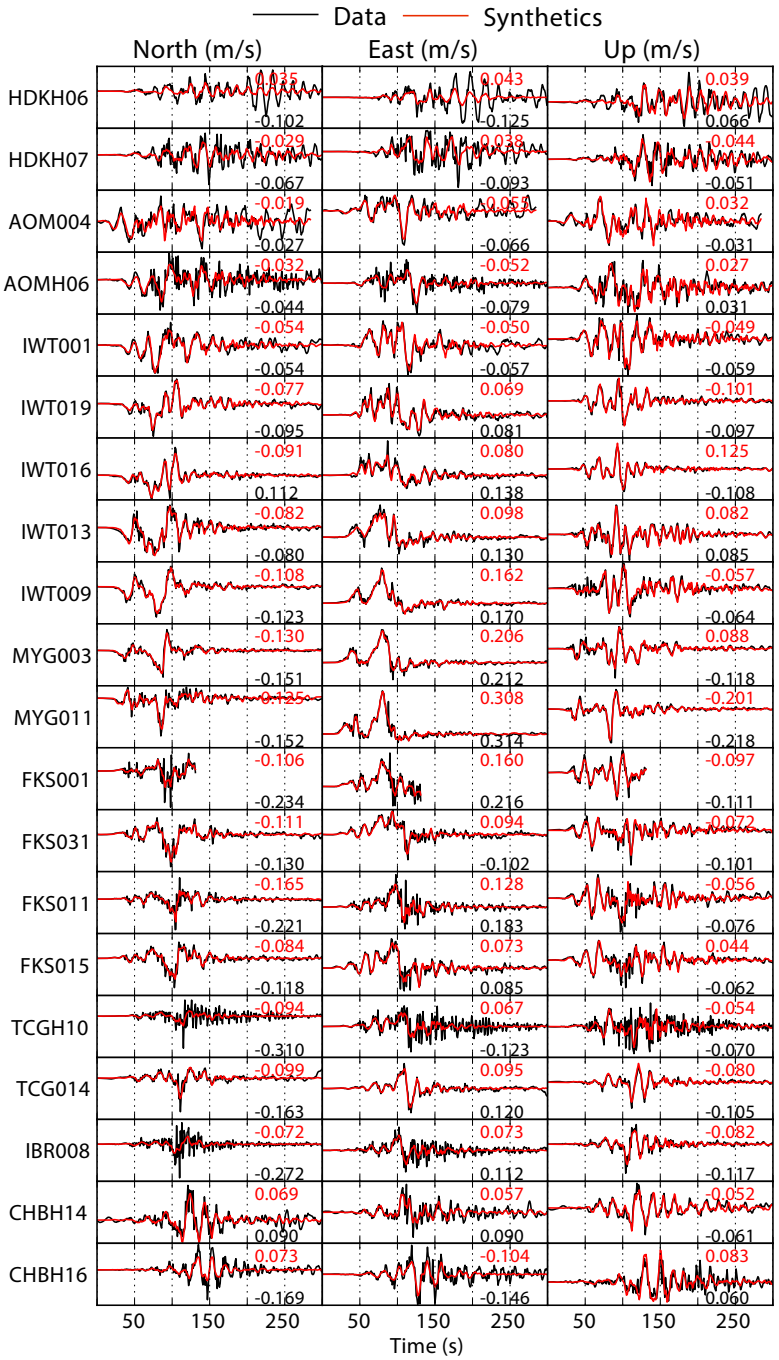


Figure 4.8: Comparison between observed (black) and synthetic (red) 3-component velocity time series. The stations are sorted by latitude from north to south (see Figure 4.4). The numbers next to the time series represent the value of peak velocity

in length. Down dip the behavior is very different. There is an initial slip pulse that propagates down from the hypocenter at around 2.5km/s until about 50s and to about 45km depth. This is followed by a second pulse of deep slip starting at about 60s that propagates down from the epicenter and then laterally, very quickly, mostly along-strike to the south. There is very little slip at depths larger than 50km.

Another way to examine the time dependent behavior of rupture is to study the individual source time functions (STFs) of each subfault. Figure 4.10 illustrates precisely this. Plotted is the moment rate for every subfault with their respective 90% confidence intervals (CIs). The white lines indicate the lower bounds of the 90% CIs and the grey hatched areas the upper bound of the CI. The STFs are colored by pseudo-rupture velocity. This coloring serves the same purpose as the pseudo rupture fronts in Figure 4.9. It indicates how fast a rupture front would have to travel to each that subfault at a particular instant in time. They are a visual aid to understand the changes in rupture speed in the model. We observe the same pattern as in Figure 4.9. Rupture begins slowly at first but accelerates up-dip reaching the the shallowest portions of the model at a pseudo velocity of around 3km/s and spreading along strike. Down dip there seem to be at least two pulses of slip, the second one indicating a very low initial rupture speed down dip from the hypocenter that spreads laterally quite quickly. The CI are a guide to avoid over-interpretation of the STFs. Another feature present in this plot is the duration of the source time functions. Up dip of the hypocenter rupture durations are long, usually 50s or longer while down dip the two pulses of slip are closer to 20s each. This makes the up dip STFs very smooth and the deeper ones very peaked suggesting a a depth dependence of the physical properties of the source.

4.3.2 The Effect of Spatial Regularization

In Section 4.2.1 we discussed modifications to the Laplacian smoothing kernel used for regularization. We argued that the traditional 5 point stencil would place a large penalty on slip at the trench and suggested a modification. A brief demonstration shows this is indeed justified. The model of Figures 4.6 and 4.10

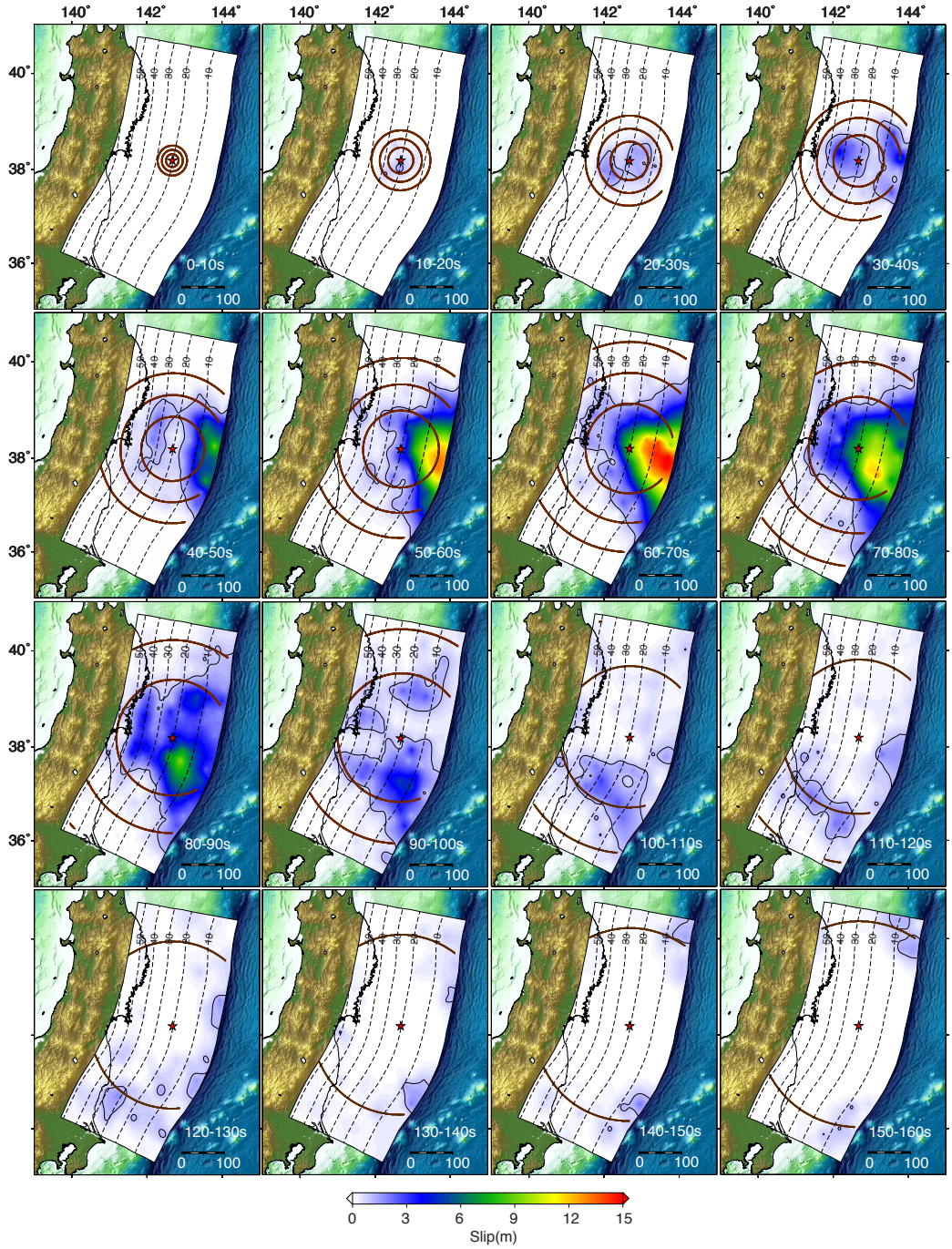


Figure 4.9: Snapshots of slip propagation in 10s increments, the red star is the epicenter and the black contour is the 1m of slip contour. The three brown concentric circles represent pseudo rupture fronts propagating at 1.5, 2.5 and 3.5 km/s respectively.

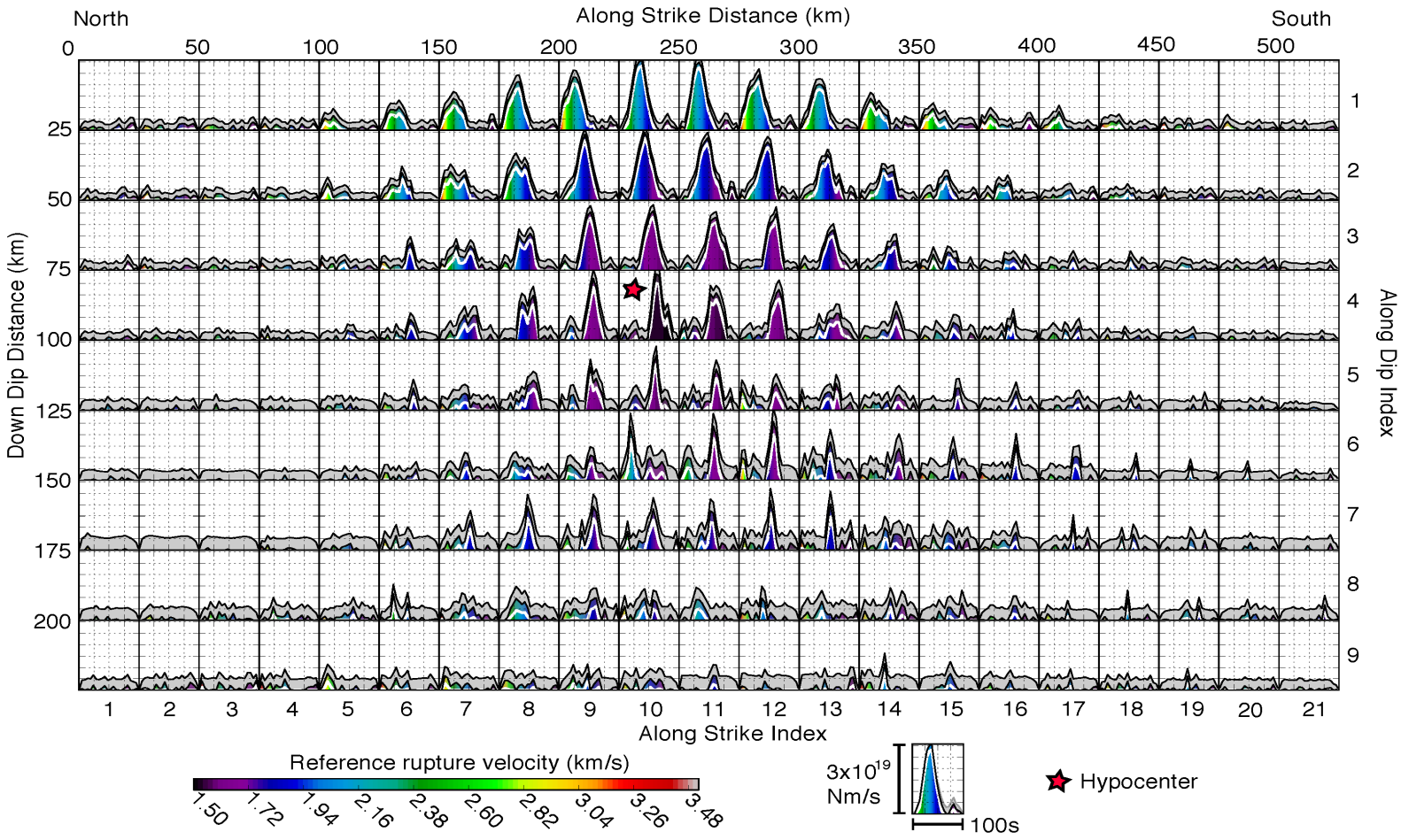


Figure 4.10: Subfault source-time functions (STFs). The 90% confidence intervals are indicated by the white line and the solid grey hatched area. The coloring under the STFs represents the pseudo rupture velocity. The red star indicates the hypocenter. All STFs are plotted at the same scale.

shows large slip and moment release in the shallowest parts of the fault. However, if we apply the traditional locked boundary condition we obtain the model shown in Figure 4.11. Total slip in this model is marginally larger (53m) than out preferred model while total moment is almost identical ($4.73 \times 10^{22} Nm$ or $Mw9.05$). However, peak slip is now at around 12km depth and slip at the trench is significantly smaller (25m or less) than that of the preferred model. External sources of information such as repeat multi beam surveys and seafloor geodesy(*Fujiwara et al.*, 2011; *Sato et al.*, 2011) as well as tsunami inversions and modeling from Chapter 5 show that large amounts of slip are needed at the trench. The model with the locked boundary condition is not a likely one for the Tohoku-oki source. As discussed, large slip is discouraged with the traditional Laplacian stencil.

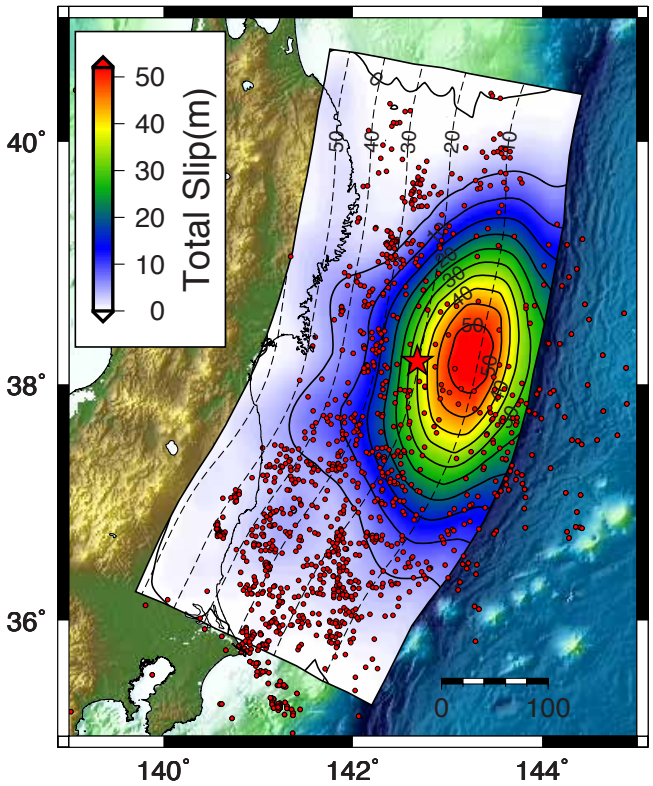


Figure 4.11: Total slip from the kinematic inversion with a locked boundary condition at the trench, peak slip is 53m. The red star is the epicenter and the red circles are two weeks of aftershocks from the NIED catalogue. Slip is contoured every 10m and the slab depths are contoured every 10km in dotted lines.

4.3.3 The Displacement-only Solution

We inverted for a kinematic model using only the seismogeodetic displacements. The total slip results are shown in Figure 4.12a. Slip is considerably larger (71m at the trench) while moment is 5.32×10^{19} or M_w9.08 only slightly larger than the combined displacement and velocity solution. The peak moment rate (Figure 4.12b is larger at $13\times10^{20}Nm/s$, almost 50% more than for the combined solution. Furthermore, while the duration of rupture is similar (180s) peak moment release occurs earlier (65s) than in the combined solution; the displacement only solution has very little moment after 140s. This is best seen in Figure 4.13 where the two STFs are plotted for comparison. The models are similar up to 50s, then the displacement-only model accelerates its moment release quickly to its peak, while the combined model shows a smoother evolution to peak moment release. After the peak, the ramp-down is similar for both events, but after 100s the displacement only model tapers off to low moment rates very quickly while the joint model continues to have significant moment release during the ramp-down. The longer source time function of the joint model is supported by almost all teleseismic inversions (*Shao et al.*, 2011), the low frequency back projection studies (*Kiser and Ishii*, 2012) and hybrid back-projection models that include depth phases (*Yagi et al.*, 2012).

Another view of the differences between the displacement-only and joint solutions can be seen in Figure 4.14 . Here we have plotted once more the individual source-time functions for each subfault. Significant differences can be seen. Notice that the scale is different between Figures 4.10 and 4.14. Peak moment rate is 3×10^{19}Nm/s in the joint solution and 5×10^{19}Nm/s in the displacement-only model. Broadly speaking the shapes of the STFs are similar but, in this solution, they are smoother than in the joint solution. There also seem to be some inconstancies in the timing of rupture. The shallow subfaults (row No.1) have a mixture of fast rupture along strike that has not been reported in other results. Specifically the subfaults at positions 4-6 and 14-17 favor a fast rupture of 3+km/s while the central one with the largest moment (Nos. 8-12) favor a slower rupture closer to 2.3 km/s. This behavior of subfaults favoring fast rupture surrounded by slower rupture subfaults

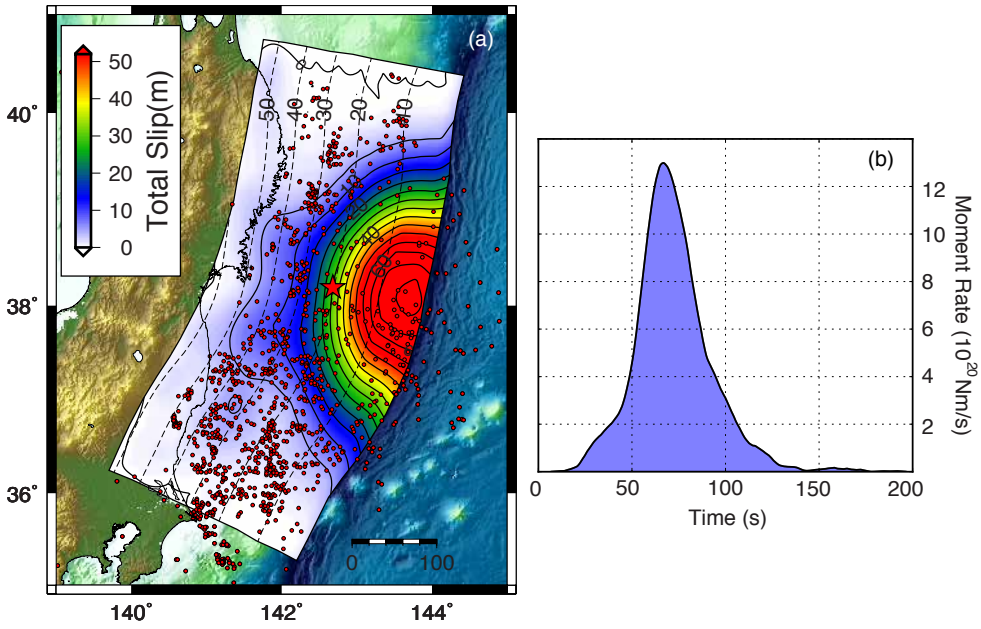


Figure 4.12: Total slip from the kinematic inversion with only seismogeodetic displacements, peak slip is 71m. we have retained the color scheme from Figure 4.6 to facilitate comparisons. The red star is the epicenter and the red circles are two weeks of aftershocks from the NIED catalogue. Slip is contoured every 10m and the slab depths are contoured every 10km in dotted lines.

is also seen in rows 4 and 5. Down-dip moment is also significantly smaller in the displacement only solution.

These observations, together with the longer total source time function of the joint model, suggest that the net effect of including the velocity time series is that they provide improved control on the timing of rupture. In this case, this has the secondary effect of reducing the peak slip from 71 to 52m with a minimal reduction in total moment. The displacement only solution from the Kalman filter still has significant detail and some of the broad features agree with the combined solution. This is important; models derived from low pass filtered GPS data alone (*Yue and Lay*, 2011) show much less detail in the subfault source-time functions. Furthermore they are fairly insensitive to rupture velocity. *Yue and Lay* (2011) showed that data fits to the GPS data were mostly unchanged when assuming maximum rupture velocities anywhere between 1.5 and 3km/s and even higher. This lead them to prefer a model with a maximum rupture speed of 1.5 km/s which

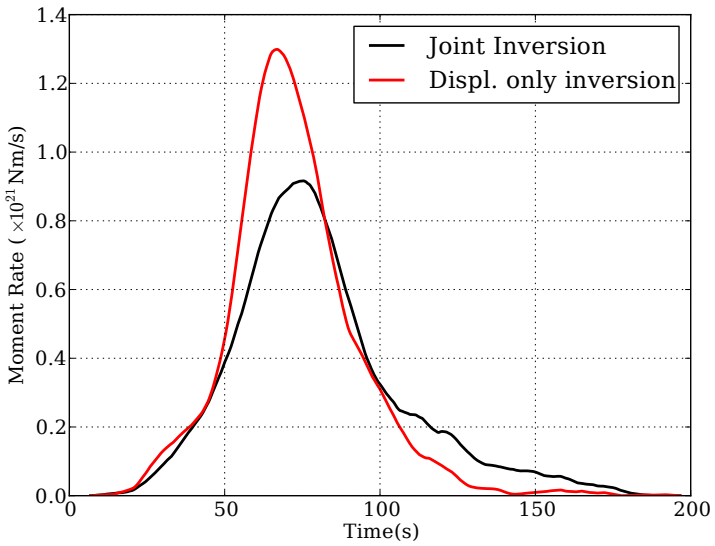


Figure 4.13: Comparison between the source time functions of the joint inversion of displacement and velocity data and the displacement-only solution

we now know from back projection studies (*Wang and Mori*, 2011; *Kiser and Ishii*, 2012) is adequate in the early stages of the rupture but far too slow for the whole event. In fact if we choose such a slow rupture velocity in our inversions the fits to the velocity waveforms are severely degraded. Again, the velocity data provide improved control on the timing of slip, but we recognize that the seismogeodetic displacement only results still provide a significant improvement over GPS-only solutions.

4.3.4 Implications of the Model

We have discussed at length the effect of adding the seismogeodetic time series to the inversion procedure; they provide better control on the timing of rupture. It is important as well to discuss the frequency limits of our inversion results which rely on data low pass filtered at 0.5Hz. Figure 4.15 shows the coherence between data and synthetics for the preferred model. Coherence is typically high at periods longer than 7-8s and lower at higher frequencies. However we still see bands of high coherence at higher frequencies in both the displacement and ve-

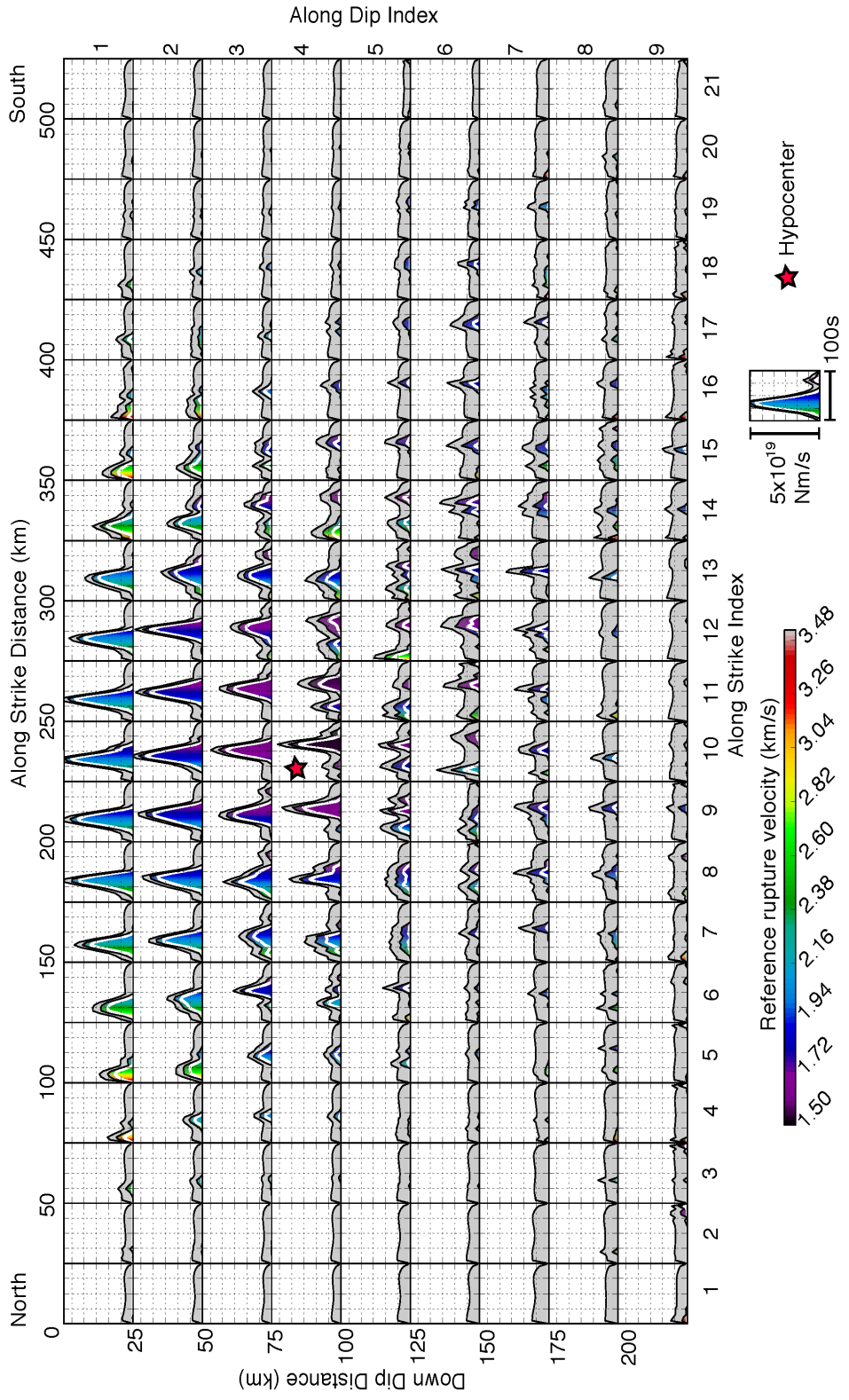


Figure 4.14: Subfault source-time functions (STFs) for the displacement-only solution. The 90% confidence intervals are indicated by the white line and the solid grey hatched area. The coloring under the STFs represents the pseudo rupture velocity. The red star indicates the hypocenter. All STFs are plotted at the same scale.

locity data. We attempted to invert data low pass filtered at 1Hz and found in general very low coherence at frequencies higher than 0.5Hz. It is quite likely that the degradation in the fits to the data at periods shorter than 7-8s is due to the large spatial discretization we have chosen as well as un-modeled Earth structure (*Graves and Wald*, 2001; *Wald and Graves*, 2001). One area of immediate improvement would be to use GFs for more realistic Earth models. These are not available everywhere. An interesting earthquake for such a study is the M_w7.2 El Mayor-Cucapah event in northern Baja California. There exists a good 3D model for the US portion of the Salton trough which is perhaps useful for such a computation.

The elevated coherence at higher frequencies does seem to indicate that inversion of seismogeodetic data is capable of modeling a broadband set of source features. Typically, back projection studies are conducted at frequencies higher than 0.5-1.0 Hz. For the 2011 Tohoku-oki event this was the case for the earlier studies (*Wang and Mori*, 2011; *Koper et al.*, 2011). While the model results shown here broadly agree with those high frequency source images, it is difficult to defend such an assertion given the different frequency ranges over which these studies image the source. There have been long period back projection studies, particularly *Kiser and Ishii* (2012) (0.05-0.5Hz) and *Yagi et al.* (2012) (0.1-0.5Hz) that we can compare our results against. The comparison shows good agreement, the hybrid back projection of *Yagi et al.* (2012) shows an initial up dip rupture speed of 3km/s which is similar to what we find. Down dip they image a fast (4km/s) pulse of slip followed by a slower one (1.5km/s) that then expands along strike, mostly to the south. Meanwhile *Kiser and Ishii* (2012) do not resolve the initial up-dip slip but do see the slow down dip pulse (0.8km/s) which then rapidly expands laterally to the south at (3.4km/s). We see similar features in our preferred model (Figures 4.9 and 4.10).

The model is also in agreement with longer period observations as well. Particularly with the teleseismic model of *Shao et al.* (2011) which uses the wavelet analysis technique of *Ji et al.* (2002a). Such a model assigns equal weights to all frequency components and is not biased by short period body waves or long period

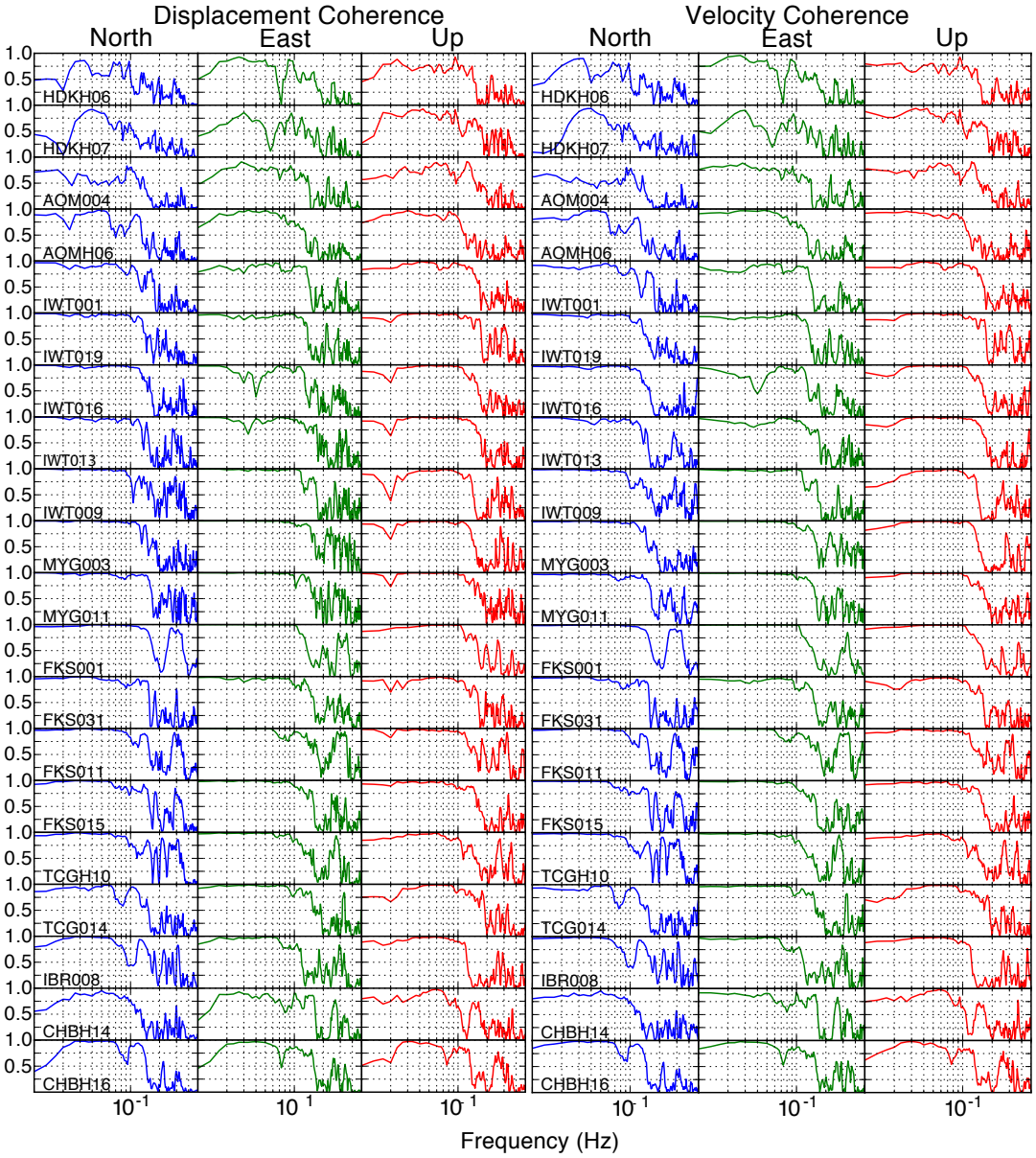


Figure 4.15: Coherence between 100s and 0.5Hz between observed and synthetic data for the joint inversion results. The stations are sorted from north to south (Figure 4.4)

surface waves, and is thus easier to compare against. The total slip is similar as is the time evolution of rupture. Additionally we are able to model large amounts of slip in the shallowest portion of the model in agreement with seafloor geodetic observations and repeat bathymetry (*Fujiwara et al.*, 2011; *Sato et al.*, 2011). This

suggests that the seismogeodetic inversion with displacement and velocity data provides a broadband image of the source, we can capture both the high frequency features of rupture and the longer period detail.

The preferred kinematic model shown in Figures 4.6 and 4.10 can be interpreted under the framework of the depth varying properties of subduction zone megathrusts (*Lay et al.*, 2012). The megathrust can be divided into 4 domains, domain A which extends from the trench to around 10-15km and experiences either aseismic stable sliding or large coseismic rupture during tsunami events. Domain B then extends down to around 35km and has large total slip while being relatively depleted of coherent high frequency radiation. Domain C extends from there down to 55km depth and usually has reduced amounts of slip but higher content of short period radiation. Domain D is the transition to stable sliding where slow slip and tremor tend to occur. This is a conceptual model and there is significant variability worldwide. The difference between domains B and C lies in that in Domain B are the shallow, large asperities while deeper in domain C there are only smaller asperities surrounded by conditionally stable material.

The reason for these differences is varied and disputed. Variations in geometry, mineral phases, fault roughness, pore fluids, thermodynamic conditions and rock types likely all contribute (*Heuret et al.*, 2011). However the conceptual model of (*Lay et al.*, 2012) indicates that whatever the cause, there should be observable differences in the behavior of the fault as depth increases and that the Tohoku event ruptured the three seismogenic domains (A-C). From our source model we can make some interesting observations about the rupture. It nucleates at 21km depth in domain B and after a modest initial phase produces large amounts of moment release in domain A in a steady, smooth fashion. There is evidence of a tsunami event, the 1896 Sanriku earthquake which ruptured the shallowest part of the northern half of the Tohoku-oki source region with about 6m of slip (*Tanioka and Sataka*, 1996). This is significantly smaller than the large slip (50m) we observe in our results. This indicates that the shallow domain A section must be capable of strain accumulation, if only slowly, and is not simply slipping aseismically. It is also possible that dynamic weakening can change the rate and state properties of

domain A (*Noda and Lapusta*, 2013) such that it can participate in coseismic rupture. This means that under certain conditions rupture from below can instigate shear failure in the usually creeping shallow section of the mega-thrust.

If the megathrust properties vary with depth then the nature of rupture should as well (*Lay et al.*, 2012). Indeed, we can observe such behavior in our model. Figure 4.16a shows the normalized multi-taper power spectral densities of the slip rate functions from Figure 4.10. We can see a marked difference between the shallow and deep slip rate spectra. Figure 4.16b shows the spectra stacked by the along-dip row number. It is clear that the shallow sub faults are depleted in short-period energy. High frequency radiation increases with depth. The confidence intervals on the source-time functions (Figure 4.10) imply that this interpretation must be taken with caution. Particularly for the deeper sub faults with smaller moment release. However, the slip model we have derived agrees well with modern conceptual frameworks of megathrust ruptures. The long, smooth, source time functions with large slip on the shallow parts of the fault could be related to slip on a low friction fault and fast, sharp slip of short duration at depth is likely related to brittle failure on a high friction fault (*Kanamori and Brodsky*, 2004). Initial results from deep drilled cores obtained by the JFast drilling project suggest a very low coefficient of friction in the shallow megathrust (*Fulton et al.*, 2013). The source models derived from seismogeodetic data are useful not only for rapid hazards applications (as discussed below) but are also suitable for detailed analyses of the earthquake source.

4.3.5 Suitability for Rapid Implementation

The issues facing real-time or rapid implementation of a kinematic inversion algorithm like the one discussed in this chapter are similar to those highlighted for the static case in Chapter 3. The style of faulting needs to be independently determined, this is paramount to selecting an adequate fault geometry for the slip inversion. The *fast*CMT moment tensor solution can be used; once thrust faulting is ascertained and its location placed close to the megathrust a precomputed slab model such as Slab 1.0 (*Hayes et al.*, 2012) can be employed. The spatial

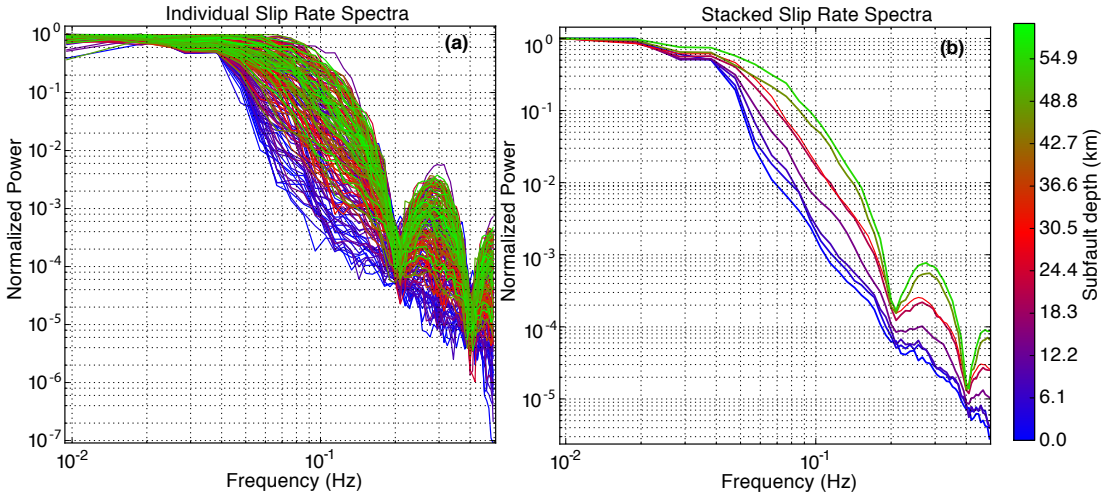


Figure 4.16: (a) Normalized power spectral densities for the slip rate functions of all sub faults shown in Figure 4.10.(b) Normalized stacked PSDs for the sub fault source time functions. The spectra are stacked per down-dip row of the model and the color corresponds to their average depth.

discretization should also be determined a priori. In our case we chose a rather coarse discretization out of a need to balance the computational cost of the inversions and the large extent of rupture. However with suitable parallelization one can envision a standard discretization of say 10km which could be used to model earthquakes from magnitudes 6.5 and above. The selection of a rise time is also somewhat arbitrary but with a rigorous analysis of the biases incurred by selecting a certain rise time, could be determined in a advance as well and used for earthquakes of varying magnitudes. In this approach the GFs would be precomputed before the event. Other approaches are possible of course; recall that the first limitation facing implementation of an automated slip inversion with regional data is the unreliability of strong motion data at long periods and the slow sampling rates and high noise levels of GPS data. The seismogeodetic approach overcomes these difficulties and allows the analyst to rely on the whole suite of source modeling methods discussed in Section 4.1. Non-linear inversions or wavelet based techniques can be utilized. Bayesian approaches that can determine the style of faulting as well as the geographic extent of rupture from measurements of the static field are appealing (*Minson et al.*, 2014). One can also then consider fully Bayesian

approaches to kinematic inversion (*Simons et al.*, 2011; *Minson et al.*, 2013). The advantage of these approaches is that regularization is unnecessary and it is easy to quantify the uncertainty of a given model. However, in order to obtain reliable posterior pdfs one needs to compute many thousands of forward models. For large parametrizations this is computationally expensive, perhaps prohibitively so and is often referred to as the curse of dimensionality. However, advances in the sampling algorithms are promising (*Minson et al.*, 2013) and research in this field is progressing rapidly.

The rapid kinematic models can also be used as as input or as a guide for higher level products. As we will show in Chapter 5 and as has been discussed recently (*Satake et al.*, 2013), kinematic models provide time varying deformation of bathymetry whose effect is important to capture the details of tsunami intensity and inundation patterns in the tsunami near-field. The models can also be used to improve rapid determinations of shaking intensity. *Kurahashi and Irikura* (2011) found 5 sources of strong ground motions during the 2011 Tohoku-oki event all located deeper than the hypocenter, one to the north and 4 to the south. They found the strong ground motions were generated by high frequency generating areas associated with large peak moment rates (perhaps breaking domain C of the megathrust). We observe similar features in the source time functions of Figure 4.10. There is a small section to the north and a larger one to the south, deeper than the hypocenter with large peak slip rate and short source time function duration. The frequency analyses of Figure 4.16 also support this. So perhaps models such as ours can be used for rapid intensity assessments. *Colombelli et al.* (2013) showed that simple static parameters derived from GPS such as rupture length provided a significant improvement over point source models in determining shaking intensities. They relied on the simple ground motion prediction equations (GMPEs) of *Boore et al.* (1997) and *Si and Midorikawa* (2000). However kinematic parameters such as directivity can be important for ground motion prediction (*Somerville et al.*, 1997). New generations of GMPEs are incorporating an increasingly large number of regression parameters (*Bozorgnia et al.*, 2014; *Gregor et al.*, 2014) and the use of the ambient noise field can provide GMPE parameters in areas not cov-

ered by the current catalogues of events (*Denolle et al.*, 2013, 2014). An exciting area of research will be to consider how to employ rapid kinematic models with these new advances to better determine shaking intensities immediately after large events.

4.4 Acknowledgements

The research contained in this chapter is previously unpublished. We'd like to thank Douglas Dreger, Thomas O'Toole, Fabrizio Romano and Gavin Hayes for helpful discussions on kinematic slip inversion and the Slab 1.0 model. This research was funded by the NASA Earth and Space Science Fellowship NNX12AN55H, and NASA AIST-11 NNX09AI67G and ROSES NNX12AK24G as well as Southern California Earthquake Center (SCEC), University of Southern California Subaward No. Y86564, awarded under the prime NSF Award No. EAR1033462 (funding also provided by USGS and cost sharing from Scripps Institution of Oceanography Earth Science Division and the Cecil H. and Ida M. Green Foundation) We extend our thanks to the Japanese Meteorological Agency for access to accelerometer and the Geospatial Information Authority for access to GPS data.

Chapter 5

Offshore Data and Tsunami Modeling

The rapid estimation of realistic tsunami models along the coast immediately adjacent to large earthquakes (the "near-field" or "near-source" region) continues to be a pressing problem for tsunami warning, as the number of people and infrastructure located in areas of tsunami hazard grows (*Basher*, 2006). Tsunamigenic earthquakes in the last decade have had catastrophic consequences with a large loss of life and impact on the built and natural environments. Most notably the 2004 Mw 9.2 Sumatra-Andaman event (*Ammon et al.*, 2005; *Ishii et al.*, 2005; *Lay et al.*, 2005; *Stein and Okal*, 2005; *Subarya et al.*, 2006) resulted in over 250,000 casualties, the majority of them on the nearby Sumatra mainland, with run-up heights of up to 30m (*Paris et al.*, 2007). The Mw 8.8 2010 Maule earthquake in Chile (*Lay et al.*, 2010; *Delouis et al.*, 2010) resulted in 124 tsunami related fatalities and run-up heights as high as 15-30m in the near-source coast (*Fritz et al.*, 2011). The 2011 Mw 9.0 Tohoku-oki earthquake (*Simons et al.*, 2011; *Lay and Kanamori*, 2011) generated a tsunami with inundation amplitudes as high as 40m resulting in over 15,000 casualties (*Mori et al.*, 2012) and was the first case of a large tsunami impinging upon a heavily developed and industrialized coastline in modern times. Tsunami induced damage was heavy on port infrastructure, major roadways and railways were severed, energy generating power stations (in particular, nuclear power) were forced offline for extended periods of time, defense

infrastructure was compromised, and telecommunications were impeded as well as destruction of countless homes, offices and other industries. In addition to the tragic loss of life the economic collapse of the near-source coastline, which spans nearly 400km, was almost complete (*Hayashi*, 2012). Throughout this chapter we will focus on how the techniques developed in Chapters 3 and 4 to rapidly image the earthquake source can be utilized to forecast tsunami intensity. Furthermore, we will demonstrate that land-based sensors alone provide only limited forecasts and that utilizing ocean-based measurements in the source estimation process greatly improves estimates of the earthquake source as well as tsunami forecasting and modeling.

5.1 Background

Japan possesses the only fully operational tsunami early warning system (TEW) worldwide capable of delivering alerts in the near-source coastline as well as numerous defenses against tsunami attack such as seawalls. The Tohoku-oki event demonstrated that early warning must be complemented with a comprehensive understanding of regional hazards and a prepared response in order to have the greatest impact. It also underscored some significant limitations of existing TEW methods, particularly in the near-field. Currently, operating algorithms to rapidly estimate tsunami intensity can be broadly divided into two classes: (i) those that use rapid estimates of simple earthquake source parameters like epicenter and magnitude, derived from land-based sensors, to guide warning and (ii) those that use direct measurements of sea-surface disturbances from ocean-based sensors to assess the intensity of an event without the need to characterize the earthquake source. The system of the Japanese Meteorological Authority (JMA) (*Tatehata*, 1997) is of the first kind; rapid determination of magnitude and event location from seismological measurements is used to seed a database query of pre-computed scenarios. These scenarios, determined well in advance of an event, are earthquakes of different magnitudes and locations that are used offline as initial conditions to produce simulations of tsunami propagation and metrics of inundation intensity

at points along the Japanese coastline. Thus, when an earthquake strikes, from its rapidly determined magnitude and location the most appropriate scenario is extracted from the database and used to guide the warning.

During the Tohoku-oki earthquake, early estimates of earthquake magnitude from JMA were too low by 1-2 orders of magnitude; an estimate of Mw 7.2 was determined after 30s and revised to Mw 8.0 by 107s (*Hoshiba et al.*, 2011). It took 20 minutes for a reliable estimate of magnitude to be made teleseismically through the W phase method (*Duputel et al.*, 2011; *Hayes et al.*, 2011). Maximum tsunami amplitudes of ∼40 m (*Mori et al.*, 2012) were reached in the Sanriku coast within 30 minutes of rupture initiation. The underestimate of the earthquake size lead to early estimates of wave heights that were too low by several meters to tens of meters (*Ozaki*, 2011). These complications in adequate magnitude estimation arise from reliance solely on seismic data to compute source parameters. Weak-motion seismometers, traditionally used for such tasks as monitoring local seismicity or Earth structure studies with teleseismic data, mechanically clip during strong shaking. Strong-motion accelerometers, designed to stay on-scale during periods of intense shaking, but, as demonstrated throughout Chapter 2, are not easily integrated to displacement because of unresolved baseline offsets in the acceleration data (*Boore and Bommer*, 2005). Numerous schemes have been proposed to correct strong motion data and deal with this difficulty and a few of them show encouraging results and could possibly be automated (*Wang et al.*, 2013). However even when strong motion waveforms are corrected carefully, it remains exceedingly hard to ensure that a corrected record reflects ground motion across the frequency band necessary to adequately characterize large sources. In Chapters 3 and 4 we showed that the long-period band of a record is the most critical to accurate magnitude computation of large events. Yet, in real-time inertial strong motion sensors it remains the most unreliable one, leading to saturation of near-source magnitude computations which result in underestimation of the earthquake size.

The second form of warning relies on direct measurements of sea-surface height disturbances (η). Most notably used for this purpose are the Deep-ocean Assessment and Reporting of Tsunamis (DART) buoys. They compose a network

of ocean bottom pressure sensors installed in deep water (4000-6000m), acoustically relaying pressure information to a buoy equipped with satellite telemetry that communicates with a centralized processing facility (*González et al.*, 2005; *Mungov et al.*, 2013). One reason for deploying in deep water is that the propagation of tsunami waves can be considered a linear process while in shallower water the non-linear behavior increases (*Arcas and Segur*, 2012) complicating the analysis of the tsunami source and forecasting. With these deep water measurements a linear inverse problem is solved for the tsunami source by superposition of previously computed unit sources of vertical seafloor displacement. This tsunami source is then used as the initial conditions in propagation of tsunami waves on a nested grid by solving the shallow water equations with numerical dispersion to simulate physical dispersion (*Titov and Gonzalez*, 1997). Once tsunami propagation has been modeled it is analyzed to generate site-specific warnings (*Titov et al.*, 2005). This approach has the advantage that it directly measures the tsunami rather than just rely on estimates of the size of the seismic source. However, bottom-pressure recordings like DART are expensive and sparse and because they are not deployed in the near-source coast provide no warning in the region immediately adjacent to the event. This method of warning has been mostly employed for ocean basin-wide forecasts.

With advances in real-time GPS such as instantaneous relative positioning (*Bock et al.*, 2000, 2004; *Larson et al.*, 2003) and precise point positioning (*Zumberge et al.*, 1997), after the 2004 Sumatra event proposals for tsunami warning based on geodetic measurements and earthquake source models more complex than just magnitude and location emerged in the literature. (*Blewitt et al.*, 2006) used permanent deformation estimates produced by the earthquake from GPS to grid search a database of possible, pre-computed, earthquake finite fault models. (*Sobolev et al.*, 2007)proposed and demonstrated the viability of a system that uses coseismic offsets from GPS to directly invert for a heterogeneous slip model. In the intervening period, before the 2011 Tohoku-oki event, the W phase method for computation of centroid moment tensors (*Kanamori and Rivera*, 2008) started producing rapid solutions with far-field seismic data routinely (*Hayes et al.*, 2009).

The *fast*CMT algorithm discussed in Chapter 3 also demonstrated that CMTs could be computed with coseismic offsets from GPS, without regard for saturation at high magnitudes, a problem often faced by seismic methods. *O'Toole et al.* (2012) demonstrated the viability of full waveform CMT inversions from the high-rate real-time GPS data. *Singh et al.* (2012) tested an algorithm for estimation of rapid rectangular source models with uniform slip and *Crowell et al.* (2012) produced heterogeneous coseismic slip inversions from real-time data for two large events. The pace of research in the field accelerated after the 2011 Tohoku-oki event. *Guilhem et al.* (2013) as well as our own work that extends the *fast*CMT algorithm to a line source are a solution to the problem of violation to the point source assumption often faced with near-field CMT determination of large events. *Ohta et al.* (2012) were able to produce in simulated real-time mode a simple uniform slip source model for the 2011 Tohoku-oki event; *Pérez-Campos et al.* (2013) computed similar models for one scenario and one recorded subduction event in Mexico. *Wright et al.* (2012) produced source models with 4 fault patches from precise point positioning data.

Furthermore, we've shown in Chapter 3 that a slip inversion, in simulated real-time mode, for the Tohoku-oki event from improved coseismic offsets by the optimal combination of accelerometer and GPS data is possible. This was achieved through a Kalman filter formulation (Chapter 2). Notably, in Chapter 3 we've shown that the fault plane used for the slip inversion can be determined without operator interaction, a problem not addressed before, by means of a finite-extent line source CMT inversion that bounds the geographic extent of moment release. This is important because a CMT determination allows discernment between thrust, normal and strike-slip events, all of which are possible in a subduction setting, but pose distinct tsunami hazards. This often ignored step is crucial because not all large events in a subduction zone can be assumed to happen on the megathrust. The Mw 8.6 event off Sumatra, Indonesia, on 11 April 2012 (*Satriano et al.*, 2012) was a predominantly strike-slip event that produced no significant tsunami. Similarly, the Mw 8.1 Samoa event on 29 September 2009 was a normal faulting, outer-rise type event that produced a sizable tsunami with 189 fatalities (*Okal*

et al., 2010). More recently the 2012 Mw 7.8 Haida Gwai thrust event offshore British Columbia produced a tsunami and was followed 2 months later by a Mw 7.5 strike-slip event on the fore-arc sliver (*Lay et al.*, 2013). Additionally the availability of a finite-extent CMT estimate is crucial to determining the fault plane on which to parameterize the slip inversion. We've argued throughout this work that geodetic and especially seismogeodetic data can rapidly characterize earthquakes of arbitrarily large magnitude and faulting type with minimum assumptions.

This extensive body of research by the community cohesively argues that improved earthquake source models should play an important role in guiding tsunami warning. However, in spite of mentioning that source characterization could aid tsunami warning, before *Ohta et al.* (2012), none of the above works gauged the impact of their source models on inundation forecasting. Neither did they propose how to map an earthquake source estimate into a forecast of tsunami intensity. This class of warning, where a tsunami propagation model is initiated from an earthquake source inversion, is often called indirect (*Arcas and Segur*, 2012) because it does not involve measurement of the tsunami itself. *Ohta et al.* (2012) used their uniform slip source estimates as initial conditions for a tsunami that they propagated using the algorithm of *Tsushima et al.* (2009), which assumes tsunami Green functions (tGF) from unit sources of vertical sea floor displacement (*Satake*, 1995), and compared it with off-shore GPS buoys, bottom pressure sensors and tide gauges with mixed results.

MacInnes et al. (2013) tested ten source models obtained from inversion of GPS, far-field seismic and tsunami wave gauge data as initial conditions to model tsunami propagation. When simulation results were compared to DART buoys and post-event field survey measurements (*Mori et al.*, 2012), it was found that indeed the diversity of source models produces significant variations in the simulated tsunami. This reiterates a recurring problem in tsunami science; for indirect warning the non-uniqueness of source inversions poses a hurdle. However *MacInnes et al.* (2013) showed that in spite of this, many source models retain the capacity to produce realistic tsunami scenarios. The source inversion techniques analyzed in that study, however, are problematic for real-time implementation. They rely

heavily on far-field geophysical data as well as decision-making by the researcher to define the parameterization to be used in the inverse problem. *Hoechner et al.* (2013) also produced tsunami intensity estimates in the near-source coastline from a 30 s sampled GPS-derived static slip inversion; that work however did not asses the accuracy of the inundation model or provide an automated way to determine faulting style, select the slab segment or determine the regularization parameter in the inverse problem.

Additionally, offshore shallow water measurements from coastal tide gauges, GPS buoys and ocean bottom pressure sensors can be used in a linear inverse problem (*Satake et al.*, 2013) for the earthquake source. Furthermore the joint inversion of both data sets (*Romano et al.*, 2012; *Gusman et al.*, 2012) produces a slip pattern significantly different from the land-based static offset inversions only of *Hoechner et al.* (2013) and Chapter 3, albeit with similar seismic moment. This is important because it suggests that indirect warning can then rely on actual measurements of tsunami propagation to improve the earthquake source model.

Follwing we will demonstrate first the improvements to static-offset derived models since these are the ones easiest to compute and that necessitate the fewest assumptions. We will employ line-source CMT and finite fault slip models derived from a seismogeodetic analysis of Chapter 3 and tsunami wave gauge data for the 2011 Tohoku-oki event to accurately forecast the tsunami intensity and inundation levels. We will emphasize the need for careful algorithm design to ensure minimal interaction from the network operator and assure that the process can be fully automated. This multi-sensor approach can then be applied as a basis for more timely and effective early warning for residents of the near-source coastline.

5.2 Static Modeling: Data and Method

5.2.1 Description

The real-time combination of strong motion and GPS data via a multi-rate Kalman filter produces broadband strong motion displacement waveforms (Chapter 2) that are reliable at all frequencies of seismological interest. These seismo-

geodetic data, can be used in a real-time environment to obtain high accuracy coseismic offsets and rapidly compute line-source CMT solutions and finite fault slip models as a regularized linear inverse problem (Chapter 3). We use the same data as before, from 139 collocated GPS and accelerometer station pairs (within 1.5 km) in Japan (Figure 5.1) in the computations for the 2011 Mw 9.0 Tohoku-oki earthquake. A finite extent CMT solution is calculated with the fastCMT algorithm to determine type of faulting and geographical extent of rupture, followed by estimation of a finite fault slip model. The regional 3D slab model for the subduction zone is established a priori from *Hayes et al.* (2012). In a real-time scenario, the relevant segment of the slab is extracted from the regional model based on the moment release of the finite extent CMT. It is then discretized to sub-fault patches and the slip inversion is performed. This approach using the seismogeodetic data yields slip inversions with more shallow slip than the GPS-only inversions due to improved precision in the vertical channel. This distinction is critical, while the algorithm described here can be employed with GPS data alone, the addition of the strong motion data reduces the uncertainty of the vertical component of motion. For the Tohoku-oki case this model is determined at 157s after earthquake origin time and in the timeline of warnings provides the first estimate of the slip distribution.

As time progresses data from coastal and offshore wave gauges begin to accrue and are incrementally ingested into the inversion process. We employ data from 8 coastal tide gauges, 6 off-shore GPS buoys and 2 ocean bottom pressure (OPB) sensors for a total of 16 wave gauges (Table 5.1, Figure 5.1). The data for all stations are resampled at 15 s. To compute the tGFs we calculate the seafloor deformation for 1 m of thrust and 1 m of strike-slip motion at each one of the subfaults. We then compute the resulting tsunami waveform at each one of the 16 wave gauges from this unit amount of slip using the open source GeoClaw software (www.clawpack.org). These time series of sea-surface motion are what we consider the tsunami Green functions for every subfault wave gauge pair.

We ingest the tsunami observation data in 10 minute increments and jointly invert them with the seismogeodetic offsets assigning relative weights of 1 to the

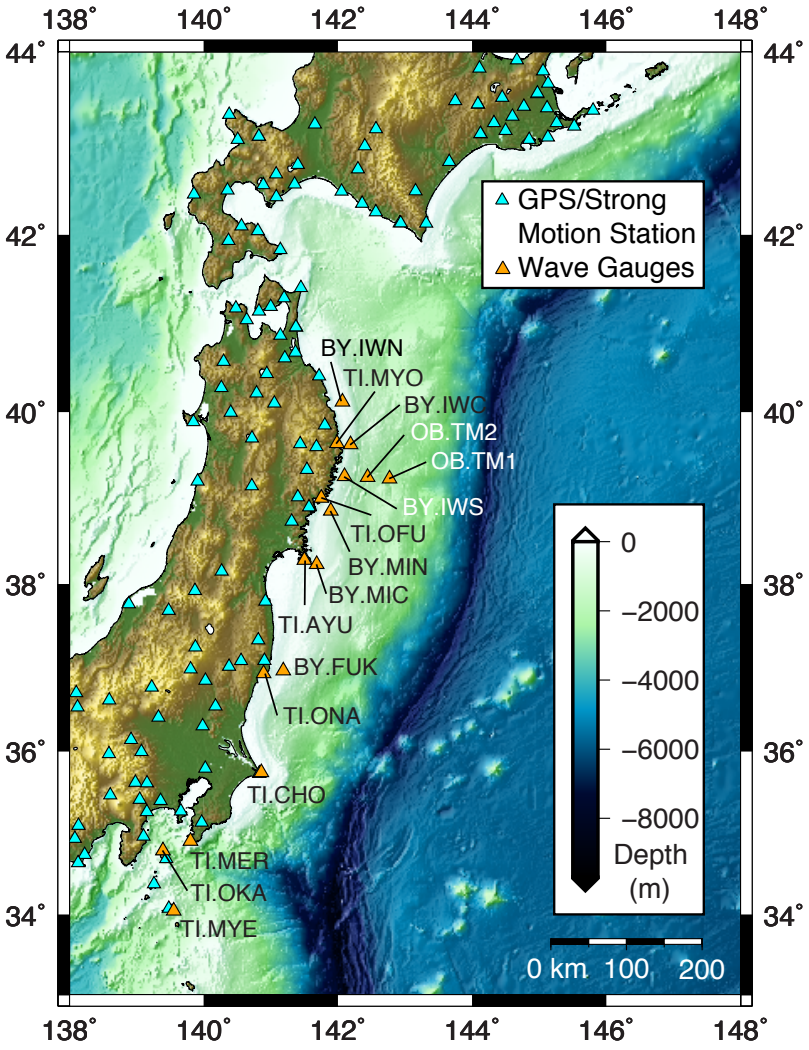


Figure 5.1: Distribution of stations used in this study. Blue triangles are land-based GPS/strong motion stations. Orange triangles are ocean-based stations: tide gauges (labeled TI), GPS Buoys (labeled BY) and cabled ocean bottom pressure sensors (labeled OB).

tide gauges, 5 to the GPS-buoys and 10 to the ocean bottom pressure sensors (*Satake et al.*, 2013). These weights arise from an analysis in Section 5.2.2 on the linearity of tsunami propagation at the different sensor locations. They are also in line with recent inversion techniques that employ these data (*Satake et al.*, 2013). We thus have a source estimate at 157s after rupture initiation from just the seismogeodetic data and then at 10, 20, 30, 40 and 50 minutes from the joint

Table 5.1: Wave gauges used in the inversion. All the time series are resampled to 15 s. The agencies responsible for the stations are the Earthquake Research Institute (ERI), the Nationwide Ocean Wave information network (NOW) and the Japan Meteorological Agency (JMA).

Station	Instrument	Code	Lat (°)	Lon (°)	Depth
TM1	OBP	OB.TM1	142.7683	39.2311	1618
TM2	OBP	OB.TM2	142.4411	39.2489	1013
Fukushima	GPS Buoy	BY.FUK	141.1856	36.9714	137
Central Iwate	GPS Buoy	BY.IWC	142.1867	39.6272	200
Northern Iwate	GPS Buoy	BY.IWN	142.0667	40.1167	125
Southern Iwate	GPS Buoy	BY.IWS	142.0969	39.2586	204
Central Miyagi	GPS Buoy	BY.MIC	141.6836	38.2325	144
Northern Miyagi	GPS Buoy	BY.MIN	141.8944	38.8578	160
Ayukawa	Tide Gauge	TI.AYU	141.5002	38.2820	0
Choshigyoko	Tide Gauge	TI.CHO	140.8583	35.7444	0
Mera	Tide Gauge	TI.MER	139.8023	34.9056	0
Miyakejima Tsubota	Tide Gauge	TI.MYE	139.5518	34.0459	0
Miyako	Tide Gauge	TI.MYO	141.9864	39.6396	0
Ofunato	Tide Gauge	TI.OFU	141.7529	39.0066	0
Okada	Tide Gauge	TI.OKA	139.3913	34.7894	0
Onahama	Tide Gauge	TI.ONA	140.8919	36.9369	0

inversion of land- and ocean-based data for a total of 6 models. The segment of the slab where the inversion is performed is that determined from the line source CMT in Chapters 3 and 4 and is held fixed throughout. For automated selection of smoothing in the slip inversions we, once again, employ Akaikes Bayesian Information Criterion. At each instance we compute 200 slip inversions with varying degree of smoothing and select as our preferred model the one with smallest ABIC. The computation of 200 source models takes only a few minutes on a four-core computer and is easily parallelizable since each computation is independent of the others.

For each preferred source model (the one with smallest ABIC) we compute the predicted vertical seafloor deformation and use it as the initial condition for a tsunami simulation. To propagate the tsunami we employ GeoClaw (http://clawpack.org), by which two-dimensional shallow water equations are solved with the finite volume technique (*LeVeque*, 2002). The code simulates non-linear water wave propagation and can deal with discontinuities in the

solution, such as turbulent bore formation, by shock capturing. Furthermore it employs adaptive mesh refinement (AMR) such that regions of larger tsunami complexity are automatically refined to higher discretization levels according to heuristics prescribed by the user. The code is suitable for near shore inundation analysis. It employs a Manning-type law for bottom friction (we held the coefficient fixed at 0.025) and has a moving sea/land boundary condition that allows cells to be wetted or dried as the simulation progresses and has a non-reflecting outflow boundary condition at the edges of the model domain. The algorithms are described in detail in *George and LeVeque* (2006), *George* (2008) and *Berger et al.* (2011). GeoClaw has been benchmarked by the National Tsunami Hazard Mitigation Program (NTHMP) (*Gonzalez et al.*, 2011) and approved for use in hazard modeling products. A simulation run takes ∼1 hour on the same four-core computer using the standard open source multi-processor platform openMP. Ostensibly for real-time performance the code can be optimized and the run time can be significantly improved by parallelization to a suitable level.

Topography for the simulations is taken from the Shuttle Radar Topography Mission (SRTM3) (*Farr et al.*, 2007) with a resolution of 3 arcseconds (∼90m pixel size). Off shore bathymetry has a resolution of 30 arcseconds (∼1km pixel size) from the SRTM30+ dataset (*Becker et al.*, 2009; *Sandwell and Smith*, 2009), which represents a synthesis of marine soundings and spaceborne altimeter measurements. The vertical datum of both data sets is mean seal level (MSL).

The simulations are run for 120 minutes of model time with output at 15s intervals. The simulation domain is between 34°N and 41°N and 139°E and 146°E. From the model output we extract 2 distinct sets of inundation information. First, we collect maximum inundation amplitudes at the coordinates of 2256 quality A and B survey measurements located inside the model domain from *Mori et al.* (2012). We also collect the inundation amplitude at all points on the coastline (at mean sea level, MSL) as defined by the SRTM3 water body data information. For each point where inundation output is desired we use the finite volume cell whose center is nearest the observation point at any given instant. The distinction between these two types of inundations can be appreciated in Figure 5.2. Inunda-

tion at the coastline is the maximum amplitude of the tsunami at the water-land boundary as defined before the event and it is equal to the maximum flow depth at that point. The inundation at the survey points is the maximum amplitude of the flow, with respect to the vertical datum defined by MSL. Its inundation at a point that is on land before the event. The inundation amplitudes at the survey points are not the amplitude of the tsunami with regards to the local elevation (the flow depth). The inundation at the survey points is used to verify the predictive power (often referred to in forecasting as the skill of the model) of each simulation. In contrast the predicted inundations at the coastline are what we propose could be used as intensity metric to guide the warning. The simulations also produce wave gauge output at the locations (Figure 5.1) of the ocean bottom pressure sensors, GPS buoys, and tide gauges located along the coast.

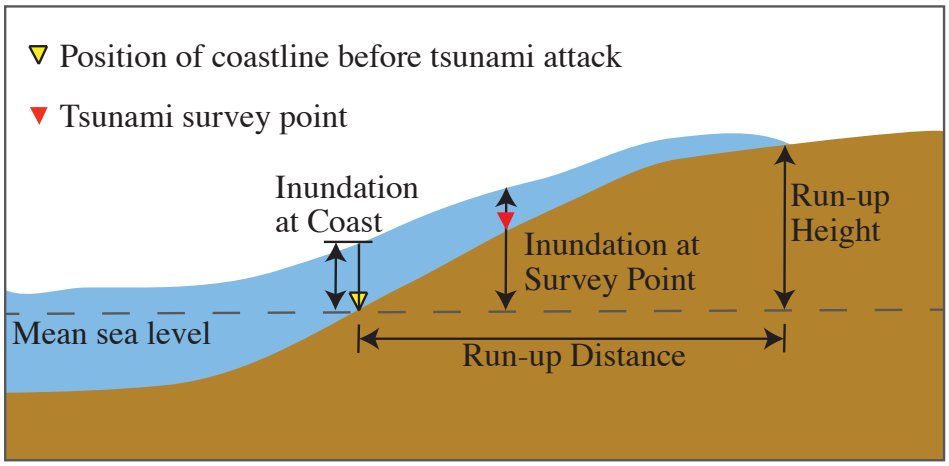


Figure 5.2: A schematic of the measures of tsunami intensity used in this study. The inundation at the coast and the inundation at the survey points from *Mori et al.* (2012) are both referenced to the vertical datum defined by mean sea level.

5.2.2 Linearity in Tsunami Propagation

Underlying the joint inversion procedure is the assumption that tsunami propagation in shallow water (at the locations of the wave gauges) is a linear process. That is, tsunami waves generated by uplift due to slip on distinct subfaults

can be linearly superimposed. Recent studies have made this assumption when using these measurements to analyze the earthquake source even at coastal tide gauges (*Romano et al.*, 2012; *Gusman et al.*, 2012; *Satake et al.*, 2013) and indeed the same assumption is made in this study. However, it is well known that the non-linearity of tsunami propagation increases as the wave shoals. That linearity can be invoked for modeling with data from such shallow depths is controversial (*Arcas and Segur*, 2012) and the assumption that it cannot is one of the reasons for deploying DART buoys in deep water (*Titov et al.*, 2005). The GeoClaw simulation code solves the non-linear shallow water equations so it is possible to test this assumption, at least numerically, and at the level of precision allowed by the bathymetry and topography we employ here.

We develop two simple tests of linearity. First we test for homogeneity to ensure that, for a given model, $f(x)$, $f(\alpha x) = \alpha f(x)$ where α is a scalar. We place 1m of thrust slip on a shallow fault patch in the middle of the fault model (patch 10) and simulate the tsunami, we then place 2m of slip on the same patch, simulate the tsunami and compare this output to the result of multiplying the output of the 1 m simulation by 2. The results are in (Figure 5.3). The second test is for additivity such that, for two models $f(x)$ and $f(y)$, $f(x + y) = f(x) + f(y)$. We again place 1m of slip on subfault patch 10 and place 1m of slip on a deeper subfault (patch 37). We model the tsunami from simultaneous slip on both patches and compare it to the addition of the output from the independent simulations of each fault patch (Figure 5.4). The results of these two tests show that non-linearities exist but that they are small compared to the maximum amplitude of the tsunami at each wave gauge. Also the non-linearities are larger at the tide gauges (which are in shallower water) than at the GPS buoys and OBP sensors. This is the reason for the relative weighting scheme discussed in the previous section. Generally the non-linearities are more pronounced at longer times after the first arrival. We perform similar analysis on different combinations of subfaults with similar results. We conclude that non-linearities exist, are quantifiable but small enough to allow for a joint inversion. Because non-linearities are smallest during the first wavelength of the tsunami the linearity assumption will degrade as longer and longer segments of the

wave gauge record are used.

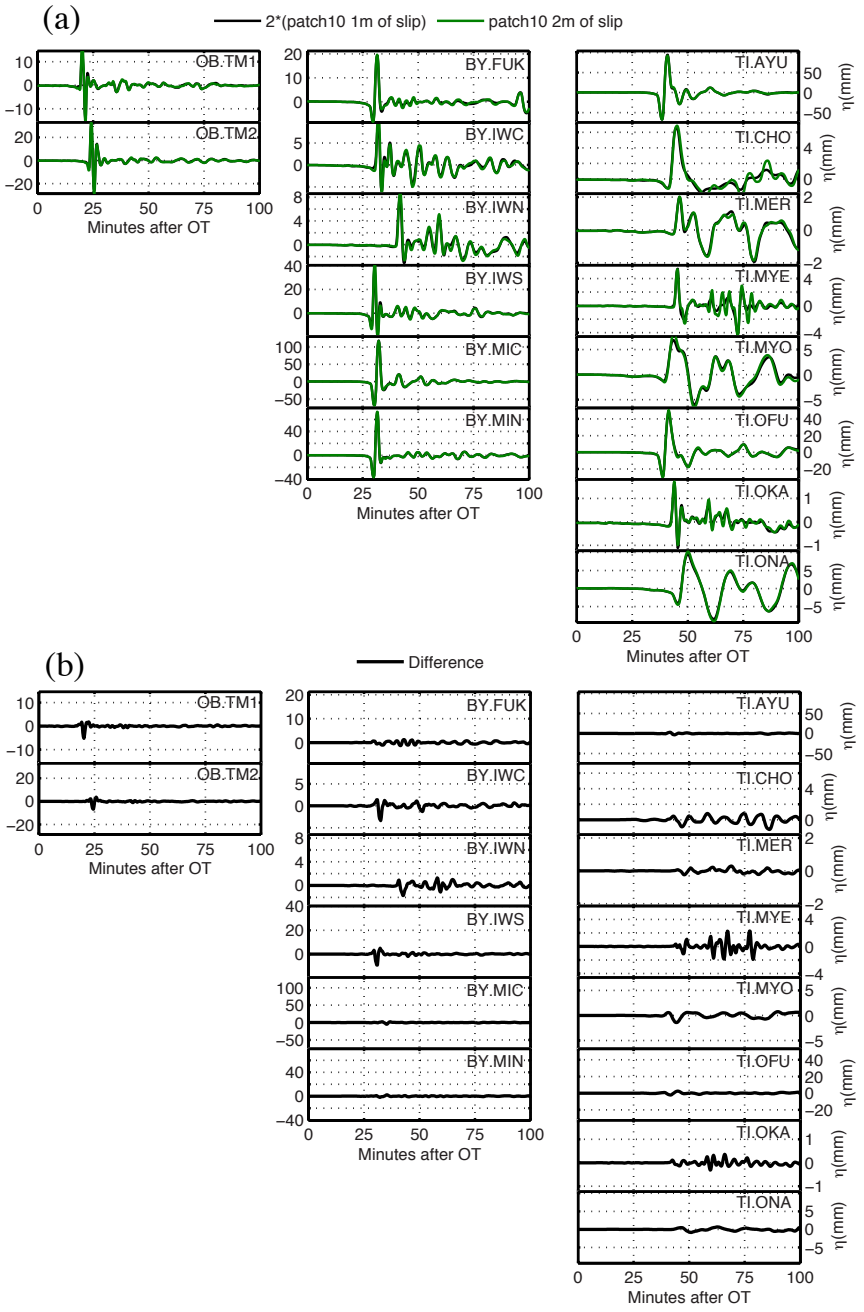


Figure 5.3: Result of testing the assumption of linearity in tsunami propagation. (a) is the result of testing for homogeneity, the black line is the result of the linear superposition and the green the result of the GeoClaw non-linear simulation. (b) is the difference between the two results

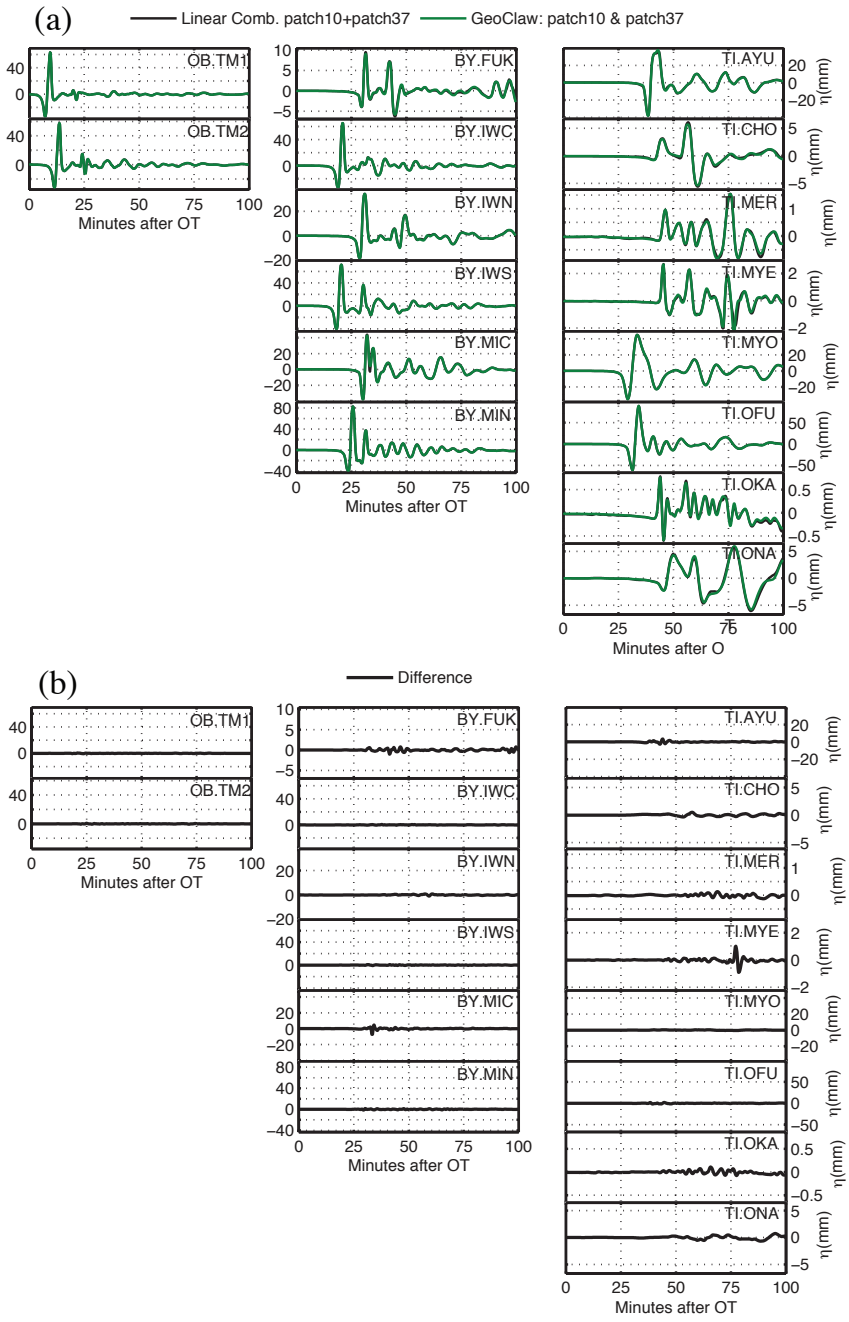


Figure 5.4: Result of testing the assumption of linearity in tsunami propagation. (a) is the result of testing for superposition, the black line is the result of the linear superposition and the green the result of the GeoClaw non-linear simulation. (b) is the difference between the two results

5.3 Inversion and Forecast Results

The results of the inversions at the 6 time intervals are summarized in Figures 5.5 and 5.6 and Table 5.2. Figure 5.5 shows the results of the finite fault slip inversion from the land-based data obtained at 157s after earthquake origin time (OT). Peak slip as reported in Chapter 3 for the static case is close to 30m and maximum seafloor uplift is ∼6m. The fit to 50min of wave gauge data (Figure 5.5) (not used in the inversion) is poor, with a root mean square (RMS) value of 1.42m. The OBP stations are not well fit and the tsunami amplitude is underestimated; similar results are observed for the buoy measurements indicating that the tsunami is systematically underestimated. This rather smooth slip model, however, fits the coseismic offsets from the seismogeodetic data with a 99% variance reduction (Table 5.2). The joint inversion with the first 10 minutes (Figure 5.5) of wave gauge data shows minimal differences from the inversion using just the land data. The fit to the coseismic offsets is reduced slightly to 98% variance reduction, and the fit to the 10 min of wave gauge data improves (RMS of 0.26 m). Only the pressure gauges have a significant signal of ∼1 m amplitude. The remaining stations have yet to register a significant disturbance. At 20 min (Figure 5.5) significant differences arise. The peak tsunami amplitude has been reached in the OBP records and all GPS buoys register a sizeable signal. As a result, the slip inversion is noticeably altered; it has a peak displacement of ∼60 m over a large asperity and peak seafloor uplift is ∼20 m. The fit to the wave gauge data is very good (RMS of 0.24m) while the fit to the coseismic offsets is significantly reduced to a variance reduction of 66%. The magnitude has increased from Mw 8.9 in the previous inversions to 9.1. Between 30min and 50min (Figure 5.6) the inversion stabilizes as the first peaks of the tsunami waveform have been fit at the deeper water (TI and BY) stations (Table 5.1); subsequent changes are a result of fitting the later part of the time series and the lower-weight coastal tide gauge data. Peak slip settles at around 60m on a very shallow patch at 38°N and on a deeper patch at 15km depth around 37°N; magnitude is Mw 8.98-9.04. The fit to the coseismic offsets over this period oscillates (Table 5.2) and settles to 70% on the last inversion while the fit to the wave gauges remains stable at 0.9 m RMS. We note that the

Table 5.2: Statistics of the inversions and inundation models. The first column is variance reduction (VR) between the coseismic offset measurements and the synthetic offsets from the inversion. The second column is RMS of the fit to the wave gauge measurements. The third column is variance reduction of the modeled inundation compared to the surveyed inundation from *Mori et al.* (2012). The 4th column is the number of inundation survey points inundated by the model

Time	Coseismic VR(%)	Wave Gauge RMS (m)	Survey VR(%)	Survey Points Inundated
157s	99	1.42	85	956/2250
10min	98	0.26	79	905/2250
20min	68	0.24	60	1913/2250
30min	78	0.55	73	1538/2250
40min	57	0.87	65	1604/2250
50min	70	0.85	78	1611/2250

peak amplitudes at both pressure gauges and 4 of the 6 buoys are consistently well modeled. However, for two buoys, BY.IWC and BY.IWN off-shore Iwate prefecture, (Table 5.1, Figure 5.1) the peak amplitude is underestimated by about 50%. The tide gauges contribute little to the inversion since they receive the smallest weight and provide information too late to be of use for early warning for this event. We note that for two of the distant tide gauges, TI.CHO and TI.MYE, the peak amplitude is not well resolved (Figures 5.5,5.6). We also note that these two stations exhibit the strongest non-linear behavior (Figures 5.3,5.4). The tide gauge stations with small non-linear behavior and closest to the source (TI.AYU, TI.MYO and TI.OFU) appear to be well modeled, in spite of having a clipped record.

Using the slip inversions and seafloor uplift maps in Figures 5.5 and 5.6 we model the ensuing tsunami with GeoClaw as described in Section 5.2. Figure 5.7 shows the maximum expected amplitude near the earthquake source. We note that the inversions at 157s and 10min that have little or no information from the wave gauges predict smaller amplitudes than the inversions relying on more complete wave gauge records. After 20 min a sizable tsunami is forecast in the near shore region. It is interesting to note a large lobe of high amplitude waves radiating in the trench normal direction. This lobe seems to initiate above the deeper (10-20 km) asperity in Figures 5.5 and 5.6 and not above the very shallow patch of high slip.

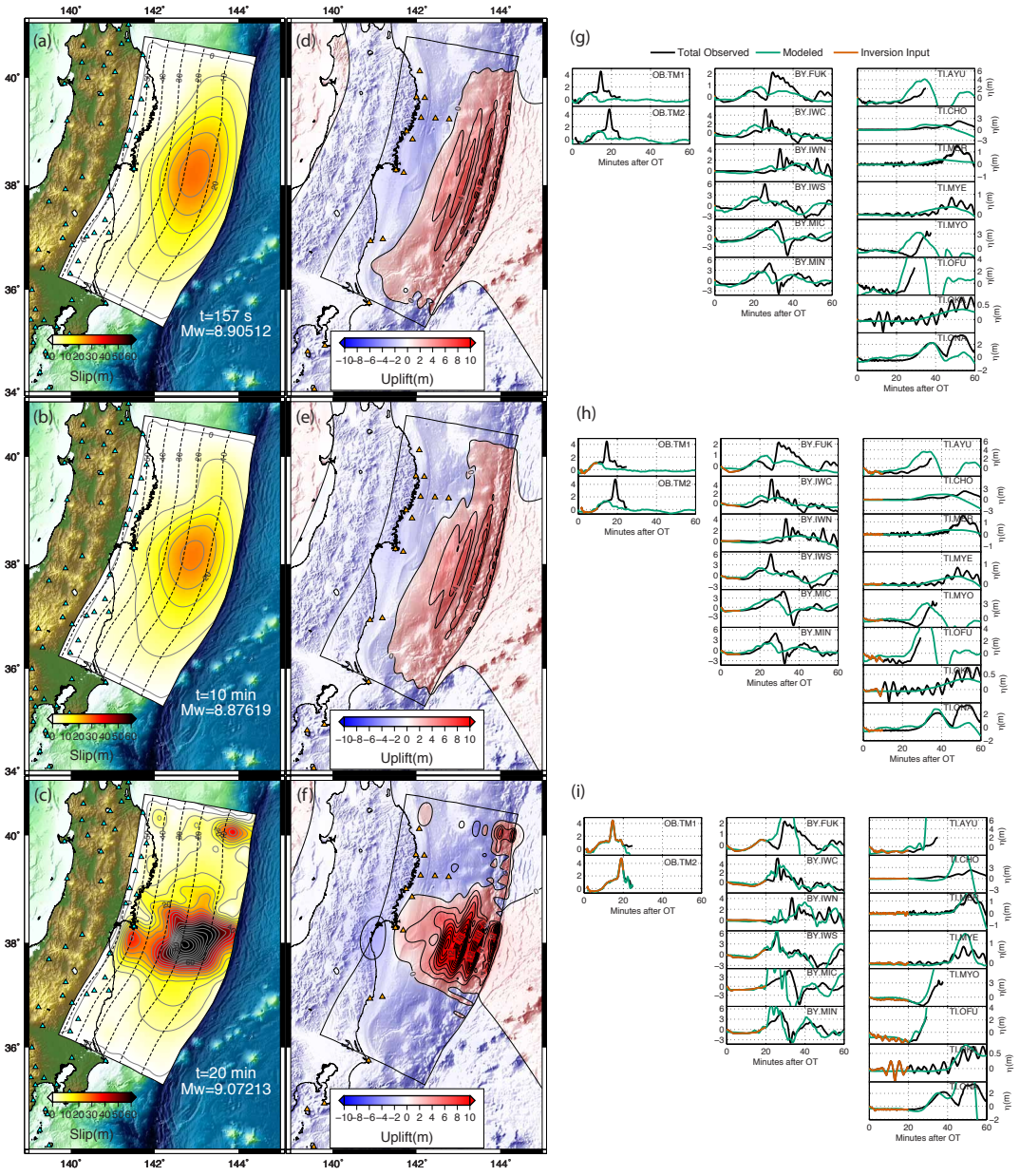


Figure 5.5: Inversion results. (a)-(c) Slip inversions at 157 s, 10 min and 20 min after earthquake origin time. The inversion at 157 s is from land-based measurements. Subsequent inversions are of the joint data set. Grey lines are the slip contours at 5 m intervals and black dashed lines are the slab depths. (d)-(f) Predicted seafloor uplift from the inversions. (g)-(i) Comparison between observed (black) and synthetic (green) data for the wave gauges. The orange portion of the waveforms is the input for the inversion.

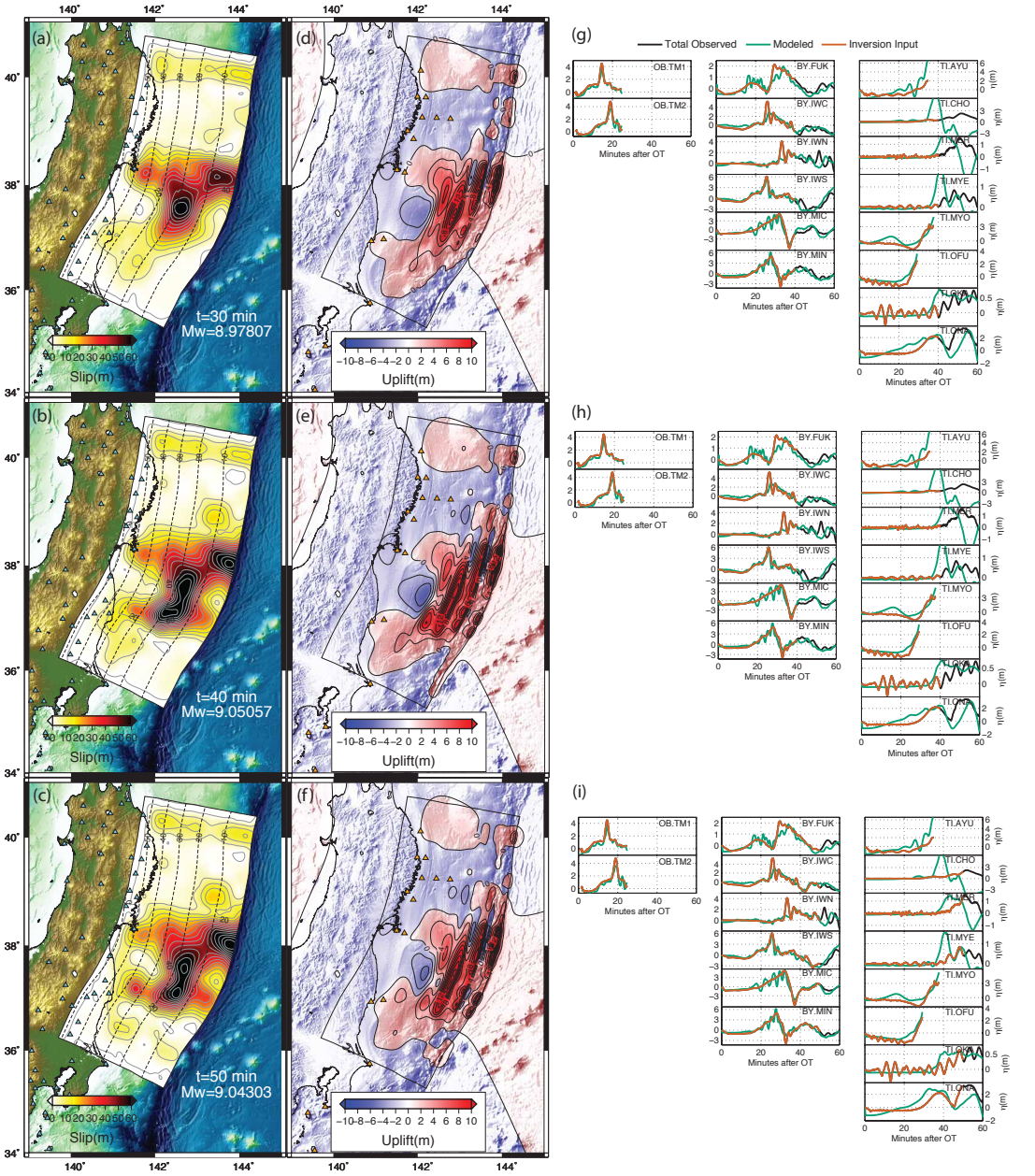


Figure 5.6: Inversion results. (a)-(c) Slip inversions at 30, 40 and 50 min after earthquake origin time. Inversions are of the joint data set. Grey lines are the slip contours at 5 m intervals and black dashed lines are the slab depths. (d)-(f) Predicted seafloor uplift from the inversions. (g)-(i) Comparison between observed (black) and synthetic (green) data for the wave gauges. The orange portion of the waveforms is the input for the inversion.

At 50 minutes a second lobe of high amplitude is forecast to radiate from the very shallow patch of slip at 38°N. The intersection of these high amplitude lobes with the coastline matches the pattern of maximum observed inundation amplitudes from the survey points (Figure 5.8). For the smooth land-based models the first wave is almost continuous along the fault strike, however for the more complex models from the joint inversions the first pulse is broken into two or three distinct waves that jog along strike. There are persistent oscillations in Sendai bay and the smaller inlets of the Sanriku coast (38°N to 40°N) and along the continental shelf akin to basin and shelf resonance. Diffraction along the Oshika peninsula that juts north of Sendai bay is also apparent. The complex behavior in the models shows the repeated and long-lasting attack of multiple waves on the coastline after the main arrival.

Figure 5.8 shows the inundation computed at the coast as defined by the pre-tsunami water-land boundary for each simulation. It also shows the comparison between the inundation measured by *Mori et al.* (2012) at the survey points and the inundation predicted by our simulations at those same survey points. The first two models at 157s and 10min show a relatively smooth distribution of expected coastal inundations between 0 and 10m. They also show a systematic under-prediction of the inundation at the survey points and only 900-950 of the 2256 survey points are inundated (Table 5.2). The variance reduction is high for these points (80-85%, Table 5.2). This indicates that even though many points are not inundated, those that are inundated are accurately modeled. As noted in the slip inversion (Figure 5.5), at 20 min the modeled sea floor deformation increases substantially and this has a noticeable impact on the inundation. The coastal inundation is now 10-20m and 1913 of the 2256 survey points are inundated (Table 5.2). However the comparison at the survey points shows a systematic over-estimation of the inundation. This is evidenced as well by the low variance reduction of the survey inundation (59%). Between 30 and 50min. as the slip inversion stabilizes the inundation estimates at the coast stabilize as well. The number of inundated survey points in this time interval is reduced to 1600 out of 2256 (Table 5.2) and the variance reduction improves to 77% by 50min. The majority of the survey

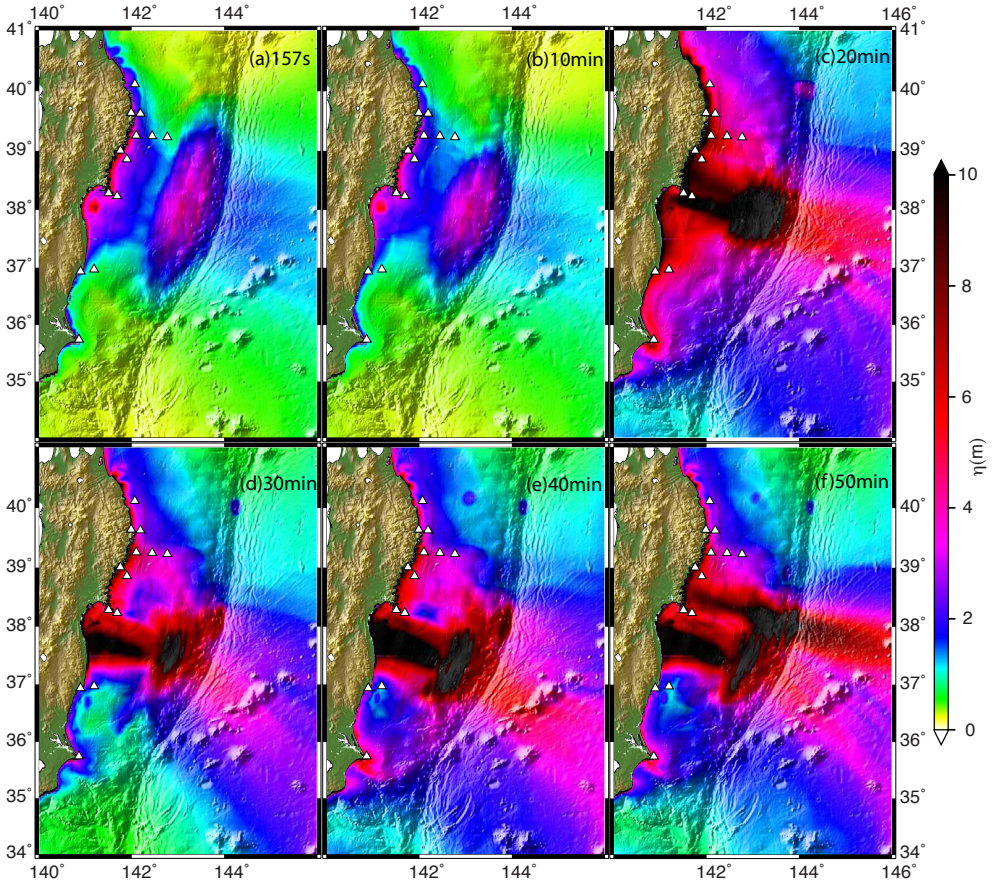


Figure 5.7: Tsunami forecast results. (a)-(f) Maximum expected tsunami amplitude at different intervals after earthquake origin time. The white triangles denote the positions of the wave gauges used in the joint inversion.

points that are not inundated by the slip inversions lie in the Sanriku coast between 38.4°N and 40°N.

5.4 Limitations and Implications for Warning

We have demonstrated in Chapter 3 how precise estimates of coseismic motion from seismogeodetic data could produce slip inversions of the Tohoku-oki event in about 3 min. For tsunami early warning the inundation results computed in this work show that the smooth slip inversion computed only from land data under-predicts the tsunami. However, this estimate is available quickly (157s after

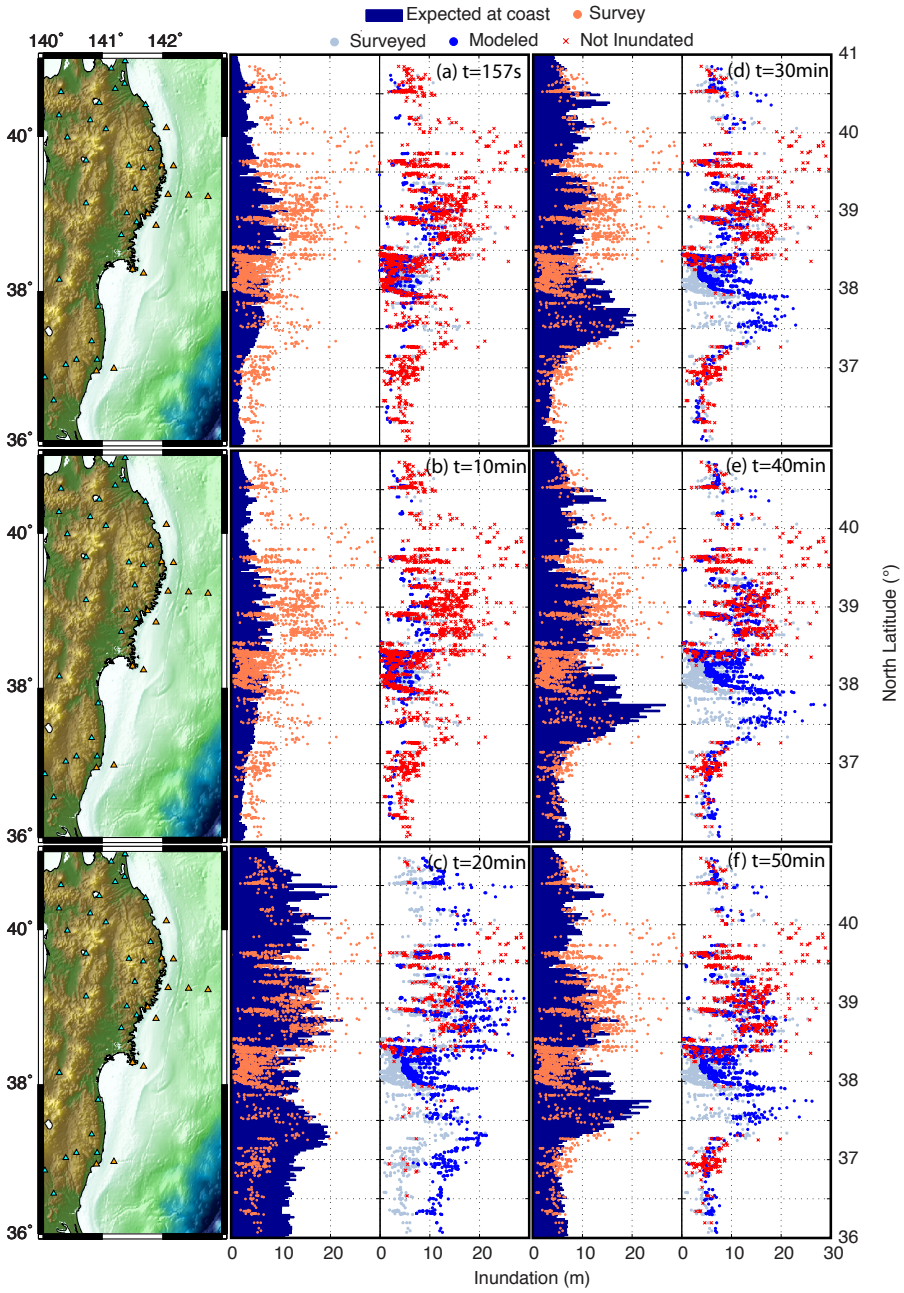


Figure 5.8: Inundation forecast results. (a)-(f) the left panel shows with blue bars the inundation predicted by the model at the coastline (the pre-tsunami land-water boundary) compared to the surveyed inundation inland (orange dots). The right panel shows the direct comparison between the observed survey inundation (grey dots) and the inundation predicted by the model at the survey points (blue dots). The red crosses are survey points that were not inundated by the model.

rupture initiation) and is a significant improvement over the initial wave height estimates that relied on the first magnitude estimate of Mw 7.9 (*Ozaki*, 2011), indicating more accurate magnitude estimation and improved depiction of the geographic extent of moment release. This result is significant for more reliable early forecasts and hazard mitigation. Furthermore, the situation rapidly improves as offshore wave gauge data are ingested into the inversion. By 20min after OT the forecast of inundation (Figures 5.7 and 5.8) shows an acute increase in intensity that better reflects the observed inundation pattern the first waves arrived at about 30min after OT. This could in an operational setting lead to a revised warning with higher predicted intensities. By 30min a solution, which can be considered final, is available and it successfully predicts most of the gross features of inundation. This is most significant for rapid response by providing an improved determination of the hardest hit areas.

As noted by *Arcas and Segur* (2012) the multiplicity of possible earthquake source models that arise by virtue of the non-uniqueness of the inversion pose a challenge to forecast and warning. The results discussed here convincingly demonstrate that in spite of this, the objectively determined slip inversions discussed herein can replicate the pattern of inundation with minimum assumptions. We have quantified the models skill by comparing to inundation measurements. We also argue that coseismic offset estimates (land-based data only) can serve to initiate response for tsunami early warning. Additionally, and perhaps more importantly, these results demonstrate that wave gauges in relatively shallow water ($\sim$100-1000 m) can be successfully employed to determine the earthquake source and forecast the ensuing tsunami. One need not deploy the sensors in deep water to allow for successful forecast of tsunami intensity. It remains true however, that the non-linearity in tsunami propagation exists. It is manifested most strongly in shallow tide gauge stations and at longer times after the first arrival, limiting their utility. In light of this and the discussion on linearity in Section 5.2.2, when performing a joint inversion, it would be ill-advised to use long segments of the wave gauge records after the first arrival. Furthermore, before performing a joint inversion at other locations and with other wave gauge data one must exercise due

diligence and ascertain that the non-linearities are indeed small. However, that shallow water wave gauges can be used for warning is an important result. The time taken to obtain a solution that forecasts a tsunami of the observed intensity (20min) is a function of the distribution of such wave gauges. Figure 5.7 shows that the distribution of such stations is not optimal for observation of this particular event. It remains possible that the forecast and warning timeline will continue to diminish as such networks of sensors become denser. GPS buoys are particularly attractive. In their current mode of operation they rely on baseline positioning and are referenced to a GPS station on-shore. This limits how far off-shore they can be deployed (∼20-30km) without losing accuracy and also means that if the reference station moves, as was the case with this large earthquake, then the position solution at the buoy will be degraded. However, recent advancements in precise point positioning and tightly coupled Kalman filtering with accelerometers (*Geng et al.*, 2013a) show that it is possible to do away entirely with the nearby reference station and retain the same level or even improve the precision obtained with relative positioning. This makes it possible to deploy GPS buoys at arbitrarily large distances offshore only limited by telemetry considerations.

The results and analysis shown here have some limitations and it is important to understand them. In the linear inverse framework we have sacrificed some of the fit to the coseismic data (Table 5.2) to fit the tsunami data as best we can, especially, the ocean bottom pressure and GPS buoy stations. The general pattern of coseismic deformation is still modeled and provides a valuable constraint. However, the fit to the coseismic data is reduced from 99% variance reduction in the land-based inversion to $\sim$ 70% levels in the joint inversion. As noted by *Hill et al.* (2012) this can be ameliorated by placing slip where the model resolution of coseismic offsets is the lowest. This effectively locates the slip in the null-space of the coseismic data and hence doesnt affect the data fit. We are exploring these null-space techniques and assessing their utility for real-time algorithms. Additionally, the short-wavelength along-strike features in the computed vertical deformation (Figure 5.5) are an artifact of the fault discretization. Very shallow subfault patches have such peaked vertical deformations that if discretiza-

tion is not fine enough (our subfaults are 25x25 km) this behavior arises. This is a common problem in inversions that allow slip to go to the trench axis while keeping subfault size constant along the slab model. Given the good fits to the tsunami wave gauges we do not consider this a substantive issue for rapid computations. Future improvements to the inversion techniques might include employing irregular grids to allow for finer discretization at shallow depths. We are however interested in a speedy computation so we have chosen to keep the discretization at its current coarseness.

MacInnes et al. (2013) noted that tsunami simulations from different geophysical data sets and techniques failed to capture the large inundation levels observed in the Sanriku coast between 38.4◦N and 40°N. Although we can forecast large inundation amplitudes in Sanriku we observe a similar pattern. It is noteworthy that inversions that directly employ wave measurements, like ours, fail to completely model the intricacies of the inundation. We believe that in large part this is due to limited resolution in the publicly available topography (~90 m pixels) and bathymetry (~1 km pixels) data sets used in this study. Consider Figure 5.9 where we compute the terrain ruggedness index (TRI) (*Riley et al.*, 1999) of the topography/bathymetry grid. TRI is the mean difference between elevation at a pixel and its neighboring 8 pixels. The geomorphic features of the Sanriku coastline are characterized by rias, which are rugged and steep coastal inlets made from submergence of fluvial valleys. The Sanriku region has the most instances of inundation survey points that are not wetted by our simulations.

Figure 5.9a shows that indeed this region has the largest TRI. Also of note in Figure 5.9 is that at the coastline in Sanriku the TRI drops abruptly from ∼30m on the landward side to 0m on the seaward side. It is unlikely that such abrupt change of geomorphology at the waterline is real; the rias should continue offshore forming significant underwater canyons. More likely is that because the bathymetric portion of the grid has a lower resolution (30 arcseconds, as opposed to 3 arcseconds onshore) it fails to resolve the jagged offshore features associated with rias. Figure 5.9b shows the TRI values of the topography pixels containing the inundation survey points. It shows the TRI values for survey points that are

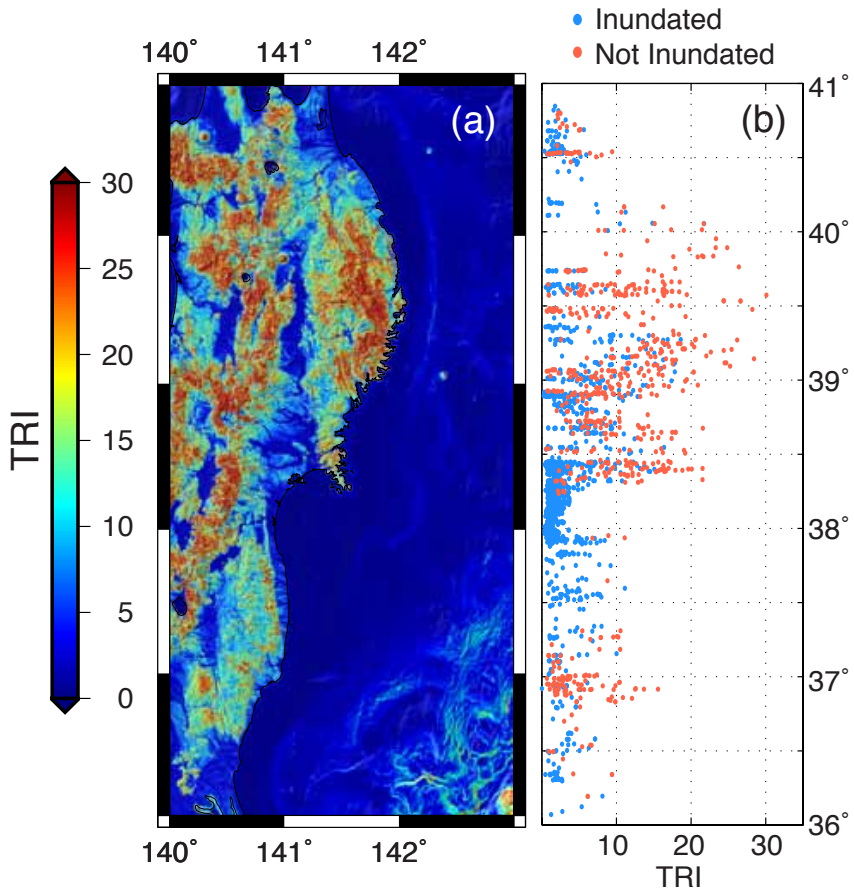


Figure 5.9: (a) Terrain ruggedness index (TRI) of the topography/bathymetry grid used in this study. (b) Distribution of inundated and non-inundated survey points for the simulation at 50min after OT as a function of TRI.

wetted by the simulation and for those that remain dry (i.e., where the simulation fails to model an inundation) for the final run obtained with the data accrued at 50 min after OT. We can see from this plot that although the simulation inundates some of the survey points with high TRI, most of the survey points that remain dry have consistently high values of TRI. This can be best seen in Figure 5.10 where we bin the dry/wet survey points in 2.5 TRI intervals. It is clear, that with increasing terrain ruggedness, the model fit diminishes. Thus we believe that terrain complexity not captured by the grids is an important factor. One way to improve the capacity of earthquake source models to accurately forecast the inundation is to employ better quality grids in regions of high TRI. GeoClaw

can easily handle this without a prohibitive increase in computation time with its adaptive mesh refinement approach, but currently such datasets are proprietary.

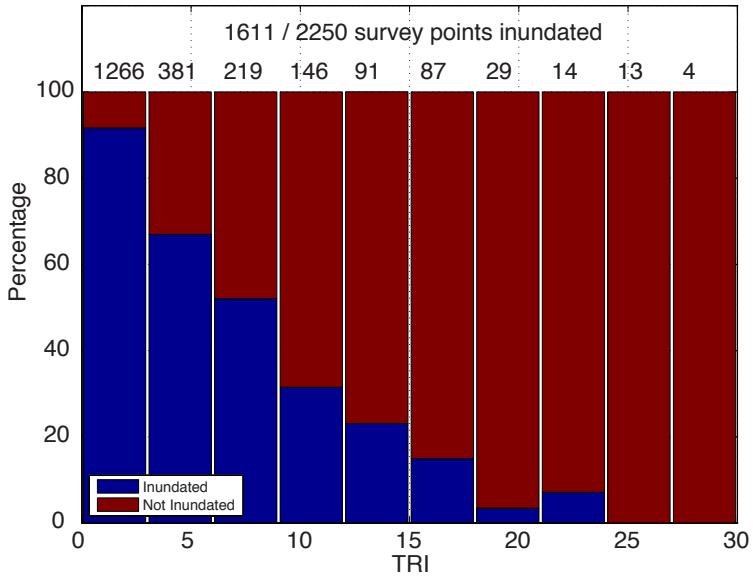


Figure 5.10: Inundation of the survey points for the model obtained at 50min after origin time. This is the distribution of survey points by terrain ruggedness index (TRI) binned every 2.5 units. The number above the bar is the total number of survey points in that bin. The blue portion of the bar represents the inundated points and the red represents the fraction that is not inundated by the simulation.

It is also important that early warning systems be coupled with judicious analysis of the hazard before an event occurs. For example, pre-event analyses with better bathymetry would undoubtedly show that a 10m tsunami at the mouth of a ria, as in the Sanriku coast, could be greatly amplified by the local bathymetry. Thus even if the first estimation of tsunami intensity (Figure 5.8a) is an underestimate, coupling with a priori knowledge of the hazard can lead to a better response. Warning is only one part of the response system. Pre-event analysis of the hazard and societal education are just as important, and without them a warning is of little use.

Additional close inspection of the GPS buoy records (i.e. Figure 5.6g) shows that all models underestimate the peak tsunami amplitude at the northernmost buoys, BY.IWC and BY.IWN (Table 5.1). This is one of the regions of higher TRI. Nearby BY.IWS and tide gauges TI.OFU and TI.MYO are well modeled

although the tide gauge records are clipped and we are unable to say if maximum amplitude would have been correctly modeled. We also note that the final source model consistently places a streak of 5-10m of slip on the northern portion of the fault at around 40°N. These two observations (the underestimate at the northern buoys and the streak of slip on the northern part of the model) imply that we cannot discard the possibility that secondary sources of tsunami energy (*Morra et al.*, 2013) (i.e., submarine landslides, splay faults, etc.) are contributing to the wave records and contaminating the inversion results. Quantifying and modeling the contributions of such sources to the overall radiation pattern of the tsunami remains a challenge to early warning and tsunami science in general. It is possible that other assumptions lead to the observed discrepancy. For example GeoClaw does not consider the contribution of horizontal momentum to tsunami generation. It is possible that motion of large vertical features such as continental slopes might have an important contribution to the tsunami energy budget. Only recently has this assumption been seriously studied (*Satake et al.*, 2013). Additionally, in tsunami modeling it is customary to assume instantaneous tsunami generation. For example, for the 2004 Sumatra event it was shown that time dependent rupture models had little effect on the observed tsunami (*Fujii and Satake*, 2007). However (*Satake et al.*, 2013) argues that for Tohoku-oki, near-source observations are best modeled with a kinematic slip model. Part of our future research is to employ near-field broadband strong motion displacement data recorded for this event [Melgar et al., 2013a] and wave gauge data to derive kinematic models. It will be important to assess the impact of such techniques on rapid tsunami response.

The Japanese GPS network (GEONET) is very dense and its inter-station spacing an exception rather than a norm worldwide. In this study we used a sparser subset of 139 stations (the collocated GPS/accelerometer pairs) to compute the first inversion. This was done to demonstrate the capabilities of the seismogeodetic solution and also to illustrate the performance with a station distribution more akin to other regional GPS networks. We found that the sparse seismogeodetic solution is adequate and can be computed quickly but in general it underestimates the inundation. The effect of this undersampling the land-based network is illustrated

in Figure 5.11 where we present the inundation predicted by the optimal inversion resulting from employing the displacement waveforms from the 816 GEONET stations in the affected region. The maximum amplitude forecast is larger than in the seismogeodetic solution alone and closer to the result from the joint inversion. The comparison with the survey points improves, 1538 out of the 2250 survey points are inundated by the full GPS network solution and variance reduction is 70%. Not surprisingly, a denser land GPS network provides a better early forecast of the tsunami and would be further ameliorated by collocation with accelerometers at all stations. In general, the methodology described herein can be employed with GPS data alone, however we've shown that the improved vertical resolution resulting from the seismogeodetic combination improves the derived finite fault slip model. Furthermore, the prospect of real-time coseismic source modeling with corrected strong motion records alone remains elusive.

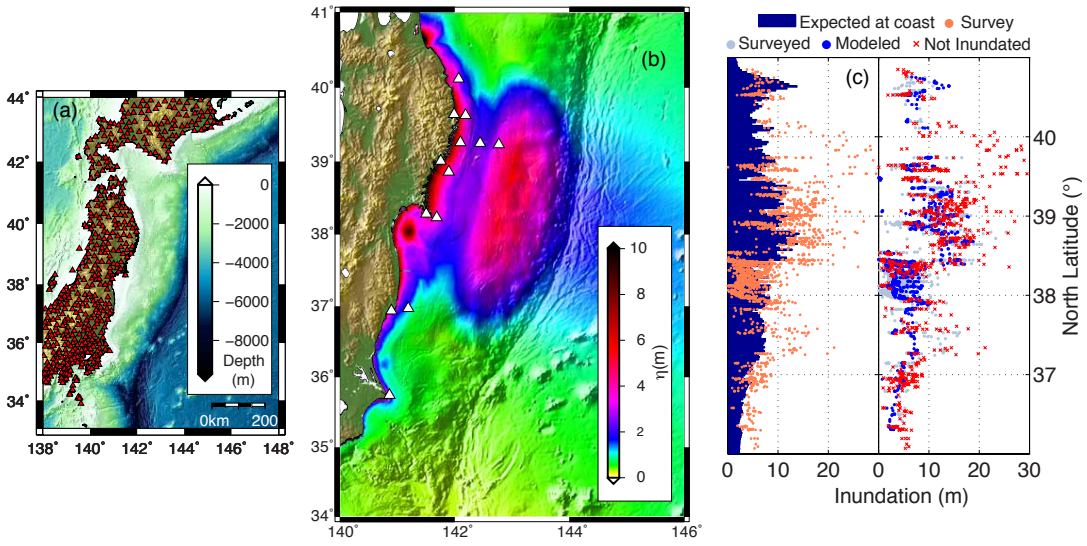


Figure 5.11: Inundation results at 157s after OT from the inversion employing the dense 816-station GPS network. (a) Outline map of the station distribution; (b) Forecast of maximum expected amplitudes; (c) Inundation results as in Figure 5.8.

Although in this work we have focused on the immediate impact of the tsunami, i.e., the inundation, the time evolution of the models shows that there is significant structure to the tsunami even hours after origin time. This can

have important impact on coastal and ship operations (*Lynett et al.*, 2012). Thus longer-range forecasts could be aided by the results discussed here.

We also note that the algorithm employed in this study relies on the traditional method of regularization to solve an ill-conditioned inverse problem. The results are encouraging and driven by the requirement of rapid computation. Inversions for 200 distinct sources at different smoothing levels takes only a few minutes on a four-core machine and are easily parallelizable since each inversion is independent of all the others. Nonetheless the issue of selecting the smoothing parameter automatically and objectively remains irksome. We have employed the statistical argument of minimizing information loss by using the ABIC. However, we foresee that as computational power increases it will become feasible to use fully probabilistic techniques to determine the earthquake source (*Minson et al.*, 2013). Such Bayesian approaches are desirable because they sample all models that are consistent with observations while restricting the ensemble to those that fit the assumptions about the underlying physics. This is preferable over solutions that require regularization or smoothing which is, in a sense, an artificial numerical restriction not strictly based on a tangible physical constraint. Such Bayesian algorithms are currently burdensome because of the large number of free parameters involved in computing the earthquake source. Recently these approaches have become more computationally tractable with better sampling techniques [Minson et al., 2013] but not yet to the degree where they can be computed immediately after the earthquake origin with ease. However, the advances are promising. In this probabilistic paradigm one can produce rapid estimates of hazard curves along the coastline (*González et al.*, 2009) instead of point estimates of inundation intensity. One could then more adequately characterize the hazard and contemplate the creation of higher-level products such as expected economic impact and rapid loss calculations similar to what the PAGER product does for earthquake shaking.

This is a rapidly evolving field. Leveraging earlier results from Chapter 3 we have demonstrated an end-to-end automatable methodology that minimizes operator interaction. Starting with the land-based data that are available many minutes before sea-borne measurements, we determine basic source parameters,

i.e., magnitude, type of faulting and geographic extent from the line source CMT inversion. This then allows selection of appropriate fault-model geometry to launch a heterogeneous finite fault slip inversion. Once the slip inversion is computed, sea floor deformation can be calculated and used as the initial conditions for a model of the tsunami. This yields a first forecast of tsunami intensity and can be used for warning. Then, as time goes on, wave gauges information is ingested and the inversion rerun. The new updated earthquake source is used to obtain a new tsunami model and forecast. For the Tohoku-oki earthquake the first forecast is available at 157s after OT. At 20 minutes after origin time a revised forecast that has high inundation amplitudes is determined; recall maximum inundation at the closest points on the coast was not reached until 30 minutes (*Ozaki*, 2011). After this time (OT+30min) the earthquake source and tsunami forecasts remain without major changes. We have proposed an indirect form of forecast and warning that is much improved because it relies partly on direct measurements of tsunami wave propagation to compute the earthquake source and not just on traditional seismological measurements.

Thus, we contend that we have demonstrated that with current geophysical sensor technology and algorithms the expectation of detailed and timely tsunami forecast and warning in the coastal areas adjacent to large earthquakes, regardless of their faulting type and location, is a realistic one.

5.5 Joint Kinematic Inversion of Land- and Ocean-Based Sensors

We can incorporate the tsunami waveforms into the kinematic inversion following the same modelings steps as in Chapter 4 and Section 5.2 and study the effects on the source and tsunami propagation and inundation pattern. We compute the time dependent motion of the seafloor using the frequency wavenumber method of (*Zhu and Rivera*, 2002) for 1m of slip on each of the 189 subfaults. The time dependent coseismic motions of the seafloor are then used as the starting conditions for tsunami simulations in Geoclaw. We model 60 minutes of the resulting

tsunami from slip on each of the subfaults at the locations of the wave gauges. These are then considered kinematic tsunami Green's functions and incorporated into the kernel matrix **G**. We then follow the same approach as before and utilize Akaike's Bayesian information criterion to determine the optimal spatial and temporal smoothing for the inversion.

There is good reason for incorporating the tsunamis waveforms into he modeling process. Generally it was believed that instantaneous slip as in Sections 5.1-5.4 was sufficient to model tsunami propagation. *Fujii and Satake* (2007) found for the 2004 M_w9.2 Sumatra event that the tsunami waveform data were largely insensitive to kinematic models of the source. However, in that study they relied mainly on far field data. Later *Satake et al.* (2013) demonstrated that for the 2011 Tohoku-oki case kinematic models better explained the tsunamis waveforms and inundation data of *Mori et al.* (2012). It is reasonable to assume that in the tsunami near-field time dependent deformation of the sea floor provides a better initial condition for propagation modeling. Following we show the results of the joint kinematic inversion of the seismogeodetic displacement, velocity and tsunami data. *Satake et al.* (2013) performed the kinematic inversion of only the tsunami data on a coarse 55 subfault model and obtained 69m of slip at the trench and up to 10m of slip at depth. By incorporating the land data as well we can obtained a finer picture of the source. Furthermore, *Satake et al.* (2013) used a totally reflecting boundary condition at the coast while with Geoclaw we can compute physically realistic tGFs that allow wetting and drying of the coastal cells in the model. Additionally, since the coastal tide gauges display significant non-linear behavior (Figures 5.3 and 5.4) and are not well fit by the linear inversion (Figure 5.15) we will disregard them for the following models and we will retain only the 2 ocean bottom pressure gauges and the 6 RTK GPS buoys (Table 5.1).

5.5.1 Tsunami Generation with 3D Coseismic Motion

Another improvement on the static modeling results of Sections 5.1-5.4 is that we account for the tsunami generation effects of horizontal coseismic motions as well as the vertical ones. *Tanioka and Sataka* (1996) recognized that

steeply sloping bathymetric features subject to large horizontal motions contribute to tsunamigenesis. This effect is generally disregarded and only coseismic vertical deformation is incorporated into the tsunami source, as we did in the static modeling case. *Fujiwara et al.* (2011) observed 50+m of horizontal motion at the trench, this encourages us to account for these effects. Figure 5.12 illustrates how horizontal advection of sloping bathymetry can cause pseudo-uplift of the seafloor.

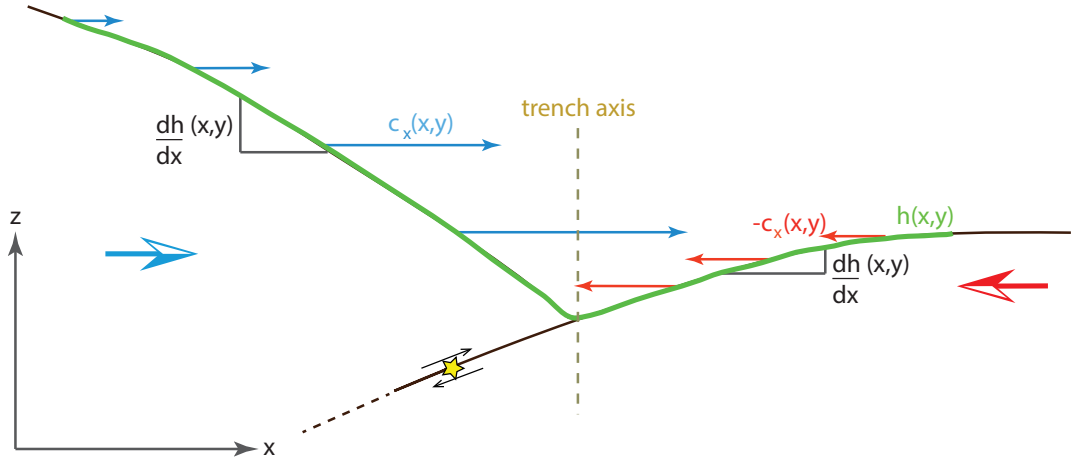


Figure 5.12: Schematic of tsunami generation from horizontal coseismic motion c_x, see text for details.

We approximate bathymetry as a smooth function which depends on two horizontal coordinates $h(x, y)$. A dislocation at depth will cause coseismic motions $c_x(x, y)$ and $c_y(x, y)$ of the bathymetry in both horizontal directions. If there are sloping features in the bathymetry this horizontal deformation causes an apparent vertical motion which we can locally approximate by considering the directional derivative of bathymetry. Then the total apparent vertical deformation Δh will be the sum of the coseismic vertical deformation, Δz and the horizontal one due to the motion of the sloping features such that

$$\Delta h(x, y) = \Delta z(x, y) - c_x(x, y) \cdot \frac{dh}{dx}(x, y) - c_y(x, y) \cdot \frac{dh}{dy}(x, y) \; . \qquad (5.1)$$

Note the negative signs in front of the directional derivatives. These indicate that the downward sloping feature west of the trench axis (negative derivative) moving in the positive x direction should cause uplift, as should the upwards

sloping feature east of the trench axis moving in the negative x direction. This differs from the initial condition we used in the static approximation where we simply have $\Delta h(x, y) = \Delta z(x, y)$. These adjustments are considered in generating the kinematic Green's functions as well as the inundation models that follow. To further illustrate the effect that the sloping bathymetry can have in vertical deformation consider Figure 5.13 where we show the directional derivative of the SRTM30+ bathymetry computed along the average trench-normal direction. The red colors indicate that positive horizontal motion causes uplift, while the blue ones that positive motion causes apparent subsidence. Along the frontal part of the continental slope and close to the trench the values of the derivative are as high as 0.3, the values are also high along the sea mounts south of 37°N. This means that for every meter of horizontal motion 30cm of apparent vertical motion will be generated. Clearly, this is not a signal that should be ignored.

5.5.2 Inversion Results

Figures 5.14 and 5.15 show the results after incorporating the 8 wave gauge stations into the inversion procedure. Peak slip is now 63m, compared to the 52m from the land-only inversion of Chapter 4 and moment is 5.51×10^{22}N-m (M_w9.09) compared to 4.89×10^{22}N-m (M_w9.06) for the land-only inversion. The final slip of the land-only model (Figure 5.14a) prefers a horizontally symmetric slip distribution about the hypocenter. For the joint inversion (Figure 5.14b) slip is 25m or larger for the top 20km of the fault only south of the hypocenter while north of the hypocenter large slip is confined to the shallowest 10km. There is also a notable shallowing of peak slip in general with the joint model having a larger accumulation of shallow slip. The total source time functions (Figure 5.15a) are very similar. The timing of peak moment rate is delayed in the joint model from 75 to 80s but its value is unaltered. Furthermore, the joint model has an increase in moment relative to the land-only model at times after peak moment rate although the total duration is similar (190s). A notable difference between both slip inversions are the two patches of 10m of slip on the shallowest portions of both northern and southern extremes. While the land-only inversion does have

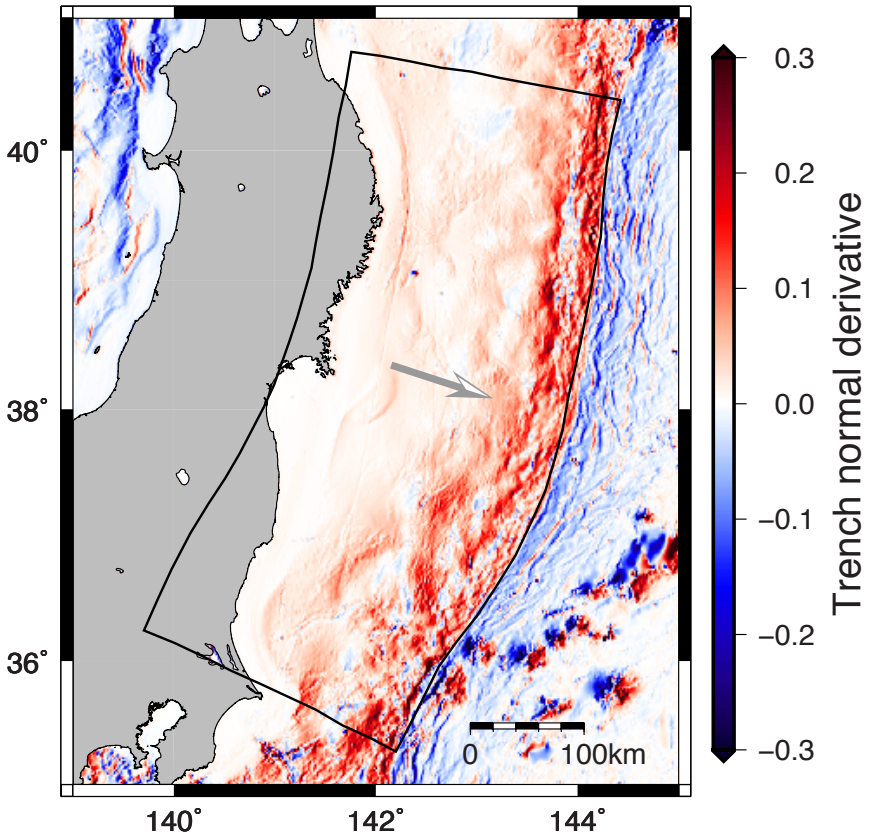


Figure 5.13: Trench normal derivative of bathymetry computed in the direction indicated by the grey arrow. The black outline is that of the fault model used for the inversion.

slip at the edges of the model (about 5m) there is a visible increase of slip in the joint model. The fits to the wave gauge data are good (VR is 71%) (Figure 5.15b), notably the peak amplitudes at both pressure gauges (OB.TM1 and OB.TM2) are well modeled. As in the static case we note that the northernmost buoy (BY.IWN) shows the poorest fit between data and synthetics.

As before we can also study the individual subfault source time functions (Figure 5.16). Recall that plotted is the moment rate for every subfault with their respective 90% confidence intervals (CIs). The white lines indicate the lower bounds of the 90% CIs and the grey hatched areas the upper bound of the CI. The STFs are colored by pseudo-rupture velocity. This coloring indicates how fast a rupture front would have to travel to each subfault at a particular instant in

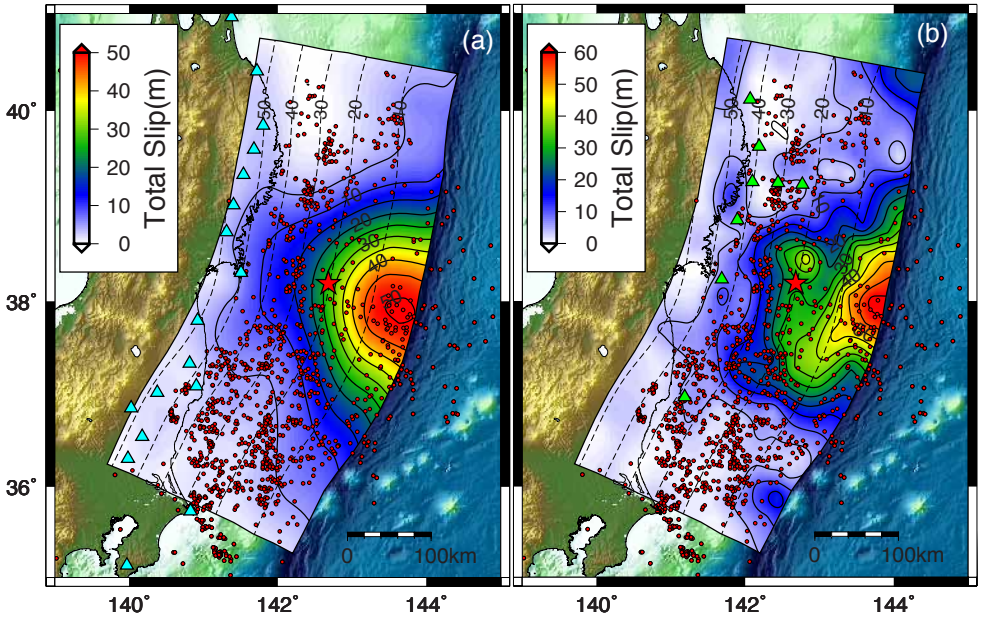


Figure 5.14: Joint land- and ocean-based data inversion results. (a) Is the preferred result from the inversion of seismogeodetic displacement and velocity waveforms (Chapter 4). Triangles are the land stations, red dots are 2 weeks of aftershocks and the star is the hypocenter. Slip is contoured every 5m and depths to the slab every 10km. (b) Is the result after incorporating the 8 wave gauge stations denoted by triangles. Red dots are 2 weeks of aftershocks and the star is the hypocenter. Slip is contoured every 5m and depths to the slab every.

time. A comparison with the solution from Chapter 4 (Figure 4.10) shows that the model is largely unchanged for the subfaults down-dip from the hypocenter. There seem to be at least two pulses of slip, the first one has low peak moment and very short durations. The second pulse propagates down dip from the hypocenter and then spreads laterally quite quickly, it has longer durations (about 20s) and higher moment rates.

Up dip the behavior in the joint model is different from the model in Chapter 4 (Figure 4.10). As we noted in the total slip distribution from Figure 5.14b moment release north of the hypocenter is smaller. More importantly the source time functions are significantly longer for the shallowest 2 rows of subfaults and north of the hypocenter (along strike indices 5-9). In the preferred model from Chapter 4 those shallow source functions had durations of the order of 50s, while

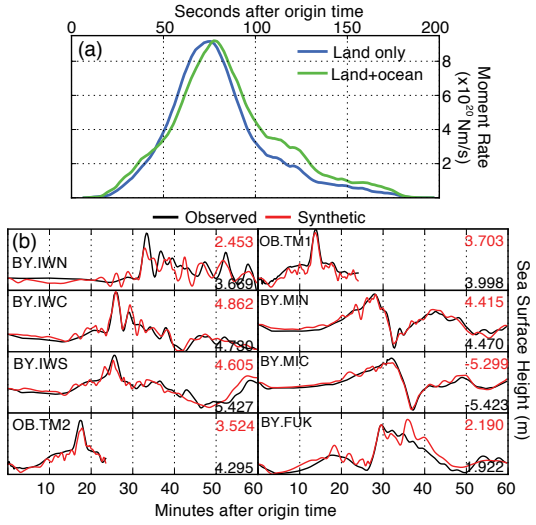


Figure 5.15: Joint land- and ocean-based data inversion results. (a) Is the comparison between the source time functions of both inversions. (b) Is the fits to the wave gauge data. The black lines are the observed and the red the synthetics. The numbers denote peak amplitudes

in the joint inversion here the STFs can be as long as 100s, essentially occupying the entire allowed duration. South of the hypocenter on the shallow subfaults duration of the STFs does not increase as much, but there is a second pulse of slip in the subfaults with largest moment release (along-strike indices 10-12) whose amplitude is larger than in the preferred model of Chapter 4. Overall, the effect of including the tsunami data is to produce a more pronounced pattern of shallow slip, to shift more of the moment release to the southern half of the slab model and to produce longer duration STFs on the shallowest subfaults.

Static inversion with tsunami data has been performed by other authors (*Fujii and Satake*, 2007; *Gusman et al.*, 2012; *Romano et al.*, 2012) and by us in Section 5.1-5.4. Additionally, it has become routine to adjust geodetic (*Hill et al.*, 2012) and seismic source models (*Simons et al.*, 2011; *Lay et al.*, 2013) iteratively until they fit observed tsunami waveforms or inundation observations. Kinematic inversion is only a recently demonstrated possibility (*Satake et al.*, 2013) with tsunami waveforms. To our knowledge this is the first time that a kinematic inversion has included both tsunami waveforms and land-based data. As discussed in Chapter 4 down-dip of the hypocenter our results are consistent with other seismic

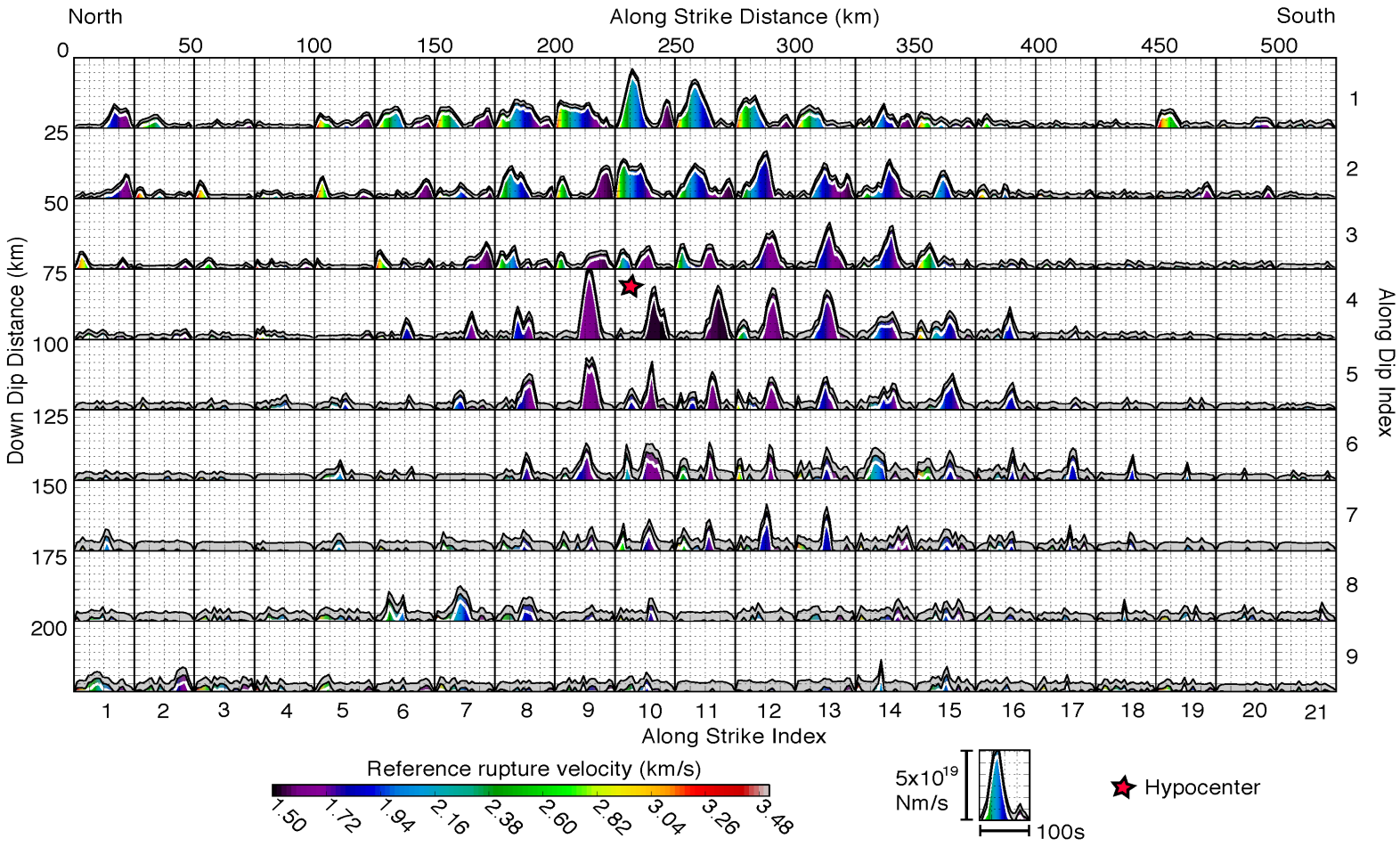


Figure 5.16: Subfault source-time functions (STFs). The 90% confidence intervals are indicated by the white line and the solid grey hatched area. The coloring under the STFs represents the pseudo rupture velocity. The red star indicates the hypocenter. All STFs are plotted at the same scale.

slip inversions and with back projection studies. Up-dip our results are wholly consistent with the tsunami-only inversions of *Satake et al.* (2013); they observe a similar two step slip pattern with equally long rise times. These extended slip durations at shallow depth are intriguing. The shallower portion of the megathrust is expected to have low friction material (*Lay et al.*, 2012) and drilling results support this for the 2011 Tohoku-oki event(*Fulton et al.*, 2013), which should result in long STFs (*Kanamori and Brodsky*, 2004), however the seismogeodetic data only inversion of Chapter 4 in no way require STFs as long as observed with the inclusion of tsunami data. Irrespective of the smoothing applied we do not observe 100s long STFs in the seismogeodetic-only inversion. It is unclear whether the tsunami data themselves are sensitive at temporal scales of tens of seconds to changes in source duration and further sensitivity and resolution studies are necessary to ascertain whether these long slip durations are a robust feature. Perhaps the protracted slip durations on the shallow sub faults is aseismic. The patches of large slip at the northern and southern extremes of the fault model are also observed by the tsunami-only inversion of *Satake et al.* (2013). Note from the aftershock distribution in Figure 5.14b that the main asperity produces a significant number of events in the outer rise, most of them normal faults (*Asano et al.*, 2011). However, in the outer-rise of the two higher slip patches at either extreme of the fault model there is no aftershock activity. This raises the possibility that those are artifacts introduced by the tsunami data. If there are secondary and unmodeled sources of tsunami energy these will be mapped onto the slip inversion. It is quite likely this is the case and future improvements will include a more physically realistic tsunami source. For example *Kawamura et al.* (2012) documented compelling evidence from underwater cameras for mass wasting offshore Sanriku. *Arai et al.* (2013) also demonstrated from ocean bottom pressure sensor data, heat flow measurements and cores the existence of wide-spread turbidity currents in the northern region of the Tohoku-oki source; these could very well contribute to tsunami genesis. Additionally *Tsuji et al.* (2013) found extensive extensional faulting with measurable vertical motion in the overriding crust landwards of the continental backstop. *Grilli et al.* (2013) also showed with 3D finite element modeling that

using realistic earth structure models can improve models of tsunami generation while *Ma and Hirakawa* (2013) demonstrated that inelastic behavior of the wedge can also significantly alter the vertical deformation pattern of the shallowest portion of the megathrust environment. The tsunami waveforms are likely sensitive to most if not all of these phenomena and it is possible that some of the differences between the land-only and the joint models arise as a consequence of this. Nonetheless, and overall it seems that inclusion of the tsunami data produces a slip pattern with significantly more detail in the shallow portion of the megathrust than previous studies have been able to resolve.

5.5.3 Tsunami Modeling Results

When employed as an initial condition for tsunami modeling, the kinematic inversion result of Figures 5.14 and 5.16 has a significant effect on the tsunami intensity and propagation pattern. Figure 5.17a shows the total vertical deformation including the contribution of the horizontal motion of bathymetry. There is a broad region around the epicenter of long wavelength uplift between zero and about 7m which is largely responsible for the first pulse of tsunami energy observed at the wave gauges (Figure 5.15b) as a slow and steady increase in sea-surface height. At the frontal part of the continental slope and particularly at the trench we have much larger uplift with shorter wavelength features (up to 22m of uplift). This deformation is associated with the short wavelength high amplitude tsunami peak which is especially visible on stations OB.TM1 and OB.TM2 at 14 and 18 minutes after origin time respectively. It is interesting to note that both deep slip and shallow slip contribute to tsunamigenesis. It is also important to remark on the contribution of horizontal motion of bathymetry to the uplift pattern. Figure 5.17b shows the contours of eastward horizontal displacement predicted at the seafloor and the associated predicted uplift computed using Equation 5.1. The uplift is largest in the regions of largest horizontal motion and steepest terrain (Figure 5.13), namely closest to the trench (up to 3m), making this an important contributor to the tsunami initial condition. On the continental shelf as expected horizontal motions contribute very little to the vertical deformation pattern. These

results agree well with the predictions of *Tanioka and Sataka* (1996) who argued that horizontal motions could account for a significant portion of the tsunamigenic uplift.

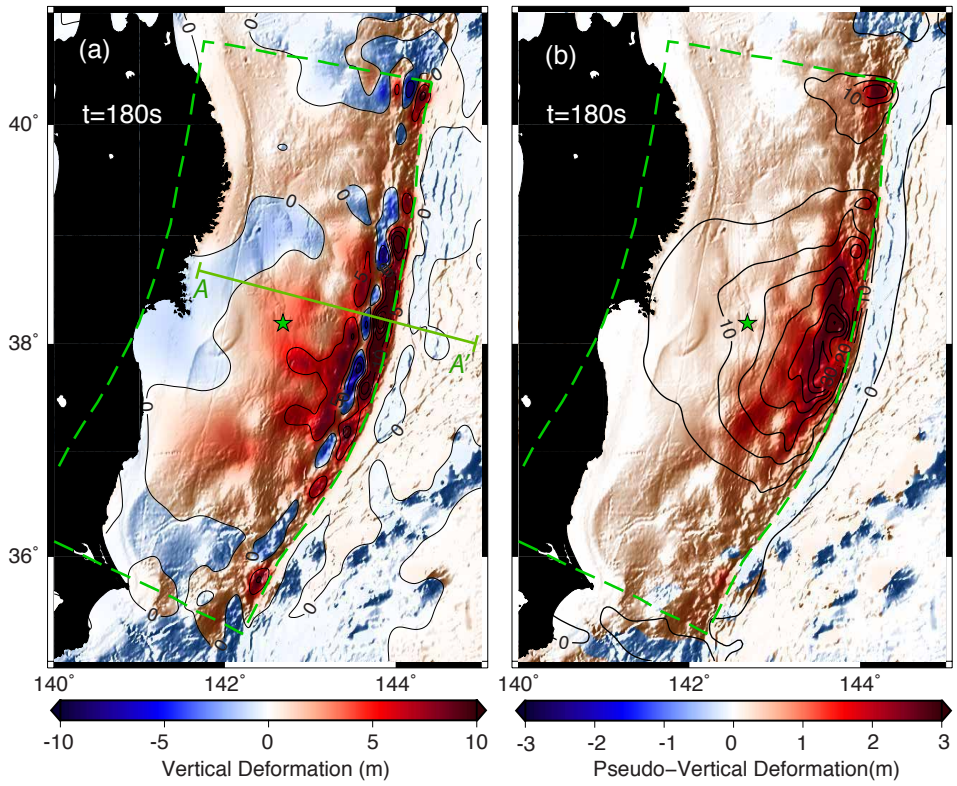


Figure 5.17: Vertical deformation predicted by the joint slip inversion at t=180s after origin time. (a) Total vertical deformation including effects from horizontal motion of sloping bathymetry. Contours are every 5m, the green star is the epicenter and the green box is the outline of the fault model. The profile A-A' is used later on in Figure 5.19(b) Contribution to vertical deformation exclusively from the horizontal motion of the sloping bathymetry. The contours are the eastward horizontal deformation predicted by the slip inversion.

The net effect of the improvements to the tsunamis source discussed in this section can be seen in Figure 5.18. Figure 5.18a is the maximum tsunami amplitude predicted when using the joint kinematic inversion as the initial condition. It predicts large tsunami amplitudes, in excess of 10m along the coast between 37.5°N and 40°N. There are two main lobes of tsunami energy that focus on the Sanriku coast, while amplitudes in Sendai Bay are also large, most likely due to bay resonance effects (*Satake et al.*, 2013). The model in Figure 5.18b is

the result of removing the contribution of horizontal advection of bahtymetry from the tsunami's initial condition. The basic propagation pattern is similar but the amplitudes are diminished.

The result in Figure 5.18c is interesting. This is the maximum tsunami amplitude that results from applying the deformation pattern of the joint solution instantaneously, as we did for the static cases in Section 5.2. The expected maximum amplitude is significantly larger. This can be understood by studying Figure 5.19 where we plot snapshots of the first 180s of tsunami propagation on a trench-perpendicular profile for both the kinematic and the static initial condition. Even though the total final uplift is the same for both models, for the static initial condition this deformation pattern is applied instantaneously and the resulting initial tsunami peak is as large as the maximum uplift in the model (22m). The tsunami wave then propagates outwards. In the kinematic initial conditions we observe a smoother transition from the rest state to the uplift of the sea surface. Additionally, recall that tsunami propagation speed is $\sqrt{gH}$ where g is the acceleration due to gravity and H the water depth. Water depths of 3000-8000m between the shelf break and the trench yield propagation velocities of 10 to 17 km/min. This means that there is ample time during the approximately 3 minutes of source duration for the tsunami waves to propagate away from their particular source regions and interfere with tsunami waves being generated elsewhere. This also explains why at basin-wide distances considering a kinematic versus a static source has little impact on propagation modeling (*Fujii and Satake*, 2007), as time progresses the differences between the two become smaller.

These results do not mean however, that static source models produce larger tsunami amplitudes. When we use static tsunami GFs as in Figure 5.7 we obtain similar maximum expected amplitudes. With static tGFs the inversion process adjusts by placing slip elsewhere on the slab in order to account for the observed time series at the wave gauges. Rather the importance of this relies in that if a tsunami modeler uses a seismically derived kinematic model as an initial condition to study near-field tsunami propagation (*MacInnes et al.*, 2013) then they will most likely obtain larger amplitudes if applying it as a static model. We find

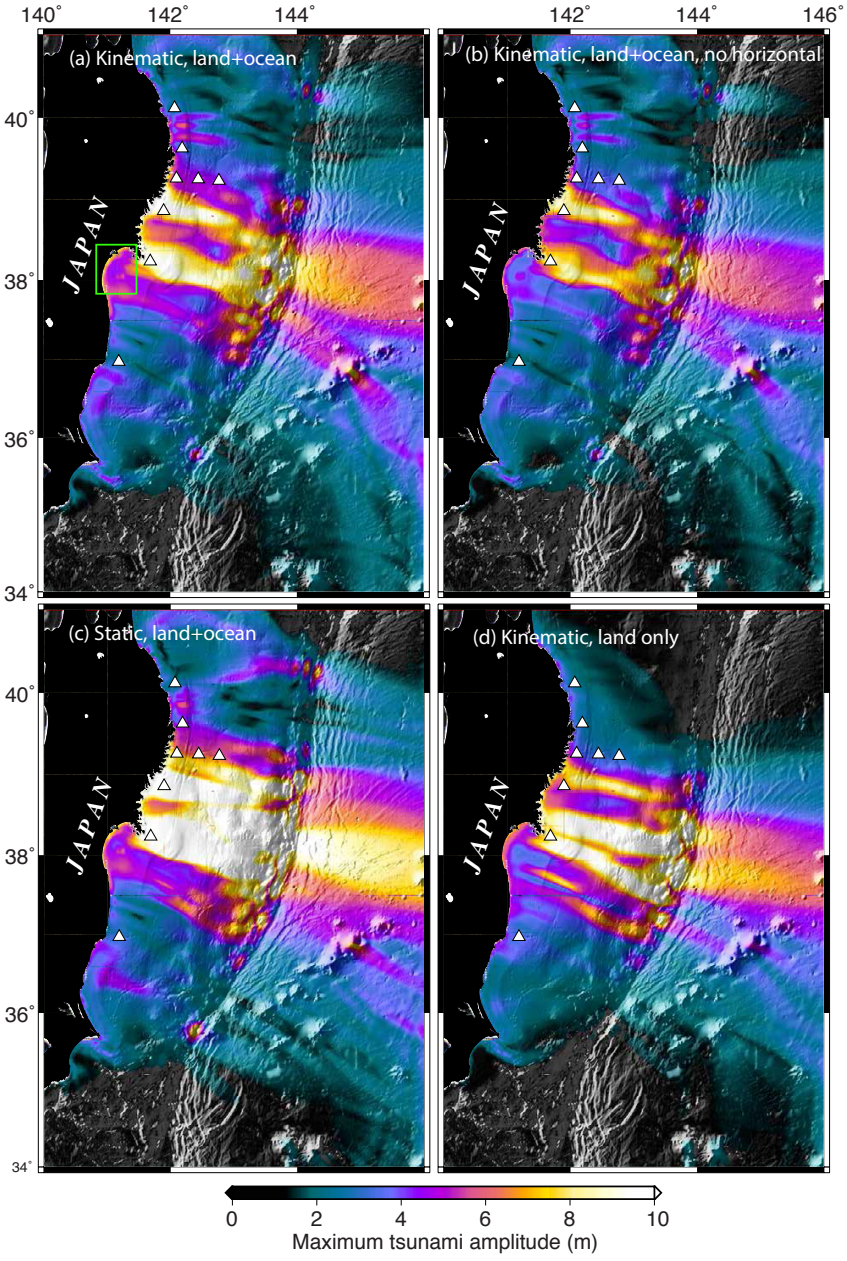


Figure 5.18: Maximum tsunami amplitudes with several source models. (a) is the model from the kinematic joint inversion of land- and ocean-based data. The green rectangle is the area used in Figure 5.21 (b) Is the model from the joint kinematic inversion with the contributions of the horizontal motion of bathymetry removed. (c) Is the model from the joint inversion but applied instantaneously as a static model. (d) Is the model resulting from the land-based only kinematic inversion of Chapter 4

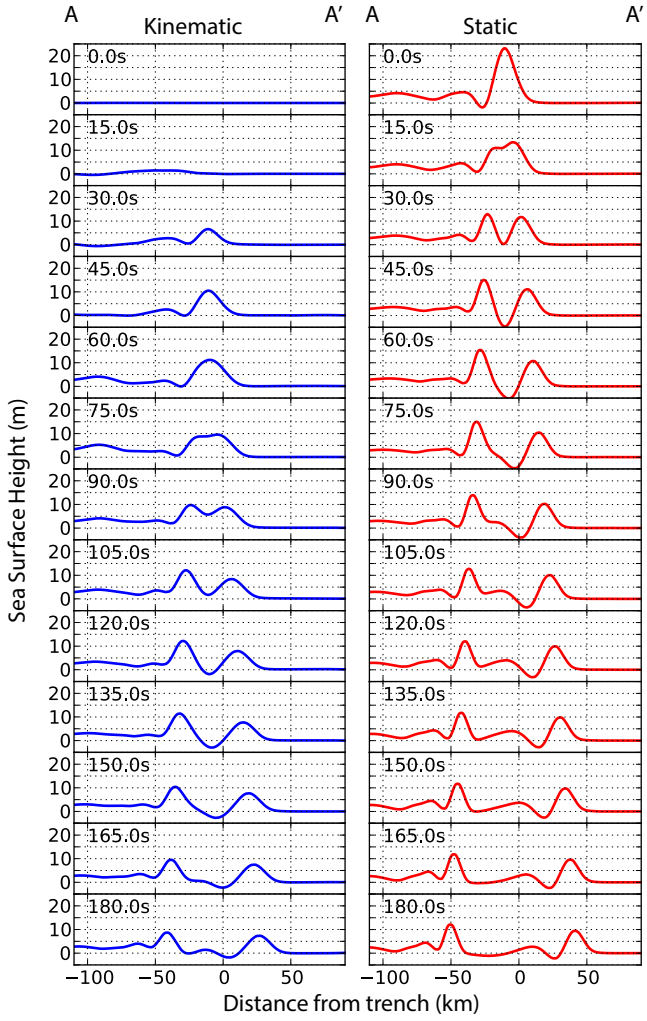


Figure 5.19: Trench perpendicular profile of tsunami propagation along profile A-A' (Figure 5.17). Shown are snapshots of the first 180s of tsunami propagation for (left) the kinematic initia condition and (right) the static initial condition)

that accounting for the time-dependent deformation of bathymetry is important. Finally, in Figure 5.18d we plot the maximum expected tsunami amplitude using the land-only kinematic inversion as the initial condition. The pattern is similar, but in general smaller, this is unsurprising considering the joint model places more slip at the trench than the land-only model. However it does underscore that even if wave gauges are unavailable an earthquake source model derived from regional seismic and geodetic data can provide a much improved estimate of the tsunami intensity.

Table 5.3: Forecast statistics of the inversions and inundation models. The first column is variance reduction of the modeled inundation compared to the surveyed inundation from *Mori et al.* (2012). The 2nd column is the number of inundation survey points inundated by the model

Model	Survey VR(%)	Survey Points Inundated
Static, land-only	85	956/2250
Kinematic, land-only	87	1334/2250
Kinematic, land+ocean	86	1598/2250
Kinematic, land+ocean, no horizontal	85	1209/2250

A detailed analysis of the small scale inundation pattern produced by the different models reveal their capabilities at producing detailed forecasts. Figures 5.20a-d and Table 5.3 compare the inundation forecast results of the kinematic model to those of the land-only static inversion of Section 5.3 (Figure 5.8a). The improvement from the kinematic inversion of land-only data is significant; the kinematic forecast inundates 1334 of the 2250 survey points compared to only 956 from the static forecast. Addition of the tsunami wave-gauges to the inversion further improves the forecast so that 1598 of the 2250 forecast points are inundated with 86% variance reduction. Particularly in the full (land/ocean) model's forecast, the high inundation amplitudes along the southern portion of the Sanriku coast (between 38.4°N and 39.2°N) is well captured. This is an improvement over the joint static models of Figure 5.8 which had trouble predicting large tsunami amplitudes in some portions of this segment of the coast. The forecast of the northern Sanriku coast is slightly better with more points inundated but we remain unable to model the large inundation amplitudes in the narrow valleys. We argued before (Section 5.3) that this is due to the limited resolution of the bathymetry data set used here. Note, however, that removing the tsunami generating contributions of horizontal advection of topography greatly diminishes the intensity of the predicted inundation (Figure 5.20d and Table 5.3) further demonstrating the importance of this source term. We conclude that the full (land/ocean) kinematic model provides the best prediction of tsunami inundation. We stress again that the land-only kinematic model is a significant improvement over static dislocation models and provides a reliable tsunami source to produce inundation forecasts.

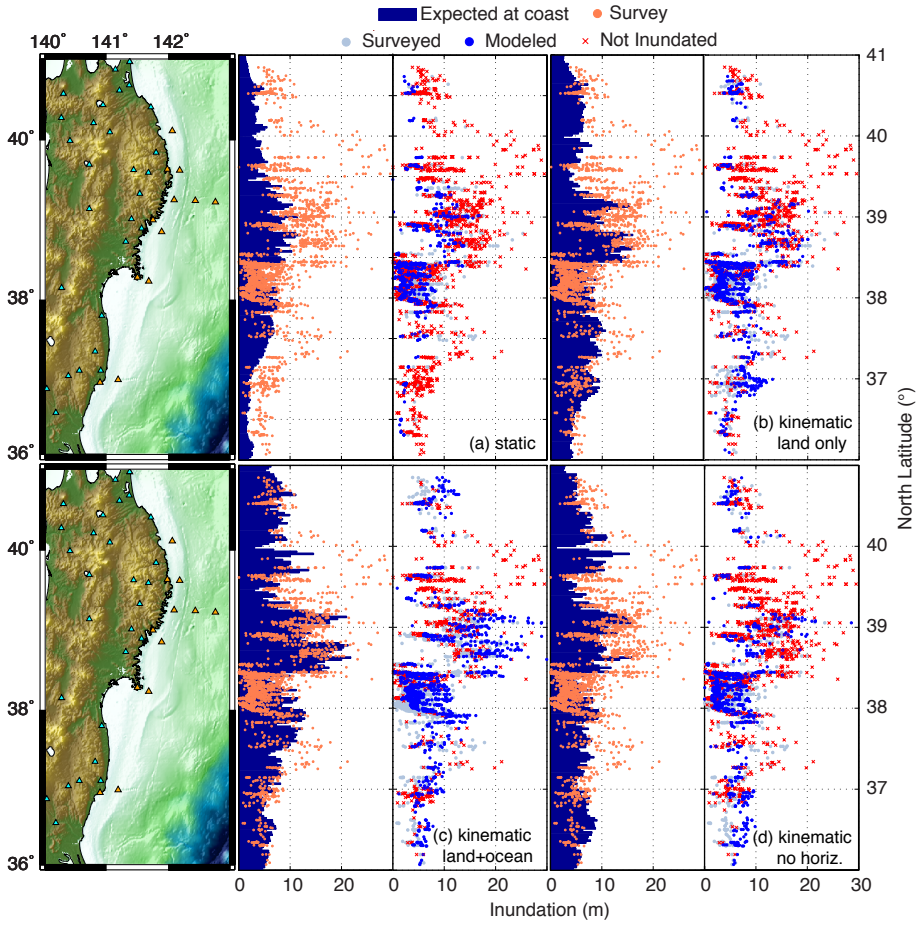


Figure 5.20: (a)Inundation results for the land-only static inversion of Section 5.3. The left side of each of the four model panels shows with blue bars the inundation predicted by the model at the coastline (the pre-tsunami land-water boundary) compared to the surveyed inundation inland (orange dots). The right side of each of the four model panels shows the direct comparison between the observed survey inundation (grey dots) and the inundation predicted by the model at the survey points (blue dots). The red crosses are survey points that were not inundated by the model. (b) Inundation forecast results for the land-only kinematic inversion. (c) Inundation forecast results for the full land and ocean kinematic inversion. (d) Inundation forecast results for the full land and ocean kinematic inversion without the contribution of horizontal topographic advection.

Of all the source models computed in this dissertation for the 2011 Tohoku-oki event, the full kinematic inversion of land and ocean based data is the most comprehensive one. The tsunami forecast statistics are good enough that we can, with some confidence, produce inundation maps of both regional and local scale.

Such tsunami intensity maps can be extracted from the simulation output for any region of interest. The scale of these maps is inherently limited by the discretization of the topography and bathymetry data sets used in the simulation. If a certain application requires more detail in the inundation forecast then it will be necessary to use finer data sets, as provided, for example, by lidar and multi-beam. In Figure 5.21 we show an example for Sendai Bay where run-up distances were long (*Mori et al.*, 2012), often of the order of kilometers. The snapshot at zero minutes shows the initial configuration of the coastline as defined by the SRTM3 and SRTM30+ topography and bathymetry data sets. At 45 minutes the main tsunami arrival enters the bay, at 60 minutes inundation commences on the northern portion of the bay, previously dry cells in the model become inundated. The main wavefront arrives at the shoreline of the central and southern portions of the bay. At 80 minutes there is significant inundation along the entire coastline of the bay with sunup distances of the scale of kilometers. We can observe detailed wave structure as the inundation channels up valleys and rivers. The blue dots in the snapshots are the locations of the survey points from *Mori et al.* (2012). We can observe that the general inundation pattern matches well the distribution of survey points in agreement with the high variance reduction of the simulation and the results shown in Figure 5.20. The importance of post-event surveys cannot be overstated. As demonstrated throughout this Chapter they provide the only ground truth and, thus, critical for correct assessment of the forecasting capabilities of the any inverse model of the earthquake or tsunami source, regardless of the approach or data types used.

With adequate planning and selection of target areas it should be possible to produce inundation maps like these for key areas (such as nuclear power plants) where a detailed forecast of inundation is required to make emergency response decisions. We can also see from Figure 5.21 that there is significant structure to the tsunami in the open waters of the bay. We have not discussed other physical variables in this work but quantities such as flow speed are often more important for infrastructure such as ports and harbors (*Lynett et al.*, 2014) than the tsunami amplitude. It is possible to model them with the same techniques discussed in this

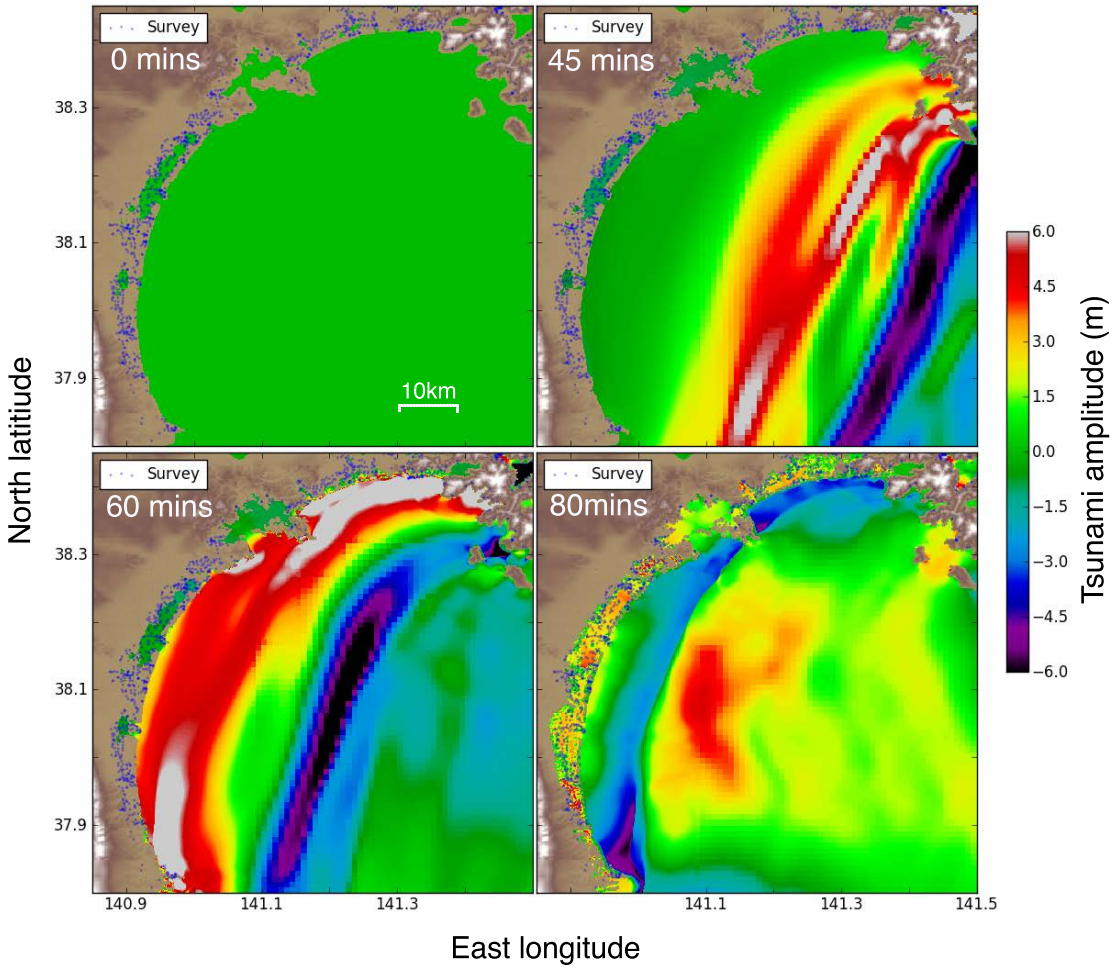


Figure 5.21: Four snapshots in time of inundation modeling of the coast surrounding Sendai Bay. The tsunami amplitude refers to sea surface height for a tsunami over the ocean and flow depth for a tsunami over land (Figure 5.2. The blue dots are the locations of the survey measurements from (*Mori et al.*, 2012).

Chapter.

There are still significant improvements to be made. We have assumed with both the static and kinematic initial conditions that the water column responds instantaneously to the vertical motion of the sea floor. Realistically there is a finite time over which the sea floor deformation is transferred to the sea surface. This can be modeled as a superposition of acoustic waves (*Ohmachi et al.*, 2001), but there are few studies that take this into account and the magnitude of the error incurred from neglecting acoustic waves is unclear. *Ohmachi et al.* (2001) suggests, for ex-

ample, that when the natural acoustic period of the sea water layer (which depends exclusively on depth) is close to that of the oceanic Rayleigh waves then these can be significant tsunamigenic contributors and amplify the sea surface height. At higher frequencies *Kozdon and Dunham* (2014) have shown that acoustic waves might reflect important characteristics of the shallow source. Future developments should include this extra source term and quantify its importance. As far as inundation is concerned by using the depth-averaged shallow water equations we are neglecting vertical flow velocities (*Lynett*, 2006). We have also not accounted for the entrainment of sediments into the flow (*Simpson and Castelltort*, 2006). Both of these assumptions may need to be relaxed for meter scale forecasts of tsunami inundation to become reliable.

5.6 Acknowledgments

Sections 5.1-5.4 have been published in **Melgar, D. and Bock, Y. "Near-Field Tsunami Models with Rapid Earthquake Source Inversions from Land- and Ocean-Based Observations: The Potential for Forecast and Warning", *J. Geophys. Res.*, 118(11), 2013**. This research was funded by the NASA Earth and Space Science Fellowship NNX12AN55H, and NASA AIST-11 NNX09AI67G and ROSES NNX12AK24G awards. Diego Melgar Moctezuma conceived this study, wrote the code and analyzed a large portion of the data. He was also the lead author and coordinated the manuscript preparation. Brendan Crowell developed and selflessly shared the first version of the coseismic inversion code that is the kernel of the joint inversion code. Discussions with Randy LeVeque and David George were invaluable to our understanding of tsunami science and modeling. We are indebted to Emanuel Garcia, Xiaopeng Tong, Paul Wessel, and David Sandwell for their assistance with manipulation of the topography and bathymetry data sets. Ergin Ulutas provided helpful pointers on dealing with the wave gauge measurements. This work was largely conceived during the 2012 Gene Golub SIAM Summer School on Simulation and Supercomputing in the Geosciences and the 2013 Pan-American Advanced Sciences Institute on The science

of predicting and understanding tsunamis, storm surges and tidal phenomena. We are grateful to the organizers, lecturers, and students at both those workshops. We extend our thanks to the Japanese Meteorological Agency for access to accelerometer and tide gauge data; the Geospatial Information Authority for access to GPS data, the Earthquake Research Institute for access to ocean-bottom pressure data, and the Nationwide Ocean Wave information network for GPS buoy data. GeoClaw is available from the developers at http://www.clawpack.org.

Chapter 6

Conclusions and Future Outlook

The unifying theme throughout this dissertation has been that the optimal combination of geophysical data sets provides faster and more robust images of the seismic source and that this in turn can be used for hazards mitigation.

In Chapter 2 with data from the M_w7.2 April 4, 2010 El Mayor-Cucapah earthquake in northern Baja California we convincingly demonstrated that regional high-rate real-time GPS networks can become an essential tool for early warning and rapid earthquake response. We took this one step further by applying a Kalman filter to obtain an optimal combination of data from collocated high-rate GPS and very-high-rate accelerometer stations, which takes advantage of the strengths and minimizes the weaknesses of both data types. The result is a new methodology for providing displacement time series with millimeter precision which can be used to better characterize the seismic source. It provides an improved broadband record of ground displacements and velocities over the full range of frequencies sampled by the accelerometer data, as well as the static deformation. This approach is capable of precisely detecting P-wave arrivals of medium to large near-source earthquakes with dense networks of collocated GPS and seismic instruments, making it particularly valuable for earthquake early warning systems and rapid earthquake response. It also provides a powerful new analysis tool to study the rupture characteristics of large earthquakes. These results have been published in *Bock et al.* (2011) and it's applications to early warning magnitude scaling have been published in *Crowell et al.* (2013).

We also showed that automatic baseline correction schemes from accelerometer data alone can, for selected stations, provide useful strong motion (dynamic) displacements information. However, the static offsets determined by such automated schemes are often unreliable. Furthermore, adding a static field constraint to the baseline correction procedure does not guarantee convergence to the correct value and even if the correct static offset is obtained; other parts of the waveform might be in error by large amounts. The objective estimation of baseline-corrected displacements, even when incorporating reliable and independent information such as the static field estimated from GPS remains elusive. We have demonstrated that such a scheme, which eliminates the need for subjective judgment, is still fraught with problems. We tested the assumption that baseline corrections introduce errors only at long periods outside what is of engineering interest and find it does not hold for the 2011 Tohoku-oki data set. Analysis of the power spectral densities and displacement response spectra demonstrate that the frequency domain error incurred by the baseline correction is well within the frequency range of interest to both seismology and engineering. The Kalman filter method, which combines high rate GPS and accelerometer data, is not affected by these problems. We demonstrated that even for K-net accelerometer data set which displays behavior associated with large baseline offsets the Kalman filter solution routinely produces reliable broadband displacements. These results have been published in *Melgar et al.* (2013a)

In Chapter 3 we discussed the issue of rapid modeling of the earthquake source with static field data. We presented an approach for real-time computation of centroid moment tensors for large events from local and regional GPS displacement records. We used the coseismic offsets and Greens functions for a layered Earth to relate the deformation at the surface with source parameters at depth. We demonstrated the algorithm with two test cases, the 2010 M_w 7.2 El Mayor-Cucapah earthquake and the 2003 M_w 8.3 Tokachi-oki earthquake. In both cases we have shown that provided with low latency access to displacement data it is feasible to obtain a robust centroid location and moment tensor solution within the first 2-3 minutes after rupture initiation. The algorithm is computationally

efficient and thus amenable for rapid modeling and early detection. These results were published in *Melgar et al.* (2012)

Also in Chapter 3 we discussed the application of the CMT methodology as a starting point for a static slip inversion of the 2011 M_w 9 Tohoku-oki event. Considering the review of the sequence of events at the USGS National Earthquake Information Center (NEIC) (*Hayes et al.*, 2011), there are several stages where the independent information provided by the seismogeodetic time series could have been helpful for a great event such as Tohoku-oki. Both the NEIC and the Pacific Tsunami Warning Center obtained preliminary teleseismic P wave locations and mechanisms within 5 minutes of the origin time, but the first public release was delayed until 9.7 minutes. Independent confirmation of the source size would provide confidence for releasing information earlier. The first two versions of ShakeMap and PAGER alerts were released with the affected areas based on point sources. The ShakeMap and Pager alerts were updated to a finite fault source, significantly extending the length of affected coastline after 2 hours and 42 minutes. Within 57 seconds after origin time the result of the line source *fast*CMT and slip inversion solutions reproduced the main features of the rupture, approximately 340 km long with average slip of 15 m over the main source region. Additionally the *fast*CMT solution has the correct fault orientation of 204° as opposed to 230° for the rapid finite fault inversion based on the W phase fault orientation. Early access to this information could provide confidence for earlier release of the finite fault corrected Global ShakeMap. Full integration and combination of GPS into seismic monitoring is essential for a hazard system that is more robust than either traditional seismic or geodetic monitoring alone. Because the *fast*CMT algorithm does not require assumptions about the fault geometry, it is also applicable to source regions outside subduction zones. The ability to produce seismogeodetic displacement and velocity time series in real time implies that the delay for calculating near-real-time kinematic rupture models can also be significantly reduced. These results were published in *Melgar et al.* (2013b).

In Chapter 4 we further elaborated on the kinematic problem. We showed that the seismogeodetic data can be easily employed to obtain a time dependent

rupture model of the 2011 Tohoku-oki source. Inversion of 3-component seismogeodetic data for 20 stations revealed features of the source which largely agree with teleseismic inversions and back projection results. We demonstrated that inclusion of the velocity time series produced by the seismogeodetic solution sharpens the picture of the source. We relied on Akaike's Bayesian information criterion formalism for determining optimal smoothing, thus largely removing the human element from the decision-making for the inversion parameters. The seimogeodetic kinematic inversion could potentially be available within minutes of rupture initiation of a large event. We also showed that rupture models from the seimogeodetic data can provide insights into the source process. We observe a heterogeneous rupture for the 2011 Tohoku-oki event, with marked differences between the up dip and down dip rupture behaviors. Very slow initial rupture is followed by fast up-dip rupture that expands quickly along-strike once rupture reaches the trench. Down dip we observe two distinct pulses of moment release with the later pulse possibly driven by the long duration of slip up-dip. Our results are in agreement with observations from low frequency back projection (*Yagi et al.*, 2012) as well s broadband tele-seismic inversions (*Shao et al.*, 2011). We also showed that the model captures depth-dependent behavior of rupture. Frequency domain analysis of the source spectra shows that shallow subfaults are depleted in high frequency radiation with deeper subfaults being progressively enriched in short period energy. This agrees with the observations of *Kurahashi and Irikura* (2011) who found that strong motions originated down-dip from the hypocenter as well as with the conceptual model of (*Lay et al.*, 2012) who proposed that such depth-dependent observations are a consequences of changing frictional properties at depth.

In Chapter 5 we discussed the addition of offshore data in the form of tide gauges, real-time kinematic GPS buoys and ocean bottom pressure sensors into the source inversion process. First we show with the example of the 2011 Tohoku-oki earthquake a source modeling approach that relies on joint inversion of land-based estimates of coseismic deformation from collocated GPS/accelerometer stations and ocean-based wave gauges. We showed that the earthquake sources thus determined can be used as initial conditions to model tsunami propagation in

the near-source coastline. We compared the results of such models against post-event survey data and concluded that the inundation forecasts could be used for tsunami early warning. We deduced that off-shore wave gauges in water shallower than previously thought (100-1000m) can be useful for tsunami forecast. However we found that coastal tide gauges are of limited use for the event studied. We argued that in the future joint inversion of these near source geophysical data and deployment of further ocean-based instruments can help to deliver timely and accurate early warning in regions of tsunami hazard. These results were published in *Melgar and Bock* (2013)

We also showed in Chapter 5 the effect of adding the off-shore data into the kinematic modeling process and produce a time dependent model of the source that relies on both the land- and ocean-based observables. The tsunami data increases the level of complexity in the shallow portion of the fault model, it also increases the amplitude and duration of moment release in the shallow subfaults while leaving the deeper part of the model largely unchanged. The net-effect of the tsunami data is to increase the complexity of the shallowest portion of the fault model; it also produces significantly longer duration source time functions than the land-only kinematic inversion in the shallow sub-faults. We discussed the robustness of these features and argued that there are secondary sources of tsunami energy that might not be accounted for. Finally, we showed the differences between employing the time-varying deformation of bathymetry versus instantaneous deformation of the sea-floor as well as the effect of considering the tsunamigenic contributions of horizontal advection of sloping bathymetry. We argued that for near-field propagation simulations these two often ignored effects can be significant.

It is clear that employing more diverse geophysical data for modeling the earthquake source will aid in developing a more comprehensive image of the underlying processes. This stands to impact both our understanding of large ruptures and our capability to respond to them rapidly. The ocean bottom stands to be the next frontier of seismological and geodetic exploration as technological improvements produce more and better instruments capable of measuring geophysical signals on the sea floor. Sea-floor geodesy has made significant advances (*Bürgmann*

and Chadwell, 2013) and technological developments such as wave gliders promise to make observations of sea-floor deformation denser and more widespread in the future. There exists also many deployments of ocean bottom seismic networks. These typically consist of high-gain broadband seismometers that cannot be used to study the rupture process of large events up close. Deployments of ocean-bottom strong motion sensors are few and far between. Nonetheless it is possible to re-purpose already existing ocean bottom infrastructure to study large ruptures. For example most broadband ocean bottom seismometer deployments include pressure gauges. It has been known for some time that at long periods (*Webb*, 1998) bottom pressure fluctuations are proportional to vertical acceleration.

Consider Figure 6.1 where we have plotted the time series of a rare occurrence of an ocean bottom strong motion sensor and a collocated pressure gauge for the Clayoquot Slope station located 100km from the 2014 M_w6.5 event offshore Vancouver Island. At long periods (longer than 10s in this example) we can assume full water column response to the bottom accelerations (Figure 6.1a) (*Filloux*, 1983; *Webb*, 1998; *Mofjeld et al.*, 2001). We can convert between pressure and acceleration because the pressure recording (Figure 6.1b) will be proportional and in phase to the vertical acceleration. You can see from the 10s low-pass filtered comparisons in Figure 6.1c that the vertical accelerations predicted by the bottom pressure recording match the strong motions sensor well. The Clayoquot Slope station is an exception, rather than the norm, since strong motion sensors are seldom found at ocean bottom sites. Pressure sensors however are widespread. In fact DART buoys (which rely on absolute pressure gauges) routinely record seismic waves (*Mofjeld et al.*, 2001). Figure 6.2 shows an example of two DART buoys the day of the M_w 6.8 Ferndale event offshore Northern California. Both buoys record transient sea-surface height changes of up to 20cm peak-to-peak, but no tsunami follows. This is because the Ferndale event was a strike slip earthquake with no appreciable vertical deformation of the sea floor. In fact the timing of the arrivals at the DART buoys coincides with the Rayleigh waves. The bottom pressure sensor of the buoys incorrectly identifies the vertical accelerations as actual changes of the sea surface height. These observations suggest that it is possible that dense

networks of ocean bottom strong motion sensors, in the form of pressure gauges, already exist. An exciting avenue of research will be how to incorporate these, and other ocean bottom sensing techniques into the study of large earthquakes.

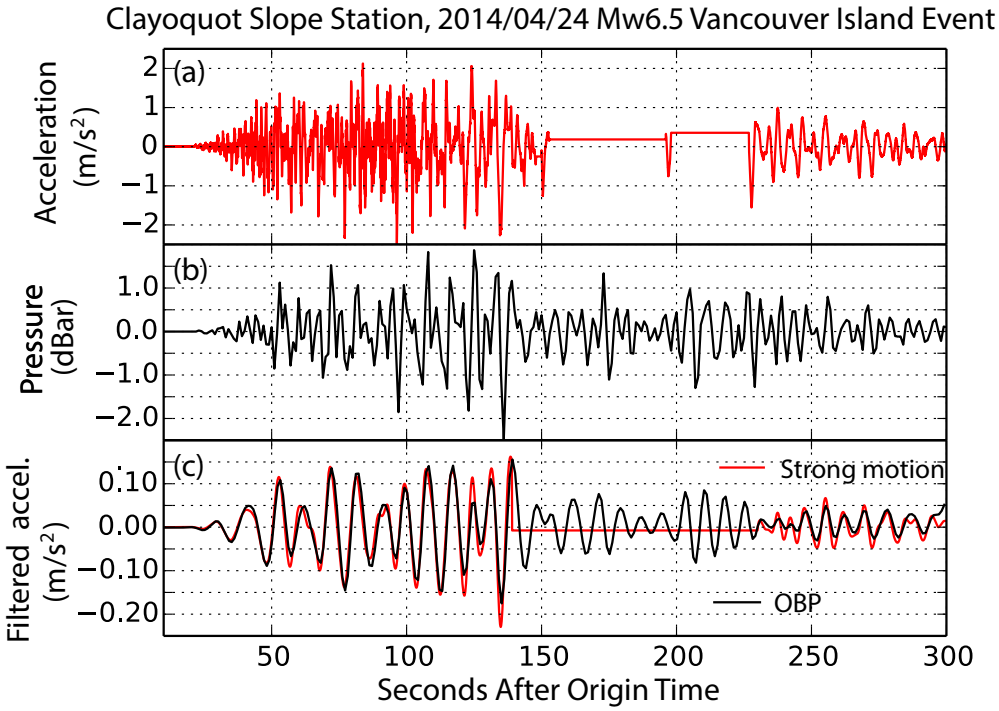


Figure 6.1: Ocean bottom strong motion recording for the M_w6.5 2014 Vancouver Island event. (a) is the raw vertical strong motion accelerogram, (b) is the raw pressure recording and (c) is the 10s low pass filtered accelerogram and predicted acceleration from the pressure gauge. The flat segments in the accelerometer time series are gaps in the data

A similar situation exists for tsunami observations. High quality pressure gauges such as DART buoys and the cabled observatories used in Chapters 4 and 5 offshore Japan are sparse. Seldom do we have dense observations of tsunami propagation. The differential pressure gauges often deployed with high-gain OBS deployments can offer a unique opportunity to study tsunami physics. Figure 6.3 shows the differential pressure gauge recordings for 26 stations around the Hawaii islands deployed as part of the PLUME project (*Wolfe et al.*, 2009). Comparatively dense observations such as these can elucidate details on the propagation characteristics of tsunamis. Local bathymetry plays a major role in tsunami in-

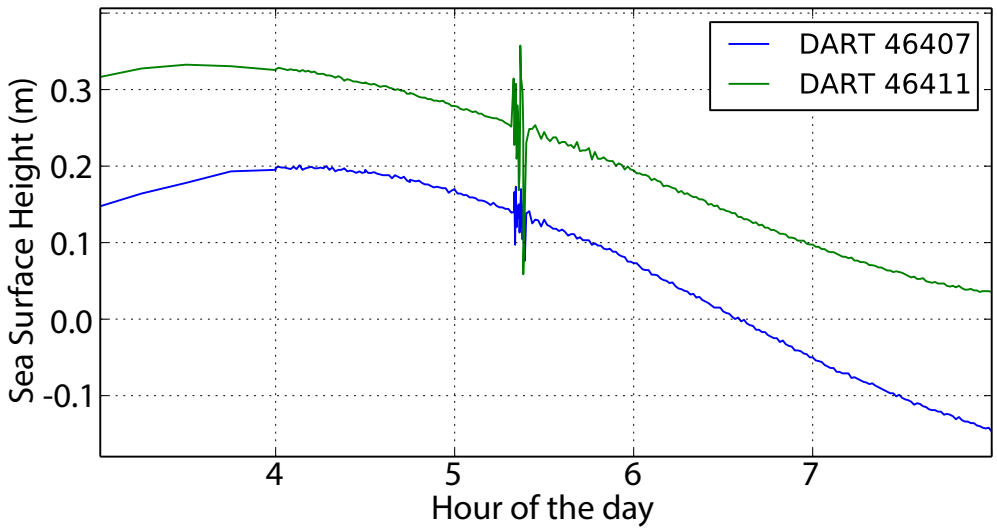


Figure 6.2: DART buoy recordings following the M_w 6.8 Ferndale strike slip event off-shore Northern California

tensity (*Wang and Liu*, 2007; *Iglesias et al.*, 2014), akin to site amplification due to local geology in seismology. Understanding these effects is important to quantifying local hazards both from tele-tsunamis and regional ones. Indeed there is significant heterogeneity in the recordings shown in Figure 6.3.

Typically, tsunami and seismic waves have been considered parts of different disciplines, in reality, they are part of the same wavefield and it makes sense to study them jointly. The intersection of these two wavefields can provide new insights into source physics (*Kozdon and Dunham*, 2014) and perhaps even new avenues to improve early warning and rapid response algorithms (*Lotto et al.*, 2013). With the simple examples of Figures 6.1-6.3 we have shown that there is already infrastructure in place to further this avenue of research and in the future we expect significant developments from joint geophysical observations such as these.

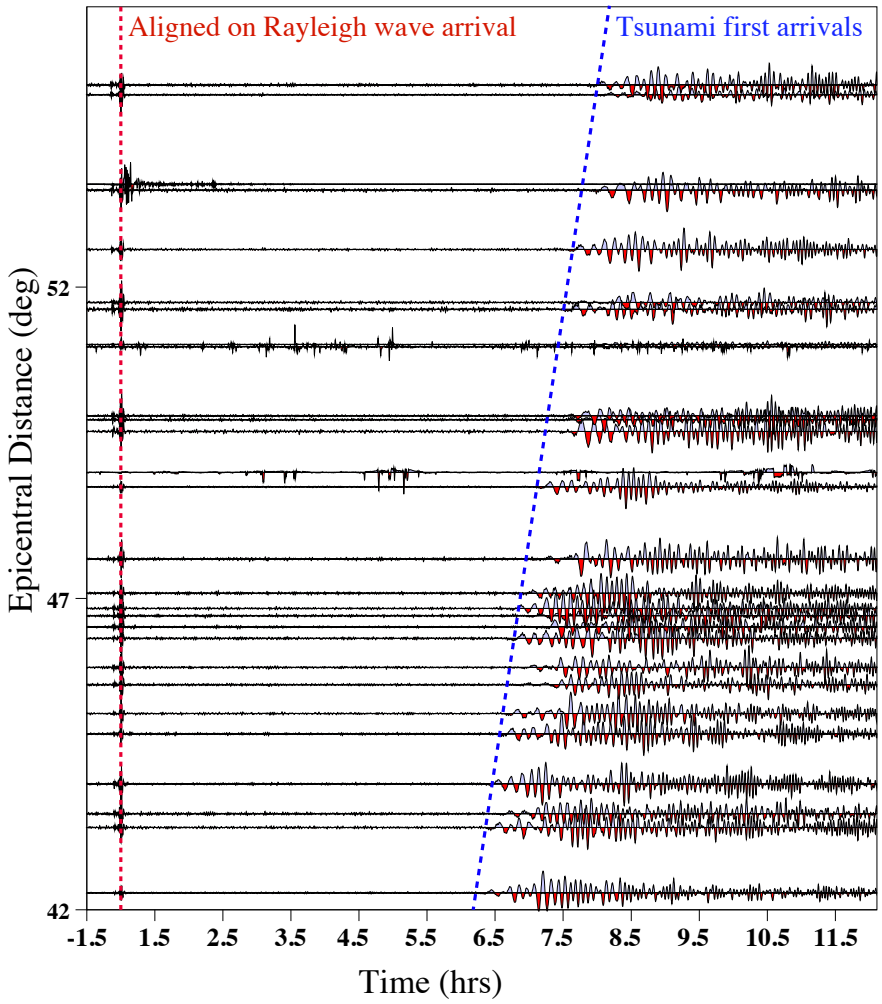


Figure 6.3: Differential pressure gauge recordings at 26 ocean bottom stations during the 2006 Kuril Islands tsunami. The waveforms are aligned on the Rayleigh wave arrivals (red dotted line). The tsunami first arrivals are indicated by the blue dotted line.

6.1 Acknowledgments

The contents of this chapter are unpublished. We'd like to thank Ocean Networks Canada for the data for the Clayoquot Canyon station and the National Oceanographic and Atmospheric Administration for the DART buoy data. We would also like to thank Gabi Laske for providing the differential pressure gauge data for the PLUME project.

Chapter 7

Bibliography

Adamová, P. and Šílenỳ, J. (2010). Non-double-couple earthquake mechanism as an artifact of the point-source approach applied to a finite-extent focus. *Bulletin of the Seismological Society of America*, 100(2):447–457.

Akaike, H. (1980). Likelihood and the Bayes procedure. *Trabajos de estadística y de investigación operativa*, 31(1):143–166.

Aki, K. (1968). Seismic displacements near a fault. *Journal of Geophysical Research*, 73(16):5359–5376.

Aki, K. and Richards, P. M. (2002). *Quantitative Seismology*. University Science Books, 2 edition.

Allen, R. M., Gasparini, P., Kamigaichi, O., and Böse, M. (2009a). The status of earthquake early warning around the world: an introductory overview. *Seismological Research Letters*, 80(5):682–693.

Allen, T. I., Wald, D. J., Earle, P. S., Marano, K. D., Hotovec, A. J., Lin, K., and Hearne, M. G. (2009b). An atlas of shakemaps and population exposure catalog for earthquake loss modeling. *Bulletin of Earthquake Engineering*, 7(3):701–718.

Altamimi, Z., Collilieux, X., Legrand, J., Garayt, B., and Boucher, C. (2007). ITRF2005: A new release of the international terrestrial reference frame based on time series of station positions and earth orientation parameters. *Journal of Geophysical Research*, 112(B9).

Ammon, C. J., Ji, C., Thio, H. K., Robinson, D., Ni, S., Hjorleifsdottir, V., Kanamori, H., Lay, T., Das, S., and Helmberger, D. (2005). Rupture process of the 2004 Sumatra-Andaman earthquake. *Science*, 308(5725):1133–1139.

Amoruso, A., Crescentini, L., and Fidani, C. (2004). Effects of crustal layering on source parameter inversion from coseismic geodetic data. *Geophysical Journal International*, 159:353–364.

Arai, K., Naruse, H., Miura, R., Kawamura, K., Hino, R., Ito, Y., Inazu, D., Yokokawa, M., Izumi, N., and Murayama, M. (2013). Tsunami-generated turbidity current of the 2011 Tohoku-oki earthquake. *Geology*, 41(11):1195–1198.

Arcas, D. and Segur, H. (2012). Seismically generated tsunamis. *Philosophical Transactions of the Royal Society A: Mathematical, Physical and Engineering Sciences*, 370(1964):1505–1542.

Asano, Y., Saito, T., Ito, Y., Shiomi, K., Hirose, H., Matsumoto, T., Aoi, S., Hori, S., and Sekiguchi, S. (2011). Spatial distribution and focal mechanisms of aftershocks of the 2011 off the Pacific coast of Tohoku earthquake. *Earth, planets and space*, 63(7):669–673.

Aster, R. C., Borchers, B., and Thurber, C. H. (2013). *Parameter estimation and inverse problems*. Academic Press.

Basher, R. (2006). Global early warning systems for natural hazards: systematic and people-centred. *Philosophical Transactions of the Royal Society A: Mathematical, Physical and Engineering Sciences*, 364(1845):2167–2182.

Becker, J., Sandwell, D., Smith, W., Braud, J., Binder, B., Depner, J., Fabre, D., Factor, J., Ingalls, S., and Kim, S. (2009). Global bathymetry and elevation data at 30 arc seconds resolution: SRTM30+. *Marine Geodesy*, 32(4):355–371.

Berger, M. J., George, D. L., LeVeque, R. J., and Mandli, K. T. (2011). The GeoClaw software for depth-averaged flows with adaptive refinement. *Advances in Water Resources*, 34(9):1195–1206.

Beroza, G. C. and Spudich, P. (1988). Linearized inversion for fault rupture behavior: Application to the 1984 Morgan Hill, California, earthquake. *Journal of Geophysical Research*, 93(B6):6275–6296.

Bielak, J., Graves, R. W., Olsen, K. B., Taborda, R., Ramírez-Guzmán, L., Day, S. M., Ely, G. P., Roten, D., Jordan, T. H., and Maechling, P. J. (2010). The shakeout earthquake scenario: Verification of three simulation sets. *Geophysical Journal International*, 180(1):375–404.

Blewitt, G. (1989). Carrier phase ambiguity resolution for the global positioning system applied to geodetic baselines up to 2000 kilometers. *Journal of Geophysical Research*, 94:10187–10203.

Blewitt, G., Heflin, M. B., Hurst, K. J., Jefferson, D. C., Webb, F. H., and Zumberge, J. F. (1993). Absolute far-field displacements from the 28 june 1992 Landers earthquake sequence. *Nature*, 361(6410):340–342.

Blewitt, G., Kreemer, C., Hammond, W. C., Plag, H., Stein, S., and Okal, E. (2006). Rapid determination of earthquake magnitude using GPS for tsunami warning systems. *Geophysical Research Letters*, 33(11).

Bock, Y., Agnew, D. C., Fang, P., Genrich, J. F., Hager, B. H., Herring, T. A., Hudnut, K. W., King, R. W., Larsen, S., and Minster, J.-B. (1993). Detection of crustal deformation from the Landers earthquake sequence using continuous geodetic measurements. *Nature*, 361(6410):337–340.

Bock, Y., Melgar, D., and Crowell, B. W. (2011). Real-time strong-motion broadband displacements from collocated GPS and accelerometers. *Bulletin of the Seismological Society of America*, 101(6):2904–2925.

Bock, Y., Nikolaidis, R. M., Jonge, P. J., and Bevis, M. (2000). Instantaneous geodetic positioning at medium distances with the global positioning system. *Journal of Geophysical Research*, 105(B12):28223–28253.

Bock, Y., Prawirodirdjo, L., and Melbourne, T. (2004). Detection of arbitrarily large dynamic ground motions with a dense high-rate GPS network. *Geophysical Research Letters*, 31.

Boore, D. M. (1999). Effect of baseline corrections on response spectra for two recordings of the 1999 Chi-Chi, Taiwan, earthquake. *U.S. Geol. Surv. Open-File Rept.*, 99(545):1–37.

Boore, D. M. (2001). Effect of baseline corrections on displacements and response spectra for several recordings of the 1999 Chi-Chi, taiwan, earthquake. *Bulletin of the Seismological Society of America*, 91(5):1199–1211.

Boore, D. M. and Bommer, J. J. (2005). Processing of strong-motion accelerograms: needs, options and consequences. *Soil Dynamics and Earthquake Engineering*, 25(2):93–115.

Boore, D. M., Joyner, W. B., and Fumal, T. E. (1997). Equations for estimating horizontal response spectra and peak acceleration from western North American earthquakes: a summary of recent work. *Seismological Research Letters*, 68(1):128–153.

Boore, D. M., Stephens, C. D., and Joyner, W. B. (2002). Comments on baseline correction of digital strong-motion data: Examples from the 1999 Hector Mine, California, earthquake. *Bulletin of the Seismological Society of America*, 92(4):1543–1560.

Bowman, A. W. and Azzalini, A. (1997). *Applied Smoothing Techniques for Data Analysis: The Kernel Approach with S-Plus Illustrations*. Oxford University Press.

Boyd, S. and Vandenberghe, L. (2004). *Convex Optimization*. Cambridge University Press, 1st edition.

Bozorgnia, Y., Abrahamson, N. A., Atik, L. A., Ancheta, T. D., Atkinson, G. M., Baker, J. W., Baltay, A., Boore, D. M., Campbell, K. W., and Chiou, B. S.-J. (2014). Nga-west2 research project. *Earthquake Spectra*.

Bozorgnia, Y. and Bertero, V. V. (2004). *Earthquake engineering: from engineering seismology to performance-based engineering*. CRC press.

Brown, H. M., Allen, R. M., Hellweg, M., Khainovski, O., Neuhauser, D., and Souf, A. (2011). Development of the ElarmS methodology for earthquake early warning: Realtime application in California and offline testing in Japan. *Soil Dynamics and Earthquake Engineering*, 31(2):188–200.

Brune, J. N. (1970). Tectonic stress and the spectra of seismic shear waves from earthquakes. *Journal of Geophysical Research*, 75(26):4997–5009.

Bürgmann, R. and Chadwell, D. (2013). Seafloor Geodesy. *Annual Review of Earth and Planetary Sciences*, 42:509–534.

Chao, W.-A., Wu, Y.-M., and Zhao, L. (2010). An automatic scheme for baseline correction of strong-motion records in coseismic deformation determination. *Journal of Seismology*, 14(3):495–504.

Colombelli, S., Allen, R. M., and Zollo, A. (2013). Application of real-time GPS to earthquake early warning in subduction and strike-slip environments. *Journal of Geophysical Research*, 118(7):3448–3461.

Cotton, F. and Campillo, M. (1995). Frequency domain inversion of strong motions: Application to the 1992 Landers earthquake. *Journal of Geophysical Research*, 100(B3):3961–3975.

Crowell, B. W. (2013). *Using GPS to rapidly detect and model earthquakes and transient deformation events*. University of California San Diego, Doctoral Dissertation.

Crowell, B. W., Bock, Y., and Melgar, D. (2012). Realtime inversion of GPS data for finite fault modeling and rapid hazard assessment. *Geophysical Research Letters*, 39(9).

Crowell, B. W., Bock, Y., and Squibb, M. (2009). Demonstration of earthquake early warning using total displacement waveforms from real time GPS networks. *Seismological Research Letters*, 80:772–782.

Crowell, B. W., Melgar, D., Bock, Y., Haase, J. S., and Geng, J. (2013). Earthquake magnitude scaling using seismogeodetic data. *Geophysical Research Letters*.

Delouis, B., Nocquet, J.-M., and Vallée, M. (2010). Slip distribution of the February 27, 2010 Mw= 8.8 Maule earthquake, central Chile, from static and high-rate GPS, InSAR, and broadband teleseismic data. *Geophysical Research Letters*, 37(17).

Denolle, M., Dunham, E., Prieto, G., and Beroza, G. (2013). Ground motion prediction of realistic earthquake sources using the ambient seismic field. *Journal of Geophysical Research*, 118(5):2102–2118.

Denolle, M., Dunham, E., Prieto, G., and Beroza, G. (2014). Strong ground motion prediction using virtual earthquakes. *Science*, 343(6169):399–403.

Dong, D. and Bock, Y. (1989). Global positioning system network analysis with phase ambiguity resolution applied to crustal deformation studies in California. *Journal of Geophysical Research*, 94:3949–3966.

Dreger, D. (2003). TDMTINV time domain seismic moment tensor inversion. *International Handbook of Earthquake and Engineering Seismology*, page 1627.

Dreger, D. S. and Helmberger, D. V. (1990). Broadband modeling of local earthquakes. *Bulletin of the Seismological Society of America*, 80(5):1162–1179.

Dreger, D. S. and Helmberger, D. V. (1993). Determination of source parameters at regional distances with three-component sparse network data. *Journal of Geophysical Research*, 98(B5):8107–8125.

Duputel, Z., Rivera, L., Kanamori, H., Hayes, G. P., Hirshorn, B., and Weinstein, S. (2011). Real-time W phase inversion during the 2011 off the Pacific coast of Tohoku earthquake. *Earth, planets and space*, 63(7):535–539.

Dziewonski, A., Chou, T. A., and Woodhouse, J. (1981). Determination of earthquake source parameters from waveform data for studies of global and regional seismicity. *Journal of Geophysical Research*, 86(B4):2825–2852.

Dziewonski, A. M. and Woodhouse, J. H. (1983). An experiment in systematic study of global seismicity: Centroid-moment tensor solutions for 201 moderate and large earthquakes of 1981. *Journal of Geophysical Research*, 88(B4):3247–3271.

Emore, G. L., Haase, J. S., Choi, K., Larson, K. M., and Yamagiwa, A. (2007). Recovering seismic displacements through combined use of 1Hz GPS and strong-motion accelerometers. *Bulletin of the Seismological Society of America*, 97(2):357–378.

Espinosa-Aranda, J., Cuellar, A., Garcia, A., Ibarrola, G., Islas, R., Maldonado, S., and Rodriguez, F. (2009). Evolution of the Mexican seismic alert system (SASMEX). *Seismological Research Letters*, 80(5):694–706.

Evans, J., Allen, R., Chung, A., Cochran, E., Guy, R., Hellweg, M., and Lawrence, J. (2014). Performance of several low-cost accelerometers. *Seismological Research Letters*, 85(1):147–158.

Farr, T. G., Rosen, P. A., Caro, E., Crippen, R., Duren, R., Hensley, S., Kobrick, M., Paller, M., Rodriguez, E., and Roth, L. (2007). The shuttle radar topography mission. *Reviews of geophysics*, 45(2).

Filloux, J. H. (1983). Pressure fluctuations on the open-ocean floor off the Gulf of California: Tides, earthquakes, tsunamis. *Journal of physical oceanography*, 13(5):783–796.

Fritz, H. M., Petroff, C. M., Catalán, P. A., Cienfuegos, R., Winckler, P., Kalligeris, N., Weiss, R., Barrientos, S. E., Meneses, G., and Valderas-Bermejo, C. (2011). Field survey of the 27 February 2010 Chile tsunami. *Pure and Applied Geophysics*, 168(11):1989–2010.

Fujii, Y. and Satake, K. (2007). Tsunami source of the 2004 Sumatra–Andaman earthquake inferred from tide gauge and satellite data. *Bulletin of the Seismological Society of America*, 97(1A):S192–S207.

Fujiwara, T., Kodaira, S., No, T., Kaiho, Y., Takahashi, N., and Kaneda, Y. (2011). The 2011 Tohoku-oki earthquake: Displacement reaching the trench axis. *Science*, 334(6060):1240–1240.

Fukahata, Y., Nishitani, A., and Matsu'ura, M. (2004). Geodetic data inversion using ABIC to estimate slip history during one earthquake cycle with viscoelastic slip-response functions. *Geophysical Journal International*, 156(1):140–153.

Fukahata, Y., Yagi, Y., and Matsu'ura, M. (2003). Waveform inversion for seismic source processes using ABIC with two sorts of prior constraints: Comparison between proper and improper formulations. *Geophysical research letters*, 30(6).

Fukuyama, E., Ishida, M., Dreger, D., and Kawai, H. (1998). Automated seismic moment tensor determination by using on-line broadband seismic waveforms. *J. Seismol. Soc. Jpn*, 51:149–156.

Fulton, P., Brodsky, E., Kano, Y., Mori, J., Chester, F., Ishikawa, T., Harris, R., Lin, W., Eguchi, N., and Toczko, S. (2013). Low coseismic friction on the Tohoku-oki fault determined from temperature measurements. *Science*, 342(6163):1214–1217.

Geng, J. (2010). *Rapid integer ambiguity resolution in GPS precise point positioning*. PhD thesis, University of Nottingham, Nottingham, UK.

Geng, J., Bock, Y., Melgar, D., Crowell, B. W., and Haase, J. S. (2013a). A new seismogeodetic approach applied to GPS and accelerometer observations of the 2012 Brawley seismic swarm: Implications for earthquake early warning. *Geochemistry, Geophysics, Geosystems*.

Geng, J., Melgar, D., Bock, Y., Pantoli, E., and Restrepo, J. (2013b). Recovering coseismic point ground tilts from collocated highrate GPS and accelerometers. *Geophysical Research Letters*, 40(19):5095–5100.

Genrich, J. F. and Bock, Y. (2006). Instantaneous geodetic positioning with 10–50 Hz GPS measurements: Noise characteristics and implications for monitoring networks. *Journal of Geophysical Research*, 111(B3).

George, D. L. (2008). Augmented Riemann solvers for the shallow water equations over variable topography with steady states and inundation. *Journal of Computational Physics*, 227(6):3089–3113.

George, D. L. and LeVeque, R. J. (2006). Finite volume methods and adaptive refinement for global tsunami propagation and local inundation. *Science of Tsunami Hazards*, 24(5):319.

González, F., Geist, E., Jaffe, B., Kânoğlu, U., Mofjeld, H., Synolakis, C., Titov, V., Arcas, D., Bellomo, D., and Carlton, D. (2009). Probabilistic tsunami hazard assessment at Seaside, Oregon, for near-and far-field seismic sources. *Journal of Geophysical Research: Oceans (1978–2012)*, 114(C11).

Gonzalez, F., LeVeque, R., Chamberlain, P., Hirai, B., Varkovitzky, J., and George, D. (2011). Geoclaw results for the NTHMP tsunami benchmark problems. In *Proceedings and Results of the 2011 NTHMP Model Benchmarking Workshop*.

González, F. I., Bernard, E. N., Meinig, C., Eble, M. C., Mofjeld, H. O., and Stalin, S. (2005). The NTHMP tsunameter network. *Natural Hazards*, 35(1):25–39.

Graizer, V. M. (1979). Determination of the true ground displacement by using strong motion records. *Izvestiya Academy of Sciences, USSR, Physics of the Solid Earth*, 15(12):875–885.

Graizer, V. M. (2006). Tilts in strong ground motion. *Bulletin of the Seismological Society of America*, 96(6):2090–2102.

Graves, R. W. and Wald, D. J. (2001). Resolution analysis of finite fault source inversion using one-and three-dimensional Green's functions: 1. strong motions. *Journal of Geophysical Research*, 106(B5):8745–8766.

Gregor, N., Abrahamson, N. A., Atkinson, G. M., Boore, D. M., Bozorgnia, Y., Campbell, K. W., Chiou, B. S.-J., Idriss, I., Kamai, R., and Seyhan, E. (2014). Comparison of NGA-West2 GMPEs. *Earthquake Spectra*.

Grilli, S. T., Harris, J. C., Bakhsh, T. S. T., Masterlark, T. L., Kyriakopoulos, C., Kirby, J. T., and Shi, F. (2013). Numerical simulation of the 2011 Tohoku tsunami based on a new transient FEM co-seismic source: Comparison to far-and near-field observations. *Pure and Applied Geophysics*, 170(6-8):1333–1359.

Guilhem, A., Dreger, D. S., Tsuruoka, H., and Kawakatsu, H. (2013). Moment tensors for rapid characterization of megathrust earthquakes: the example of the 2011 M9 Tohoku-oki, Japan earthquake. *Geophysical Journal International*, 192(2):759–772.

Gusman, A. R., Tanioka, Y., Sakai, S., and Tsushima, H. (2012). Source model of the great 2011 Tohoku earthquake estimated from tsunami waveforms and crustal deformation data. *Earth and Planetary Science Letters*, 341:234–242.

Hamada, N. and Suzuki, Y. (2004). Re-examination of aftershocks of the 1952 Tokachi-oki earthquake and a comparison with those of the 2003 Tokachi-oki earthquake. *Earth Planets Space*, 56:341–345.

Hanks, T. and Kanamori, H. (1979). A moment magnitude scale. *Journal of Geophysical Research*, 84(B5):2348–2350.

Hansen, P. C. (2010). *Discrete inverse problems: insight and algorithms*, volume 7. SIAM.

Hansen, P. C., Jensen, T. K., and Rodriguez, G. (2007). An adaptive pruning algorithm for the discrete L-curve criterion. *Journal of computational and applied mathematics*, 198(2):483–492.

Hartzell, S. and Langer, C. (1993). Importance of model parameterization in finite fault inversions: Application to the 1974 Mw 8.0 Peru earthquake. *Journal of Geophysical Research*, 98(B12):22123–22134.

Hartzell, S. H. and Heaton, T. H. (1983). Inversion of strong ground motion and teleseismic waveform data for the fault rupture history of the 1979 Imperial Valley, California, earthquake. *Bulletin of the Seismological Society of America*, 73(6A):1553–1583.

Haskell, N. (1964). Total energy and energy spectral density of elastic wave radiation from propagating faults. *Bulletin of the Seismological Society of America*, 54(6A):1811–1841.

Haskell, N. A. (1969). Elastic displacements in the near-field of a propagating fault. *Bulletin of the Seismological Society of America*, 59(2):865–908.

Hauksson, E., Stock, J., Hutton, K., Yang, W., Vidal-Villegas, J. A., and Kanamori, H. (2011). The 2010 Mw 7.2 El Mayor-Cucapah earthquake sequence, Baja California, Mexico and southernmost California, USA: Active seismotectonics along the Mexican Pacific margin. *Pure and applied geophysics*, 168(8-9):1255–1277.

Havskov, J. and Alguacil, G. (2006). *Instrumentation in Earthquake Seismology*. Springer, New York, NY, first edition.

Havskov, J. and Ottemoller, L. (2010). *Routine Data Processing in Earthquake Seismology*. Springer, New York, NY, first edition.

Hayashi, T. (2012). Japan's post-disaster economic reconstruction: From Kobe to Tohoku. *Asian Economic Journal*, 26(3):189–210.

Hayashi, Y., Tsushima, H., Hirata, K., Kimura, K., and Maeda, K. (2011). Tsunami source area of the 2011 off the Pacific coast of Tohoku earthquake determined from tsunami arrival times at offshore observation stations. *Earth, planets and space*, 63(7):809–813.

Hayes, G. P., Earle, P. S., Benz, H. M., Wald, D. J., and Briggs, R. W. (2011). 88 hours: The US Geological Survey National Earthquake Information Center response to the 11 March 2011 Mw 9.0 Tohoku earthquake. *Seismological Research Letters*, 82(4):481–493.

Hayes, G. P., Rivera, L., and Kanamori, H. (2009). Source inversion of the W-phase: real-time implementation and extension to low magnitudes. *Seismological Research Letters*, 80(5):817–822.

Hayes, G. P., Wald, D. J., and Johnson, R. L. (2012). Slab1.0: A three-dimensional model of global subduction zone geometries. *Journal of Geophysical Research*, 117(B1).

Hearn, E. H. and Bürgmann, R. (2005). The effect of elastic layering on inversions of GPS data for coseismic slip and resulting stress changes: Strike-slip earthquakes. *Bulletin of the Seismological Society of America*, 95(5):1673–1653.

Heuret, A., Lallemand, S., Funiciello, F., Piromallo, C., and Faccenna, C. (2011). Physical characteristics of subduction interface type seismogenic zones revisited. *Geochemistry, Geophysics, Geosystems*, 12(1).

Hill, E. M., Borrero, J. C., Huang, Z., Qiu, Q., Banerjee, P., Natawidjaja, D. H., Elosegui, P., Fritz, H. M., Suwargadi, B. W., and Pranantyo, I. R. (2012). The 2010 Mw 7.8 Mentawai earthquake: Very shallow source of a rare tsunami earthquake determined from tsunami field survey and near-field GPS data. *Journal of Geophysical Research*, 117(B6).

Hingee, M., Tkalčić, H., Fichtner, A., and Sambridge, M. (2011). Seismic moment tensor inversion using a 3-d structural model: applications for the Australian region. *Geophysical Journal International*, 184(2):949–964.

Hoechner, A., Ge, M., Babeyko, A., and Sobolev, S. (2013). Instant tsunami early warning based on real-time GPS–Tohoku 2011 case study. *Natural Hazards and Earth System Science*, 13(5):1285–1292.

Hoshiba, M., Iwakiri, K., Hayashimoto, N., Shimoyama, T., Hirano, K., Yamada, Y., Ishigaki, Y., and Kikuta, H. (2011). Outline of the 2011 off the Pacific coast of Tohoku earthquake (Mw 9.0)-earthquake early warning and observed seismic intensity. *Earth, planets and space*, 63(7):547–551.

Ide, S. (2007). *Treatise on geophysics: Earthquake seismology*, volume 4, chapter Slip Inversion, pages 193–222. Elsevier.

Ide, S., Takeo, M., and Yoshida, Y. (1996). Source process of the 1995 Kobe earthquake: Determination of spatio-temporal slip distribution by Bayesian modeling. *Bulletin of the Seismological society of America*, 86(3):547–566.

Iglesias, O., Lastras, G., Souto, C., Costa, S., and Canals, M. (2014). Effects of coastal submarine canyons on tsunami propagation and impact. *Marine Geology*, 350:39–51.

Ishii, M., Shearer, P. M., Houston, H., and Vidale, J. E. (2005). Extent, duration and speed of the 2004 Sumatra–Andaman earthquake imaged by the Hi-Net array. *Nature*, 435(7044):933–936.

Iwan, W. D., Moser, M. A., and Peng, C.-Y. (1985). Some observations on strong-motion earthquake measurement using a digital accelerograph. *Bulletin of the Seismological Society of America*, 75(5):1225–1246.

Jackson, D. D. and Matsu'Ura, M. (1985). A Bayesian approach to nonlinear inversion. *Journal of Geophysical Research*, 90(B1):581–591.

Jaiswal, K. S. and Wald, D. J. (2010). Development of a semi-empirical loss model within the USGS prompt assessment of global earthquakes for response (PAGER) system. In *Proceedings of the 9th US and 10th Canadian conference on earthquake engineering: reaching beyond borders*, pages 25–29.

Ji, C., Helmberger, D. V., Wald, D. J., and Ma, K.-F. (2003). Slip history and dynamic implications of the 1999 Chi-Chi, Taiwan, earthquake. *Journal of Geophysical Research*, 108(B9).

Ji, C., Wald, D. J., and Helmberger, D. V. (2002a). Source description of the 1999 Hector Mine, California, earthquake, part I: Wavelet domain inversion

theory and resolution analysis. *Bulletin of the Seismological Society of America*, 92(4):1192–1207.

Ji, C., Wald, D. J., and Helmberger, D. V. (2002b). Source description of the 1999 Hector Mine, California, earthquake, part II: Complexity of slip history. *Bulletin of the Seismological Society of America*, 92(4):1208–1226.

Kalman, R. E. (1960). A new approach to linear filtering and prediction problems. *Journal of basic Engineering*, 82(1):35–45.

Kamigaichi, O., Saito, M., Doi, K., Matsumori, T., Tsukada, S., Takeda, K., Shimoyama, T., Nakamura, K., Kiyomoto, M., and Watanabe, Y. (2009). Earthquake early warning in Japan: warning the general public and future prospects. *Seismological Research Letters*, 80(5):717–726.

Kanamori, H. (1993). W-phase. *Geophysical Research Letters*, 20(16):1691–1694.

Kanamori, H. and Brodsky, E. E. (2004). The physics of earthquakes. *Reports on Progress in Physics*, 67(8):1429.

Kanamori, H. and Rivera, L. (2008). Source inversion of W phase: speeding up seismic tsunami warning. *Geophysical Journal International*, 175(1):222–238.

Kanamori, H. and Stewart, G. S. (1978). Seismological aspects of the Guatemala earthquake of February 4, 1976. *Journal of Geophysical Research*, 83(B7):3427–3434.

Kawamura, K., Sasaki, T., Kanamatsu, T., Sakaguchi, A., and Ogawa, Y. (2012). Large submarine landslides in the Japan Trench: A new scenario for additional tsunami generation. *Geophysical Research Letters*, 39(5).

Kiser, E. and Ishii, M. (2012). The March 11, 2011 Tohoku-oki earthquake and cascading failure of the plate interface. *Geophysical Research Letters*, 39(7).

Kohler, M., Magistrale, H., and Clayton, R. (2003). Mantle heterogeneities and the SCEC reference three-dimensional seismic velocity model version 3. *Bulletin of the Seismological Society of America*, 93(2):757–774.

Koketsu, K., Hikima, K., Miyazaki, S., and Ide, S. (2004). Joint inversion of strong motion and geodetic data for the source process of the 2003 Tokachi-oki, Hokkaido, earthquake. *Earth, planets and space*, 56(3):329–334.

Koper, K. D., Hutko, A. R., Lay, T., Ammon, C. J., and Kanamori, H. (2011). Frequency-dependent rupture process of the 2011 Mw 9. 0 Tohoku earthquake: Comparison of short-period p wave backprojection images and broadband seismic rupture models. *Earth, planets and space*, 63(7):599–602.

Kouba, J. and Héroux, P. (2001). Precise point positioning using IGS orbit and clock products. *GPS solutions*, 5(2):12–28.

Kozdon, J. E. and Dunham, E. M. (2014). Constraining shallow slip and tsunami excitation in megathrust ruptures using seismic and ocean acoustic waves recorded on ocean-bottom sensor networks. *Earth and Planetary Science Letters*, 396:56–65.

Kurahashi, S. and Irikura, K. (2011). Source model for generating strong ground motions during the 2011 off the Pacific coast of Tohoku earthquake. *Earth, planets and space*, 63(7):571–576.

Langbein, J. and Bock, Y. (2004). High-rate real-time GPS network at Parkfield: Utility for detecting fault slip and seismic displacements. *Geophysical Research Letters*, 31(15).

Larson, K. M., Bodin, P., and Gomberg, J. (2003). Using 1-Hz GPS data to measure deformations caused by the denali fault earthquake. *Science*, 300(5624):1421–1424.

Lawson, C. L. and Hanson, R. J. (1974). *Solving least squares problems*, volume 161. SIAM.

Lay, T., Ammon, C., Kanamori, H., Koper, K., Sufri, O., and Hutko, A. (2010). Teleseismic inversion for rupture process of the 27 February 2010 Chile (Mw 8.8) earthquake. *Geophysical Research Letters*, 37(13).

Lay, T., Ammon, C. J., Kanamori, H., Xue, L., and Kim, M. J. (2011). Possible large near-trench slip during the 2011 Mw 9. 0 off the Pacific coast of Tohoku earthquake. *Earth, planets and space*, 63(7):687–692.

Lay, T. and Kanamori, H. (2011). Japan earthquake. *Phys. Today*, 64(12):33.

Lay, T., Kanamori, H., Ammon, C. J., Koper, K. D., Hutko, A. R., Ye, L., Yue, H., and Rushing, T. M. (2012). Depth-varying rupture properties of subduction zone megathrust faults. *Journal of Geophysical Research*, 117(B4).

Lay, T., Kanamori, H., Ammon, C. J., Nettles, M., Ward, S. N., Aster, R. C., Beck, S. L., Bilek, S. L., Brudzinski, M. R., and Butler, R. (2005). The great Sumatra-Andaman earthquake of 26 December 2004. *Science*, 308(5725):1127–1133.

Lay, T., Ye, L., Kanamori, H., Yamazaki, Y., Cheung, K. F., Kwong, K., and Koper, K. D. (2013). The october 28, 2012 Mw 7.8 Haida Gwaii underthrusting earthquake and tsunami: Slip partitioning along the Queen Charlotte fault transpressional plate boundary. *Earth and Planetary Science Letters*, 375:57–70.

Lee, V. W. and Trifunac, M. D. (2009). Empirical scaling of rotational spectra of strong earthquake ground motion. *Bulletin of the Seismological Society America*, 99:1378–1390.

LeVeque, R. J. (2002). *Finite volume methods for hyperbolic problems*, volume 31. Cambridge university press.

LeVeque, R. J., George, D. L., and Berger, M. J. (2011). Tsunami modelling with adaptively refined finite volume methods. *Acta Numerica*, 20(1):211–289.

Lewis, F. L., Xie, L., and Popa, D. (2008). *Optimal and robust estimation: with an introduction to stochastic control theory*, volume 26. CRC.

Lotto, G., Belair, G., Kozdon, J., and Dunham, E. (2013). Modeling tsunamis and hydroacoustic waves from megathrust earthquakes. In *AGU Fall Meeting Abstracts*, volume 1, page 1706.

Lynett, P. J. (2006). Nearshore wave modeling with high-order boussinesq-type equations. *Journal of waterway, port, coastal, and ocean engineering*, 132(5):348–357.

Lynett, P. J., Borrero, J., Son, S., Wilson, R., and Miller, K. (2014). Assessment of the tsunami-induced current hazard. *Geophysical Research Letters*, 41(6):2048–2055.

Lynett, P. J., Borrero, J. C., Weiss, R., Son, S., Greer, D., and Renteria, W. (2012). Observations and modeling of tsunami-induced currents in ports and harbors. *Earth and Planetary Science Letters*, 327:68–74.

Ma, S. and Hirakawa, E. T. (2013). Dynamic wedge failure reveals anomalous energy radiation of shallow subduction earthquakes. *Earth and Planetary Science Letters*, 375:113–122.

MacInnes, B. T., Gusman, A. R., LeVeque, R. J., and Tanioka, Y. (2013). Comparison of earthquake source models for the 2011 Tohoku event using tsunami simulations and near-field observations. *Bulletin of the Seismological Society of America*, 103(2B):1256–1274.

Melgar, D. and Bock, Y. (2013). Near-field tsunami models with rapid earthquake source inversions from land-and ocean-based observations: The potential for forecast and warning. *Journal of Geophysical Research: Solid Earth*, 118(11):5939–5955.

Melgar, D., Bock, Y., and Crowell, B. W. (2012). Real-time centroid moment tensor determination for large earthquakes from local and regional displacement records. *Geophysical Journal International*, 188(2):703–718.

Melgar, D., Bock, Y., Sanchez, D., and Crowell, B. W. (2013a). On robust and reliable automated baseline corrections for strong motion seismology. *Journal of Geophysical Research: Solid Earth*, 118(3):1177–1187.

Melgar, D., Crowell, B. W., Bock, Y., and Haase, J. S. (2013b). Rapid modeling of the 2011 mw 9.0 tohoku-oki earthquake with seismogeodesy. *Geophysical Research Letters*, 40(12):2963–2968.

Menke, W. (2012). *Geophysical data analysis: discrete inverse theory*. Academic press.

Minson, S., Murray, J. R., Langbein, J. O., and Gomberg, J. S. (2014). Real-time inversions for finite fault slip models and rupture geometry based on high-rate GPS data. *Journal of Geophysical Research*, 119(4):3201–3231.

Minson, S., Simons, M., and Beck, J. (2013). Bayesian inversion for finite fault earthquake source models i—theory and algorithm. *Geophysical Journal International*, 194(3):1701–1726.

Miyazaki, S., Larson, K. M., Choi, K., Hikima, K., Koketsu, K., Bodin, P., Haase, J., Emore, G., and Yamagiwa, A. (2004). Modeling the rupture process of the 2003 September 25 Tokachi-Oki (Hokkaido) earthquake using 1-Hz GPS data. *Geophysical Research Letters*, 31(L21603).

Miyazaki, S., Tsuji, H., Hatanaka, Y., and Tada, T. (1998). The nationwide GPS array as an earth observation system. *Bulletin of the Geographical Survey Institute*, 44:11–22.

Moaveni, B., He, X., Conte, J. P., Restrepo, J. I., and Panagiotou, M. (2010). System identification study of a 7-story full-scale building slice tested on the UCSD-NEES shake table. *Journal of Structural Engineering*, 137(6):705–717.

Mofjeld, H. O., Whitmore, P. M., Eble, M. C., Gonzlez, F., and Newman, J. C. (2001). Seismic-wave contributions to bottom pressure fluctuations in the North Pacific: Implications for the DART tsunami array. *Proc. Int. Tsunami Sym*, pages 5–10.

Mori, N., Takahashi, T., and Group, T. . T. E. T. J. S. (2012). Nationwide post event survey and analysis of the 2011 Tohoku earthquake tsunami. *Coastal Engineering Journal*, 54(01).

Mori, N., Takahashi, T., Yasuda, T., and Yanagisawa, H. (2011). Survey of 2011 Tohoku earthquake tsunami inundation and run-up. *Geophysical Research Letters*, 38(7).

Morra, G., Geller, R. J., Grilli, S. T., Karato, S.-i., King, S., Lee, S.-M., Tackley, P., and Yuen, D. (2013). Growing understanding of subduction dynamics indicates need to rethink seismic hazards. *Eos, Transactions American Geophysical Union*, 94(13):125–126.

Mungov, G., Eblé, M., and Bouchard, R. (2013). Dart® tsunameter retrospective and real-time data: A reflection on 10 years of processing in support of tsunami research and operations. *Pure and Applied Geophysics*, 170(9-10):1369–1384.

Nakamura, Y. and Saita, J. (2007). Uredas, the earthquake warning system: Today and tomorrow. In *Earthquake Early Warning Systems*, pages 249–281. Springer.

Nikolaidis, R. M., Bock, Y., Jonge, P. J., Shearer, P., Agnew, D. C., and Van Domselaar, M. (2001). Seismic wave observations with the global positioning system. *Journal of Geophysical Research*, 106(B10):21897–21916.

Noda, H. and Lapusta, N. (2013). Stable creeping fault segments can become destructive as a result of dynamic weakening. *Nature*, 493(7433):518–521.

Ohmachi, T., Tsukiyama, H., and Matsumoto, H. (2001). Simulation of tsunami induced by dynamic displacement of seabed due to seismic faulting. *Bulletin of the seismological society of America*, 91(6):1898–1909.

Ohta, Y., Kobayashi, T., Tsushima, H., Miura, S., Hino, R., Takasu, T., Fujimoto, H., Iinuma, T., Tachibana, K., and Demachi, T. (2012). Quasi realtime fault model estimation for nearfield tsunami forecasting based on rtkGPS analysis: Application to the 2011 Tohokuoki earthquake (Mw 9.0). *Journal of Geophysical Research*, 117(B2).

Okada, Y., Kasahara, K., Hori, S., Obara, K., Sekiguchi, S., Fujiwara, H., and Yamamoto, A. (2004). Recent progress of seismic observation networks in Japan-Hi-net, F-net, K-NET and KiK-net. *Earth Planets and Space*, 56(8):xv–xxviii.

Okal, E. A., Fritz, H. M., Synolakis, C. E., Borrero, J. C., Weiss, R., Lynett, P. J., Titov, V. V., Foteinis, S., Jaffe, B. E., and Liu, P. L.-F. (2010). Field survey of the Samoa tsunami of 29 September 2009. *Seismological Research Letters*, 81(4):577–591.

Olson, A. H. and Anderson, J. G. (1988). Implications of frequency-domain inversion of earthquake ground motions for resolving the space-time dependence of slip on an extended fault. *Geophysical Journal*, 94(3):443–455.

Olson, A. H. and Apsel, R. J. (1982). Finite faults and inverse theory with applications to the 1979 Imperial Valley earthquake. *Bulletin of the Seismological Society of America*, 72(6A):1969–2001.

Olson, E. L. and Allen, R. M. (2005). The deterministic nature of earthquake rupture. *Nature*, 438(7065):212–215.

O'Toole, T. B., Valentine, A. P., and Woodhouse, J. H. (2012). Centroid–moment tensor inversions using high-rate GPS waveforms. *Geophysical Journal International*, 191(1):257–270.

Ozaki, T. (2011). Outline of the 2011 off the Pacific coast of Tohoku earthquake (Mw 9. 0)-tsunami warnings/advisories and observations. *Earth, planets and space*, 63(7):827–830.

Panagiotou, M. (2008). *Seismic design, testing and analysis of reinforced concrete wall buildings*, volume PhD Thesis. University of California San Diego.

Paris, R., Lavigne, F., Wassmer, P., and Sartohadi, J. (2007). Coastal sedimentation associated with the December 26, 2004 tsunami in Lhok Nga, west Banda Aceh (Sumatra, Indonesia). *Marine Geology*, 238(1):93–106.

Pérez-Campos, X., Melgar, D., Singh, S. K., CruzAtienza, V., Iglesias, A., and Hjörleifsdóttir, V. (2013). Rapid estimation of fault parameters for tsunami warning along the Mexican subduction zone: A scenario earthquake in the Guerrero seismic gap. *Seismological Research Letters*, 84(3):474–484.

Pillet, R. and Virieux, J. (2007). The effects of seismic rotations on inertial sensors. *Geophysical Journal International*, 171(3):1314–1323.

Rauch, H. E., Striebel, C., and Tung, F. (1965). Maximum likelihood estimates of linear dynamic systems. *AIAA journal*, 3(8):1445–1450.

Riley, S. J., DeGloria, S. D., and Elliott, R. (1999). A terrain ruggedness index that quantifies topographic heterogeneity. *International Journal of Science*, 5:23–27.

Romano, F., Piatanesi, A., Lorito, S., D'Agostino, N., Hirata, K., Atzori, S., Yamazaki, Y., and Cocco, M. (2012). Clues from joint inversion of tsunami and geodetic data of the 2011 Tohoku-oki earthquake. *Scientific reports*, 2.

Saikia, C. K. (1994). Modified frequency-wavenumber algorithm for regional seismograms using filon's quadrature: modelling of Lg waves in eastern North America. *Geophysical Journal International*, 118(1):142–158.

Sandwell, D. T. and Smith, W. H. (2009). Global marine gravity from retracked Geosat and ERS-1 altimetry: Ridge segmentation versus spreading rate. *Journal of Geophysical Research*, 114.

Satake, K. (1995). Linear and nonlinear computations of the 1992 Nicaragua earthquake tsunami. In *Tsunamis: 1992–1994*, pages 455–470. Springer.

Satake, K., Fujii, Y., Harada, T., and Namegaya, Y. (2013). Time and space distribution of coseismic slip of the 2011 Tohoku earthquake as inferred from tsunami waveform data. *Bulletin of the seismological society of America*, 103(2B):1473–1492.

Sato, M., Ishikawa, T., Ujihara, N., Yoshida, S., Fujita, M., Mochizuki, M., and Asada, A. (2011). Displacement above the hypocenter of the 2011 Tohoku-oki earthquake. *Science*, 332(6036):1395–1395.

Satriano, C., Kiraly, E., Bernard, P., and Vilotte, J.-P. (2012). The 2012 Mw 8.6 Sumatra earthquake: Evidence of westward sequential seismic ruptures associated to the reactivation of a N-S ocean fabric. *Geophysical Research Letters*, 39(15).

Sekiguchi, H., Irikura, K., and Iwata, T. (2000). Fault geometry at the rupture termination of the 1995 Hyogo-ken Nanbu earthquake. *Bulletin of the Seismological Society of America*, 90(1):117–133.

Shao, G., Li, X., Ji, C., and Maeda, T. (2011). Focal mechanism and slip history of the 2011 Mw 9.1 off the Pacific coast of Tohoku earthquake, constrained with teleseismic body and surface waves. *Earth, planets and space*, 63(7):559–564.

Si, H. and Midorikawa, S. (2000). New attenuation relations for peak ground acceleration and velocity considering effects of fault type and site condition. In *Proceedings of 12th World Conference on Earthquake Engineering*.

Silver, P. and Jordan, T. (1982). Optimal estimation of scalar seismic moment. *Geophys Journal of the Royal Astronomical Society*, 70:755–787.

Simons, M., Minson, S. E., Sladen, A., Ortega, F., Jiang, J., Owen, S. E., Meng, L., Ampuero, J.-P., Wei, S., and Chu, R. (2011). The 2011 magnitude 9.0 tohoku-oki earthquake: Mosaicking the megathrust from seconds to centuries. *Science*, 332(6036):1421–1425.

Simpson, G. and Castelltort, S. (2006). Coupled model of surface water flow, sediment transport and morphological evolution. *Computers & Geosciences*, 32(10):1600–1614.

Singh, S., Pérez-Campos, X., Iglesias, A., and Melgar, D. (2012). A method for rapid estimation of moment magnitude for early tsunami warning based on coastal GPS networks. *Seismological Research Letters*, 83(3):516–530.

Smalley, R. (2009). High-rate GPS: How high do we need to go? *Seismological Research Letters*, 80(6):1054–1061.

Smyth, A. and Wu, M. (2007). Multi-rate Kalman filtering for the data fusion of displacement and acceleration response measurements in dynamic system monitoring. *Mechanical Systems and Signal Processing*, 21(2):706–723.

Sobolev, S. V., Babeyko, A. Y., Wang, R., Hoechner, A., Galas, R., Rothacher, M., Sein, D. V., Schröter, J., Lauterjung, J., and Subarya, C. (2007). Tsunami early warning using GPS-shield arrays. *Journal of Geophysical Research*, 112(B8).

Somerville, P. G., Smith, N. F., Graves, R. W., and Abrahamson, N. A. (1997). Modification of empirical strong ground motion attenuation relations to include the amplitude and duration effects of rupture directivity. *Seismological Research Letters*, 68(1):199–222.

Stein, S. and Okal, E. A. (2005). Speed and size of the Sumatra earthquake. *Nature*, 434(7033):581–582.

Subarya, C., Chlieh, M., Prawirodirdjo, L., Avouac, J.-P., Bock, Y., Sieh, K., Meltzner, A. J., Natawidjaja, D. H., and McCaffrey, R. (2006). Plate-boundary deformation associated with the great Sumatra–Andaman earthquake. *Nature*, 440(7080):46–51.

Suzuki, W., Aoi, S., Sekiguchi, H., and Kunugi, T. (2011). Rupture process of the 2011 Tohoku-oki mega-thrust earthquake (M9. 0) inverted from strong-motion data. *Geophysical Research Letters*, 38(7).

Tanioka, Y. and Ruff, L. J. (1997). Source time functions. *Seismological Research Letters*, 68(3):386–400.

Tanioka, Y. and Sataka, K. (1996). Fault parameters of the 1896 Sanriku tsunami earthquake estimated from tsunami numerical modeling. *Geophysical Research Letters*, 23(13):1549–1552.

Tatehata, H. (1997). The new tsunami warning system of the Japan meteorological agency. In *Perspectives on Tsunami Hazard Reduction*, pages 175–188. Springer.

Titov, V. and Gonzalez, F. (1997). *Implementation and testing of the Method of Splitting Tsunami (MOST) model*. US Department of Commerce, National Oceanic and Atmospheric Administration, Environmental Research Laboratories, Pacific Marine Environmental Laboratory.

Titov, V. V., Gonzalez, F. I., Bernard, E., Eble, M. C., Mofjeld, H. O., Newman, J. C., and Venturato, A. J. (2005). Real-time tsunami forecasting: Challenges and solutions. In *Developing Tsunami-Resilient Communities*, pages 41–58. Springer.

Trifunac, M. (1974). A three-dimensional dislocation model for the San Fernando, California, earthquake of February 9, 1971. *Bulletin of the Seismological Society of America*, 64(1):149–172.

Trifunac, M. D. and Todorovska, M. I. (2001). A note on the useable dynamic range of accelerographs recording translation. *Soil Dynamics and Earthquake Engineering*, 21(4):275 – 286.

Tromp, J., Komatitsch, D., Hjörleifsdóttir, V., Liu, Q., Zhu, H., Peter, D., Bozdag, E., McRitchie, D., Friberg, P., and Trabant, C. (2010). Near real-time simulations of global CMT earthquakes. *Geophysical Journal International*, 183(1):381–389.

Tsuda, K., Steidl, J., Archuleta, R., and Assimaki, D. (2006). Site-response estimation for the 2003 Miyagi-oki earthquake sequence considering nonlinear site response. *Bulletin of the Seismological Society of America*, 96(4A):1474–1482.

Tsuji, T., Kawamura, K., Kanamatsu, T., Kasaya, T., Fujikura, K., Ito, Y., Tsuru, T., and Kinoshita, M. (2013). Extension of continental crust by anelastic deformation during the 2011 Tohoku-oki earthquake: The role of extensional faulting in the generation of a great tsunami. *Earth and Planetary Science Letters*, 364:44–58.

Tsuruoka, H., Kawakatsu, H., and Urabe, T. (2009). GRiD MT (grid-based real-time determination of moment tensors) monitoring the long-period seismic wavefield. *Physics of the Earth and Planetary Interiors*, 175(1):8–16.

Tsushima, H., Hino, R., Fujimoto, H., Tanioka, Y., and Imamura, F. (2009). Near-field tsunami forecasting from cabled ocean bottom pressure data. *Journal of Geophysical Research*, 114(B6).

Tu, R., Wang, R., Zhang, Y., and Walter, T. R. (2014). Application of a net-based baseline correction scheme to strong-motion records of the 2011 Mw 9.0 Tohoku earthquake. *Geophysical Journal International*.

Wald, D. J. and Graves, R. W. (2001). Resolution analysis of finite fault source inversion using one-and three-dimensional Green's functions: 2. Combining seismic and geodetic data. *Journal of Geophysical Research*, 106(B5):8767–8788.

Wang, D. and Mori, J. (2011). Rupture process of the 2011 off the Pacific coast of Tohoku earthquake(Mw 9. 0) as imaged with back-projection of teleseismic P-waves. *Earth Planets and Space*, 63(7):603.

Wang, R., Martin, F., and Roth, F. (2003). Computation of deformation induced by earthquakes in a multi-layered elastic crust – FORTRAN programs EDGRN/EDCMP. *Computers and Geosciences*, 29:195–207.

Wang, R., Parolai, S., Ge, M., Jin, M., Walter, T. R., and Zschau, J. (2013). The 2011 Mw 9.0 Tohoku earthquake: Comparison of GPS and strong motion data. *Bulletin of the Seismological Society of America*, 103(2B):1336–1347.

Wang, R., Schurr, B., Milkereit, C., Shao, Z., and Jin, M. (2011). An improved automatic scheme for empirical baseline correction of digital strong-motion records. *Bulletin of the Seismological Society of America*, 101(5):2029–2044.

Wang, X. and Liu, P. L.-F. (2007). Numerical simulations of the 2004 Indian Ocean tsunamis—coastal effects. *Journal of Earthquake and Tsunami*, 1(03):273–297.

Webb, S. C. (1998). Broadband seismology and noise under the ocean. *Reviews of Geophysics*, 36(1):105–142.

Wei, S., Fielding, E., Leprince, S., Sladen, A., Avouac, J.-P., Helmberger, D., Hauksson, E., Chu, R., Simons, M., and Hudnut, K. (2011). Superficial simplicity of the 2010 El Mayor-Cucapah earthquake of Baja California in Mexico. *Nature geoscience*, 4(9):615–618.

Wolfe, C. J., Solomon, S. C., Laske, G., Collins, J. A., Detrick, R. S., Orcutt, J. A., Bercovici, D., and Hauri, E. H. (2009). Mantle shear-wave velocity structure beneath the Hawaiian hot spot. *science*, 326(5958):1388–1390.

Wright, T. J., Houlié, N., Hildyard, M., and Iwabuchi, T. (2012). Realtime, reliable magnitudes for large earthquakes from 1 Hz GPS precise point positioning: The 2011 Tohokuoki (Japan) earthquake. *Geophysical research letters*, 39(12).

Wu, C., Takeo, M., and Ide, S. (2001). Source process of the Chi-Chi earthquake: A joint inversion of strong motion data and global positioning system data with a multifault model. *Bulletin of the Seismological Society of America*, 91(5):1128–1143.

Wu, Y.-M., Kanamori, H., Allen, R. M., and Hauksson, E. (2007). Determination of earthquake early warning parameters, τc and Pd, for southern California. *Geophysical Journal International*, 170(2):711–717.

Wu, Y.-M. and Wu, C.-F. (2007). Approximate recovery of coseismic deformation from taiwan strong-motion records. *Journal of seismology*, 11(2):159–170.

Yabuki, T. and Matsu'Ura, M. (1992). Geodetic data inversion using a Bayesian information criterion for spatial distribution of fault slip. *Geophysical journal international*, 109(2):363–375.

Yagi, Y. (2004). Source rupture process of the 2003 Tokachi-oki earthquake determined by joint inversion of teleseismic body wave and strong ground motion data. *Earth Planets Space*, 56:311–316.

Yagi, Y., Nakao, A., and Kasahara, A. (2012). Smooth and rapid slip near the Japan trench during the 2011 Tohoku-oki earthquake revealed by a hybrid back-projection method. *Earth and Planetary Science Letters*, 355:94–101.

Yoshida, S. and Koketsu, K. (1990). Simultaneous inversion of waveform and geodetic data for the rupture process of the 1984 Naganoken–Seibu, Japan, earthquake. *Geophysical Journal International*, 103(2):355–362.

Yoshida, Y., Ueno, H., Muto, D., and Aoki, S. (2011). Source process of the 2011 off the Pacific coast of Tohoku earthquake with the combination of teleseismic and strong motion data. *Earth, planets and space*, 63(7):565–569.

Yue, H. and Lay, T. (2011). Inversion of high-rate (1 sps) GPS data for rupture process of the 11 March 2011 Tohoku earthquake (mw 9.1). *Geophysical Research Letters*, 38(7).

Zhu, L. and Rivera, L. A. (2002). A note on the dynamic and static displacements from a point source in multilayered media. *Geophysical Journal International*, 148(3):619–627.

Zumberge, J. F., Heflin, M. B., Jefferson, D. C., and M, W. M. (1997). Precise point positioning for the efficient and robust analysis of GPS data from large networks. *Journal of Geophysical Research*, 102:5005–5017.